

Special Issue Reprint

Finishing Operations to Enhance Surface Integrity of Parts

Edited by
Gilles Dessein and J. Antonio Travieso-Rodriguez

mdpi.com/journal/materials

Finishing Operations to Enhance Surface Integrity of Parts

Finishing Operations to Enhance Surface Integrity of Parts

Editors

Gilles Desein

J. Antonio Travieso-Rodriguez



Basel • Beijing • Wuhan • Barcelona • Belgrade • Novi Sad • Cluj • Manchester

Editors

Gilles Dessein
Université de Toulouse
Tarbes, France

J. Antonio Travieso-Rodriguez
Universitat Politècnica de
Catalunya
Barcelona, Spain

Editorial Office

MDPI
St. Alban-Anlage 66
4052 Basel, Switzerland

This is a reprint of articles from the Special Issue published online in the open access journal *Materials* (ISSN 1996-1944) (available at: https://www.mdpi.com/journal/materials/special_issues/finishing_manufacturing).

For citation purposes, cite each article independently as indicated on the article page online and as indicated below:

Lastname, A.A.; Lastname, B.B. Article Title. <i>Journal Name</i> Year , <i>Volume Number</i> , Page Range.
--

ISBN 978-3-0365-9284-8 (Hbk)

ISBN 978-3-0365-9285-5 (PDF)

doi.org/10.3390/books978-3-0365-9285-5

Cover image courtesy of J. Antonio Travieso-Rodriguez

© 2023 by the authors. Articles in this book are Open Access and distributed under the Creative Commons Attribution (CC BY) license. The book as a whole is distributed by MDPI under the terms and conditions of the Creative Commons Attribution-NonCommercial-NoDerivs (CC BY-NC-ND) license.

Contents

About the Editors vii

Stoyan Slavov, Diyan Dimitrov, Mariya Konsulova-Bakalova and Dimka Vasileva
Impact of Ball Burnished Regular Reliefs on Fatigue Life of AISI 304 and 316L Austenitic
Stainless Steels
Reprinted from: *Materials* **2021**, *14*, 2529, doi:10.3390/ma14102529 1

Víctor Meana, Eduardo Cuesta and Braulio J. Álvarez
Testing the Sandblasting Process in the Manufacturing of Reference Spheres for Non-Contact
Metrology Applications
Reprinted from: *Materials* **2021**, *14*, 5187, doi:10.3390/ma14185187 23

**Ismael Fernández-Osete, Aida Estevez-Urra, Eric Velázquez-Corral, David Valentin,
Jordi Llumà, Ramón Jerez-Mesa and J. Antonio Travieso-Rodriguez**
Ultrasonic Vibration-Assisted Ball Burnishing Tool for a Lathe Characterized by Acoustic
Emission and Vibratory Measurements
Reprinted from: *Materials* **2021**, *14*, 5746, doi:10.3390/ma14195746 37

Ariadna Chueca de Bruijn, Giovanni Gómez-Gras and Marco A. Pérez
A Comparative Analysis of Chemical, Thermal, and Mechanical Post-Process of Fused Filament
Fabricated Polyetherimide Parts for Surface Quality Enhancement
Reprinted from: *Materials* **2021**, *14*, 5880, doi:10.3390/ma14195880 55

Irene Buj-Corral, Lourdes Roderode-Lamo and Lluís Marco-Almagro
Optimization and Sensitivity Analysis of the Cutting Conditions in Rough, Semi-Finish and
Finish Honing
Reprinted from: *Materials* **2022**, *15*, 75, doi:10.3390/ma15010075 69

Mikel Casuso, Antonio Rubio-Mateos, Fernando Veiga and Aitzol Lamikiz
Influence of Axial Depth of Cut and Tool Position on Surface Quality and Chatter Appearance
in Locally Supported Thin Floor Milling
Reprinted from: *Materials* **2022**, *15*, 731, doi:10.3390/ma15030731 91

Nabil Jouini, Philippe Revel and Guillaume Thoquenne
Investigation of Surface Integrity Induced by Various Finishing Processes of AISI 52100 Bearing
Rings
Reprinted from: *Materials* **2022**, *15*, 3710, doi:10.3390/ma15103710 109

**Agnieszka Skoczylas, Kazimierz Zaleski, Jakub Matuszak, Krzysztof Ciecieląg,
Radosław Zaleski and Marek Gorgol**
Influence of Slide Burnishing Parameters on the Surface Layer Properties of Stainless Steel and
Mean Positron Lifetime
Reprinted from: *Materials* **2022**, *15*, 8131, doi:10.3390/ma15228131 123

**Alejandra Torres, Nuria Cuadrado, Jordi Llumà, Montserrat Vilaseca and
J. Antonio Travieso-Rodriguez**
Influence of the Stainless-Steel Microstructure on Tribological Behavior and Surface Integrity
after Ball Burnishing
Reprinted from: *Materials* **2022**, *15*, 8829, doi:10.3390/ma15248829 143

Eric Velázquez-Corral, Vincent Wagner, Ramón Jerez-Mesa, Jordi Lluma,
J. Antonio Travieso-Rodríguez and Gilles Desein
Analysis of Ultrasonic Vibration-Assisted Ball Burnishing Process on the Tribological Behavior
of AISI 316L Cylindrical Specimens
Reprinted from: *Materials* **2023**, *16*, 5595, doi:10.3390/ma16165595 155

About the Editors

Gilles Desein

Dr. Desein is currently working as a Full Professor at Ecole Nationale d'Ingénieurs de Tarbes, France. He received his Ph.D. degree from Université Paul Sabatier TOULOUSE, in 1997. His research lines are in the areas of Manufacturing Engineering, Aeronautics, Finite Element Method, Vibration Machining, CAD, Machine Tools. He has published more than 130 research papers and has been supervisor of more than 15 doctoral theses.

J. Antonio Travieso-Rodriguez

Dr. Travieso-Rodriguez works as Associate Professor at Mechanical Engineering department at Universitat Politècnica de Catalunya, from 2006. He received his PhD degree in Mechanical Engineering, fluids and Aeronautic, in 2010. His research lines are in the areas of Development and characterization of the Burnishing process in metals and Additive Manufacturing. He has published more than 60 research paper in indexed journals, 3 invention patents and 2 utility models. He has been Supervisor of 6 Doctoral theses as well.

Article

Impact of Ball Burnished Regular Reliefs on Fatigue Life of AISI 304 and 316L Austenitic Stainless Steels

Stoyan Slavov^{1,*}, Diyan Dimitrov², Mariya Konsulova-Bakalova¹ and Dimka Vasileva¹

¹ Department of Mechanical Engineering and Machine Tools, Technical University of Varna, 9010 Varna, Bulgaria; mbakalova@tu-varna.bg (M.K.-B.); d.vasileva@tu-varna.bg (D.V.)

² Department of Mechanics and Machine Elements, Technical University of Varna, 9010 Varna, Bulgaria; dm_dimitrov@tu-varna.bg

* Correspondence: sdslavov@tu-varna.bg; Tel.: +359-52-383-690

Abstract: The present work describes an experimental investigation of the fatigue durability of AISI 304 and AISI 316L austenitic stainless steels, which have regular reliefs (RR) of the IV-th type, formed by ball burnishing (BB) on flat surfaces, using a computer numerical control (CNC) milling center. The methodology and the equipment used for obtaining regular reliefs, along with a vibration-induced fatigue test setup, are presented and described. The results from the BB process and the fatigue life experiments of the tested austenitic stainless steels are gathered, using the approach of factorial design experiments. It was found that the presence of RR of the IV-th type do not worsen the fatigue strength of the studied steels. The Pareto, *t*-test and Bayesian rule techniques are used to determine the main effects and the interactions of significance between ball burnishing regime parameters. A stochastic model is derived and is used to find when the probability of obtaining the maximum fatigue life of parts made of AISI 304 or 316L reaches its maximum value. It was found that when the deforming force, the amplitude of the sinewaves and their wavenumber are set at high values, and the feed rate is set at its low value, the probability to reach maximum fatigue life for the parts made of AISI 304 or 316L is equal to 97%.

Citation: Slavov, S.; Dimitrov, D.; Konsulova-Bakalova, M.; Vasileva, D. Impact of Ball Burnished Regular Reliefs on Fatigue Life of AISI 304 and 316L Austenitic Stainless Steels. *Materials* **2021**, *14*, 2529. <https://doi.org/10.3390/ma14102529>

Keywords: ball burnishing; regular reliefs; surface topography; austenitic stainless steel; fatigue life; *t*-test; Bayesian rule

Academic Editors: Gilles Dessein, Stanislaw Legutko and J. Antonio Travieso-Rodriguez

Received: 5 April 2021
Accepted: 8 May 2021
Published: 13 May 2021

Publisher's Note: MDPI stays neutral with regard to jurisdictional claims in published maps and institutional affiliations.



Copyright: © 2021 by the authors. Licensee MDPI, Basel, Switzerland. This article is an open access article distributed under the terms and conditions of the Creative Commons Attribution (CC BY) license (<https://creativecommons.org/licenses/by/4.0/>).

1. Introduction

Austenitic stainless steels, such as AISI 304 and AISI 316L, have wide usage in various types of parts, mechanisms and constructions in many different industries. For instance, they have wide application in chemical and food industries, pharmaceuticals, medicine, and automotive, aircraft, and maritime industries, etc. The parts used in these industrial and life care fields are subjected to many strict requirements, such as high corrosion and wear resistance, surface hardness and mechanical strength, and must have high integrity contact surfaces with little roughness asperity, etc., in order to achieve the intended operational characteristics. Often, the operational conditions of their work include cyclic loads, which could lead to fatigue failures, resulting in significant shortening of their operational lifetime. While in some cases machine parts destroyed due to fatigue from mechanical devices are relatively easy and not too costly to replace, in other cases, such as orthopedic prostheses [1], this is not an easy and simple task. Therefore, the fatigue durability of such prostheses is of great importance for the patient. Destruction of mechanical parts due to fatigue or wear, for example, when food processing machines are used, can lead to small particles (debris) getting into the food, thus endangering the health and even the lives of consumers. Even an auxiliary part's fatigue failure can cause severe operational issues, violation of the whole mechanism or even destruction of the entire device or machine.

There are many approaches developed over the years in order to minimize fatigue failures. They can be divided into two large areas: the first one is related to the design

of the machine parts, and the second is related to the development of specific finishing processing technologies, which have led to improvement of fatigue strength.

Among the design approaches the most notable is “Infinite-life design” [2] which keeps all stresses below the limits of fatigue effects. This approach is used where safety and/or long life are more important than space and weight limitations. “Safe-life design” [3] allows fatigue cracks to occur during the operational period, but they never grow to a critical length. Some structures subjected to high stresses, such as aircraft wings and hulls, pressure vessels, and heavy duty bearings, employ this type of design. The designed “safe life” usually is about one-fourth of the predicted fatigue life. “Fail-safe design” allows cracks to occur, but they never lead to fatigue failure earlier than the scheduled maintenance. The maintenance process must detect, repair, or replace the damaged parts. This approach is employed mainly in the aircraft industry since the weight requirements are crucial and there are strict regulations for maintenance in comparison with other industries. “Damage-tolerant design” [4] includes fracture mechanics and takes into account the initial imperfections in the material structure. The approach is based on the assumption that imperfections (flaws, cracks, etc.) can exist in any structure, and these cracks propagate (and grow) during the usage period. This approach is commonly used in civil engineering, mechanical engineering, and aircraft engineering to manage the extension of cracks in structures by using the principles of fracture mechanics. In this approach, a corresponding specific maintenance program must provide detection and repair of accidental damage, corrosion, and fatigue failure before the structure residual strength is reduced below an allowable limit. Although the abovementioned fatigue-based design approaches have been implemented for a long time in engineering practice, it is still possible for fatigue failure situations to occur because of different shortcomings of design and omissions in implementation. There are many influencing factors which affect fatigue behavior [5], the most important of which are stress and strain concentrations; material properties and metallurgical factors; surface finish and directional properties; and type and nature of loading, etc.

Reduction of fatigue failures by using specific methods for parts production is the second strategic approach [6–10]. By choosing an appropriate processing method, the effect of various “defects”—caused by metallurgical factors, surface hardness, residual compressive or tensile stresses in the surface layer, surface roughness and topography, etc.—on fatigue endurance can also be significantly reduced. The surface roughness is of great importance among the technological factors because it is well known that fatigue failure usually originates on the surface of the part. There is evidence that, for steel, the higher the tensile strength, the more critical is the surface finish [11,12]. Because the surface condition has a significant effect on fatigue strength, some of the traditionally used finishing processes of machine parts, such as milling, turning, grinding, polishing, lapping, etc., cannot completely meet all requirements. The surface roughness after most of these processes has a typical topography with notches due to imperfections that occurred after removing the allowance. Residual tensile stresses and even cracks can occur after grinding, for example, due to intensive heating of the surface layer, which is usual for this finishing process [5,13,14].

A considerable increase of the fatigue strength can be achieved if finishing processes such as shot peening, deep rolling, ball burnishing (BB), etc., which are based on plastic deformation of the surface layer in a cold state, are applied [5,15,16]. After their application, compressive residual stresses are obtained in the surface layer, combined with the removal (or minimization of depth) of the notches from previous cutting operations [17]. Processes based on plastic deformation also increase the hardness of the surface layer, which favors wear resistance. When rolling or BB is applied to metastable austenitic stainless steels, such as the aforementioned AISI 304 and AISI 316L, the austenite (γ -phase) transforms into martensite (ϵ - and/or α' -) due to a recrystallization change caused by deformation energy, even at ambient temperature. On the other hand, a smooth surface topography with very little roughness (Ra criterion from 0.8 to 0.025 μm) can be achieved after rolling or BB is

applied as a finishing process [18,19]. This way, two of the abovementioned negative effects of the cutting finishing methods on fatigue resistance can be avoided.

Ball burnishing has several different varieties, depending on the purposes for which it is applied [20]. They are all related to the plastic deformation of the surface layer, but can differ in the way the deforming element moves along the parts' surface. When the goal is to achieve only surface smoothing, the classic BB schemes can be used [21], in which the trajectory of the deforming element is the same as that of the cutting tools in drilling, turning, and milling cutting operations. Recently, there has emerged more and more evidence that the BB process can be successfully implemented using computer numerical control (CNC) equipment, which allows application of different strategies and toolpaths [22–25]. Some authors [26] report improvements in BB tools that allow the simultaneous use of multiple deforming elements to increase the process productivity. Other authors [27] apply ultrasonic artificial vibrations to the deforming element in order to intensify the plastic deformation in the surface layer.

The BB process also can be applied in order to create a specific surface roughness (or so-called “regular reliefs”) in addition to improving the other aspects of surface layer integrity [28]. Regular reliefs (RR) are formed by the traces of plastic deformation that are left on the surface as result of the passage of the deforming element, which is pressed with a certain deforming force. Here the deforming tool must perform a more complex trajectory (in contrast to the classical one), involving additional oscillation with a certain frequency and amplitude. As a result, this type of BB process is called “vibratory ball burnishing” (VBB) [28]. The RR obtained by vibratory ball burnishing can be five different types, according to the classification given in [28], the most interesting of which is the IV-th type, which covers all of the processed surface and forms a completely new surface roughness. Depending on the regime parameters of the VBB, the RR of the IV-th type can have specific rectangular or hexagonal cell patterns, which significantly increase the ability to retain lubricants and micro debris and stop them from wearing the surfaces burnished by this method, in comparison with smoothed ones [29–31]. Although the roughness of the RR is greater than that of the smoothed surfaces, they offer better contact conditions, such as reaching liquid friction at lower speeds [32], optimizing the contact spots, and increasing the wear resistance, while the other advantages of the BB process remain the same.

When VBB is adapted for implementation by using a CNC lathe or milling machine, the complex toolpath for obtaining RR can be achieved by interpolation between the machine axes [33]. In this case, the additional reciprocating movement (or the “vibration” component) of the ball tool is not needed, which significantly simplifies its construction. The preliminary mathematical modeling [34,35] of the tool path and the higher precision of the CNC equipment give opportunity to obtain full or partial RR with higher dimensional precision and repeatability of the cells. In the present work this variant of the BB process was used in order to obtain RR of the IV-th type on flat surface of the test parts subjected to fatigue failure tests. This type of RR is expected to have no worse fatigue-failure behavior than the smoothed surfaces after applying other (traditional) variations of the BB process. The results from earlier conducted experiments with AISI 304 steel [36] support this expectation, but the obtained experimental data concern only few of the BB process conditions, and the statistical analysis used to evaluate the significance of the regime parameters of the process can be improved by using the Bayesian approach [37].

Based on the investigated sources, the current work's main goal is to investigate the effect of RR of the IV-th type obtained by BB on the fatigue life of AISI 304 and AISI 316L austenitic steels. Secondly, it aims to study the effects of the main BB process regime and relief parameters and their interactions over fatigue life.

Finally, it aims to create a stochastic model for calculation of the probabilities of reaching a certain number of cycles until fatigue failure, for the possible combinations of “low” and “high” levels of the BB regime's parameters for both investigated steels.

2. Materials and Methods

2.1. Materials

The materials used in this work were rolled sheets of austenitic stainless steels: AISI 304, provided by SARITAS Celik Sanayi ve Ticaret A.S. (Istanbul, Turkey) and AISI 316L, provided by Acerinox Europa SAU (Los Barrios, Spain), both with 4 mm thickness. The chemical compositions of these austenitic steels and their basic mechanical properties are given in Table 1.

Table 1. Chemical compositions and mechanical properties of austenitic stainless steels AISI 304 and AISI 316L.

Chemical Compositions %										
Material	C	Cr	Mn	Mo	N	Ni	P	S	Si	Co
AISI 304	0.021	18.20	1.550	-	0.059	8.100	0.031	0.001	0.380	-
AISI 316L	0.022	16.63	1.285	2.031	0.050	10.065	0.030	0.004	0.340	0.226
Mechanical Properties										
Material	Yield Strength, MPa	Tensile Strength, MPa	Elongation A5, %	HRB						
AISI 304	324.00	626.00	55.00	188.0						
AISI 316L	353.15	628.58	49.18	82.0						

2.2. Obtaining RR of the IV-th Type by BB Process, Implemented on CNC Milling Machine

2.2.1. Calculating the Toolpath Trajectory of the Ball Tool

Because RR were formed onto planar surfaces in the present work, the needed kinematics for the BB process could be borrowed from the classical vibratory BB process [34], but adapted for implementation with a contemporary CNC milling machine. This way the needed complex toolpath of the deforming tool (shown in Figure 1a,b), which is essential for the formation of RR of the IV-th type (see Figure 1c), could be achieved much more efficiently, and with a greater accuracy.

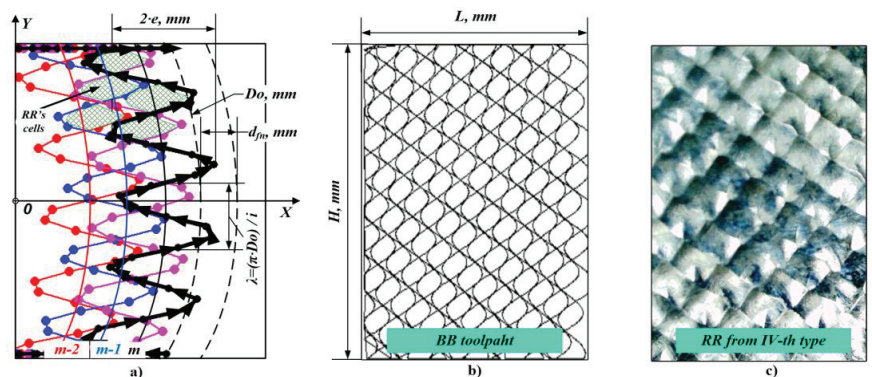


Figure 1. (a) Ball burnishing (BB) toolpath trajectory basic parameters; (b) BB toolpath distribution within the burnished surface boundaries; (c) resulting regular reliefs (RR) of the IV-th type with rectangular cells.

If we take into account the principle of the CNC equipment programming (i.e., ISO code) that the tool moves from its current position to the coordinates of the next position according to the NC code, the complex toolpath needed in the BB process can be divided into a relatively large number of short rectilinear segments that interpolate it with

a sufficient accuracy. The end point X and Y coordinates of each segment were calculated using the following system of functions [34] (see Figure 1a):

$$\begin{cases} X_{m,n} = \left(e \cdot \cos\left(\frac{2\pi \cdot n}{p}\right)_m + \frac{1}{2} \cdot \sqrt{D_0^2 + 4 \cdot e^2 \cdot \cos^2\left(\frac{2\pi \cdot n}{p}\right)_m} \right) \cdot \sin\left(\frac{2\pi \cdot n}{p} + i_p \cdot m\right) + d_{fn} \cdot m \\ Y_{m,n} = \left(e \cdot \cos\left(\frac{2\pi \cdot n}{p}\right)_m + \frac{1}{2} \cdot \sqrt{D_0^2 + 4 \cdot e^2 \cdot \cos^2\left(\frac{2\pi \cdot n}{p}\right)_m} \right) \cdot \cos\left(\frac{2\pi \cdot n}{p} + i_p \cdot m\right) \end{cases} \quad (1)$$

where p is the number of the toolpath points; n is the index of the current point from the toolpath ($n = 0, 1, 2, \dots, p$); m is the index of the current segment of the toolpath ($m = 0, 1, 2, \dots, q$); $q = L/d_{fn}$ is the number of all toolpath segments; D_0 , mm is the toolpaths' segment diameters; e , mm is half of the amplitude of the sinewaves; d_{fn} , mm is the linear distance between the toolpath segments; i_p is the fractional part of the ratio $i = \pi \cdot D_0 / \lambda$.

The parameter i_p determines the phase shift between sinewaves of the successive toolpath segments and can have values between 0 and 0.5. When $i_p \approx 0.15$, the RR have cells that resemble a hexagonal shape, and when $i_p \approx 0.45$ the cells are close to having a rectangular shape. The integer part of the parameter i sets the number of the sinewaves within each of the toolpath segments, thus determining their period λ , mm. It has an impact on the resulting RR cells' size along the Y axis (see Figure 1a).

The parameters e and d_{fn} from Equation (1) have a significant impact on the RR cells' size along the X axis. One of the important requirements to be met is that d_{fn} must be equal or less than e (i.e., $d_{fn} \leq e$) in order to guarantee obtaining RR of the IV-th type. Otherwise, if $d_{fn} > e$ there is a possibility of obtaining RR of types I-st, II-nd or III-th, which can be formed onto burnished surfaces, which contain "isles" with initial roughness obtained by the previous operation. This is undesirable because it can lead to non-uniformity of the physical and mechanical properties in the burnished surface layer. When the values of these parameters are set in the Equation (1), the results for the imprint diameter also must be taken into account.

Another important condition is that the toolpath points must be generated only within the burnished area boundaries, because there is no reason for the deforming tool to process the space outside the material. In [34] an algorithm is presented which is based on additional logical conditions to prevent generation of points outside the material boundaries. It also connects the sinewave segments with each other (see Figure 1a) and this way ensures the overall length of the toolpath is as short as possible. The outcome of the algorithm is a single polyline, defined by the points calculated by Equation (1), with an optimal length that depends on the shape and size of the area processed by the BB operation. The polyline created in this way can then be exported as a two-dimensional drawing (in DXF or DWG format), and be used in suitable CAM for further modeling of the BB operation.

2.2.2. Preparing the NC Code for the BB Operation

Unfortunately, the numerical control (NC) code cannot be written by hand in this case, because of the great number of points (sometimes several hundred thousand points) that the BB operation toolpath usually contains. The numerical control system of the most widespread milling machines also do not have preinstalled appropriate canned cycles that can be used for that purpose. However, the NC code needed to perform the BB operation in a suitable CNC milling machine can be obtained automatically, using appropriate CAM software. What particular CAM software is used is not of a great importance as long as it has a suitable milling component that allows the tool to be guided along a predetermined curve (in the present case the polyline, generated in the previous step), and a suitable postprocessor for the specific CNC milling machine that will be used.

After postprocessing the modeled toolpaths in CAM for all the BB operations according to the experimental designs, the corresponding NC codes were obtained.

2.3. Fatigue Failure Test Setup

2.3.1. Description of the Experimental Method and Setup

A reversal bending fatigue test similar to that in [36] was performed on a vibration exciter (see Figure 2). The test specimen was mounted as a cantilever beam on the exciter's vibration table. Two accelerometers were mounted: one at the free end of the specimen and the other at the exciter table. The vibration exciter was harmonically excited with a frequency close to the fundamental resonance mode shape of the specimen.

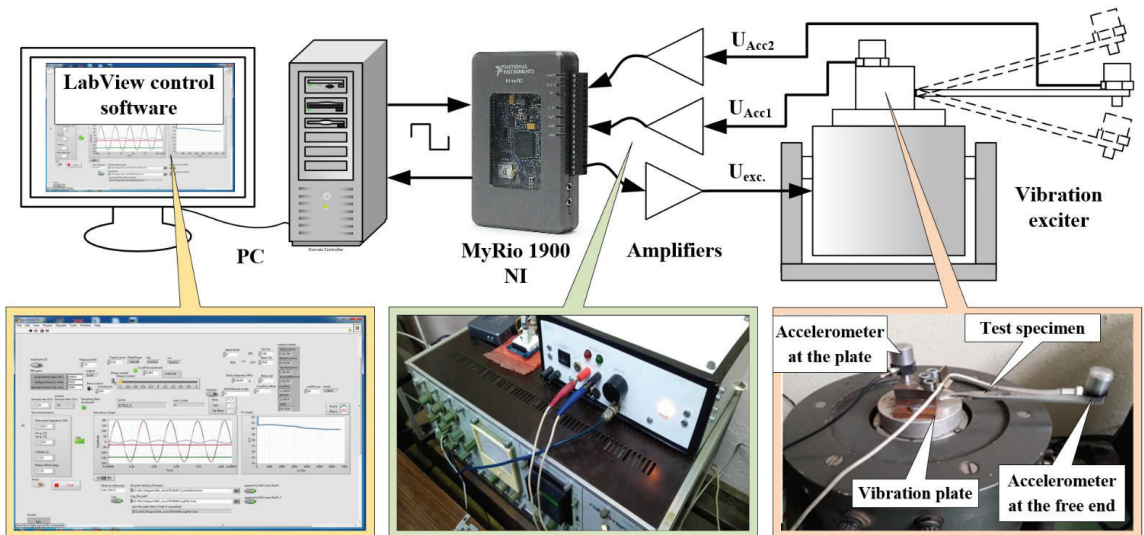


Figure 2. Components of the fatigue failure experimental setup.

As the difference between the tip and base acceleration is proportional to the applied stress, the load was controlled by adjusting the amplitude and the frequency of the shaker signal during testing. An algorithm similar to those realized in [38] was developed and installed in the MyRio 1900 (National Instruments, Austin, TX, USA) for automatic adjustment of the excitation signal frequency in order to keep the applied stress constant during the test. The test was stopped automatically when the algorithm was unable to maintain the preset stress amplitude by adjusting the frequency of the exciting signal. In order to ensure the stable working of the self-adjustment algorithm, the frequency of the exciting signal must be a little greater than that at the resonance. This way, the possibility of the exciting signal frequency starting the amendment in the wrong direction is eliminated. Using a personal computer and the LabView (National Instruments, Austin, TX, USA) visual programming environment, software was developed to monitor the experimental parameters and to count the cycles until fatigue failure of the specimens. The software saved incoming data from MyRio 1900 as logs, which were used for further analyses of the results.

All the specimens in the current experimental investigation were tested at equal loading, in order to investigate the impact of the BB regime parameters on fatigue failure.

2.3.2. Determining Experimental Conditions of the Fatigue Failure Test Using FE Analysis

The purpose of the conducted finite element (FE) analysis (see Figure 3a–d) was to determine the vibration fatigue test setup parameters, in order to assure invariable conditions of the fatigue failure experimental investigation. A linear dynamic study was carried out for the investigated materials. It was based on natural frequencies and mode

shapes to evaluate the response of the test specimens to dynamic loading, caused by shaker's table.

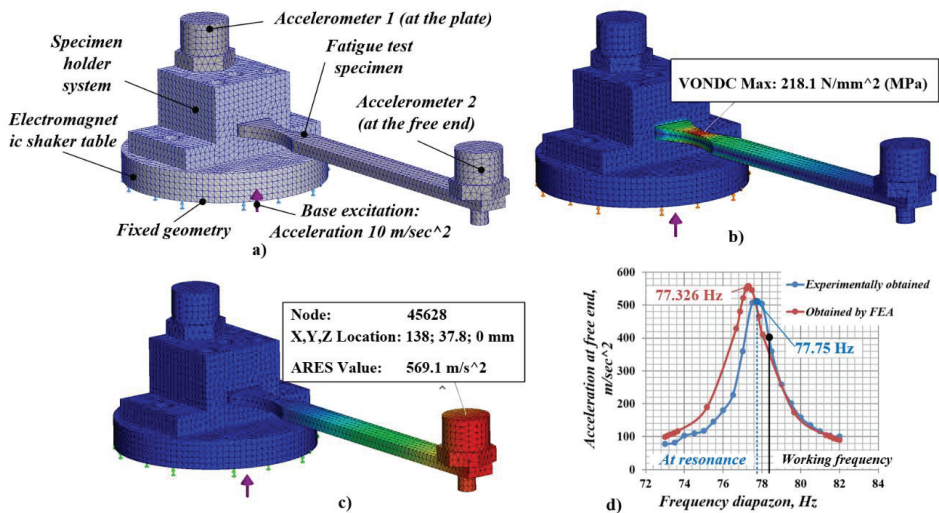


Figure 3. (a) Meshed 3D model with fixed geometry and excitation applied with (b,c) results from finite element analysis (FEA) for maximal obtained stress and acceleration at the free end of the specimen and (d) response graphs of “frequency-acceleration” (amplitude) obtained after FEA and experimental study conducted.

To conduct the FE analysis study, a SOLIDWORKS Simulation module (Education edition 2020–2021, SolidWorks Corporation, Waltham, MA, USA) was used. The input parameters in the FE model included the test specimens’ material properties (see Table 1) and applied uniform excitation (acceleration) of 10 m/s^2 which was restrained only in the vertical direction (see Figure 3a). The masses of the test specimens and the used acceleration sensor at the cantilever’s free end were set in the FE model, based on weight measurements of the real items, using a precise scale. The global damping ratio for each mode was set to be 0.01.

As the 3D components participating in the assembly had relatively simple geometric shapes, a standard high-quality mesh was used with the global size of the elements being 2.0 mm, and tolerance 0.1 mm. As a result, the total number of the obtained mesh elements was 66,382, and they had 99,510 nodes.

The obtained FE model results for maximum (Von Mises) stress (218.1 MPa) at the concentrator of the fatigue specimen, along with displacement (2.36 mm), and acceleration (569.1 m/s^2) at its free end (shown in Figure 3b–d), were calculated for the resonant frequency (77.326 Hz). The last two parameters were determined in the mesh model with the number 45,628, which was located as near as possible to the center of gravity of the accelerometer (see Figure 3c) in order to bring the simulation analysis as close as possible to the actual experimental conditions.

Using real test specimens (without RR formed by ball burnishing) and adjusting the electromagnetic shaker to sweep the frequency diapason around the obtained resonance frequency, a “frequency-acceleration” (amplitude) response graph was obtained. A similar response graph also was obtained from the FE model. Both graphs are shown together in Figure 3d for illustration. The comparison between them shows that the FE model gave results close to those obtained after the physical test. The resonant frequencies of the measured (77.75 Hz) and the calculated (77.33 Hz) response graphs differ by only 0.5%. The difference in respect to the maximum acceleration values at resonance between the measured (531 m/s^2) and the calculated (557.7 m/s^2) response graphs did not exceed 5%. Therefore, the results derived from the FE model can be considered as adequate.

Due to the algorithm implemented to automatically adjust the frequency of the excitation load of the exciter, which was used to control the acceleration at the free end of specimen and thus to keep the stresses obtained in the concentrator constant during the fatigue test, it was not advisable for the exact resonant frequency (i.e., the peak of the response graphs) to be chosen as a work point. In order to guarantee stable working of the auto-adjusting algorithm, the work frequency of the shaker had to exceed the resonant one. Using the FE model, and the obtained response graph, it was possible to specify previously the suitable initial working frequency and the corresponding acceleration at the free end, which defined the resulting stress at the concentrator of the fatigue specimens. This way the FE model facilitated the preparation of the fatigue failure experimental investigation, and allowed us to reach optimal experimental conditions without the need of carrying out many preliminary physical tests.

3. Experimental Research

In order to investigate the impact of the main regime parameters of the BB process on fatigue failure effects, an experimental investigation was conducted according to the first goal. Its purpose was to reveal the main effects and interactions between the BB regime parameters: deforming force— F , N and feed rate— f , mm/min, which were expected to have a major influence on the degree of the plastic deformation in the surface layer of the material, and the toolpath trajectory parameters: e , mm and i , which are known to determine the shape and the size of the RR cells. The experimental research was based on the approach of the full factorial designs [39]. The selected four factors (i.e., the BB regime parameters F , f , i , and e) varied on two levels—“low” and “high”. The experimental design executed is shown in Table 2.

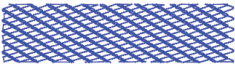
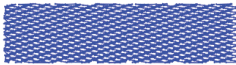
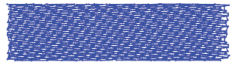

Table 2. Levels of factors (i.e., regime parameters of the BB operation).

Factor	Code	Low Level (−1)	High Level (+1)
Deforming force, F , N	A	1060	1735
Number of sinewave wavelengths, i	B	600.15	1200.15
Amplitude, e , mm	C	1.0	2.5
Feed rate, f , mm/min	D	150	300

As a response criterion, the number of cycles until fatigue failure was used. For every trial, included in the experimental design, two replicates were performed. The obtained results were subjected to several different analysis techniques, including the Pareto, t -test, and Bayesian rule.

The natural values of i , and e were selected on the basis of the previous research of the authors [40]. Their low and high levels were set to obtain RR with different size cells. In Table 3, the four toolpath types which had different unfolded lengths, derived by using Equation (1), are illustrated. The unfolded toolpath length gives the relief degree of imbrication, which is proportional to the number of passes in conventional burnishing technology.

Table 3. Unfolded length of the toolpaths at chosen factor level combinations.

Factor Level	Low Number: B = −1	High Number: B = +1
Low amplitude: C = −1	 Toolpath length: 1011.75 mm	 Toolpath length: 1783.25 mm
High amplitude: C = +1	 Toolpath length: 2231.34 mm	 Toolpath length: 4164.44 mm

The values for F and f were selected from the operational capabilities of the ball burishing tool [41], and those of the CNC milling machine (3-axes HAAS TM-1, USA [42]) used.

The rest of the BB parameters, which were not varied during the experiments, were fixed as follows: diameter of the deforming element was $dc = 14$, mm; number of points of the toolpath $p = 10,000$; the distance between toolpath segments d_{fn} was set to be equal of half of the sinewave amplitude e . In order to avoid jamming of the ball tool, Mobil DTE 25 was used as a lubricant for all ball burished experimental specimens.

The test specimens were made of austenitic stainless steels AISI 304 and AISI 316L, described in Section 2.1. They had a specific shape and dimensions, shown in Figure 4a,b. The specimens had two stress concentrators whose purpose was to guarantee the fatigue cracks developed in the narrowest section of the material (see Figure 4b), i.e., where the RR were formed after applying the BB operation. According to the experimental design shown in Table 2, $16 \times 2 = 32$ specimens were processed by BB for AISI 304 steel and another 32 specimens with the same characteristics for AISI 316L steel, respectively. Fourteen additional specimens (without RR) were also made of both of the steels (see Figure 4c,d). Their purpose was to adjust the fatigue test setup, as well as to compare the results obtained for the number of cycles to fatigue failure with and without the application of the BB operation.

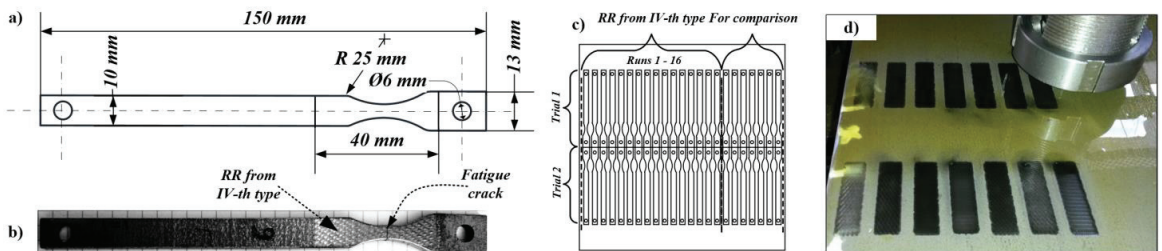


Figure 4. (a) Fatigue test specimens' shape and dimensions; (b) BB area with RR of the IV-th type; (c) arrangement of the specimens within the plates of AISI 304 and AISI 316L. (d) Physical BB-operation for obtaining the real RR from the IV-th type.

The BB operation was applied on both sides of the plates, with one and the same combinations of the regime parameter values, according to experimental design, shown in Table 2. Thus, each specimen processed by BB had two-sided RR. After all RR were formed onto both sides of the plate, the different specimens were cut off the plate using a CO₂ laser cutting machine MAZAK SUPER X48-Champion. In order to avoid the impact of the sharp edges after the laser cutting operation at the stress concentrator on fatigue life of the specimens, they were subjected to electropolishing.

4. Results

4.1. Preprocessing Data

As a result of the experiments, the fatigue testing number of cycles to failure (N_f) was obtained. According to the experimental plan, specimens of 304 and 316L steels were burished with 16 combinations. Low and high levels of the factors were coded with -1 and 1 . Levels of two- and three-factor interactions were calculated as a multiplication of main factor levels.

The specimens of both steel batches were tested successively at each combination (replication $r = 4$), resulting in a total of $16 \times 4 = 64$ specimens (32 specimens of each kind of steel). The descriptive statistics of the fatigue data are shown in Table 4. Considering that unlike AISI 316L, specimens of AISI 304 were notched, the fatigue life results were as expected. The 316L specimens' fatigue life lay predominantly in the 10^6 range, while the fatigue life of 304 specimens lay predominantly in the 10^5 range.

Table 4. Results from the fatigue tests (descriptive statistics).

Steel	Cycles to Failure (N_f)							
	Count	Mean	std	min	25%	50%	75%	max
304	32	152,909	101,099	23,929	61,192	152,450	234,882	419,450
316L	32	1,353,132	1,422,401	138,868	418,176	694,903	1,807,082	6,022,466

The fatigue life, even at constant stress amplitude, showed stochastic behavior. The materials' fatigue resistance due to the randomness of microdefect distribution, loading condition variations, and specimen preparation were the main sources of uncertainty. To model fatigue life, Normal and LogNormal distributions are commonly used.

Of particular interest in this study was the increase of the fatigue life due to burnishing operation with different combinations of regime parameters. To identify the characteristics of fatigue life gain, additional experiments with non-burnished specimens were carried out at the same loading conditions. The mean result for 304 steel was 2×10^4 cycles (tested four specimens). For 316L steel, the mean result was 14×10^4 cycles (tested three specimens). Based on these results, value $\log Cycles$ representing gain of the fatigue life due to burnishing were formed. Cycles to failure of burnished specimens are divided into base cycles of non-burnished specimens and ones, converted to logarithmic scale, using the decibel rule to get more physical meaning, (Equation (2))

$$\log Cycles = 20 \cdot \log \left(\frac{\text{cycles to failure of burnished specimen}}{\text{cycles to failure of base specimen}} \right) \tag{2}$$

Descriptive statistics of data converted to log scale are shown in Table 4. These data are considered as primary data for the statistical analysis.

To ensure comparability of the data for different materials, the $\log Cycles$ were scaled using a robust scaler from the Python library "SciKit Learn" [43]. This type of scaler uses the first and third percentile values and is more robust to outliers Equation (3). This kind of scaling can be applied to additional data (if replication of the experiment is made). The histograms of scaled data are shown in Figure 5.

$$y_{scaled} = \frac{y_i - q_1(0.25)}{q_3(0.75) - q_1(0.25)} \tag{3}$$

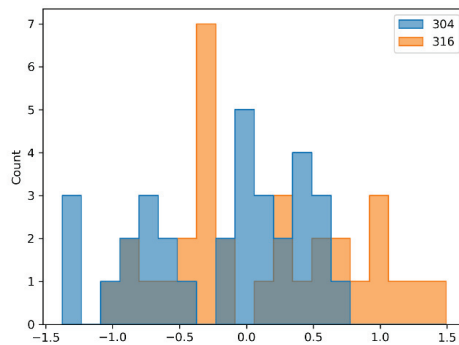


Figure 5. Scaled data histogram.

Most of the data were in the unit range $(-1; +1)$. The whole range of data was $(-1.5; +1.5)$. As shown in Table 5, for the particular materials included in this research, mean and $q_1(0.25)$ and $q_3(0.75)$ quantiles were quite similar and scaling just centered the data and converted standard deviation to 1.

Table 5. Results from the fatigue tests, converted to log scale (descriptive statistics).

Steel	logCycles (dB)							
	Count	Mean	std	min	25%	50%	75%	max
304	32.0	15.35	6.98	1.56	9.71	17.64	21.39	26.43
316	32.0	15.45	8.81	−0.07	9.50	13.68	22.22	32.67

4.2. Effects and T-Test

The main effect of a given factor is the mean difference in the level of response as the input moves from the low to the high level [44]. Combined two- and three-factor effects (interactions) are calculated by multiplication of the main factor levels. For example, two-factor interaction is positive when the inputs move in the same directions and negative when the inputs move in opposite directions. To visualize these effects, linear regression plots are presented on Figures 6–8. Each kind of steel is treated separately for comparison.

In previous research [36], only the results of fatigue testing of AISI 304 steel were analyzed. It was found that the main factors A and D, and the interactions AC and AD, had the greatest impact. The new data from the 316L steel fatigue testing showed similar behavior, according to the main factors. In contrast, interaction AD was very strong, but the slope was different, comparing steel types (positive for 316L and negative for 304), as shown in Figure 7. From the three-factor interactions, ACD seems to be important (Figure 8).

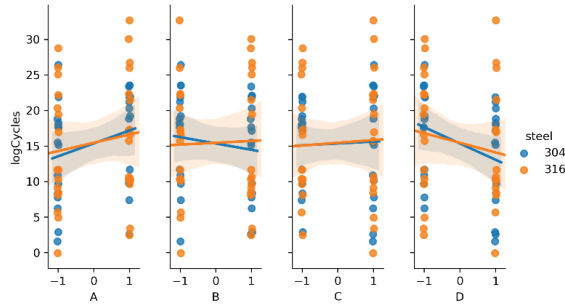


Figure 6. Regression plots representing the main effects.

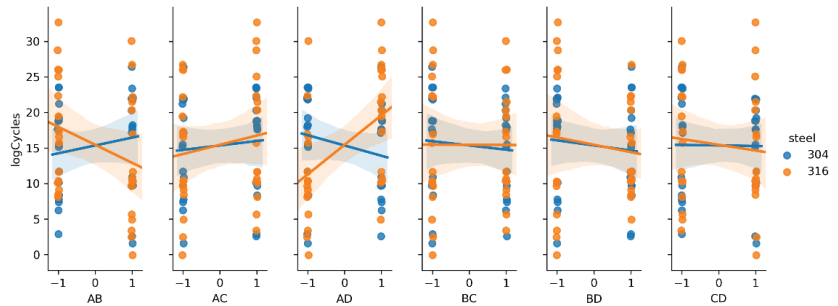


Figure 7. Regression plots representing two-factor interactions.

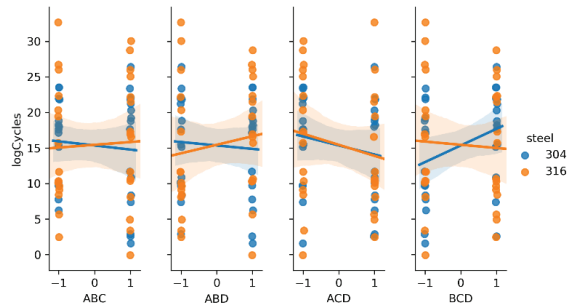


Figure 8. Regression plots representing three-factor interactions.

Since steels were burnished within the same experimental plan, and the fatigue testing procedure was the same, similar effects should be expected, so the new effects calculation was made considering the whole dataset. The main effects and interactions are given in descending order of their absolute values in Table 6. A Pareto chart (see Figure 9) shows that the first seven factors from the table should be considered significant (D, A, ACD, AD, AC, BCD, BD), because they covered about 80% of the total effect.

Table 6. Main effects, two- and three-factor interactions and *p* values.

Factors	Effect	abs(Effect)	<i>p</i> -Value
D	−3.654	3.654	0.084
A	2.984	2.984	0.108
ACD	−2.824	2.824	0.222
AD	2.707	2.707	0.206
AC	1.927	1.927	0.371
BCD	1.885	1.885	0.316
BD	−1.750	1.750	0.417
AB	−1.426	1.426	0.541
CD	−0.886	0.886	0.705
ABD	0.715	0.715	0.742

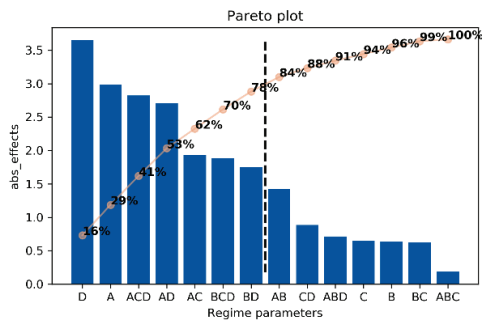


Figure 9. Pareto plot factors (regime parameters) and interactions.

The obtained results were confirmed by *t*-test. This test checks the null hypothesis if the mean values of the two groups of samples are identical. The *p*-values, calculated from the *t*-test, are given in the last column of Table 2. All of them were greater than 5% ($p > 0.05$), which means that the null hypothesis cannot be rejected with 95% level of confidence for all the factors and interactions. If value $p = 0.1$ (90% confidence) is taken as a significance level, the null hypothesis can be rejected for D and A factors and these factors are considered significant for the regression model. The values of these factors confirm the general findings for the burnishing processes: that higher force (A) and low federate

(D) guarantee a higher degree of plastic deformation, thus benefiting the fatigue life [28], but give no information about the influence of the regular relief degree of imbrication, connected with factors B and C.

More detailed statistical inference from such noisy data can be obtained, using the Bayesian approach. Bayesian models are called probability models, since as a result distribution rather than the point estimates for the unknown parameters are obtained. According to the Bayesian rule Equation (4), the posterior probability of parameters of interest θ , based on the observed data y , can be estimated, using our prior knowledge about these parameters (θ). The term $P(y|\theta)$, called likelihood, is a probabilistic model for the data. The denominator term $P(y)$ is the marginal probability of the data, called evidence. Since it is just a normalizing constant, it can be omitted and stated that posterior probability is proportional to likelihood times, prior probability.

$$P(\theta|y) = \frac{P(y|\theta) \cdot P(\theta)}{P(y)}, \tag{4}$$

where $P(\theta|y)$ —posterior; $P(\theta)$ —prior; $P(y|\theta)$ —likelihood;
 $P(y) = \int P(y|\theta) \cdot P(\theta) d\theta$ —evidence.

$$P(\theta|y) \propto P(y|\theta) \cdot P(\theta)$$

For the continuous random variables, $P(\theta|y)$ is a probability density function (PDF) of a certain distribution. So, Bayesian modeling requires first setting the appropriate likelihood distribution, which describes how the data can be generated, and second, choosing the prior probability distributions for all the unknown θ parameters. Prior distributions can be constructed as non-informative, i.e., diffuse or even improper, which PDF does not integrate to 1. If too informative (strong) prior distributions are used, there is a risk in ignoring the experimental data. Of course, in the presence of enough data, the prior choice is ignored, and likelihood dominates the posterior distribution. The Bayesian probabilistic model can be updated if new data are available just by setting the posterior distributions to prior for the new data.

For some of the simple cases, a closed form solution for the posterior density is given in the literature [37]. Nevertheless, for all probabilistic models, Bayesian inferences can be made just by simulation. To ensure random, non-correlated samples covering the whole distribution, Markov chain Monte Carlo (MCMC) sampling algorithms are used. Nowadays, numerous statistical packages and libraries for “R” and Python are available. Some of the most popular are WinBUGs, JAGS, Stan, and PyMC.

4.3. Regression Model

4.3.1. Ordinary Least Square Regression (OLS).

Ordinary least square linear regression Equation (5) assumes Gaussian distribution of the noise.

$$y = X\beta + \epsilon, \tag{5}$$

where $y \in \mathbb{R}^{n \times 1}$ —column vector of parameter of interest (regressors); $X \in \mathbb{R}^{n \times k+1} = [\{1\}, \{x_1\}, \{x_2\} \dots \{x_k\}]$, predictors (or design matrix); $\beta \in \mathbb{R}^{k+1 \times 1}$ —column vector of regression coefficients; $\epsilon \sim N(0, \sigma^2 I)$ —Gaussian noise.

As the effects and interactions are calculated, a linear regression model can be formed as Equation (6), where the first term is a mean of the dependent variable y , and to calculate the other coefficients i^{th} effect or interaction value should be divided by 2, since it shows the amount of change of the regressor as predictor x_i moves 2 steps, from -1 to $+1$.

$$\hat{y} = X\beta = \bar{y} + \frac{1}{2} \sum_{i=1}^k \sum effect_i \times x_i \tag{6}$$

The probabilistic model of linear regression can be expressed as Equation (7). Data y_i comes from Normal distribution with a mean equal to OLS estimation \hat{y} and variation $\sigma^2 = \epsilon$.

$$y_i \sim N(X\beta, \sigma^2), \tag{7}$$

where $i = 1, 2, \dots, n$ is the number of data points

From a Bayesian perspective, each regression coefficient can be treated as a random variable, coming from a Normal distribution with unknown mean and variance Equation (8).

$$\beta_i \sim N(\mu_i, s_i^2), \tag{8}$$

Under a non-informative Jeffrey’s prior, this problem has a closed form solution [37]. The resulting parameters of posterior are dominated by experimental data. The marginalized distribution for mean μ_i , with the integrated s_i^2 is a non-centered Student-t distribution Equation (9).

$$\mu_i | y \sim t_{n-k-1} (m_i, S_i^2) \tag{9}$$

The location parameter m_i is equal to the least squares estimation of regression coefficients, the scale parameter S_i^2 is equal to the standard error, and the degrees of freedom are equal to the degrees of freedom of the regression model. From this distribution, credible intervals CI and/or high-density intervals (HDI) with a certain probability can be formed.

Results from the OLS regression, including the first seven factors from the Pareto plot, are given in Table 7. To perform this regression, the Python library Statsmodels was used [45].

Table 7. Ordinary least square (OLS) regression results.

β_i Effect	β_i Mean	β_i std err	β_i 95% HDI	
			[0.025	0.975]
Intercept	15.4010	0.937	13.524	17.278
D	−1.8272	0.937	−3.704	0.050
A	1.4918	0.937	−0.385	3.369
ACD	−1.4118	0.937	−3.289	0.465
AD	1.3537	0.937	−0.524	3.231
AC	0.9636	0.937	−0.913	2.841
BCD	0.9427	0.937	−0.934	2.820
BD	−0.8748	0.937	−2.752	1.002

Looking at the 95% HDI, again the conclusion is that there was no significant factor with a significance level $\alpha = 5\%$.

4.3.2. Robust Regression

To decrease the influence of the outliers, a new probabilistic model was built. The response variable were modeled with a Student-t distribution. This distribution has the 3rd parameter ν (degrees of freedom), which controls the tails [46]. Lower values of ν lead to the distribution high tails and the regression is more robust to outliers. At about $\nu > 30$, the Student-t distribution coincides with the normal (Figure 10).

The parameters of the distribution were random variables, for which the appropriate prior distributions should be given. For regression coefficients, non-informative (Normal with high variance) were chosen. The degrees of freedom can be fixed or if treated as a random, variable exponential prior can be given.

$$\begin{aligned} y &\sim t(\hat{y}, \sigma^2, \nu), \\ \sigma^2 &\sim HalfCauchy(s_0) \\ \nu &\sim Exp(\lambda_0) \\ \beta_i &\sim N(\mu_{0i}, \sigma_{0i}^2) \end{aligned} \tag{10}$$

where v degrees of freedom; $s_0, \lambda_0, \mu_0, \sigma_0$ —known parameters.

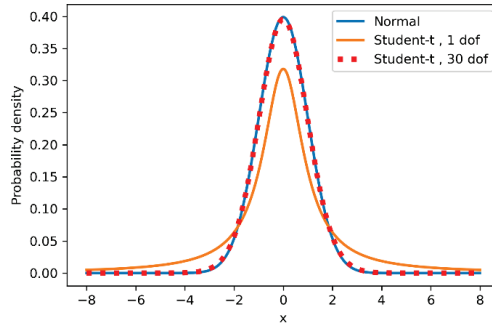


Figure 10. Student-t and normal distributions.

For sampling this Bayesian model, the PyMC3 Python library was used [47]. This probabilistic programming language uses clear and easy to understand syntax. In particular, the PyMC3 generalized linear model module (GLM) is used to define this model. It, by default, sets the non-informative priors for the regressors $\beta_i \sim N(0, 10^6)$. The model was defined just in 1 row with a string for the regression formula, data, and the family parameter, which set the likelihood to Student-t distribution (default was Normal). The degrees of freedom were fixed to $v = 1$. To sample from the mode, two independent Markov chains with length of 6000 samples were generated. The first 1000 samples of each chain were “burned” to avoid correlated samples. By default, PyMC3 uses the gradient based No-U-Turn-Sampler (NUTS).

After sampling the trace, a plot of posterior distributions was available. On the right, the generated Markov chains were presented, and on the left, the posterior distribution density of the model parameters. As can be seen from Figure 11 they converged well. There were no abrupt changes, patterns, or other weird observations.

More detailed inferences about sampling can be made by reviewing the summary statistics (Table 8). First, the r-hat for all parameters was 1.00, indicating that simulated chains came from one distribution. Effective sample size (ess_mean) shows the number of non-correlated samples in the chains. They should be more than 10% of draws. It is seen that for all the parameters, the values were in the range of 5000–7000 from 10,000 draws.

Table 8. Bayesian regression model summary.

Predictors	Summary Statistics of Posterior								
	Mean	sd	hdi_2.5%	hdi_97.5%	mcse_mean	ess_mean	ess_sd	ess_tail	r_hat
Intercept	15.007	0.991	13.007	16.883	0.012	0.008	7124.0	7105.0	1.0
A	2.074	1.035	−0.013	4.002	0.012	0.009	6936.0	6707.0	1.0
D	−1.964	0.978	−3.935	−0.077	0.011	0.008	8201.0	7225.0	1.0
AD	−0.251	1.117	−2.454	1.914	0.015	0.011	5470.0	5470.0	1.0
AC	1.133	1.000	−0.775	3.147	0.012	0.009	7253.0	6608.0	1.0
BD	−1.403	1.104	−3.508	0.844	0.014	0.010	6169.0	6169.0	1.0
ACD	−1.873	1.084	−3.873	0.352	0.014	0.010	6311.0	6311.0	1.0
BCD	1.545	1.045	−0.461	3.669	0.012	0.009	7049.0	6335.0	1.0
lam	0.063	0.023	0.026	0.109	0.000	0.000	5794.0	4586.0	1.0

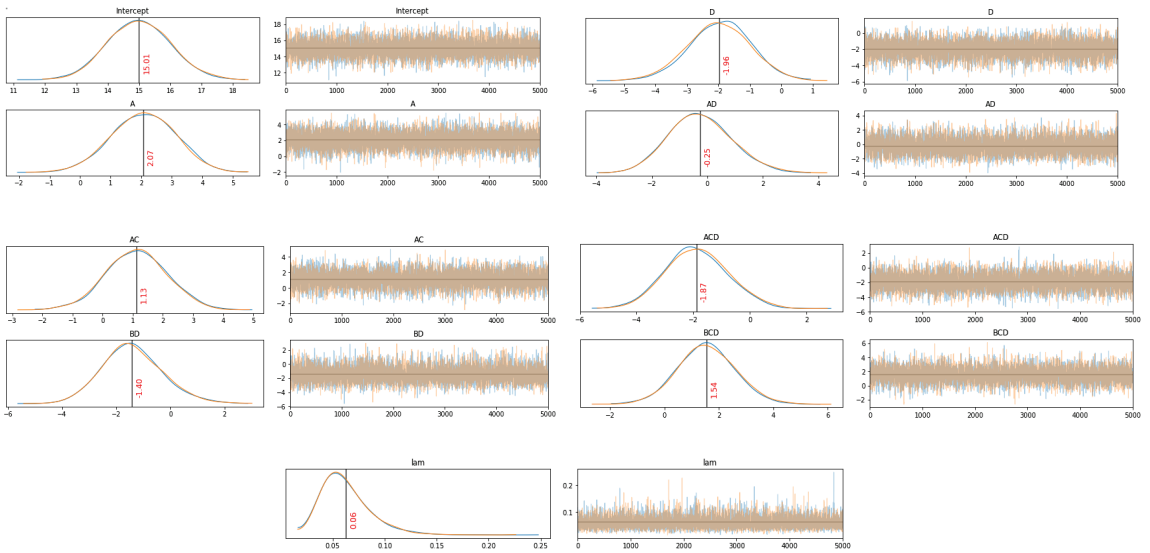


Figure 11. Trace plots (left—distributions; right—chains)

Intercept’s posterior mode was very close to the data mean (15.4). Posteriors of the regression coefficients were significantly away from zero, with the exception of AD coefficient posterior. It was centered close to zero, which indicates that it should be excluded from the model, unlike the previous OLS model, where its mean was positive with 95% HDI, predominantly on the positive side. To inspect other coefficients’ posteriors in detail, histogram plots with a highlighted 95% HDI and vertical line at zero as a reference value were plotted (Figure 12).

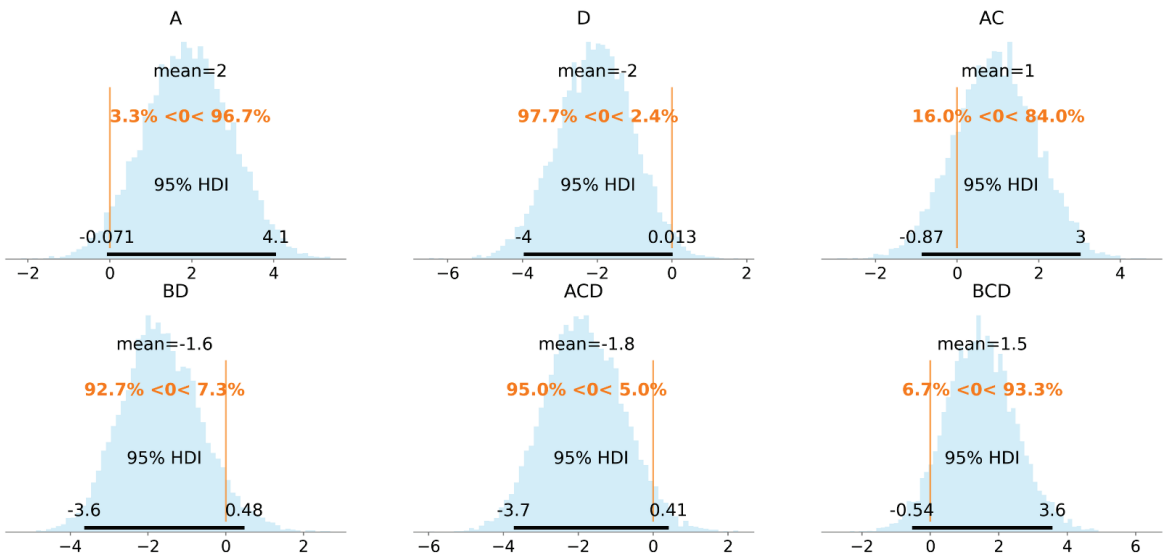


Figure 12. Posterior distributions of the proposed model coefficients. Histogram plot with 95% HDI and null reference value.

The posterior distributions of the regression coefficients AC and BD were not clearly on one of the sides (16% and 7.3% of the posterior lay below or above the reference value, respectively). Since these two factor interactions (AC, BD) were correlated with the three-factor interactions ACD and BCD, they can be considered excluded from the model due to overfitting.

The proposed probabilistic model can be further improved by centering the data by using the scaled data, setting the weakly informative priors to regression coefficients and the degree of freedom. The weakly informative is a prior distribution that covers the data behavior and generates the data at a reasonable scale but is not so strong as to influence the posterior. In addition, statements such as “weakly informative” depend crucially on what questions are being asked [48].

$$\begin{aligned}
 y_{centered} &\sim t(X\beta, \sigma^2, v) \\
 \sigma^2 &\sim HalfCauchy(s_0) \\
 v &\sim Gamma(2, 0.1) + 1 \\
 \beta_0 &\sim N(0, 1^2) \\
 \beta_i &\sim N(0, 1^2), \text{ for } i = 1, 2 \dots k
 \end{aligned}
 \tag{11}$$

Following some of the recommendations in [49], the Normal distributions with variance 1² for the regression coefficients and Gamma (2, 0.1) prior for the degrees of freedom were chosen Equation (11). By trying different numbers of regression coefficients, the final model consisted of four regression coefficients A, D, BD, ACD. The posterior histograms with a 90% HDI are given in Figure 13.

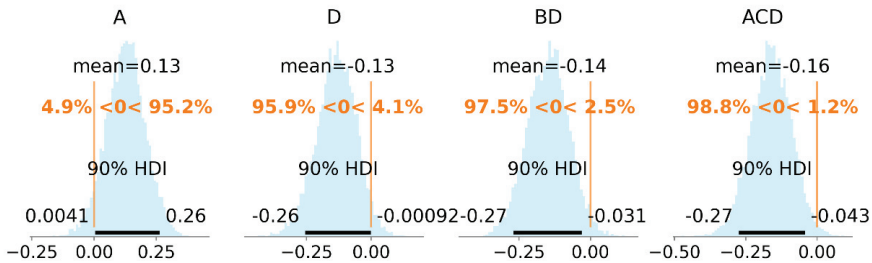


Figure 13. Posterior distributions of the final model coefficients. Histogram plot with 90% HDI and null reference value in scaled units.

5. Discussion

The proposed probabilistic model can be used for decision making. For example, in a lot of applications, a relief with certain parameters is needed, i.e., length and amplitude of the sinewave (B and C factors) are chosen due to technological requirements. So, the probabilistic question could look like: “Which force-feed rate (A–D) combination will give higher probability of reaching fatigue life gain of more than mean value (15 dB)?” To answer the question, the posterior distribution for the data (y) is formed by reversing the scaled data, fixing the regressors at a certain point, and incorporating the uncertainties of regression coefficients and data. For a relief with finer sells or a high degree of imbrication (B = 1, C = 1) the posteriors are shown in Figure 14. The probabilities $p(y > 15)$ calculated from the posteriors, for all combinations of relief parameters, are given in Table 9.

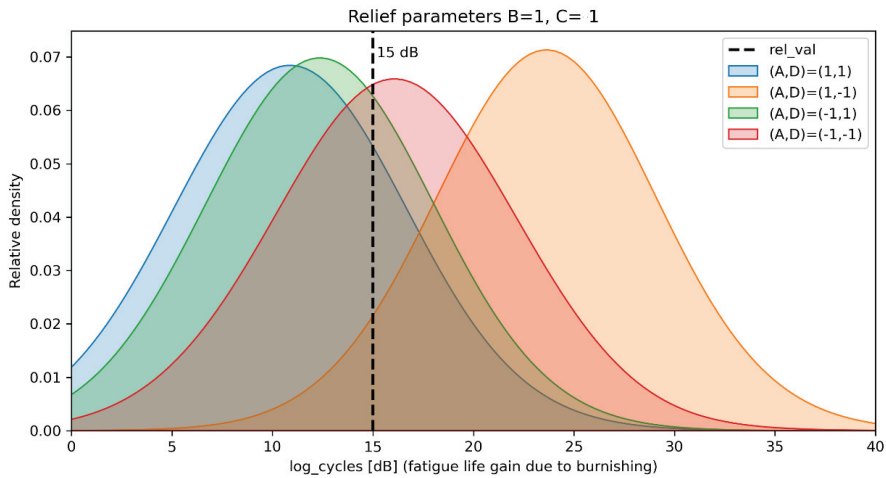


Figure 14. Posterior distributions of the fatigue life gain for relief with high degree of imbrication.

Table 9. Probability of reaching fatigue life gain of more than 15dB, $p(y > 15)$ for all combinations of relief parameters.

Relief Parameters (B, C).	Regime Parameters Values: Force Federate (A, D)			
	(1, 1)	(1, -1)	(-1, 1)	(-1, -1)
(1, 1)	0.21	0.97	0.29	0.62
(-1, 1)	0.50	0.85	0.62	0.30
(1, -1)	0.55	0.83	0.07	0.89
(-1, -1)	0.82	0.55	0.26	0.66

As an amplitude of the sinewave (factor C) gives higher effect to the relief’s degree of imbrication (see Table 9), for reliefs with high C value the feed rate should be kept low. For these kinds of reliefs, the optimal burnishing parameters are high force and low feed rate (A, D = 1, -1). For reliefs with low C value, the optimal burnishing regime is strongly dependent on sinewave length (factor B). If relief with a high B is needed, the feed rate (factor D) should be kept to a low value, unlike the relief with low B value, where high force and feed rate (A, D = 1, 1) are needed. Of course, all kinds of relief, using A, D = 1, -1 combination, result in the probability of reaching more than 15dB fatigue life gain, more than 50%.

The results from the proposed model support in general the published experimental results for conventional ball burnishing. Travieso-Rodriuez et al. investigated the fatigue life of burnished carbon steel specimens [50]. Their experimental results show that increasing the burnishing force and number of passes benefits fatigue life of the specimens. Rich experimental data for the influence of the burnishing regime on the fatigue strength is presented by Swirad [6]. He used a diamond composite burnishing element on low-alloyed carbon steel 40HM. The results showed that by increasing the burnishing force fatigue, the strength increased only to a certain threshold value. Beyond the threshold value, the fatigue strength decreased rapidly. Maximov et al. reported similar results for the influence of the burnishing force [51]. They used a diamond tool on aluminum alloy specimens and registered decrease of the fatigue life for the higher values of the burnishing force.

Other results of Swirad relate to the influence of feed rate and velocity. For burnishing tools with higher diameters, increasing the feed rate slightly decreases the fatigue strength after a certain value and the change of the velocity seems irrelevant.

The microstructural analysis of the burnished AISI 304 specimens given in [52] reports the phase composition in the surface layer. After the fatigue testing, strain-induced

martensite is developed. In specimens with a large content of the martensite phase, a shortened fatigue life has been registered. Since for austenitic steels the martensite phase is strain-induced, the higher martensite content in some of the specimens can be a result of the local fluctuation of the material properties or the burnishing force (burnishing is done on rolled sheets without annealing). In [53] the effect of strain-induced martensite on fatigue behavior is investigated. Martensitic transformation is registered during the fatigue tests. The more pronounced transformation is for prestrained specimens. In [54], a strong influence of martensitic content on fatigue limit is emphasized and optimum martensite content for a predeformed specimen of 26% is reported. These phenomena look like a reason to adopt a two-side posterior distribution ($p(\text{ACcoeff} < 0) = 16\%$) of AC regression coefficient in the first robust regression model (see Figure 3). Obviously, the chosen high value for burnishing force, combined with a high value of relief amplitude, is just below the threshold level and small random fluctuations can shorten the fatigue life.

In the above cited reference [52], a comparison of microhardness profiles of two burnished specimens is given, and the only difference in the relief is the sinewave length (factor B). There is no difference in the hardened layer depth. The only difference is the higher microhardness value, registered just below the surface in the specimen, burnished with a high B value regime, resulting in a slightly higher fatigue life. This phenomenon is captured by BD regression coefficient, whose posterior distribution lies on the negative side. This means that a low feed rate (factor D) in combination with a high sinewave length value (factor B) gives an additional improvement to the fatigue life.

6. Conclusions

The results from the conducted experiment show that the performed BB process on the test specimens leads in general to increase of the number of cycles until fatigue failure for both steels investigated. The gain in the fatigue life is more than 10 dB (about three times) for 75% of the AISI 304 and AISI 316L specimens, in comparison with those which had only preliminary plastic deformation, obtained after the steel sheets were rolled by the manufacturer (i.e., those without formed RR after applying BB). Thus, the formatted RR, after presenting a modification of the BB process, do not affect negatively the fatigue life results for these two steels. This is because the ridges of the RR cells' boundaries do not play the role of stress concentrators which cause the formation of microcracks. This can be reported as an important operational characteristic for those parts which have RR, formed by using BB on their contact surface, in order to ensure a low slip resistance and a low wear, due to increased abilities to retain lubricants, dust, and/or debris which causes wear, in comparison with the smooth surface topographies, obtained after other traditional finishing processes, such as grinding, polishing, traditional ball burnishing, etc. Surfaces with RR could be part of equipment which works in highly dusty, abrasive or saltwater environments in marine, mining, petroleum, or chemistry industries, etc., and for which there are also requirements for high fatigue strength. The experimentally obtained results give us grounds to recommend this variant of the BB process, in which a specific RR of the IV-th type could be formed as a suitable finishing operation for such parts, subjected to both cyclic loads, for work in high-wear operating conditions. Using the advances of the contemporary CNC production equipment, and the presented approach for mathematical modeling of the toolpath of the ball tool, allows BB to be carried out as a finishing operation on the same machine, along with the previous cutting operations. This makes the BB operation easy to add to standard (generic) sequences of manufacturing operations for the production of such machine parts.

As can be seen from Table 9 and Figure 14, the optimal combination of the BB regime's parameter values, in order to maximize the probability (up to 97%) of obtaining the maximum fatigue life of the parts made of AISI 304 or 316L, is $A = 1$, $B = 1$, $C = 1$ $D = -1$. In other words, the deforming force F , N , the amplitude of the sinewaves e , mm , and their number i must be set at their high values. However, the parameter feed rate f , mm/min must be set at its low values.

The presented approach for using the factorial experiment designs and Bayesian rule for data analysis reveals some tendencies about the impact of the main regime parameters of the BB process and their iterations on the fatigue life of the investigated steels. It provides good enough results in case of experimental investigations, in which it is not appropriate to perform a large number of trials, and the obtained results for the investigated parameter (i.e., fatigue failure cycles in our case) can have comparatively high variance. This can significantly shorten the time and facilitate the efforts for obtaining the needed results, in order to determine the optimal combination of BB regime parameters values in manufacturing conditions.

The methodological sequence for fatigue failure testing presented in the current work can also be applied to other materials, processing methods, and experimental plans, involving a different number of influencing factors. Our future work will be focused on its development and improvement in future research, similar to that presented in this paper.

Author Contributions: Conceptualization, S.S. and D.D.; methodology, S.S., D.D., and M.K.-B.; software, D.D. and M.K.-B.; validation, S.S. and D.D.; formal analysis, D.D.; investigation, S.S., D.D., and D.V.; resources, D.V.; data curation, D.D.; writing—original draft preparation, S.S. and D.D.; writing—review and editing, S.S., D.D., M.K.-B., and D.V.; visualization, S.S. and D.D.; supervision, S.S.; project administration, S.S. All authors have read and agreed to the published version of the manuscript.

Funding: This research received no external funding.

Institutional Review Board Statement: Not applicable.

Informed Consent Statement: Not applicable.

Data Availability Statement: The raw fatigue data and solved Bayesian models can be found and downloaded for free from the GitHub repository: <https://github.com/DMDimitrovJ/BurnishingFatigue> (accessed on 2 April 2021)

Conflicts of Interest: The authors declare no conflict of interest.

References

1. Griza, S.; Kwietniewski, C.; Tarnowski, G.; Bertoni, F.; Reboh, Y.; Strohaecker, T.R.; Baumvol, I.J.R. Fatigue failure analysis of a specific total hip prosthesis stem design. *Int. J. Fatigue* **2008**, *30*, 1325–1332. [[CrossRef](#)]
2. Olsson, E.; Ölander, A.; Öberg, M. Fatigue of gears in the finite life regime—Experiments and probabilistic modelling. *Eng. Fail. Anal.* **2016**, *62*, 276–286. [[CrossRef](#)]
3. Lambert, M.T.; Surhone, M. (Eds.) *Safe-Life Design*; Betascript Publishing: Beau Bassin, Mauritius, 2010; p. 104.
4. Stephens, R. Fatigue Design Criteria. *Encycl. Mat.: Sci. Technol.* **2001**, 2910–2918. [[CrossRef](#)]
5. Duggan, T.V.; Byrne, J. Factors Affecting Fatigue Behaviour. In *Fatigue as a Design Criterion*; Palgrave: London, UK, 1977; pp. 1–25.
6. Swirad, S. The effect of burnishing parameters on steel fatigue strength, Nonconventional Technologies Review. *Nonconv. Technol. Rev.* **2007**, *1*, 113–118.
7. Wagner, L.; Ludian, T.; Wollmann, M. Ball-Burnishing and Roller-Burnishing to Improve Fatigue Performance of Structural Alloys. In *Proceedings of the Engineering against Fracture*; Springer Science and Business Media LLC: Berlin/Heidelberg, Germany, 2009; pp. 1–11.
8. Prevéy, P.S.; Cammett, J.T. The influence of surface enhancement by low plasticity burnishing on the corrosion fatigue performance of AA7075-T6. *Int. J. Fatigue* **2004**, *26*, 975–982. [[CrossRef](#)]
9. Odintcov, L.G. Complex and combined approaches for strengthening work pieces as a way for development the ball burnishing methodologies. In Proceedings of the All Soviet Union Scientific and Technical Conference “New Technologies, Processes and Equipment for Ball Burnishing of the Materials”, Briansk, Russia, 21–23 October 1986. (In Russian).
10. Jerez-Mesa, R.; Fargas, G.; Roa, J.J.; Llumà, J.; Travieso-Rodríguez, J.A. Superficial Effects of Ball Burnishing on TRIP Steel AISI 301LN Sheets. *Metals* **2021**, *11*, 82. [[CrossRef](#)]
11. Dolan, T.J.; Sines, G.; Waisman, J.L. (Eds.) *Metal Fatigue*; McGraw-Hill: New York, NY, USA, 1959.
12. Nagîţ, G.; Slătineanu, L.; Dodun, O.; Ripanu, M.I.; Mihalache, A.M. Surface layer microhardness and roughness after applying a vibroburnishing process. *J. Mater. Res. Technol.* **2019**, *8*, 4333–4346. [[CrossRef](#)]
13. Luo, H.; Liu, J.; Wang, L.; Zhong, Q. The effect of burnishing parameters on burnishing force and surface microhardness. *Int. J. Adv. Manuf. Technol.* **2006**, *28*, 707–713. [[CrossRef](#)]
14. Kovács, Z.; Viharos, Z.J.; Kodácsy, J. The effects of machining strategies of magnetic assisted roller burnishing on the resulted surface structure. *IOP Conf. Series: Mater. Sci. Eng.* **2018**, *448*, 012002. [[CrossRef](#)]

15. Terres, M.A.; Laalai, N.; Sidhom, H. Effect of nitriding and shot-peening on the fatigue behavior of 42CrMo4 steel: Experimental analysis and predictive approach. *Mater. Des.* **2012**, *35*, 741–748. [CrossRef]
16. Hamadache, H.; Bourebia, M.; Taamallah, O.; Laouar, L. Surface hardening of 36 NiCrMo 6 steel by ball burnishing process. *Mater. Res. Express* **2019**, *6*, 106538. [CrossRef]
17. Korzynski, M. Modeling and experimental validation of the force–surface roughness relation for smoothing burnishing with a spherical tool. *Int. J. Mach. Tools Manuf.* **2007**, *47*, 1956–1964. [CrossRef]
18. Shiou, F.-J.; Huang, S.-J.; Shih, A.J.; Zhu, J.; Yoshino, M. Fine Surface Finish of a Hardened Stainless Steel Using a New Burnishing Tool. *Procedia Manuf.* **2017**, *10*, 208–217. [CrossRef]
19. Krawczyk, B.; Heine, B.; Engelberg, D.L. Performance Optimization of Cold Rolled Type 316L Stainless Steel by Sand Blasting and Surface Linishing Treatment. *J. Mater. Eng. Perform.* **2016**, *25*, 884–893. [CrossRef]
20. Mahajan, D.; Tajane, R. A review on ball burnishing process. *Int. J. Sci. and Res. Publ.* **2013**, *3*, 1–8.
21. Одинцов, Л. Упрочнение и Отделка Деталей Поверхностным Пластическим Деформированием. Справочник. 1987. Available online: <https://bg1lib.org/book/2393123/26298c?regionChanged=&redirect=185274069> (accessed on 23 February 2021).
22. Dzierwa, A.; Markopoulos, A.P. Influence of Ball-Burnishing Process on Surface Topography Parameters and Tribological Properties of Hardened Steel. *Machines* **2019**, *7*, 11. [CrossRef]
23. Gharbi, F.; Sghaier, S.; Al-Fadhalah, K.J.; Benameur, T. Effect of ball burnishing process on the surface quality and microstructure properties of aisi 1010 steel plates. *J. Mat. Eng. Perform.* **2011**, *20*, 903–910. [CrossRef]
24. Gómez-Gras, G.; Travieso-Rodríguez, J.A.; A González-Rojas, H.; Nápoles-Alberro, A.; Carrillo, F.J.; Dessein, G. Study of a ball-burnishing vibration-assisted process. *Proc. Inst. Mech. Eng. Part B J. Eng. Manuf.* **2014**, *229*, 172–177. [CrossRef]
25. Amdouni, H.; Bouzaiane, H.; Montagne, A.; Van Gorp, A.; Coorevits, T.; Nasri, M.; Iost, A. Experimental study of a six new ball-burnishing strategies effects on the Al-alloy flat surfaces integrity enhancement. *Int. J. Adv. Manuf. Technol.* **2017**, *90*, 2271–2282. [CrossRef]
26. Gharbi, F.; Sghaier, S.; Hamdi, H.; Benameur, T. Ductility improvement of aluminum 1050A rolled sheet by a newly de-signed ball burnishing tool device. *Int. J. of Adv. Manuf. Technol.* **2012**, *60*, 87–99. [CrossRef]
27. Jerez-Mesa, R.; Plana-García, V.; Llumà, J.; Travieso-Rodríguez, J.A. Enhancing Surface Topology of Udimet®720 Superalloy through Ultrasonic Vibration-Assisted Ball Burnishing. *Metals* **2020**, *10*, 915. [CrossRef]
28. Шнейдер, Ю.Г. Эксплуатационные Свойства Деталей Регулярным Микрорельефом. 2001. Available online: <https://books.ifmo.ru/file/pdf/147.pdf>. (accessed on 23 February 2021).
29. Slavov, S.D.; Dimitrov, D.M. Modelling the dependence between regular reliefs ridges height and the ball burnishing regime's parameters for 2024 aluminum alloy processed by using CNC-lathe machine. *IOP Conf. Series: Mater. Sci. Eng.* **2021**, *1037*, 012016. [CrossRef]
30. Georgiev, D.S.; Slavov, S.D. Methodology for determination of force of friction and coefficient of friction for the flat surfaces which have a regular distributed roughness obtained by using a flat vibratory burnishing. In Proceedings of the 1st International Congress MEET/MARIND, Varna, Bulgaria, 7 October 2002. Available online: <https://www.researchgate.net/publication/305754324> (accessed on 24 February 2021).
31. Iliev, I.V. Research on the influence of the five-axis ball-burnishing process regime parameters on the resulted cells properties from regularly shaped roughness. *Annu. J. Tech. Univ. Varna* **2019**, *3*, 40–53. [CrossRef]
32. Georgiev, D.S.; Slavov, S.D. Research on tribological characteristics of the planar sliding pairs which have regular shaped roughness obtained by using vibratory ball burnishing process. In Proceedings of the 3rd International Conference Research and Development in Mechanical Industry, Herceg Novi, Serbia and Montenegro, 19–23 September 2003. Available online: <https://www.researchgate.net/publication/318563346> (accessed on 24 February 2021).
33. Slavov, S.D. A contemporary approach for obtaining regularly shaped roughness by ball-burnishing process carried out using CNC controlled milling machines. *Fiabil. și Durabilitate* **2017**, *1*, 349–356.
34. Slavov, S. An Algorithm for Generating Optimal Toolpaths for CNC Based Ball-Burnishing Process of Planar Surfaces. In *Advances in Intelligent Systems and Computing*; Springer Science and Business Media LLC: Berlin, Germany, 2018; pp. 365–375.
35. Dzyura, V.; Maruschak, P.; Kozbur, H.; Kryvyi, P.; Prentkovskis, O. Determining Optimal Parameters of Grooves of Partially Regular Microrelief Formed on End Faces of Rotary Bodies. *Smart Sustain. Manuf. Syst.* **2021**, *5*, 18–29. [CrossRef]
36. Stoyan, D.S.; Diyan, M.D. Experimental research of the effect of the regular shaped roughness formatted by using new kinematical scheme for surface plastic deformation process on the number of cycles to fatigue failure of stainless steel 304L (CR18Ni8). *Евразийский Союз Ученых (ЕСУ)* **2016**, *4*, 11–22.
37. Gelman, A.; Carlin, J.B.; Stern, H.S.; Dunson, D.B.; Vehtari, A.; Rubin, D.B. *Bayesian Data Analysis*; CRC Press: Boca Raton, FL, USA, 2013.
38. Česnik, M.; Slavič, J.; Boltežar, M. Uninterrupted and accelerated vibrational fatigue testing with simultaneous monitoring of the natural frequency and damping. *J. Sound Vib.* **2012**, *331*, 5370–5382. [CrossRef]
39. Montgomery, D.C. Design and Analysis of Experiments. 2012. Available online: <http://faculty.business.utsa.edu/manderso/STA4723/readings/Douglas-C.-Montgomery-Design-and-Analysis-of-Experiments-Wiley-2012.pdf> (accessed on 24 February 2021).
40. Slavov, S.D.; Dimitrov, D.M. A study for determining the most significant parameters of the ball-burnishing process over some roughness parameters of planar surfaces carried out on CNC milling machine. *MATEC Web Conf.* **2018**, *178*, 02005. [CrossRef]

41. Slavov, S.D.; Iliev, I.V. Design and FEM static analysis of an instrument for surface plastic deformation of non-planar functional surfaces of machine parts. *Fiability Durab.* **2016**, *1*, 3–9.
42. Haas Automation, Inc. USA, TM-1 Vertical Toolroom Mill Haas CNC Machine. Available online: <https://www.haascnc.com/machines/vertical-mills/toolroom-mills/models/tm-1.html>. (accessed on 25 February 2021).
43. Pedregosa, F.; Varoquaux, G.; Gramfort, A.; Michel, V.; Thirion, B.; Grisel, O.; Duchesnay, E. Scikit-learn: Machine Learning in Python. *J. Mach. Learn. Res.* **2011**, *12*, 2825–2830.
44. Antony, J. A systematic methodology for design of experiments. In *Design of Experiments for Engineers and Scientists*, 2nd ed.; Antony, J., Ed.; Elsevier: Amsterdam, The Netherlands, 2014; pp. 33–50.
45. Seabold, S.; Perktold, J. Statsmodels: Econometric and statistical modeling with python. In Proceedings of the 9th Python in Science Conference, Austin, TX, USA, 28–30 June 2010.
46. Kruschke, J.K. Bayesian Estimation Supersedes the t Test. *PsycEXTRA Dataset* **2012**, *142*, 573–603. [[CrossRef](#)]
47. Salvatier, J.; Wiecki, T.V.; Fonnesbeck, C. Probabilistic programming in Python using PyMC3. *PeerJ Comput. Sci.* **2016**, *2*, e55. [[CrossRef](#)]
48. Gelman, A.; Simpson, D.; Betancourt, M. The Prior Can Often Only Be Understood in the Context of the Likelihood. *Entropy* **2017**, *19*, 555. [[CrossRef](#)]
49. Gelman, A.; Jakulin, A.; Pittau, M.G.; Su, Y.-S. A weakly informative default prior distribution for logistic and other regression models. *Ann. Appl. Stat.* **2008**, *2*, 1360–1383. [[CrossRef](#)]
50. Travieso-Rodríguez, J.A.; Jerez-Mesa, R.; Gómez-Gras, G.; Llumà-Fuentes, J.; Casadesús-Farràs, O.; Madueño-Guerrero, M. Hardening effect and fatigue behavior enhancement through ball burnishing on AISI 1038. *J. Mat. Res. Technol.* **2019**, *8*, 5639–5646. [[CrossRef](#)]
51. Maximov, J.T.; Anchev, A.P.; Dunchev, V.P.; Ganey, N.; Duncheva, G.V.; Selimov, K.F. Effect of slide burnishing basic parameters on fatigue performance of 2024-T3 high-strength aluminium alloy. *Fatigue Fract. Eng. Mater. Struct.* **2017**, *40*, 1893–1904. [[CrossRef](#)]
52. Dimitrov, D.M.; Slavov, S.D. Experimental research on the effect of the ball burnishing process, using new kinematical scheme on hardness and phase composition of surface layer of AISI 304L stainless steel. *MATEC Web Conf.* **2017**, *112*, 2001. [[CrossRef](#)]
53. Nakajima, M.; Akita, M.; Uematsu, Y.; Tokaji, K. Effect of strain-induced martensitic transformation on fatigue behavior of type 304 stainless steel. *Procedia Eng.* **2010**, *2*, 323–330. [[CrossRef](#)]
54. Müller-Bollenhagen, C.; Zimmermann, M.; Christ, H.-J. Very high cycle fatigue behaviour of austenitic stainless steel and the effect of strain-induced martensite. *Int. J. Fatigue* **2010**, *32*, 936–942. [[CrossRef](#)]

Article

Testing the Sandblasting Process in the Manufacturing of Reference Spheres for Non-Contact Metrology Applications

Víctor Meana, Eduardo Cuesta * and Braulio J. Álvarez

Departamento de Construcción e Ingeniería de Fabricación, Universidad de Oviedo, Calle Pedro Puig Adam, E.D.O.5, 33203 Gijón, Asturias, Spain; meanavictor@uniovi.es (V.M.); braulio@uniovi.es (B.J.Á.)

* Correspondence: ecuesta@uniovi.es

Abstract: To ensure that measurements can be made with non-contact metrology technologies, it is necessary to use verification and calibration procedures using precision artefacts as reference elements. In this environment, the need for increasingly accurate but also more cost-effective calibration artefacts is a clear demand in industry. The aim of this work is to demonstrate the feasibility of using low-cost precision spheres as reference artefacts in calibration and verification procedures of non-contact metrological equipment. Specifically, low-cost precision stainless steel spheres are used as reference artefacts. Obviously, for such spheres to be used as standard artefacts, it is necessary to change their optical behavior by removing their high brightness. For this purpose, the spheres are subjected to a manual sandblasting process, which is also a very low-cost process. The equipment used to validate the experiment is a laser triangulation sensor mounted on a Coordinate Measuring Machine (CMM). The CMM touch probe, which is much more accurate, will be used as a device for measuring the influence of sandblasting on the spheres. Subsequently, the influence of this post-processing is also checked with the laser triangulation sensor. Ultimately, the improvement in the quality of the point clouds captured by the laser sensor will be tested after removing the brightness, which distorts and reduces the quantity of points as well as the quality of the point clouds. In addition to the number of points obtained, the parameters used to study the effect of sandblasting on each sphere, both in contact probing and laser scanning, are the measured diameter, the form error, as well as the standard deviation of the point cloud regarding the best-fit sphere.

Keywords: sandblasting; precision spheres; non-contact metrology; laser scanning; laser sensors

Citation: Meana, V.; Cuesta, E.; Álvarez, B.J. Testing the Sandblasting Process in the Manufacturing of Reference Spheres for Non-Contact Metrology Applications. *Materials* **2021**, *14*, 5187. <https://doi.org/10.3390/ma14185187>

Academic Editor: Gilles Desein

Received: 22 July 2021

Accepted: 8 September 2021

Published: 9 September 2021

Publisher's Note: MDPI stays neutral with regard to jurisdictional claims in published maps and institutional affiliations.



Copyright: © 2021 by the authors. Licensee MDPI, Basel, Switzerland. This article is an open access article distributed under the terms and conditions of the Creative Commons Attribution (CC BY) license (<https://creativecommons.org/licenses/by/4.0/>).

1. Introduction

Metrological verification using optical equipment is of increasing interest in industry. In this sense, one of the most widespread technologies is laser triangulation sensors, either mounted on coordinate measuring arms or on tridimensional coordinate measuring machines, or even as independent sensors that can be integrated in multiple industrial applications. When a laser triangulation sensor is used for scanning (Figure 1), a laser beam is first projected onto the surface to scan, then the projected intersection line is captured by a digital camera, and finally the coordinates of the points are determined by trigonometric calculations (hence the term “triangulation”), taking into account the angle between the laser beam and the camera orientation, and the light intensity captured by the digital camera, among other parameters [1]. The highly extended deployment of these sensors has also been possible due to improvements in the accuracy and capabilities of these devices. Manufacturers have enhanced these instruments through adjustment and calibration processes, apart from increasing the quality of designs and materials for the internal components. Currently, many users and researchers employ these sensors for measurement (Geometrical Dimensional and Tolerancing - GD&T- verification) as well as for reverse engineering typical tasks.

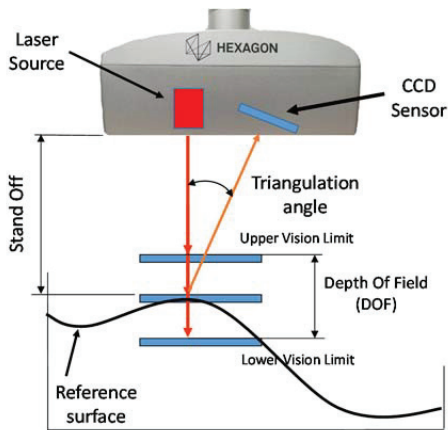


Figure 1. Principle of laser triangulation scanning.

HP-L-10.6	
Laser protection class	2 (IEC 60825-1:2014)
Laser	Visibly red (690 nm)
Standoff and depth (Z)	170 ±30 mm
Measuring accuracy ISO 10360-8:2013	ISO 10360-8:2013*
PForm.Sph.D95%.Tr:ODS (MPL) Probe dispersion value	34 µm
PForm.Sph.1x25.Tr:ODS (MPE) Probing form error	22 µm
Point Spacing (Min.)	30 µm
Laser Line Width (at mid-field)	24, 60 or 124 mm
Lines per second (max.)	53 Hz
Data rate (max.)	30,000 pts/sec
Ambient light immunity of the sensor	40,000 lx
Operating temperature	" +5 to +45 °C (41 to 113° F)"
Declared accuracy temperature range	" +15 to +32 °C (59 to 90° F)"
Relative humidity	90% non-condensing
Size LxWxH	HP-L-10.6A: 134x72x60 (87) mm
Weight	360 g – 379 g
Power supply	DC 18 to 28 V, 170 to 200 mA, protected against polarity reversal Protection
Protection against dust and water	IP64 (IEC60529) (except for warm-up connection)
Storage temperature	–25 to +70 °C (–13 to +158° F)

The improvement in accuracy, including traceability assessment [2–4], is a crucial factor to consider. It is precisely in this line of research where several factors that have an influence on laser triangulation sensors have been analyzed. Apart from the equipment's own parameters and specific tests [1,5,6], other parameters have also been taken into account, such as scanning speed [7] and scanning strategy [8,9]. Moreover, external parameters, like those derived from the part or object acting as the measurand, such as the material [10,11], color, surface roughness [12,13], ambient light [14], or even the type of the geometry to scan [3,15,16]. The idea is to assess the measurements that can be made with these non-contact technologies, thus extending their application beyond typical reverse engineering applications to metrological (GD & T inspection) ones.

Two of the fundamental parameters in the scanning quality of this type of sensors are the orientation of the sensor with regard to the target surface [8,17] and the surface finish of the part [12,18,19]. Shiny surfaces cause defects in the captured pointclouds, whereas, on the contrary, matte surfaces enhance the coverage of the capture. To achieve this type of surface finish over metallic processes, sandblasting is one of the most promising processes. In fact, for certain optical instruments, sandblasted surfaces are among the few surfaces that allow a measurement accuracy comparable to that achieved by contact measurement [18].

The aim of this work is to validate the sandblasting process as a process for modifying the surface condition of precision spheres in order to use these spheres as reference artefacts for adjustment, verification and/or calibration of optical sensors and non-contact reverse engineering equipment. Only if this process is sufficiently conservative with respect to the geometry of the precision spheres can it be valid for creating reference objects. On the contrary, if the damage or modification (dimensional or geometrical) is excessive, the process will not be suitable for this purpose.

In particular, a laser triangulation sensor (3D scanning) mounted on a Coordinate Measuring Machine (CMM) was used in this study. The CMM permits automation of the scanning process, avoiding errors derived from manual operation (as occurs with laser triangulation sensors mounted on coordinate measuring arms). Thus, factors like focal distance, scanning orientation, or scanning density were not considered as variables that can influence the experiment.

Although the finishing process is identical, the essential difference with respect to the work presented in [19] is that in that work the geometrical quality of the workpieces was qualified as very low, with a high surface roughness. The spheres were manufactured by metal laser sintering (SLM), and the post sandblasting was aimed at improving the geometrical quality, which was proved by both contact and laser measurements. In fact, the improvement ascertained by the contact measurement was very high.

However, the situation is the opposite in the case presented here. The original workpieces possess a high dimensional and geometrical accuracy, with very low deviations for the diameter and sphericity, due to the application of superfinishing processes and a final polishing. Conversely, this excellent surface finish makes it very difficult (and can even impede) the measurement of these spheres with laser triangulation sensors. By sandblasting these spheres, the purpose is to enable their use in laser measurement, but assuming a probable and unavoidable loss of accuracy caused by sandblasting.

Specifically, the objective of this article is, on one hand, to quantify the loss of dimensional and/or geometrical accuracy, and, on the other hand, to quantify the improvement in the laser capturing. The sandblasted spheres are suitable as reference elements only when the loss of accuracy is not too high and, on the contrary, when the improvement in laser capturing is substantial.

The final target of this research is to find out whether a low-cost process (manual sandblasting) can be applied to stainless steel precision spheres, of very low cost as well, to materialize calibration spheres for non-contact metrology. It is expected that the loss of precision in both diameter and form error of the post-blasting spheres will be low enough for this purpose. Ideally, the form errors of the sandblasted spheres should be at least one order of magnitude lower than the measurement uncertainty of the optical equipment. In any case, this experimentation will reveal which equipment is suitable for being calibrated with this type of sandblasted spheres.

Nowadays, the manufacturing of precision ceramic spheres (grades G3, G5 or G10, with sphericity $< 0.25 \mu\text{m}$, $Ra < 0.020 \mu\text{m}$, according to ISO 3290/DIN 5401 [20]) is very costly. This is mainly due to the fact that they are built specifically for this purpose, starting from ceramic powder, which is sintered and subsequently polished. They also require high hardness and wear resistance, using materials such as ruby, alumina, sapphire, or zirconia, among others. However, when they are intended to be used as reference elements for non-contact measurements, neither high hardness nor high wear resistance is required. In the context of the aims presented in this work, it is in fact sufficient that they are made of stainless materials, for example aluminum alloys or steels of qualities such as AISI 304, AISI 306L, or similar.

The spheres used in this research are stainless steel precision balls commonly used in the bearing industry, the cost of which is lower, but which also feature worse manufacturing qualities (G50 or G100 [20], with sphericity $< 2.5 \mu\text{m}$, $Ra < 0.1 \mu\text{m}$).

For optical applications, G100 accuracy or lower (according to ISO 3290 [20]) is enough unless the spheres show excessive brightness. Specifically, the idea of the experiment is to eliminate the very shiny finish (mirror-like) of the sphere surface, checking the variations in both diameter and form error caused by the sandblasting process. Another very important objective of the experiment is to quantify (if it exists) the improvement in the quality of the point clouds achieved by a laser triangulation equipment with respect to the cloud obtained on the polished, pre-sanded sphere.

The shot peening process, in this case sandblasting, will be carried out in a manual sandblasting machine using sand with fine grain size. Obviously, a certain variability is introduced even though the process variables are controlled (grain size, exposure time, distance, and the incident direction of the sandblasting stream onto the spheres). This variability must be studied so that the detected wear (or surface attack) will be assessed as rigorously and objectively as possible.

Therefore, the work includes sandblasting tests on stainless steel spheres of different diameters, evaluating (by CMM measurement) the variation of the mean diameter value and especially the loss of form error. In addition, it will also be interesting to analyze the variation of the standard deviation of the point cloud, as this is a crucial parameter in the measurement of the quality of the laser point cloud [19].

2. Materials and Methods

Since the process chosen to perform the modification of the surface condition is manual sandblasting, it requires statistical validation to be considered valid, minimizing the operator's influence on a given sphere. Therefore, the experimentation includes a range of different sets of spheres, each set corresponding to a different nominal diameter.

Specifically, 3 sets of spheres of different size were analyzed (3 plates including 10 spheres each, of \varnothing 10, \varnothing 18 and \varnothing 25 mm, respectively, as shown in Figure 2). From these analyses, the average values and standard deviations are determined for each one of the sets of 10 spheres, which are distributed over the corresponding plate with a similar layout. The diameter and form error values of the spheres of each set have been measured by contact (CMM with SP25M scanning probe) and by laser triangulation (Hexagon HP-L-10.6 sensor mounted on the CMM), first at their original polished state, before the surface attack, and secondly after being surface treated by sandblasting.

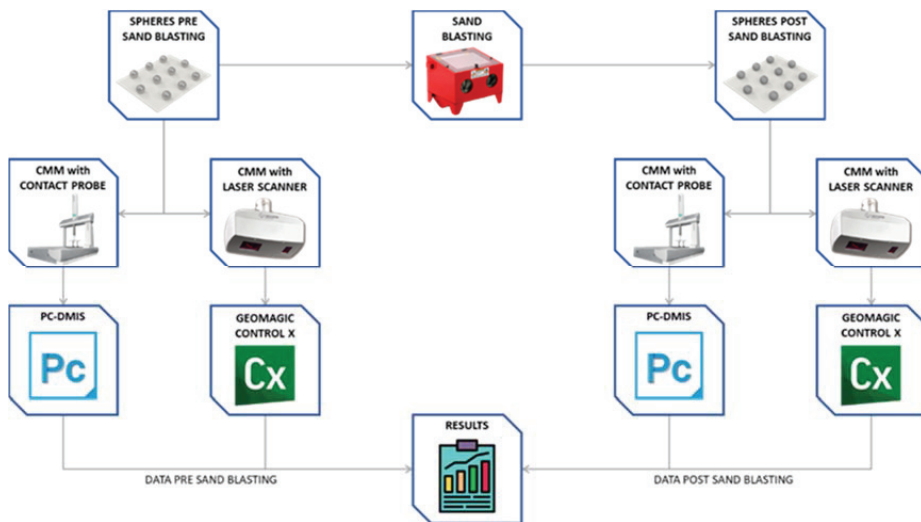


Figure 2. Research methodology.

Contact measurements of the spheres were carried out with a coordinate measuring machine (CMM), the DEA Global Image 091508 model, equipped with a PH10MQ indexing head. A Renishaw SP25 contact scanning probe can be mounted on this head. PC-DMIS 2018 R2 software was used to configure the CMM, setting parameters, paths, and number and distribution of points. The tip used was a \varnothing 1.5 mm ruby sphere for both polished and post-sanded spheres. The accuracy of this CMM is given by the manufacturer (Hexagon Metrology) according to ISO 10360-2 [21] and according to the latest calibration: $E_{0,MPE} = 2.2 + 0.003 \times L$ (μm), $R_{0,MPL} = 2.2 \mu\text{m}$.

Although this MPE parameter is not a substitute for uncertainty of dimensional or form measurement, the use of a sufficiently representative number of spheres, as well as several repetitions (at least 3 for each sphere), provides enough traceability of the measurements. This is especially true when working with calibrated equipment and obtaining average values.

For the non-contact measurement, a laser triangulation sensor from Hexagon Metrology, HP-L-10.6, was used, also attached to the CMM. This sensor comes with a calibration certificate (ISO 10360-8) [2] with a maximum error specification of 0.020 mm. On the other hand, the surface treatment of the spheres was carried out with the Sablex S-2 machine using WFA F100 alumina oxide (average grain size 106–150 μm , and true density 3.9 g/cm^3) as an abrasive element, projected onto the sphere surface at a pressure of 4 bar. Despite

being a manual process, the distance of the nozzle was kept in the range of 200–300 mm, with 5 orientations per plate (one orientation normal to the plate, and the other 4 at 45° with respect to the normal vector to the plate, distributed in 4 quadrants). The sandblasting operation time, for all orientations, was inferior to 1 min per plate.

Figure 2 shows a diagram illustrating the methodology followed and the equipment used for the development of the research.

The steps followed in the procedure were:

1. Manufacture of sphere plates. Three sets of rectangular plates were manufactured so that 10 spheres of the same diameter are mounted on each plate. The layout of the spheres of each plate makes handling easy and allows the univocal identification of each sphere inside. The base plates were also made of stainless steel.
2. Contact measurement. The 30 spheres were measured with the CMM obtaining reference values, both dimensional and geometrical, with high accuracy.
3. Non-contact measurement. All 30 spheres were digitalized using non-contact measurement techniques by means of a laser triangulation sensor controlling the power in real time and automatically.
4. Surface treatment of the samples. The surface condition of the spheres was modified by means of a sandblasting process with alumina oxide projection, obtaining sets with less brightness and a different texture.
5. Contact and non-contact measurement of the treated sets. CMM measurements were repeated for the post-sandblasted spheres, both by contact (post-sandblasting reference measurements) and non-contact with the laser triangulation sensor.
6. Analysis of results. The values of the measurements obtained from the contact measurements of the spheres before and after the sandblasting process were compared, as well as the point clouds obtained in both cases from the non-contact measurements.

Test Specimens Manufacturing and Justification of Material Selection

The material selected for the test plates is AISI 316L stainless steel. AISI 316L was an austenitic stainless steel with <0.03%C, 2%Mn, 17%Cr, 13%Ni, 3%Mo (EN symbol: X2CrNiMoN-17-14-3), with hardness HB < 215 and CTE = $14 \times 10^{-6} \text{ K}^{-1}$. The plates were also sandblasted prior to any measurement to avoid reflections on the spheres. The precision spheres were drilled using two hemispherical jaws, so that the drill bit did not produce any permanent marks or deformations. Each hole in the sphere was then threaded in order to screw the sphere onto the base plate. All spheres are made of AISI 316L of commercial grade G100 quality, with a sphericity lower than 2.5 μm and an arithmetic mean roughness $R_a < 0.1 \mu\text{m}$.

Figure 3a shows the 3-4-3 matrix design of each set of 10 spheres. This arrangement allows easy sandblasting of each sphere without influence from the adjacent sphere. In addition, it also facilitates the access of the laser triangulation sensor beam (especially above the equator) as well as the contact probe. The designations of the 10 spheres of each set and the coordinate axes of the reference system used for the measurement procedure are also presented in Figure 3a.

The coordinate system of each plate is defined from 3 spheres in such a way that it is independent of the supporting plate. According to its nomenclature (Figure 3a), the coordinate system is formed by spheres 1, 3 and 8 (XY plane), with sphere 1 being the origin and sphere 3 defining the Y axis. The same alignment definition has been applied for each of the 3 plates with spheres of $\varnothing 10$, $\varnothing 18$ and $\varnothing 25$ mm. Figure 3b shows a detail of the CMM contact measurement (pre-sandblasting) on $\varnothing 25$ mm spheres set.

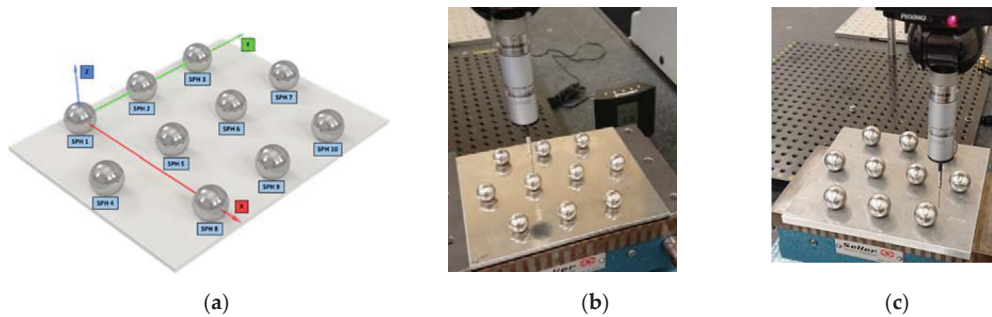


Figure 3. Plate with 10 spheres of the same diameter: (a) designation of the spheres and reference system; (b) CMM contact measurement of a set of ten spheres (25 mm diameter) on the original base plate; (c) CMM contact measurement of a sandblasted base plate.

3. Results

3.1. Pre-Sandblasting Measurements

During the non-contact measurement of the spheres in their original state (pre-sandblasting) reflections caused by the brightness of the base plate were observed (Figure 3b). These reflections added glare and reduced the quality of the point cloud captured by the laser sensor. This made it necessary to sandblast the base plate (Figures 3c and 4a), prior to the insertion of the pre-blasted spheres. Once the pre-blasted spheres had been measured by contact (CMM) and non-contact (laser), the spheres were sandblasted. A uniform and completely matt finish was obtained in the three sets (Figure 4b,c).

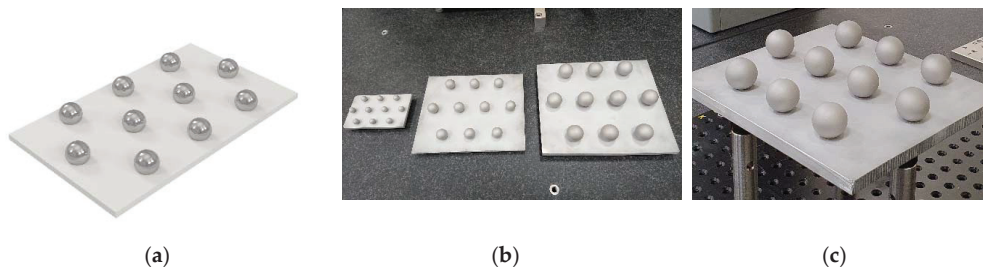


Figure 4. Sphere sets: (a) plate of 10 pre-sandblasted spheres (only the support plate has been sandblasted to avoid reflections); (b) general view of the 3 plates of 10, 18 and 25 mm diameter spheres; (c) detail of the plate with 25 mm post-sandblasting spheres.

Contact measurements were carried out with the SP25 head with a $\text{Ø} 1.5$ mm diameter ruby tip. The laboratory has an air conditioning system that maintains the temperature within 20 ± 1 °C. Measurements were performed on the three sets of spheres with a minimum scanning density of 1 point/ mm^2 for each of the hemispheres (only the upper half of each sphere is measured) of diameters of 10, 18 and 25 mm, respectively.

Table 1 shows the results of the contact measurements of the spheres in their original surface state before the sandblasting process. These data constitute the reference values for the subsequent comparative analysis that will be carried out with the measurements after sandblasting. Regarding contact measurements, the dimensions evaluated are the diameters of the spheres, the form error, and the standard deviation of the point cloud regarding the best-fit sphere. The average diameter values were 10.0026 mm for the $\text{Ø} 10$ mm spheres, 17.9977 mm for the $\text{Ø} 18$ mm spheres, and 25.0049 mm for the $\text{Ø} 25$ mm spheres, while the average form deviation was 0.0035 mm, 0.0023 mm, and 0.0028 mm, respectively. In contact measurement, the standard deviation parameter (Std. Dev.) tends to be close to 0 (in the higher case, it is lower than the CMM probing error: 0.002 mm).

In general terms, these results correspond correctly to the estimated accuracy G100 for stainless steel spheres.

Table 1. Measurement results of the original (pre-sandblasted) spheres.

Sphere Size	Average Diameter [mm]			Average Form Deviation [mm]			Average Best-Fit Sphere Std. Dev. (Laser)	Average No. Points (Laser)
	CMM	Laser	Difference	CMM	Laser	Difference		
Ø 10 mm	10.0026	10.0137	0.0111	0.0035	0.1908	0.1873	0.0309	10,431
Ø 18 mm	17.9977	17.8846	−0.1132	0.0023	0.1501	0.1478	0.0316	38,485
Ø 25 mm	25.0049	24.8608	−0.1441	0.0028	0.1492	0.1464	0.0320	73,079

The spheres were then measured using a laser triangulation sensor (HP-L-10.6 from Hexagon Metrology) assembled in the CMM (Figure 5b). To obtain a real and accurate comparison with the contact measurements, all measurements have been carried out under the same environmental conditions (light and temperature) and with the same procedure of alignment and sequence of the spheres. For the sphere captures, five orientations were used (four at 45° from the cardinal points and one from the vertical position, at 0°). These orientations were sufficient to capture at least the upper hemisphere of each sphere. The software used to capture the point clouds is the same PC-DMIS that controls the CMM, although Geomagic Control X software was preferred for point cloud processing, which involved the removal of points belonging to the base plate and those located below the equator of the spheres. Finally, a standard “2-Sigma” filter was applied to this trimmed cloud (hemisphere) to remove spurious points, clearly far from the spheres, which would distort all measurements.

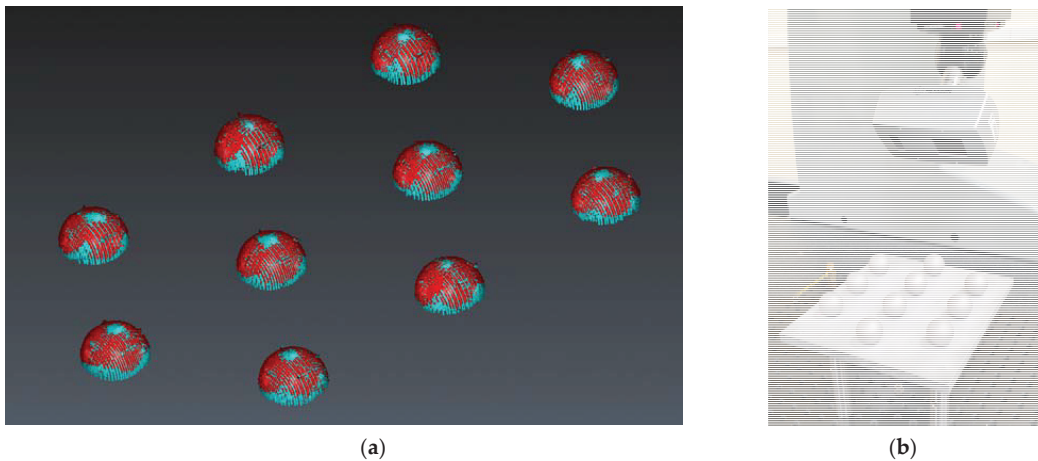


Figure 5. Laser scanning of the spheres: (a) point clouds captured at normal gain (red) and high gain (blue), both in pre-sanded state; (b) general view of the HP-L-10.6 laser sensor scanning at 45°.

The results obtained are also shown in the central area of Table 1. In addition to the diameter and the form deviation, the value of the standard deviation has been obtained when the cloud is fitted to a best-fit sphere (Least-Squares fitting). The average standard deviations are significantly larger than in the case of contact measurement, which corroborates the idea that a bright surface finish (these are “mirror polished” spheres) is not suitable for being captured with optical equipment. Note (Table 1) that both diameter and form deviation values are far from the reference values (even up to −0.144 mm for Ø 25 mm spheres or 0.187 mm for Ø 10 mm spheres).

On the other hand, the standard deviation of the values obtained by non-contact measurement on polished spheres (original state) reaches high values, on the order of

0.031 mm, regardless of the diameter value. These data show the problems that arise when non-contact measurement systems are used on polished parts because the surface brightness causes the generation of point clouds with poor metrological quality (Figure 5a).

Furthermore, laser measurements on the original spheres had to be carried out in high-gain mode (less sensitivity), because in normal-gain mode (high sensitivity), the sensor was not able to capture enough points, generating very poor clouds. As shown in Figure 5, due to the high brightness of the pre-sanded spheres, point clouds captured with normal gain (red cloud) cover the spheres very poorly, while the coverage is much higher with high gain (blue cloud). This effect is accentuated for the smaller spheres. In fact, in the case of 10 mm spheres, it was not possible to obtain accurate diameter values due to insufficient data. Thus, this high-gain mode allows the comparison between the pre- and post-sandblasting states.

3.2. Sandblasting and Post-Sandblasting Measurement

In accordance with the main objective of this work, the surface sandblasting treatment of the test samples was carried out using WFA F100 alumina oxide as the abrasive. The Sablex S-2 blasting machine was programmed to work at a constant pressure of 4 bar.

The roughness of the post-sandblasting spheres was measured with a contact roughness tester (TESA Rugosurf10[®]), and average values of $Ra = 0.5\text{--}0.6\ \mu\text{m}$ were obtained (with the original roughness values being $Ra < 0.1\ \mu\text{m}$). As an example, Figure 6 shows a roughness profile and its main parameters measured by the profilometer. Several roughness measurements were performed showing that the variability of Ra between each of the ten spheres was low, and independent of the position of the spheres on the plate. This confirms that the finishing achieved with the sandblasting process was adequate and repeatable.

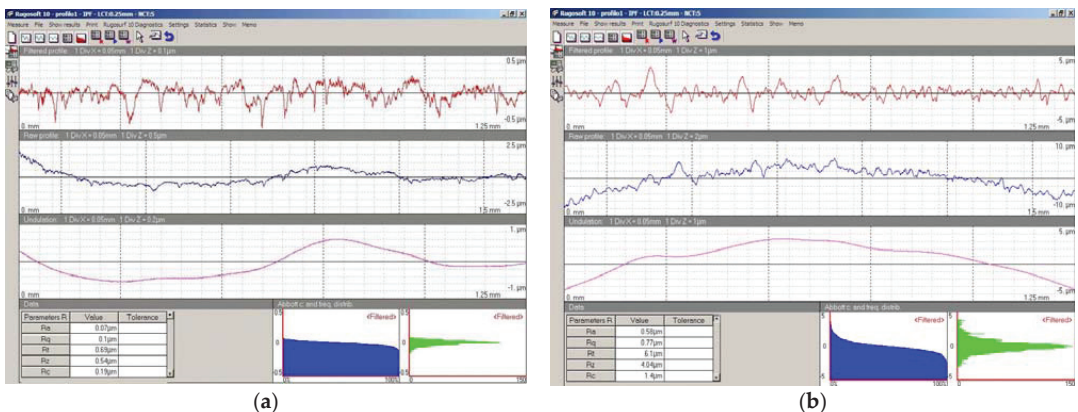


Figure 6. An example of the effect of sandblasting process in the roughness profile and parameters: (a) pre-sandblasted \varnothing 25 mm sphere, original G100; (b) post-sandblasted \varnothing 25 mm sphere.

From the geometrical and dimensional point of view analysis, and in the case of post-sandblasting, the measurements made by contact with the CMM machine show higher values for both the diameter of the spheres and the form deviation (Table 2). Please note that the sandblasting process generates a dimensional deviation with an average value of only $2.7\ \mu\text{m}$ and an increase in the form deviation of about $1.7\ \mu\text{m}$. At this point, it should be taken into account that this value is even lower than the maximum permissible error of the CMM, which is around $2.2\ \mu\text{m}$. It can therefore be concluded that, apart from a minimal variation in diameter, sandblasting also left the form deviation of the spheres practically unchanged.

Table 2. Comparison of contact measurement results regarding diameter and form deviation pre- and post-sandblasting.

Sphere Size	Average Diameter [mm]			Average Form Deviation [mm]		
	Pre	Post	Difference	Pre	Post	Difference
Ø 10 mm	10.0026	10.0054	0.0028	0.0035	0.0046	0.0010
Ø 18 mm	17.9977	18.0004	0.0027	0.0023	0.0044	0.0021
Ø 25 mm	25.0049	25.0075	0.0026	0.0028	0.0047	0.0020

The values obtained in the non-contact laser triangulation measurement were generated, as in the pre-sanding stage, using the capture mode with low sensitivity (high gain). The same type of spurious point filter was then applied, although now these defects appeared to a much lesser extent. In this case, the number of points captured with the laser sensor increased for all of the three ranges of spheres, being 13,975 points for each of the Ø 10 mm, 43,052 points for each of the Ø 18 mm, and 80,126 points for each of the Ø 25 mm spheres (Table 3). The increase with respect to the pre-sanded spheres reached 33.98%, 11.87% and 9.64%, respectively.

Table 3. Comparison of laser measurement results regarding diameter and form deviation pre- and post-sandblasting.

Sphere Size	Average Diameter [mm]			Average Form Deviation [mm]			Average No. Points
	Pre	Post	Difference	Pre	Post	Difference	
Ø 10 mm	10.0137	9.9976	−0.0161	0.1908	0.0681	−0.1227	13,975
Ø 18 mm	17.8846	18.0006	0.1161	0.1501	0.0574	−0.0927	43,052
Ø 25 mm	24.8608	25.0250	0.1642	0.1492	0.0518	−0.0974	80,126

Regarding the measured data for the diameter of spheres, Table 3 shows that, while for the larger spheres (Ø 18 and Ø 25 mm) the pre-sandblasting results were lower than the nominal value, for the Ø 10 mm sphere the average value was higher than the nominal value.

However, the comparison before and after sandblasting provides values much closer to the reference (contact) values. This can be considered a success of the sandblasting process, which, by eliminating brightness, allows the laser to measure diameters much closer to the reference ones, even compensating differences as large as 0.116 and 0.164 in spheres of Ø 18 and Ø 25 mm, respectively. A comparison of the form deviation data before and after sandblasting is also shown in Table 3. Initially, the laser measurement averaged large form deviations, on the order of 0.15 to 0.19 mm. However, once the spheres are sandblasted, the laser measurements also offer very sharp improvements, ranging from 0.092 to 0.123 mm, leaving the form deviations at values in the range of 0.052 to 0.068 mm, also closer to the reference values.

With the laser equipment available, two types of improvements could be contrasted. On the one hand, the improvement in the density and coverage of the point cloud. This improvement was evident, since the coverage with pre-sanded spheres was very poor. In fact, in some cases (Ø 10 mm spheres), not all spheres could be correctly reconstructed. Consequently, the pre- and post-sandblasted comparison was only possible on all spheres when using high gain.

The second improvement achieved is related to the dimensional approach of the laser measurements to the CMM measurements (reference). Meaning by improvement the relation (%) between the parameter measured by laser with respect to the parameter measured by contact. In other words, a 100% improvement in any of the measurements would mean that the laser obtains the same measurement as the CMM by contact. Thus, Figure 7 shows the improvements obtained in the values of the diameters, both in high gain and normal gain. The improvements are substantial, although not homogeneous, in

all the range of diameters. An even greater improvement is noted in the large spheres, Ø 18 and Ø 25 mm, where the improvements are very high (>85%). The diameters obtained are very close to the reference values of the spheres, and even more so at high gain.

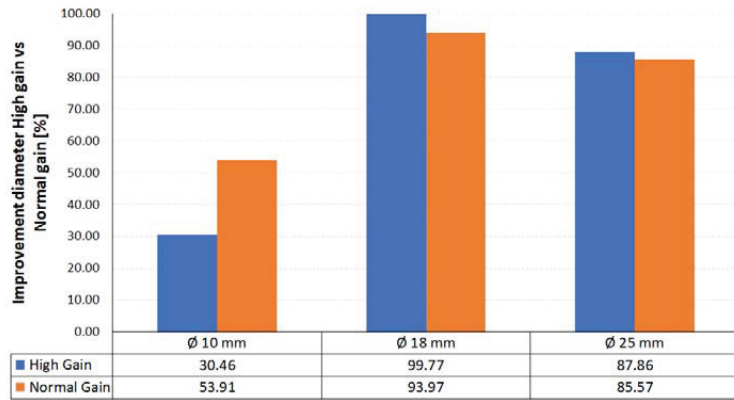


Figure 7. Diameter value improvements in non-contact measurement with medium and high gain in all three diameters.

Regarding the form deviation, the average improvement was 63.80% in high-gain mode and 69.67% in normal-gain mode. On the other hand, in the data relating to the standard deviation of the point cloud, an average percentage improvement of 59.21% was observed with the sensor filter at high gain and 66.29% at normal gain. Both parameters refer to measurements obtained on the spheres in a post-sandblasted state. In any case, homogeneous improvement values are observed regardless of the size of the sphere considered (Figure 8).

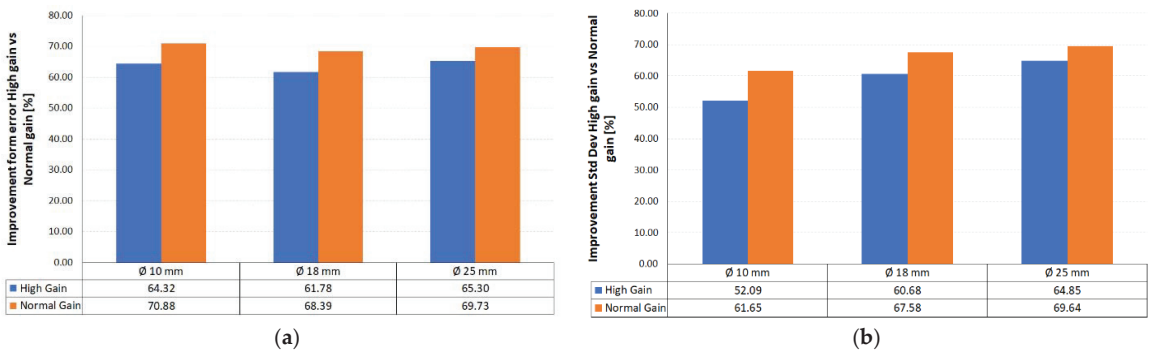


Figure 8. Improvements with medium- and high-gain laser measurements: (a) in form deviation; (b) in standard deviation.

The standard deviation value is one of the parameters that best characterizes the quality of a point cloud [5], especially when considering its approximation to a mathematically well-defined geometry, as is the case of the sphere. This value is even a good substitute for metrological form deviation (ISO 1101:2017), measuring how good the point cloud is when fitting to a perfect sphere.

As a summary, and using the standard deviation value as a measure of the quality of the cloud fit, the graph in Figure 9 was produced. Dashed lines show the standard deviation measurements on original spheres, while solid lines show the standard deviation measurements of the laser clouds on sandblasted spheres.

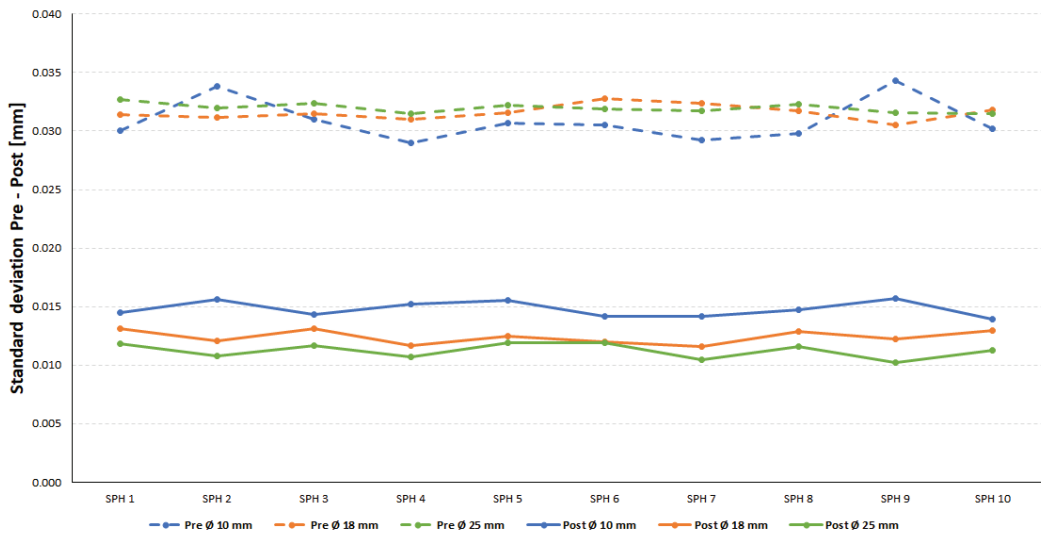


Figure 9. Standard deviation values pre- and post-sandblasting (laser measurements).

Here the qualitative leap that the sandblasting process generates on the laser measurements (at high gain) can be clearly observed. While the values of the standard deviation measured before the sandblasting process, oscillate between 0.029 and 0.034 mm, after the sandblasting process, the standard deviations have decreased substantially (between 0.010 mm and 0.015 mm).

Moreover, the graph also shows that, for any range of diameters considered, the “vertical” oscillation range in the standard deviation is very small. This gives an idea of the goodness of the sandblasting process. Despite being a manual process, it achieved a fairly uniform distribution on all the spheres of each plate, regardless of the position of each sphere within the plate.

4. Conclusions

The pre- and post-sandblasting comparison of the spheres by contact and non-contact (laser triangulation sensor) measurement provides interesting data on the modification suffered by the sphere surfaces. In the analysis, the use of a wide number of spheres (three sets of 10 spheres) ensured the repeatability of the process.

The sandblasting process has affected the surface roughness from $Ra < 0.1 \mu\text{m}$ to $Ra = 0.5\text{--}0.6 \mu\text{m}$ for all the spheres, indicating that this parameter has little influence from a dimensional and geometrical point of view. Apart from roughness, three parameters were considered for the study: the sphere diameter, the form deviation (sphericity) and the standard deviation of the point cloud with respect to the best fit sphere. The first two measurands are perfectly defined from a metrological point of view, while the third (standard deviation) is preferable as an indicator of the form deviation of the surface for high density point clouds.

As a first conclusion, the effect of sandblasting on the spheres is acceptably small, with minimal changes in diameter ($2.7 \mu\text{m}$) and, more importantly, in form deviation ($1.7 \mu\text{m}$). These characteristics validate the use of these spheres as reference artifacts for calibrating optical equipment, whose estimated accuracies are in the order of $25 \mu\text{m}$ to $40 \mu\text{m}$ (or even more).

As a second conclusion, and now derived from the laser measurements, it can be observed that the increase in the density of the point cloud after sandblasting the spheres is very remarkable. So much so that, before sandblasting and at normal gain, the laser sensor was not able to capture clouds with good coverage. This defect was much more

pronounced in small spheres. Even in the case of high gain, the improvements in the quality of the point cloud are considerable, with values of improvement in the order of 60 to 70%, both in terms of diameter and form deviation obtained with the best-fit cloud. Therefore, this type of surface finish can be considered as a good solution for the application of these spheres as reference artefacts in GD&T measurements with laser triangulation equipment.

As for the analysis performed with the standard deviation parameter, it can be seen that the value of the standard deviation between the point cloud of the pre-sandblasted and post-sandblasted sphere drops by almost half. That is, the fit of the point cloud to a sphere (value similar to the form deviation) is twice as good (almost 100% improvement) when sandblasted spheres are used. It can be stated that the brightness elimination of the spheres did not involve an important loss of sphericity that, on the contrary, remained within acceptable limits of accuracy.

This study demonstrates that sandblasted spheres, with average sphericity lower than 0.005 mm can be used as reference elements for non-contact measurement equipment with accuracies in the order of 0.040~0.050 mm. The validity of this statement is further supported by the low cost of the finishing process (manual sandblasting) and by the low cost of the stainless-steel spheres commonly used in industrial bearings.

Author Contributions: Conceptualization, E.C.; methodology, E.C. and B.J.Á.; formal analysis, V.M. and B.J.Á.; validation, V.M. and B.J.Á.; investigation, E.C. and V.M.; writing—original draft preparation, E.C. and B.J.Á.; writing—review and editing, B.J.Á.; supervision, E.C.; project administration, E.C. and V.M.; funding acquisition, E.C. and V.M. All authors have read and agreed to the published version of the manuscript.

Funding: This work was supported by the University Institute of Industrial Technology of Asturias, IUTA through the research project ref. SV-21-GIJON-1-06.

Institutional Review Board Statement: Not applicable.

Informed Consent Statement: Not applicable.

Data Availability Statement: Not applicable.

Acknowledgments: The authors are grateful for the grant awarded by the University Institute of Industrial Technology of Asturias, IUTA (ref. SV-21-GIJON-1-06), and, in particular, to the research fellow, Pablo Pastur, for his high dedication and efficiency.

Conflicts of Interest: The authors declare no conflict of interest. The funders had no role in the design of the study; in the collection, analyses, or interpretation of data; in the writing of the manuscript, or in the decision to publish the results.

References

1. Van Gestel, N.; Cuypers, S.; Bleys, P.; Kruth, J.-P. A performance evaluation test for laser line scanners on CMMs. *Opt. Lasers Eng.* **2009**, *47*, 336–342. [[CrossRef](#)]
2. ISO 10360-8. *Geometrical Product Specifications (GPS)—Acceptance and Reverification Tests for Coordinate Measuring Systems (CMS)—Part 8: CMMs with Optical Distance Sensors*; ISO: Geneva, Switzerland, 2013.
3. VDI/VDE 2634-1,2,3. *Optical 3D Measuring Systems—Imaging Systems with Point-by-Point Probing*; The Association of German Engineers VDI: Berlin, Germany, 2002.
4. Beraldin, J.-A.; Mackinnon, D.; Cournoyer, L. Metrological characterization of 3D imaging systems: Progress report on standards developments. In Proceedings of the 17th International Congress of Metrology, Paris, France, 21–24 September 2015; p. 13003. [[CrossRef](#)]
5. Bešić, I.; Van Gestel, N.; Kruth, J.-P.; Bleys, P.; Hodolič, J. Accuracy improvement of laser line scanning for feature measurements on CMM. *Opt. Lasers Eng.* **2011**, *201149*, 1274–1280. [[CrossRef](#)]
6. Boeckmans, B.; Probst, G.; Zhang, M.; Dewulf, W.; Kruth, J.-P. ISO 10360 verification tests applied to CMMs equipped with a laser line scanner. In Proceedings of the 9868 Dimensional Optical Metrology and Inspection for Practical Applications V of the SPIE Commercial + Scientific Sensing and Imaging, Baltimore, MD, USA, 17–21 April 2016. [[CrossRef](#)]
7. Satyanarayana, A.; Krishna, M.; Chandrakanth, A.; Pradyumna, R. Influence of LASER CMM Process Parameters on Dimensional Inspection of Standard Spheres. *Mater. Today Proc.* **2018**, *5*, 3965–3970. [[CrossRef](#)]
8. Wang, Y.; Feng, H.-Y. Effects of scanning orientation on outlier formation in 3D laser scanning of reflective surfaces. *Opt. Lasers Eng.* **2016**, *81*, 35–45. [[CrossRef](#)]

9. Rak, M.; Woźniak, A.; Mayer, J.R.R. The influence of the scanning path of a laser scanner integrated with measuring arm on the surface digitalization. In Proceedings of the 10th International Scientific Conference Coordinate Measuring Technique, Bielsko-Biała, Poland, 23–25 April 2012. [[CrossRef](#)]
10. Rak, M.; Woźniak, A. The influence of properties of a measured object on the surface digitalization performed by a laser scanner integrated with measuring arm. *Pomiary Autom. Robot.* **2012**, *12*, 76–81.
11. Mendricky, R.; Langer, O. Influence of the material on the accuracy of optical digitalization. *MM Sci. J.* **2019**, 2783–2789. [[CrossRef](#)]
12. Cuesta, E.; Rico, J.C.; Fernández, P.; Blanco, D.; Valiño, G. Influence of roughness on surface scanning by means of a laser stripe system. *Int. J. Adv. Manuf. Technol.* **2009**, *43*, 1157–1166. [[CrossRef](#)]
13. Mian, S.H.; Mannan, M.A.; Al-Ahmari, A.M. The influence of surface topology on the quality of the point cloud data acquired with laser line scanning probe. *Sens. Rev.* **2014**, *34*, 255–265. [[CrossRef](#)]
14. Blanco, D.; Fernández, D.B.; Cuesta, E.; Mateos, S.; Beltrán, N. Influence of surface material on the quality of laser triangulation digitized point clouds for reverse engineering tasks. In Proceedings of the 2009 IEEE Conference on Emerging Technologies Factory Automation, Palma de Mallorca, Spain, 22–25 September 2009; pp. 1–8.
15. Cuesta, E.; Álvarez, B.J.; Martínez-Pellitero, S.; Barreiro, J.; Patiño, H. Metrological evaluation of laser scanner integrated with measuring arm using optical feature-based gauge. *Opt. Lasers Eng.* **2019**, *121*, 120–132. [[CrossRef](#)]
16. Guerra, M.-G.; De Chiffre, L.; Lavecchia, F.; Galantucci, L.-M. Use of miniature step gauges to assess the performance of 3D optical scanners and to evaluate the accuracy of a novel additive manufacture process. *Sensors* **2020**, *20*, 738. [[CrossRef](#)] [[PubMed](#)]
17. Heczko, D.; Oščádal, P.; Kot, T.; Huczala, D.; Semjon, J.; Bobovský, Z. Increasing the reliability of data collection of laser line triangulation sensor by proper placement of the sensor. *Sensors* **2021**, *21*, 2890. [[CrossRef](#)] [[PubMed](#)]
18. Cuesta, E.; González-Madruga, D.; Álvarez, B.-J.; García-Diéguez, M. Development of a behaviour curve for quality evaluation with optoelectronic profilometers. *Key Eng. Mater.* **2014**, *615*, 51–57. [[CrossRef](#)]
19. Cuesta, E.; Giganto, S.; Álvarez, B.J.; Barreiro, J.; Martínez-Pellitero, S.; Meana, V. Laser line scanner aptitude for the measurement of Selective Laser Melting parts. *Opt. Lasers Eng.* **2021**, *138*, 106406. [[CrossRef](#)]
20. ISO 3290-1. *Rolling Bearings—Balls—Part 1: Steel Balls (DIN 5401: 2002-08)*; ISO: Geneva, Switzerland, 2014.
21. ISO 10360-2. *Geometrical Product Specifications (GPS)—Acceptance and Reverification Tests for Coordinate Measuring Machines (CMM)—Part 2: CMMs Used for Measuring Linear Dimensions*; ISO: Geneva, Switzerland, 2009.

Article

Ultrasonic Vibration-Assisted Ball Burnishing Tool for a Lathe Characterized by Acoustic Emission and Vibratory Measurements

Ismael Fernández-Osete ¹, Aida Estevez-Urra ², Eric Velázquez-Corral ¹, David Valentin ³, Jordi Llumà ⁴, Ramón Jerez-Mesa ^{1,*} and J. Antonio Travieso-Rodríguez ¹

¹ Department of Mechanical Engineering, Universitat Politècnica de Catalunya, 08019 Barcelona, Spain; ismael.fernandez.osete@upc.edu (I.F.-O.); eric.velazquez.corral@upc.edu (E.V.-C.); antonio.travieso@upc.edu (J.A.T.-R.)

² Department of Mechanical Engineering and Manufacturing, Universidad de Sevilla, 41092 Sevilla, Spain; aeurra@us.es

³ Centre for Industrial Diagnostics and Fluid Dynamics, Universitat Politècnica de Catalunya, 08034 Barcelona, Spain; david.valentin@upc.edu

⁴ Department of Science and Materials Engineering, Universitat Politècnica de Catalunya, 08019 Barcelona, Spain; jordi.lluma@upc.edu

* Correspondence: ramon.jerez@upc.edu; Tel.: +34-934137338

Citation: Fernández-Osete, I.; Estevez-Urra, A.; Velázquez-Corral, E.; Valentin, D.; Llumà, J.; Jerez-Mesa, R.; Travieso-Rodríguez, J.A. Ultrasonic Vibration-Assisted Ball Burnishing Tool for a Lathe Characterized by Acoustic Emission and Vibratory Measurements. *Materials* **2021**, *14*, 5746. <https://doi.org/10.3390/ma14195746>

Academic Editor: Stanislaw Legutko

Received: 3 September 2021

Accepted: 28 September 2021

Published: 1 October 2021

Publisher's Note: MDPI stays neutral with regard to jurisdictional claims in published maps and institutional affiliations.



Copyright: © 2021 by the authors. Licensee MDPI, Basel, Switzerland. This article is an open access article distributed under the terms and conditions of the Creative Commons Attribution (CC BY) license (<https://creativecommons.org/licenses/by/4.0/>).

Abstract: This paper focuses on a resonant system used to induce a low-amplitude movement and ultrasonic frequency to complement a ball burnishing process on a lathe. The system was characterized through the combination of different techniques. A full vibratory characterization of this process was undertaken with the purpose of demonstrating that the mechanical system—composed of the tool and the machine—does not present resonance phenomena during the execution of the operation that could lead to eventual failure. This dynamic analysis validates the adequateness of the tool when attached to an NC lathe, which is important to guarantee its future implementation in actual manufacturing contexts. A further aim was to confirm that the system succeeds in transmitting an oscillating signal throughout the material lattice. To this end, different static and dynamic techniques that measure different vibration ranges—including impact tests, acoustic emission measurement, and vibration measurement—were combined. An operational deflection shape model was also constructed. Results demonstrate that the only high frequency appearing in the process originated in the tool. The process was not affected by the presence of vibration assistance, nor by the burnishing preload or feed levels. Furthermore, the frequency of the assisting ultrasonic vibration was characterized and no signal due to possible damage in the material of the specimens was detected. These results demonstrate the suitability of the new tool in the vibration-assisted ball burnishing process.

Keywords: accelerometer; acoustic emission; ball burnishing; natural frequencies; operational deflection shape; piezoelectric; process monitoring; ultrasonic

1. Introduction

In order to control several parameters of machining processes, different measurements (vibrations, energy consumption, airborne noise, acoustic emission, etc.) can be determined and processed using various signal-processing techniques.

Acoustic emission (AE) is one of the most frequently used measurements for this purpose. AE can be described as a set of elastic pressure waves generated by the rapid release of energy stored within a material. This energy dissipation is basically due to dislocation motion, phase transformations, friction, and crack formation or growth [1].

Different vibration and signal measurement techniques have been used in the past for the detection of failures in manufacturing processes [2]. Several authors [3–7] discuss how AE is related to the wear mechanisms of cutting tools. Pandiyan and Tjahjowidodo [8]

applied dynamic measurements to establish the fault thresholds in grinding wheels under different conditions, while Lopes et al. [9] monitored the condition of a grinding wheel. Wang et al. [10] and Zanger et al. [11] studied the relationship between the AE and chip size.

The quality requirements of industrial products are constantly increasing and machined components are no exception. For this reason, ultrasonic-assisted tools are now used to improve surface quality. Hence, new methodologies are required to study the vibratory behavior of these kinds of tools, as described in the previous paragraph.

Referring to finishing operations, the British scientist Griffith concluded in 1921 that the strength of materials with isotropic properties was much lower (between 10 and 20 times) than could be predicted theoretically and that this is due to the lack of continuity of the material; that is, the existence of defects [12]. These defects occur in the process of obtaining the components (metallurgical defects) or in the production process due to geometric details. Defects of the surface layers of machined components are especially dangerous. In these surface layers, three properties are especially important: surface hardness, roughness, and compressive residual stresses.

Ball burnishing is one the most suitable processes with which to improve these properties [13,14]. This process consists of the plastic deformation of irregularities in the target surface through the application of a controlled force by a sphere [15]. In recent years, the technical world has witnessed the birth of vibration-assisted ball burnishing (VABB). In this technique, the ball that compresses the target surface is subjected to a high-frequency vibration (between 20 and 40 kHz) which, in turn, is transmitted to the target surface [16]. This vibration of the surface material produces a lowering of its yield limit—a phenomenon called acoustoplasticity [17]. As a result, plastic deformation of the material is achieved with forces lower than those that would be necessary without vibration assistance. Consequently, VABB provides better results than conventional or non-vibration-assisted ball burnishing (NVABB) [18].

Different systems have been used to enhance ball burnishing with vibrations in a variety of different machining processes [16–18]. Most of these systems, including the one studied in this paper, use a resonant system characterized by a low amplitude movement (between 3 and 30 μm) [19]. This system, which is described by Jerez-Mesa [20], applies a high-frequency electrical charge to a piezoelectric stack, causing it to undergo a deformation which is then transmitted to the ball. This device is called a sonotrode [21].

With regard to burnishing, there are few studies where the application of AE is so direct. Dornfeld and Liu [22] concluded that AE helps to reveal information about the frictional behavior of the ball burnishing process, as it has a strong correlation with the kinetic friction coefficient and the texture surface profile. Their work also concluded that AE demonstrates how the burnishing process can be divided into four stages from a dynamics perspective. Only in the first two can positive results during burnishing be obtained. Strömbergsson et al. [23] observed that monitoring AE parameters during the burnishing process to confirm that the operation has performed its intended function is highly beneficial. For example, inspection of an AE signal in root mean square (RMS) representation for 5 min demonstrated that the decrease in the coefficient of friction (COF) stagnated after a time, and that the tribological behavior did not remain stable. Therefore, investigators should be made aware of the effects of excessive wear of the burnishing ball and how these can affect the finishing results. Salahshoor and Guo [24] used AE to monitor the burnishing process on a magnesium-calcium alloy.

In addition to the limited studies regarding the application of AE to burnishing, some studies apply this technique to the diagnosis of possible faults in contacts between solid bodies in relative motion—a case to which burnishing is easily applicable due to the way it takes place, and which is therefore considered relevant as an antecedent to this paper [25]. Tandon et al. [26] highlighted the effectiveness of AE for detecting failures in contacts between ball bearings, and concluded that it can detect the transfer of particles from the wear of the two surfaces in contact. They also concluded that AE is more effective than vibration analysis as it can detect errors before they occur. Hase et al. [27] concluded that

the frequency spectra of the AE signals measured during the tribological tests allowed them to determine the wear mechanism between the contact surfaces. Geng et al. [28] concluded that AE signals acquired at the highest sampling frequencies were more sensitive for the detection of the friction mechanisms between two contact surfaces than the evolution of the friction coefficient that characterizes this contact.

In this paper, a full vibration characterization of a ball burnishing process performed in a lathe is presented. This ball burnishing process was performed using a tool designed by the authors [29]. The main objective was to demonstrate that the machine and the tool do not present any resonance issues during their service that could result in possible hardware malfunctions. This dynamic analysis validates the suitability of the tool when it is attached to an NC lathe and is relevant to the eventual industrial users of the system. The designed tool is particularly intended for application in industries that manufacture elements with revolution symmetry that are subjected to high-cycle fatigue or in which a particular type of wear must be prevented. The adequateness of the system to transmit vibrations through the material is assessed.

A specific methodology was applied to validate the dynamic behavior of the tool by combining several techniques based on quantification of the normal and ultrasonic vibration ranges through static and dynamic measurements. In the static measurements, the frequency response functions of the tool were measured and, consequently, the natural frequencies were determined [30]. The dynamic measurements were used to characterize the burnishing process (vibration assisted or not) under operating conditions. In this case, acoustic emission was used to detect possible damage in the material during the VABB process.

The analyses included in the previous paragraph demonstrate the fundamental importance of the traditional techniques of static and dynamic vibration analysis as applied to the VABB process discussed here. The dynamic results derived from VABB applied to two different ferric alloys are described in order to evaluate different magnitudes under different burnishing conditions: two burnishing forces (90 N and 270 N) and the existence of vibration assistance (yes or no). The measured magnitudes were burnishing force, vibrations, and acoustic emission. This allowed us to characterize the process itself and the tool's ability to transmit vibratory assistance, as well as to detect possible damage in the specimens produced by this process. From the vibration measurements, an operational deflection shape (ODS) exercise was also performed.

This research is novel as, despite the fact that the vibration-assisted ball burnishing process is not new, a new tool that is capable of carrying it out was analyzed. This tool has a series of characteristics that make it unique from those on the market. Additionally, the AE technique applied for characterization and verification of the influence of the vibration assistance did not produce any negative effects on the process results. No reference to the use of AE for this purpose was found in the reviewed literature.

2. Materials and Methods

2.1. Experimental Setup

In order to characterize the dynamic behavior of the machine-tool-part setup, two types of tests were performed: impact tests under static condition; and vibrations, forces, and acoustic emission monitoring under running (dynamic) conditions of the burnishing system. The ball burnishing tool used was a prototype designed and patented by the authors [29]. It can be used in both NVABB and VABB processes. The frequency of its ultrasonic vibration is 40 kHz. All tests were performed in a PINACHO SE 200 × 1000 mm CNC lathe (Pinacho CNC, Guipuzcoa, Spain). The specimens were fixed between a self-centering three-jaw chuck plate and the point.

Different burnishing parameters were taken into account in this study: specimen material (C45 steel, EN 10020:2000, and GJL250 grey cast iron, EN 1560:2011), burnishing force (90 N and 270 N) and ultrasonic vibration assistance (yes or no). The specimens

were previously machined. Table 1 presents their initial and final dimensions, the cutting parameters, and the measured roughness. No cutting fluids were used in the machining.

Table 1. Cutting parameters and specimen dimensions (initial and final).

Material	Initial Dimensions		Cutting Parameters			Final Dimensions		
	D [mm]	L [mm]	Cutting Speed [m/min]	Feed [mm/rev]	Cutting Depth [mm]	D [mm]	L [mm]	Roughness Ra [μm]
C45	15	133	70.7	0.15	0.2	14.8	133	1.187
GJL250	15	185	29.4	0.15	0.4	14.0	185	2.310

Different accelerometers were used. Three triaxial accelerometers were installed in the burnishing tool in order to study its vibrating behavior. Two were mounted in the frontal part near the burnishing ball (positions P1 and P2 of Figure 1a), and the third was mounted in the opposite part (position P3 of Figure 1b). The characteristics of these accelerometers are presented in Table 2. The measurement directions of the accelerometers correspond to the burnishing feed (X), vertical direction (Y), and direction of the burnishing force (Z).

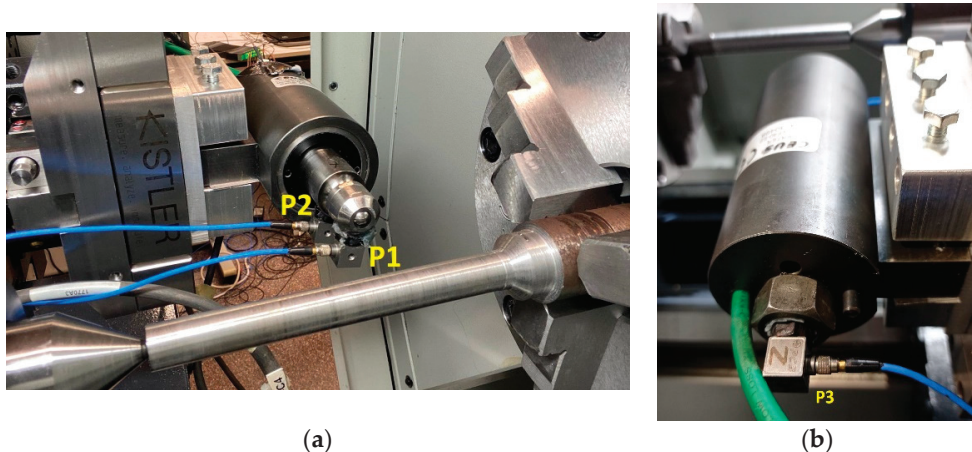


Figure 1. Triaxial accelerometers installed in the tool: (a) frontal view; (b) rear view.

Table 2. Accelerometers used for the measurements.

Measurement Position	Accelerometer	Frequency Range [Hz]
Tool (P1, P2 y P3)	PCB 356A32/NC	1 ÷ 4000 ± 5% 0.7 ÷ 5000 ± 10%
Lathe bed, directions A, V y H	KISTLER Type 8752A50	0.5 ÷ 5000 ± 5%

Three monoaxial accelerometers were installed in the lathe bed in order to determine the vibrational transmissibility from the machine during the burnishing process. Figure 2 depicts these accelerometers and their measurement directions: A (axial according to the specimen rotation), V (vertical), and H (horizontal). The characteristics of these accelerometers are presented in Table 2.

The monitoring criteria were selected taking the following into account:

- The maximum monitoring frequency allowed by the instrumentation should be applied.
- All mechanical and electrical phenomena that occur during the process should be monitored and recorded.

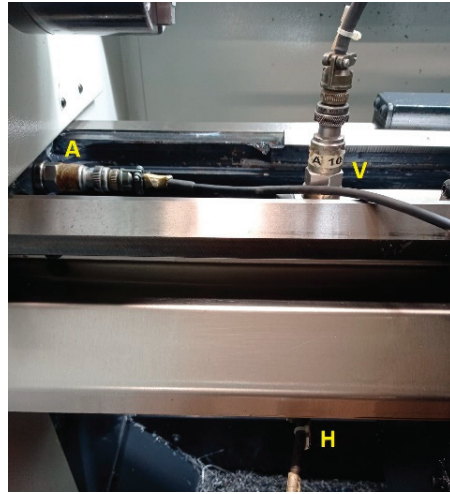


Figure 2. Accelerometers mounted on the lathe bed.

2.2. Burnishing Force Monitoring

The compressive deformation of the spring installed inside the tool-holder is linearly related to the force transmitted by the burnishing tool to the target surface [20]. In turning processes, it is linearly related to the penetration of the tool in the direction of the depth of the pass. The nominal burnishing forces of the tests were 90 N and 270 N for the steel specimen and only 90 N for the grey cast iron, as 270 N is an excessive load for this material.

The force was monitored by a KITSLER 9129AA dynamometer (Kistler, Winterthur, Switzerland) adapted to the lathe holder where the tool was mounted, as seen in Figure 1a. The force signal was conditioned by a KITSLER 5070A12100 amplifier (Kistler, Winterthur, Switzerland) Burnishing forces were acquired in impact tests under static conditions (lathe turret stopped) and in measurements under operating conditions (lathe turret moving) of the burnishing system (Figure 3).

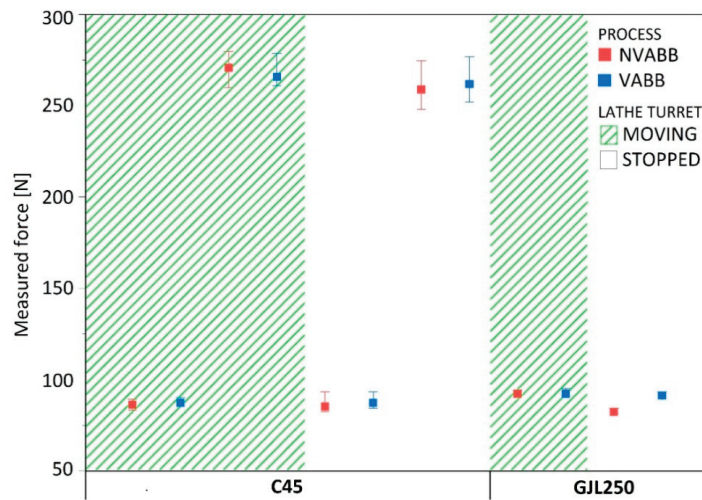


Figure 3. Average, maximum, and minimum forces recorded during the tests.

2.3. Impact Tests

Impulse excitation was used to determine the natural frequencies of the tool under different conditions. Impacts were carried out with an impact hammer (KISTLER 9722A2000) (Kistler, Winterthur, Switzerland) with steel tip (9902A) (Kistler, Winterthur, Switzerland). Its maximum frequency was 9.3 kHz and its maximum force was 11 kN. These characteristics were deemed suitable as, according to a previous study [30], the natural frequencies of a similar tool were lower than 5 kHz.

Impacts were performed at three tool points in the vertical direction (points I1, I2, and I3) and vibrations were measured at three points (P1, P2, and P3) in three directions, as seen in Figure 4. The conditions under which the impacts were carried out were as follows:

- Tool installed in its holder without any contact with the specimen (free tool).
- Tool in contact with the specimen and forces between them of 90 N or 270 N, for the steel specimen, and a force of 90 N for the grey cast iron. These conditions were repeated with the tool in two positions: one near the plate and the other near the point.

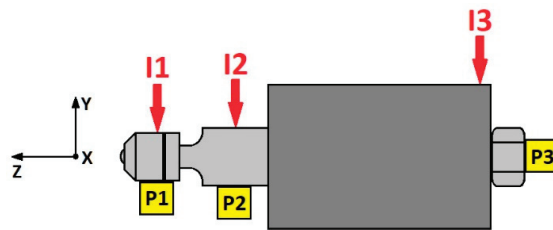


Figure 4. Lateral view of the impact points on the tool.

In total, 15 impact tests were performed. The vibration assistance was not activated during the impact tests as a previous work [31] demonstrated that the ultrasonic vibration of the assistance does not affect a tool's natural frequency.

The acquisition and further analysis of the vibration signals were performed with a 3053-B-120 analyzer (Brüel & Kjær, Nærum, Denmark) and the PULSE Reflex software (version 2.3), respectively. Ten channels were defined: three for each triaxial accelerometer and one for the impact hammer.

2.4. Vibration Monitoring during the Burnishing Process

Different burnishing tests with different forces were performed in order to characterize the machine-tool-specimen setup during the burnishing process. The burnishing forces used were 90 N and 270 N for the C45 steel and 90 N for the GLJ250 grey cast iron. The second variable was the presence (VABB) or absence (NVABB) of ultrasonic vibration in the tool. The burnishing speed was 2.33 m/min and the feed was 0.15 mm/revolution. The burnished length of each test was 10 mm, except for some tests that were carried out without feed for 3 min.

The layout of these tests are presented in Figure 5 for both the C45 and GJL250 specimens.

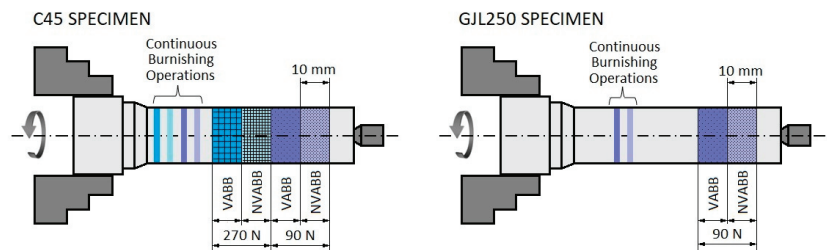


Figure 5. Burnishing test areas.

From these measurements, an ODS of the tool was obtained. ODS is a vibration analysis tool that allows for the determination of the deflection of a component or structure under real operating conditions. Vibration time histories are recorded under operating conditions and, by applying the Fourier transform to these recordings, vibration level versus frequency is determined at different points. A system's wire frame model can then be animated in order to demonstrate the movement at each measured point and at each frequency [32].

2.5. Acoustic Emission Measurements during the Burnishing Process

As previously explained, acoustic emission waves are high-frequency waves (in the ultrasonic frequency band) generated when any kind of damage is produced in a material. During manufacturing processes, different acoustic emission signals are usually emitted by machined parts as a consequence of the damage produced in them. For the burnishing process presented in this paper, the eventual presence of acoustic emission events was explored as previous studies have validated the application of this technique to the characterization of the process itself.

To this end, a Vallen acoustic emission sensor, model VS700-D (Vallen Systeme, Wolfratshausen, Germany), was installed in the tool holder. A Vallen preamplifier, model AEP4, a Vallen AMSY5 acoustic emission system (Vallen Systeme, Wolfratshausen, Germany), and Vallen acquisition software (Vallen Systeme, Wolfratshausen, Germany) were used for conditioning and recording of the acoustic emission signals. The sampling frequency of the acquisition was 625,000 samples/s.

3. Results and Discussion

3.1. Impact Tests

Impacts performed at point I3 (Figure 4) did not provide any valid information because the base housing was disconnected from the tool in order to ensure that the ultrasonic vibrations were transmitted to the lathe [29].

According to the impact position, the best responses always corresponded to the vertical direction (Y), that is, the impact direction. Frequency response functions (FRF) of point P3 revealed poor coherence between excitation and response.

Signals measured at points P1 and P2, corresponding to the tests performed without contact between tool and specimen, revealed a natural frequency of around 1.5 kHz. Figure 6 presents the FRF and the coherence function corresponding to the response at point P1 with excitation at I2. Some low peaks also appear around 500 Hz and 900 Hz. The band between 2 and 3 kHz is also noticeable but its coherence is poor.

In the tests performed with contact between the tool and specimen, no differences were noted between the different test conditions (force and tool position). Consequently, the load and tool position did not affect results. In these cases, natural frequencies in the signals measured at point P3 are noticeable. New components in the band between 1.2 and 2.8 kHz appeared. The amplitudes were lower than those obtained in measurements without contact between the tool and specimen. Figure 7 presents the FRF and coherence corresponding to response at P1 and impact at I1, in the position near to the lathe point and with a load of 90 N.

Natural frequencies were always much lower than the assisting frequency, that is, 40 kHz constituted just 5% of this magnitude.

3.2. Vibration Monitoring during the Burnishing Process

Measurement signals acquired by tool accelerometers (Figure 1) and test bed accelerometers (Figure 2) during burnishing processes were processed and analyzed in time and frequency domains. The maximum analysis frequency was 4 kHz. Spectra are presented, in some cases, up to 2 kHz as no components appeared at higher frequencies.

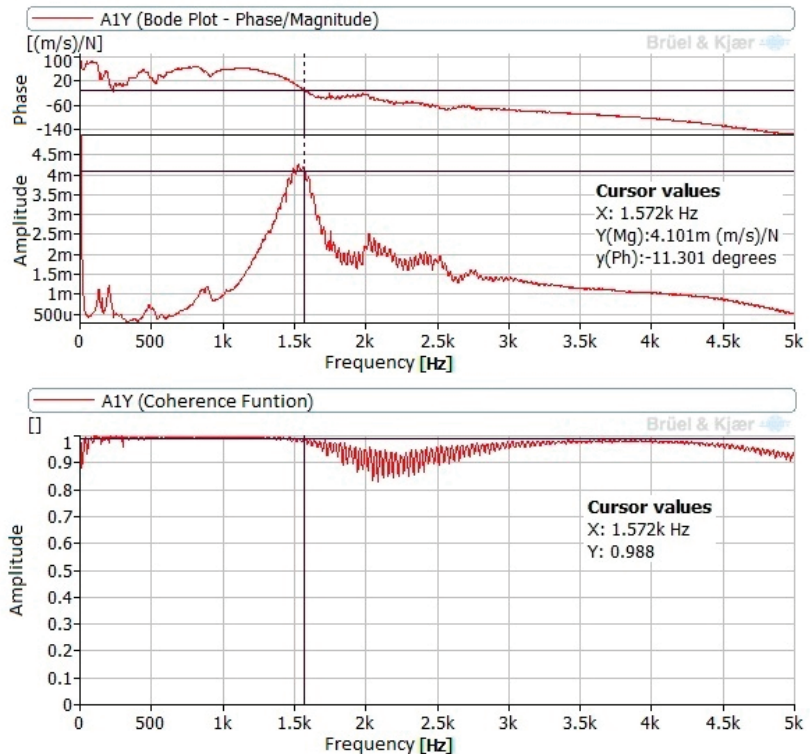


Figure 6. FRF obtained at P1 with impact at I2.

The vibration behavior of the tool during the burnishing process was similar for both materials under all burnishing conditions. Components at 15.8 Hz and 32.1 Hz were noticeable when burnishing C45, while burnishing GJL250 resulted in noticeable components at 17 Hz and 34.2 Hz. This difference is due to the slightly different burnishing speeds and the relation between these components and the mechanical and electrical operation of the lathe. In all cases, these components are very small ($\mu\text{m/s}$ RMS). According to the ISO 20816 [33] for vibrations in machines, the highest allowable vibration level is 0.28 mm/s RMS: all of the measured levels were considerably lower. Figure 8 presents the spectra in the Z direction (direction of burnishing force) for both materials with a burnishing force of 90 N and without vibration assistance.

In tests without vibration assistance, the amplitudes corresponding to points P1 and P2 in burnishing force direction (Z) were higher than amplitudes corresponding to the other two directions: burnishing feed direction (X) and vertical direction (Y). This result can be justified as these points are at the end of the tool and receive all the effort of the burnishing operation. In the case of C45, the amplitudes at point P3 were greater than at points P1 and P2, while in GJL250 the amplitudes at the three points were similar. At point P3, the highest amplitude was in the Y (vertical) direction, which may be due to point P3 being in the distal part of the tool at the time of burnishing, as shown in Figure 1b.

Figure 9 compares the spectra, measured with a burnishing force of 90 N for both materials, with and without vibration assistance, at point P3. This figure shows the Y-axis only because all directions demonstrated the same frequency peaks with very similar amplitudes. Additionally, signals measured without vibration assistance had similar behavior to those with vibration assistance.

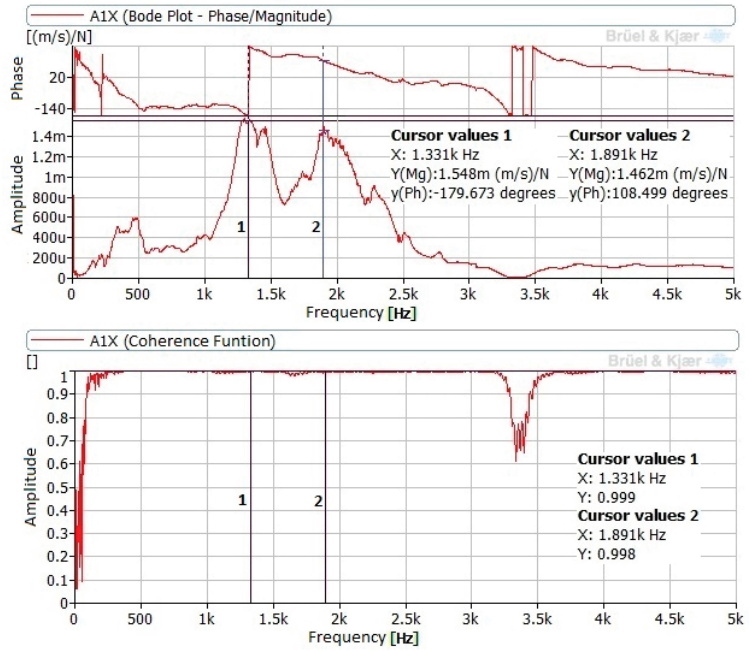


Figure 7. FRF obtained at P1 with impact at I1, with a load of 270 N.

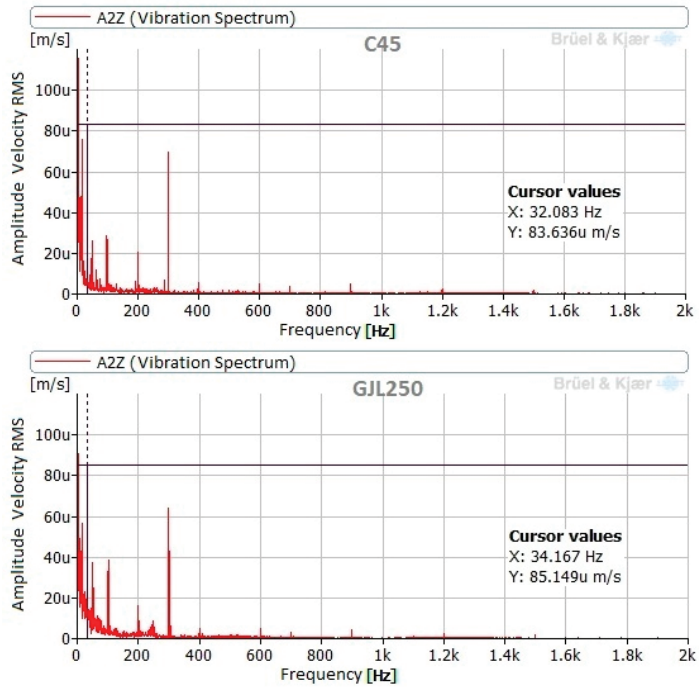


Figure 8. Vibration spectra measured at point 2, in Z direction (direction of the burnishing force), with a NVABB force of 90 N.

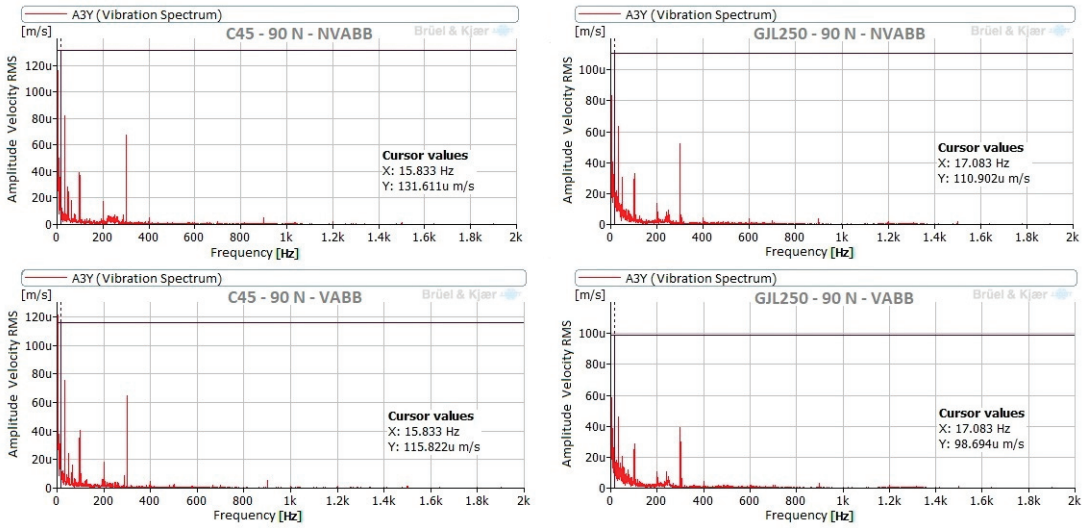


Figure 9. Comparison of spectra of both materials, using VABB and NVABB, measured at point P3, in Y (vertical) direction, and with a burnishing force of 90 N.

Two burnishing forces were used in tests with C45 steel. No differences between the signals monitored under these conditions were noted. To demonstrate this, Figure 10 presents the spectra corresponding to different points and measurement directions. All of these spectra correspond to measurements without vibration assistance.

Additionally, measurements without burnishing feed were carried out for both materials, under the same conditions previously specified. The duration of each of these measurements was 3 min. Analysis of these tests reveals similar results to those obtained with burnishing feed. The same frequency peaks appeared, with very small amplitudes. The only difference was the possible excitation of natural frequencies in the range between 800 Hz and 1400 Hz, but with very low amplitudes. Figure 11 presents an example of these signals.

The vibration measurements in the lathe test bed show normal behavior of the machine. Components that interfere with those obtained in the tool were not noted, but a possible excitation of the natural frequencies between 800 Hz and 1400 Hz was noticeable, but with very low amplitudes.

Figure 12 presents signals measured in the lathe test bed during the burnishing of the steel specimen. Comparing the signals measured with vibration assistance in the horizontal (H), vertical (V), and axial (A) measurement positions, a very similar behavior was noticeable between them, and the amplitudes were again very low. Via inspection of the non-vibration-assisted spectra measured in the horizontal direction at burnishing forces of 90 N and 270 N (Figure 12), no differences appeared between them; consequently, the burnishing force did not affect the horizontal vibrations of the lathe test bed. Additionally, no differences appeared between horizontal spectra with or without vibration assistance at both burnishing forces in Figure 12; therefore, there was no influence of the vibrating assistance in the lathe test bed. This is expected according to the tool design, lathe rigidity, and the test bed points where the measurements were performed.

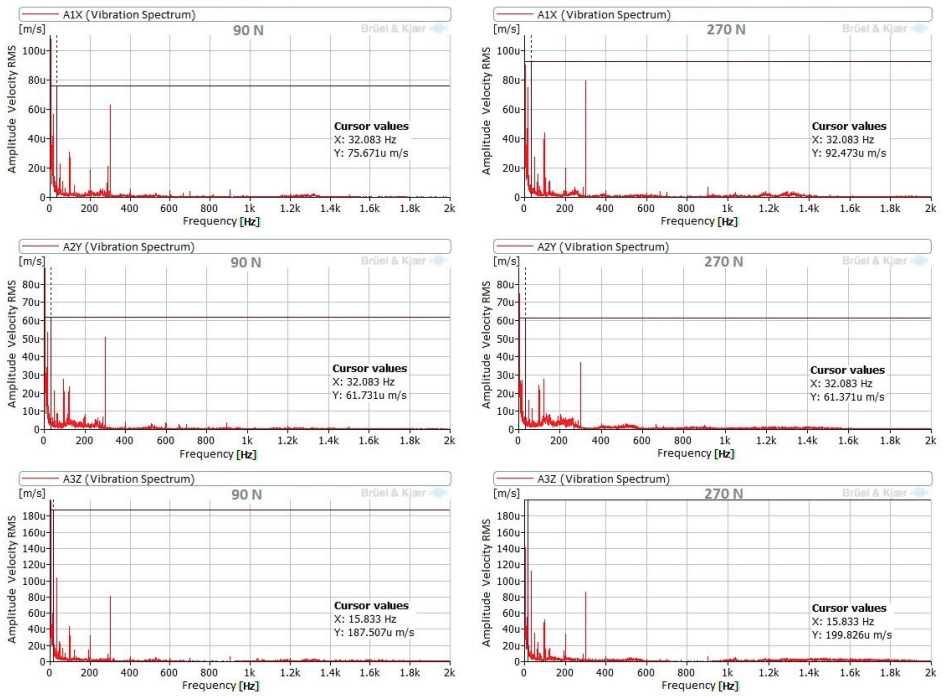


Figure 10. Comparison of spectra of C45 with burnishing forces of 90 N and 270 N, without vibration assistance.

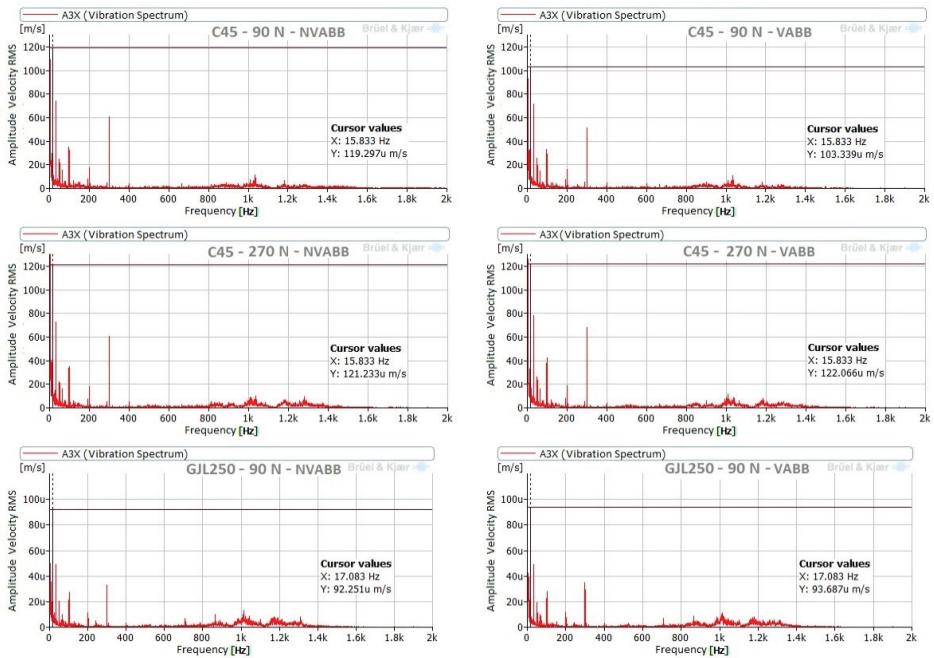


Figure 11. Measurements in burnishing without feed.

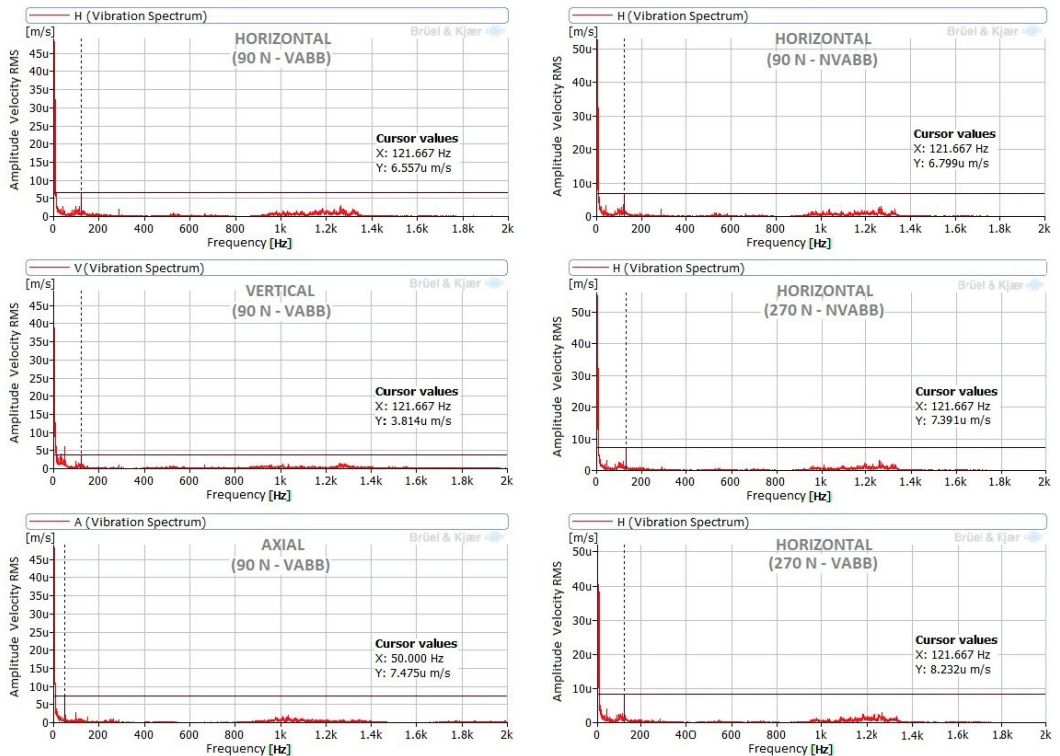


Figure 12. Spectra measured in lathe test bed at different loads and different measurement positions.

3.3. Acoustic Emission Monitoring during the Burnishing Process

Figure 13 presents acoustic emission time histories for different processes. Figure 13a presents the background noise. Figure 13b presents the acoustic emission signal during the burnishing process of the C45 steel specimen with a burnishing force of 90 N, without vibration assistance. Finally, Figure 13c presents the C45 burnishing with a burnishing force of 90 N, with vibration assistance. Figures 13a and 13b are very similar; therefore, the burnishing process without vibration assistance did not produce any acoustic emission. However, a clearly noticeable signal appears in Figure 13c, corresponding to the vibration-assisted burnishing process. This is due to the acoustic emission sensor detecting the assisting vibration signal. No acoustic emission apart from that produced by the vibration assistance appeared; consequently, the ball burnishing process did not produce any damage in the material.

Figure 14 presents the AE spectra corresponding to the VABB of both materials, burnished with different forces: (a) C45 steel specimen with 90 N, (b) C45 steel specimen with 270 N, and (c) GJL250 grey cast iron specimen with 90 N. In all figures, the frequency corresponding to the vibration assistance is the only noticeable peak. This is consistent with previous findings [20].

The vibration assisting frequency was very stable. Its variation of 100 Hz corresponds to 0.25% of the frequency. This level remained the same for both VABB of C45 steel; thus, the burnishing force did not influence it. The vibration level, in the case of GJL250 VABB, was lower than those of C45 due to the high GJL250 internal damping [34].

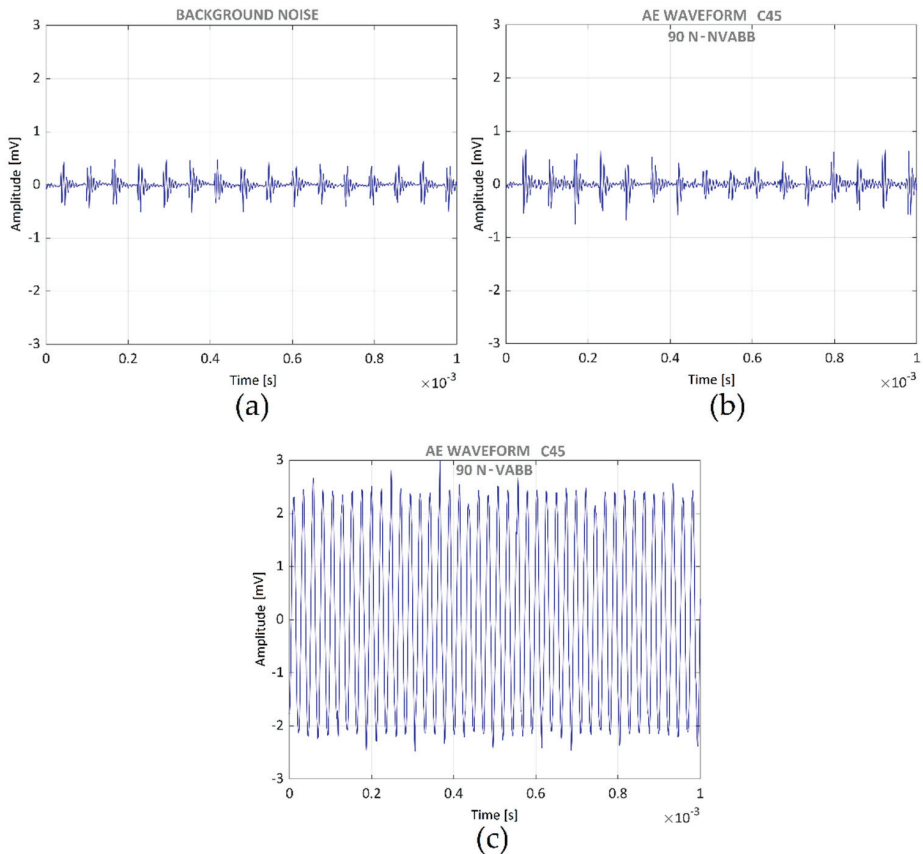


Figure 13. AE time histories of C45 under different conditions: (a) background noise; (b) NVABB; (c) VABB.

3.4. Operating Deflection Shape

According to the method presented in [35], an ODS of the tool in the burnishing process of C45 with a force of 90 N and without vibration assistance was performed to analyze the tool rigidity. A frequency of 32 Hz was selected as it had a noticeable displacement and an acceptable background noise. Figure 15 presents the ODS. Figure 15a is a lateral view and depicts the movement in the vertical direction. Red lines correspond to extreme positions and blue lines correspond to the mean position. A rotary movement around the center of the tool is clearly noticeable, with an amplitude at the extremes of around $0.6 \mu\text{m}$. Figure 15b presents the plant view. A translation movement in the burnishing feed direction of about $0.5 \mu\text{m}$ amplitude is also noticeable. In order to determine the movement in the axis of the tool direction, a zoom around the zero-point was performed (Figure 15c) and a displacement of about $0.9 \mu\text{m}$ was detected.

The methodology proposed in this paper (joining vibratory analysis with AE) allows one to extend the range of frequencies up to several hundred kHz. This approach is suitable for any machine-tool-part setup with different rigidities, configurations, and designs. Therefore, this may be used in the near future to characterize tools used in ultrasonic vibration-assisted machining operations such as those presented in [36]. Unfortunately, this methodology does not allow one to quantify the amplitude of the vibration in the AE range.

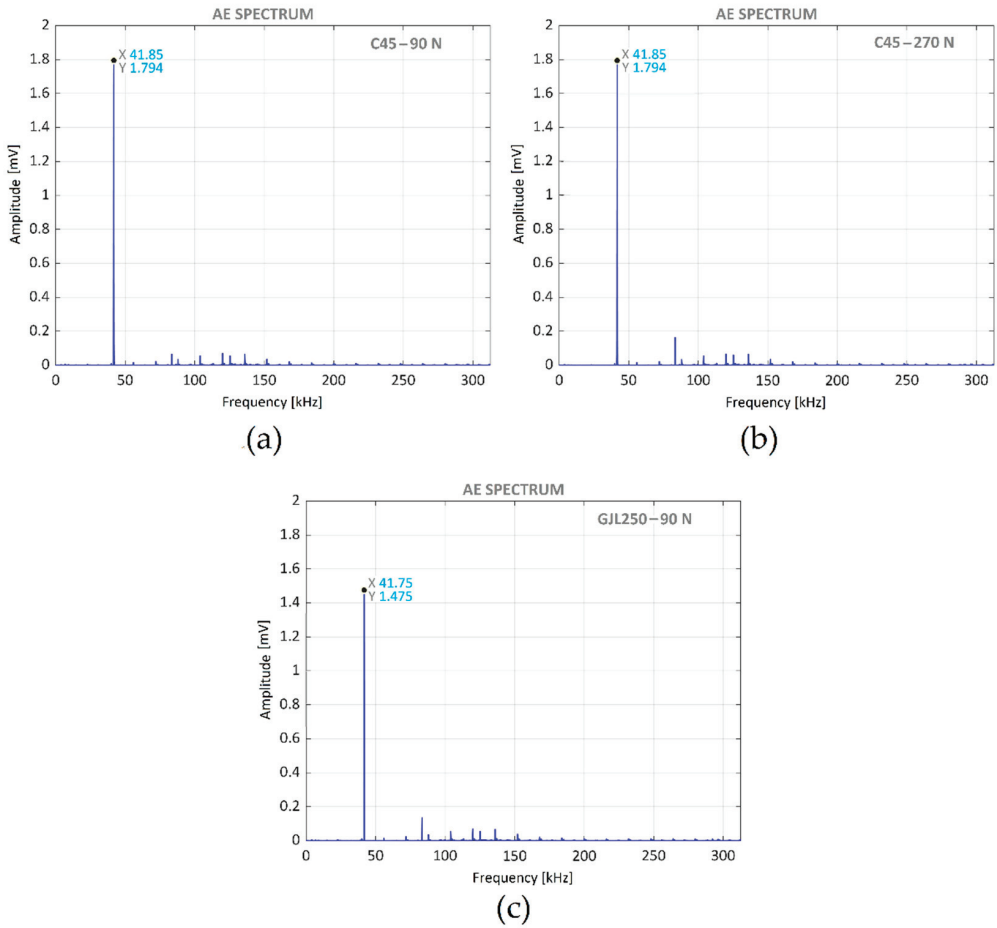


Figure 14. AE spectra corresponding to different VABB: (a) C45 steel with 90 N; (b) C45 steel with 270 N; (c) GJL250 cast iron with 90 N.

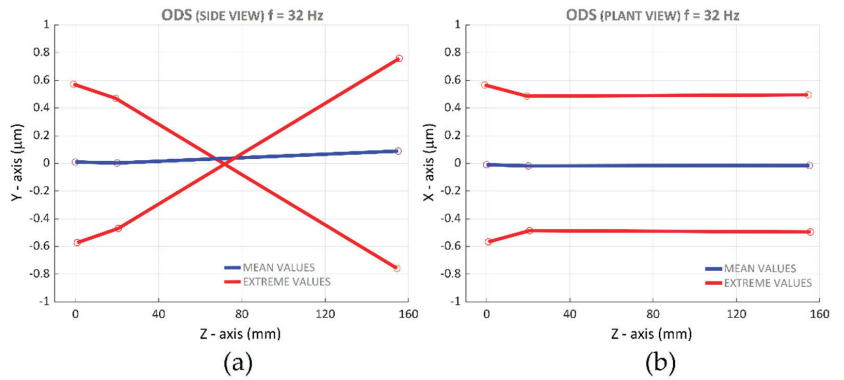


Figure 15. Cont.

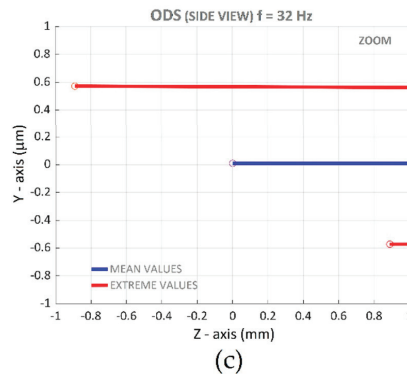


Figure 15. ODS of the tool at 32 Hz: (a) lateral view; (b) plant view; (c) zoom of lateral view.

4. Conclusions

The conclusions of this paper are clustered according to the test through which they were obtained.

Impact tests

No natural frequencies higher than 2 kHz were noted (about 5% of 40 kHz, the vibration assisting frequency); consequently, the high frequency that appeared in the process was only that of the tool.

The structural behavior of the tool was affected by the contact between tool and specimen but was not affected by their contact force value.

Vibration measurements

The material of the workpieces, the vibration assistance, the burnishing force, and the feed movement did not affect the frequency spectra measured.

Spectrum lines appeared in the frequency range 800–1400 Hz during the burnishing process at the rear point and in the lathe bed with much lower amplitudes than those considered to be standard for a new machine, in accordance with the operation deflection shape results.

The vibration levels measured in the tool axis had higher amplitudes than those corresponding to the other directions, due to the burnishing force.

The amplitudes of the signals measured in the rear of the tool were slightly higher than those measured at the frontal part.

Acoustic emission measurements

The only signal detected was the ultrasonic vibration assistance, which permits the frequency characterization of the assisting ultrasonic vibration.

Any signal due to possible damage in the material of the specimens was detected.

Author Contributions: Conceptualization, I.F.-O., A.E.-U., J.L., R.J.-M. and J.A.T.-R.; methodology, I.F.-O., E.V.-C., A.E.-U., J.L., R.J.-M. and J.A.T.-R.; software, A.E.-U., E.V.-C. and D.V.; validation, A.E.-U., D.V. and J.L.; formal analysis, I.F.-O., A.E.-U. and J.L.; investigation, R.J.-M.; resources, A.E.-U., J.L., R.J.-M. and J.A.T.-R.; data curation, A.E.-U.; writing—original draft preparation, I.F.-O., A.E.-U. and R.J.-M.; writing—review and editing, J.A.T.-R.; visualization, R.J.-M.; supervision, A.E.-U.; project administration, J.A.T.-R.; funding acquisition, J.A.T.-R. and R.J.-M. All authors have read and agreed to the published version of the manuscript.

Funding: Financial support for this study was provided by the Ministry of Science, Innovation and Universities of Spain, through grant RTI2018-101653-B-I00, which is greatly appreciated. Additional support was provided by the regional government of Catalonia and FEDER funds for regional development through grant 001-P-001822.

Institutional Review Board Statement: Not applicable.

Informed Consent Statement: Not applicable.

Data Availability Statement: Not applicable.

Acknowledgments: We want to thank the CDIF research group for their support.

Conflicts of Interest: The authors declare no conflict of interest.

References

- Martínez-González, E.; Ramírez, G.; Romeu, J.; Casellas, D. Damage induced by a spherical indentation test in tool steels detected by using acoustic emission technique. *Exp. Mech.* **2015**, *55*, 449–458. [\[CrossRef\]](#)
- Feng, P.; Borghesani, P.; Smith, W.A.; Randall, R.B.; Peng, Z. A Review on the relationships between acoustic emission, friction and wear in mechanical systems. *Appl. Mech. Rev.* **2020**, *72*, 020801. [\[CrossRef\]](#)
- Maia, L.H.A.; Abrao, A.M.; Vasconcelos, W.; Sales, W.; Machado, Á. A new approach for detection of wear mechanisms and determination of tool life in turning using acoustic emission. *Tribol. Int.* **2015**, *92*, 519–532. [\[CrossRef\]](#)
- Klocke, F.; Döbbeler, B.; Pullen, T.; Bergs, T. Acoustic emission signal source separation for a flank wear estimation of drilling tools. *Procedia CIRP* **2019**, *79*, 57–62. [\[CrossRef\]](#)
- Chethan, Y.; Ravindra, H.; Krishnegowda, Y. Optimization of machining parameters in turning Nimonic-75 using machine vision and acoustic emission signals by Taguchi technique. *Measurement* **2019**, *144*, 144–154. [\[CrossRef\]](#)
- Olufayo, O.; Abou-El-Hossein, K. Acoustic wear monitoring during the milling of tool steel for machining 4.0. In *Lecture Notes in Mechanical Engineering, Proceedings of 8th International Conference on Fracture, Fatigue and Wear FFW 2020, Singapore, 26–27 August 2020*; Abdel Wahab, M., Ed.; Springer: Singapore, 2020. [\[CrossRef\]](#)
- Khripunov, N.V.; Gorshkov, B.M.; Samokhina, N.S. Machinability metallic materials estimation based on acoustic emission of turning. *J. Phys. Conf. Ser.* **2021**, *1889*, 042072. [\[CrossRef\]](#)
- Pandiyani, V.; Tjahjowidodo, T. Use of Acoustic emissions to detect change in contact mechanisms caused by tool wear in abrasive belt grinding process. *Wear* **2019**, *436–437*, 203047. [\[CrossRef\]](#)
- Lopes, W.N.; Junior, P.O.C.; Aguiar, P.R.; Alexandre, F.A.; Dotto, F.R.L.; da Silva, P.S.; Bianchi, E.C. An efficient short-time Fourier transform algorithm for grinding wheel condition monitoring through acoustic emission. *Int. J. Adv. Manuf. Technol.* **2021**, *113*, 585–603. [\[CrossRef\]](#)
- Wang, B.; Liu, Z. Acoustic emission signal analysis during chip formation process in high speed machining of 7050-T7451 aluminum alloy and Inconel 718 superalloy. *J. Manuf. Process.* **2017**, *27*, 114–125. [\[CrossRef\]](#)
- Zanger, F.; Kacaras, A.; Bächle, M.; Schwabe, M.; León, F.P.; Schulze, V. FEM simulation and acoustic emission based characterization of chip segmentation frequency in machining of Ti-6Al-4V. *Procedia CIRP* **2018**, *72*, 1421–1426. [\[CrossRef\]](#)
- Griffith, A.A. The phenomena of rupture and flow in solids. *Philos. Trans. R. Soc.* **1921**, *221*, 163–198.
- Shivalingappa, D. The influence of ball and roller burnishing process parameters on surface integrity of Al 2024 alloy. *Mater. Today Proc.* **2020**, *27*, 1337–1340. [\[CrossRef\]](#)
- Kalisz, J.; Żak, K.; Wojciechowski, S.; Gupta, M.; Krolczyk, G. Technological and tribological aspects of milling-burnishing process of complex surfaces. *Tribol. Int.* **2021**, *155*, 106770. [\[CrossRef\]](#)
- Gomez-Gras, G.; Travieso-Rodríguez, J.A.; Jerez-Mesa, R.; Lluma-Fuentes, J.; De La Calle, B.G. Experimental study of lateral pass width in conventional and vibrations-assisted ball burnishing. *Int. J. Adv. Manuf. Technol.* **2016**, *87*, 363–371. [\[CrossRef\]](#)
- Amini, S.; Bagheri, A.; Teimouri, R. Ultrasonic-assisted ball burnishing of aluminum 6061 and AISI 1045 steel. *Mater. Manuf. Process.* **2017**, *33*, 1250–1259. [\[CrossRef\]](#)
- Kozlov, A.; Mordiyuk, B.; Chernyashevsky, A. On the additivity of acoustoplastic and electroplastic effects. *Mater. Sci. Eng. A* **1995**, *190*, 75–79. [\[CrossRef\]](#)
- Jerez-Mesa, R.; Landon, Y.; Travieso-Rodríguez, J.; Dessein, G.; Lluma-Fuentes, J.; Wagner, V. Topological surface integrity modification of AISI 1038 alloy after vibration-assisted ball burnishing. *Surf. Coat. Technol.* **2018**, *349*, 364–377. [\[CrossRef\]](#)
- Brehl, D.E.; Dow, T.A. Review of vibration-assisted machining. *Precis. Eng.* **2008**, *32*, 153–172. [\[CrossRef\]](#)
- Jerez-Mesa, R.; Travieso-Rodríguez, J.A.; Gomez-Gras, G.; Lluma-Fuentes, J. Development, characterization and test of an ultrasonic vibration-assisted ball burnishing tool. *J. Mater. Process. Technol.* **2018**, *257*, 203–212. [\[CrossRef\]](#)
- Arnau, A. *Piezoelectric Transducers and Applications*; Springer: Berlin, Germany, 2004; Volume 2004.
- Dornfeld, D.; Liu, J.B. Abrasive texturing and burnishing process monitoring using acoustic emission. *CIRP Ann. Manuf. Technol.* **1993**, *42*, 397–400. [\[CrossRef\]](#)
- Strömbergsson, D.; Marklund, P.; Edin, E.; Zeman, F. Acoustic emission monitoring of a mechanochemical surface finishing process. *Tribol. Int.* **2017**, *112*, 129–136. [\[CrossRef\]](#)
- Salahshoor, M.; Guo, Y.B. Contact Mechanics in low plasticity burnishing of biomedical magnesium-calcium alloy. In *Proceedings of the STLE/ASME 2010 International Joint Tribology Conference, San Francisco, CA, USA, 17–20 October 2010*; American Society of Mechanical Engineers: New York, NY, USA, 2010; Volume 44199, pp. 349–351.
- Hu, S.; Huang, W.; Shi, X.; Peng, Z.; Liu, X.; Wang, Y. Bi-Gaussian stratified effect of rough surfaces on acoustic emission under a dry sliding friction. *Tribol. Int.* **2018**, *119*, 308–315. [\[CrossRef\]](#)
- Tandon, N.; Choudhury, A. A review of vibration and acoustic measurement methods for the detection of defects in rolling element bearings. *Tribol. Int.* **1999**, *32*, 469–480. [\[CrossRef\]](#)

27. Hase, A.; Mishina, H.; Wada, M. Correlation between features of acoustic emission signals and mechanical wear mechanisms. *Wear* **2012**, *292*, 144–150. [[CrossRef](#)]
28. Geng, Z.; Puhan, D.; Reddyhoff, T. Using acoustic emission to characterize friction and wear in dry sliding steel contacts. *Tribol. Int.* **2019**, *134*, 394–407. [[CrossRef](#)]
29. Travieso-Rodríguez, J.A.; Lluma-Fuentes, J.; Jerez-Mesa, R.; Dessein, G.; Wagner, V.; Landon, Y. Ultrasonic vibration assisted burnishing tool for lathe. In *Spanish Utility Model*; Spanish Intellectual Property Bulletin: Madrid, Spain, 2020; Publication number ES1253044.
30. Ewins, D.J. *Modal Testing: Theory and Practice*; Research Studies Press: Letchworth, UK, 1984; Volume 15.
31. Estevez-Urra, A.; Llumà, J.; Jerez-Mesa, R.; Travieso-Rodríguez, J.A. Monitoring of Processing conditions of an ultrasonic vibration-assisted ball-burnishing process. *Sensors* **2020**, *20*, 2562. [[CrossRef](#)]
32. Fernández, I.; Montané, F.X.; García, J.J.; Maureso, M. *Advanced Analysis of In-Service Movements of Vehicle Closures*; FISITA World Automotive Congress: Prague, Czech Republic, 2004; pp. 1–10.
33. ISO 20816-1. *Mechanical Vibration—Measurement and Evaluation of Machine Vibration—Part 1: General Guidelines*; ISO: Geneva, Switzerland, 2016.
34. Callister, W.D. *Fundamentals of Materials Science and Engineering*; Wiley: London, UK, 2000; Volume 471660817.
35. Sales, W.F.; Becker, M.; Gurgel, A.G.; Júnior, J.L. Dynamic behavior analysis of drill-threading process when machining AISI Al-Si-Cu4 alloy. *Int. J. Adv. Manuf. Technol.* **2009**, *42*, 873–882. [[CrossRef](#)]
36. Yang, Z.; Zhu, L.; Zhang, G.; Ni, C.; Lin, B. Review of ultrasonic vibration-assisted machining in advanced materials. *Int. J. Mach. Tools Manuf.* **2020**, *156*, 103594. [[CrossRef](#)]

Article

A Comparative Analysis of Chemical, Thermal, and Mechanical Post-Process of Fused Filament Fabricated Polyetherimide Parts for Surface Quality Enhancement

Ariadna Chueca de Bruijn, Giovanni Gómez-Gras * and Marco A. Pérez

IQS School of Engineering, Universitat Ramon Llull, Via Augusta 390, 08017 Barcelona, Spain; ariadnachuecad@iqs.url.edu (A.C.d.B.); marcoantonio.perez@iqs.url.edu (M.A.P.)

* Correspondence: giovanni.gomez@iqs.url.edu

Abstract: Additive manufacturing technologies are increasingly being used in production systems because they shorten product development time and production cost, but surface integrity remains a limitation to meet the standards set by conventional manufacturing. In this research article, two chemical, one thermal, and three mechanical finishing operations are proposed to post-process fused filament fabricated Ultem 9085 parts. Their effects on the parts' surface quality and dimensional accuracy (changes in their width, height, length, and mass) are examined through optical and electron scanning microscopy, and the advantages and disadvantages of each method are discussed. Microscope evaluation has proven to be a powerful tool to observe apparent differences and understand the nature of different morphological changes. Results indicate that chemical and thermal treatments and ball burnishing are good candidates to significantly enhance the finish of the parts, despite requiring the use of solvents or provoking dimensional changes to the parts. The effects of abrasive mechanical treatments are more moderate at a macroscopic scale, but the surface of the filaments suffers the most remarkable changes.

Keywords: additive manufacturing; fused filament fabrication; PEI Ultem 9085; postprocessing; finishing operations; surface enhancement; vapor smoothing; thermal annealing; abrasive shot blasting; shot peening

Citation: Chueca de Bruijn, A.; Gómez-Gras, G.; Pérez, M.A. A Comparative Analysis of Chemical, Thermal, and Mechanical Post-Process of Fused Filament Fabricated Polyetherimide Parts for Surface Quality Enhancement. *Materials* **2021**, *14*, 5880. <https://doi.org/10.3390/ma14195880>

Academic Editors: Stanislaw Legutko, Carola Esposito Corcione and Antonio Santagata

Received: 29 July 2021
Accepted: 5 October 2021
Published: 8 October 2021

Publisher's Note: MDPI stays neutral with regard to jurisdictional claims in published maps and institutional affiliations.



Copyright: © 2021 by the authors. Licensee MDPI, Basel, Switzerland. This article is an open access article distributed under the terms and conditions of the Creative Commons Attribution (CC BY) license (<https://creativecommons.org/licenses/by/4.0/>).

1. Introduction

The surface characteristics of a component determine how it will interact with its environment. In some cases, irregularities on the surface will constitute weak regions where cracks or corrosion may start to nucleate. Therefore, surface roughness could be a good indicator of the potential mechanical performance of a part [1]. In other cases, however, specific roughness values may be desirable to enhance the adhesion of cosmetic or functional finish coatings such as painting or metal plating [2].

Within the specific context of additive manufacturing (AM), the layer-by-layer material deposition that is characteristic of these technologies creates an uneven surface profile known as “stair-stepping effect” [3,4]. This issue poses a challenge in terms of superficial integrity and dimensional accuracy and has been recognized as a major concern in employing AM technologies for final part applications [5]. For this reason, monitoring, modeling, and compensation for surface roughness in AM have become popular fields of research [6–12].

The reviewed literature reveals that the most common approach to address this subject consists of optimizing pre-printing parameters, including the slicing strategy, raster angle, part orientation, infill percentage, printing temperature, and layer thickness. In this sense, Boschetto et al. [13] proposed a geometrical model of the filament that considers the radius and spacing of the profile section and can predict the dimensional deviations of acrylonitrile butadiene styrene (ABS) fused filament fabricated (FFF) parts as a function

of the layer thickness and deposition angle. Their findings correlate with those published by Pérez et al. [14] and Buj-Corral [15]. The former performed an experimental study with polylactic acid (PLA) samples and found that layer height and wall thickness are the most important factors controlling surface roughness. The latter presented a geometrical model for the simulation of roughness profiles obtained with different print orientation angles in FFF PLA specimens and compared it to experimental results. Their findings were that roughness values increase with print orientation angle as the stair-stepping effect is accentuated.

Despite accurate optimization of process parameters, the desired surface quality of parts may not be achieved, or perhaps only a fraction of the surface needs to be conditioned to meet the end customer's specifications. Thus, post-processing techniques constitute a complementary tool to refine the finish of additively manufactured parts [16]. In broad terms, these processes can be grouped into thermochemical and mechanical treatments. Thermochemical treatments take advantage of chemical substances or the application of general or localized heat to smooth the part's surface. These methods include vapor smoothing, painting, electroplating or metallization, annealing, and laser finishing.

Many research works have investigated the vapor smoothing process; it is a relatively straightforward and well-established process. Chohan et al. [17–19] published a series of articles where they performed a parametric optimization to treat FFF ABS hip replicas with acetone vapors. They evaluated the impact of smoothing duration and repetition of smoothing cycles on surface finish, dimensional accuracy, and stability of the parts, and they concluded that small smoothing duration (30 s) and repeated cycles could yield remarkably lower surface roughness. They also developed a mathematical model for the prediction of the average surface roughness of the treated parts. Mu et al. [20] compared the effect of different mixtures of acetone and ethyl acetate to improve the surface coarseness of ABS specimens with different building orientations and concluded that the tensile strength of samples treated with the acetone or the mixed vapor decreased with increasing the exposure time. The best results in terms of mechanical performance were obtained when vapors of pure ethyl acetate were used. Jin et al. [21] and Rajan et al. [22] explored the use of tetrahydrofuran and dichloromethane, respectively, to smooth the surface and improve the toughness of PLA specimens, despite reporting a decline in their tensile properties.

Some works combine vapor smoothing with other finishing techniques. For instance, Nguyen et al. [23] carried out a design-of-experiments-based investigation on the treatment of ABS parts combining an acetone-based chemical treatment, drying, and aluminum coating, observing a decrease in surface roughness and heat absorption of radiative heating. Maciag et al. [24] performed a study on the influence of acetone smoothing and subsequent galvanic copper plating over the surface parameters of ABS prints. Studies considering the feasibility of laser polishing for FFF PLA parts include the ones presented by Chen et al. [25] and Moradi et al. [26].

Regarding thermal treatments, one can find more published data concerning the treatment of semicrystalline polymers such as PLA. For example, an increase in the crystallinity degree through thermal annealing over the glass transition temperatures (T_g) of PLA samples was reported by Wach et al. [27]. This enhancement favorably impacted the flexural stress of the samples by an average of 14%. Improvements in interlayer tensile strength of the same polymer were reported by Bhandari et al. [28]. Increased inter-laminar toughness of specimens made from amorphous ABS when these were treated over T_g was noted by Hart et al. [29]. In these studies, though, less attention is put into evaluating the surface characteristics of the treated parts.

A relevant study concerning the post-processing of polyetherimide (PEI) parts was recently presented by Zhang et al. [30]. They used thermal annealing to post-process the samples and noted a relaxation of thermal stresses when PEI specimens were treated for long periods at temperatures only below its T_g .

Mechanical post-processing methods aim to replicate conventional metal finishing techniques applied to thermoplastics by cutting or pressing the peaks of the outer profile

of the manufactured parts. The treatment of complex or intricate shapes using these processes may seem challenging, but some recent studies have shown progress in this direction [31,32]. Machining, barrel finishing, ball burnishing, and sanding are examples of mechanical post-processing finishes found in the published literature. In particular, Boschetto et al. [33] conducted an experimental analysis and designed a theoretical model to study the integration between FFF technology and barrel finishing (BF) to improve the surface quality of printed parts. A significant contribution of the study was that BF's action is deeply affected by the deposition angle of the initial profiles of the substrates. The same research group explored the finishing of FFF parts by computer numerical control [34]. They managed to set the cutting depth as a function of the deposition angle and reported a reduced average roughness and reliable uniformity of finished surfaces. Mali et al. [35] proposed the use of abrasive flow for the finishing of FFF ABS parts. The process was carried out with a self-synthesized abrasive media made of marble powder and Karanja oil and increases in the average surface roughness were encountered with the increase in active cutting particles and extrusion pressure.

One of the few comparative studies regarding different post-processing techniques applied to AM parts was published by Nsengimana et al. [36]. Differences between tumbling, shot peening, hand finishing, spray painting, CNC machining, and chemical treatment on the dimensional accuracy of laser-sintered Nylon and Alumide[®], as well as FFF ABS parts, were investigated, and the advantages and disadvantages of each of these methods discussed.

As shown, most of the references focus on the post-processing of readily available materials, often used for prototyping, i.e., PLA or ABS. However, there is a scarcity of published research that considers the post-processing of higher performance thermoplastics. Some industries, such as aerospace, biomedical, and automotive, have adopted AM manufacturing technologies beyond prototyping to produce intermediate tooling and end-use parts [37]. These sectors often require products capable of working at elevated temperatures, in the presence of flames or harsh solvents, and under high mechanical loads [38]. In this regard, the engineering-grade thermoplastic such as ULTEM[™] 9085 (Ultem) offers a remarkable potential opportunity to fulfill the industries' needs, owing to its unique combination of high mechanical properties [39] and flame, smoke, and toxicity rating [40].

Based on the above, this work aims to investigate a series of post-processing techniques to treat FFF Ultem specimens, namely vapor smoothing, chemical solvent immersion, high-temperature thermal annealing, ball burnishing, abrasive shot blasting, and shot peening, providing optimized process parameters and a comparative overview of the applicability and effect regarding the surface quality enhancement.

2. Materials and Methods

2.1. Manufacturing of the Samples

The engineering-grade thermoplastic ULTEM[™] 9085 (Ultem) was chosen as a model material to fabricate all samples in a Fortus[®] 400mc professional fused filament fabrication (FFF) printer (Stratasys Ltd., Edina, MN, USA). This printer is equipped with a thermally controlled chamber that ensures a stable temperature of 195 °C during the printing process. Rectangular solid parts (infill of 100%) were printed with a flat surface of 10 × 127 mm², a height of 4 mm, a 0.254 mm layer height, ±45° raster angle, one external contour, and a flat horizontal orientation. Three repetitions were fabricated for each studied post-treatment.

2.2. Chemical Post-Processing

2.2.1. Vapor Smoothing

The first treatment was intended to improve the surface quality of Ultem parts through the partial dissolution of their outer layer due to prolonged contact with a chemical vapor (a process known as vapor smoothing). Due to the low compatibility between Ultem and chlorinated solvents [41], and its low boiling point (around 61 °C), chloroform (purity of 99.9%) was chosen for the smoothing process.

Vapor smoothing was performed by placing the substrates on an elevated sample bed (whose function was to avoid direct contact between the liquid solvent and the parts) within a $200 \times 130 \times 60$ mm glass container. Next, 50 mL of chloroform were added to the bottom of the container, which was then sealed for 120 min. After the 120-min cycle, samples were removed and allowed to dry in ambient laboratory conditions for at least 24 h before further processing. Finally, two more sets of samples were treated for 180 and 270 min, respectively.

2.2.2. Support Removal Solvent

The second chemical treatment was aimed at analyzing the surface integrity of Ultem parts after being treated with a solvent mixture capable of dissolving polysulfone, a thermoplastic commonly used as support material for Ultem in FFF. The effect of this treatment on the mechanical performance of Ultem and the optimal treatment time has been previously demonstrated [42].

Samples were submerged in a mixture of equal volumetric parts of 1,4-dioxane and toluene for a period of 4 hours. A similar setup as the one used for the vapor smoothing was used. This time, though, samples were fully immersed in the solvent (the volume used was 400 mL), and the liquid mixture was constantly agitated using a magnetic stirrer. After the treatment cycle, samples were removed and allowed to dry in a vacuum chamber for at least 12 h before further processing.

2.3. Thermal Annealing

A differential scanning calorimetry (DSC) of Ultem enabled identifying its glass transition temperature at $181\text{ }^{\circ}\text{C}$. This analysis was performed using a DSC821 measuring device from Mettler Toledo and a heating rate of $10\text{ K}\cdot\text{min}^{-1}$. The lack of other phase transitions such as crystallization or melting, indicated the amorphous nature of the studied polymer. A sudden release of energy at $370\text{ }^{\circ}\text{C}$ revealed a loss of integrity and irreversible degradation of the material. Another point to consider is that, during manufacturing, the material is exposed to a temperature of $195\text{ }^{\circ}\text{C}$ for long periods inside the printing chamber. For these reasons, temperatures of $210\text{ }^{\circ}\text{C}$, $225\text{ }^{\circ}\text{C}$, and $240\text{ }^{\circ}\text{C}$ were chosen as annealing temperatures. Thermal annealing of Ultem samples was performed at the set temperature for 30 min in an electric furnace from Hobersal, preheated before introducing the samples. Once the treatment was completed, cooling was performed at a constant rate of $1.5\text{ }^{\circ}\text{C}\cdot\text{min}^{-1}$ until it reached a temperature of $150\text{ }^{\circ}\text{C}$ to minimize thermal stresses. Then, the cooling rate was increased to $8\text{ }^{\circ}\text{C}\cdot\text{min}^{-1}$ until room temperature.

2.4. Mechanical Post-Processing

2.4.1. Ball Burnishing

Ball burnishing is a finishing operation based on the plastic deformation of a work-piece's surface via the application of a hard, highly polished ball subjected to a constant external force. Ball burnishing of Ultem specimens was conducted with a burnishing tool designed to be coupled to a CNC milling machine. This tool has an innerspring, the stiffness of which determines the range of ball burnishing forces exerted by a 10 mm chrome-hardened steel ball. The process was made following the procedure described in a previous publication [43] using the optimal configuration of a force of 400 N, 10 passes of the tool, a lateral path width of 0.32 mm, and a forward speed of $2000\text{ mm}\cdot\text{min}^{-1}$. Samples were ball burnished on the top side.

2.4.2. Abrasive Shot Blasting

Shot blasting is a cold surface treatment that involves projecting beads on the work-piece to change its surface state, causing plastic deformation to prepare the surface for subsequent processes such as applying a coating layer. In the present study, shot blasting was performed in a manually operated pressure-controlled sandblasting cabinet. The working pressure was set at 5 bar, and samples were individually blasted for 10 to 20 s,

using either a mix of spherical glass beads (100 to 850 μm) or white corundum (220 to 36 FEPA (Federation of European Producers of Abrasives) grit, or about 53 to 500 μm). The angle of incidence was kept between 75° and 90° .

2.4.3. Shot Peening

The process of shot peening resembles abrasive shot blasting but uses metallic beads to treat the surface of the samples. In the present case, a small hole was drilled at one end of the samples to facilitate their hanging on a rotary unit and allowing the shot peening process in an automated chamber. Spherical stainless-steel beads with diameters ranging from 0.2 to 0.3 mm were propelled at the samples using a 2500 rpm turbine working at a pressure of 5 bar during a total treatment time of 10 min.

A summary of the post-processing techniques and experimental conditions used in the present study can be found in Table 1.

Table 1. Post-processing techniques and procedures applied to Ultem pieces.

Post-Processing Technique	Fixed Experimental Conditions	Variable Experimental Conditions
Vapor smoothing	Solvent: Chloroform vapors Temperature: ambient laboratory conditions	Exposure times: 2, 3 and, 4.5 h
Support removal solvent	Solvent: equivolumetric mixture of 1,4-dioxane and toluene Temperature: ambient laboratory conditions Constant agitation using a magnetic stirrer Exposure time: 4 h	
Thermal annealing	Preheating of the furnace prior to the introduction of the samples Exposure time at the set temperature: 30 min Cooling rate: $1.5^\circ\text{C}\cdot\text{min}^{-1}$ until 150°C , $8^\circ\text{C}\cdot\text{min}^{-1}$ until room temperature	Temperatures: 210, 225, and 240°C
Ball burnishing	Ball burnishing force: 400 N Number of passes of the tool: 10 Lateral path width: 0.32 mm Forward speed: $2000\text{ mm}\cdot\text{min}^{-1}$	
Abrasive shot blasting	Pressure: 5 bar Treatment time: 10–20 s	Abrasive media: White corundum, and glass beads
Shot peening	Spherical stainless-steel beads Pressure: 5 bar Treatment time: 10 min	

2.5. Dimensional Accuracy and Surface Roughness

The effects of each post-processing technique on the surface of the FFF parts were firstly investigated through changes in their width, height, and length dimensions. Secondly, changes in mass and surface roughness were also examined. The latter was evaluated in terms of the average roughness (R_a) and the average maximum peak-to-valley height of the roughness profile (R_z), using a portable roughness gauge Rugosurf 20 from Tesa Technology. The sampling length and cut-off values were set based on the ISO 4288:1996 standard [44].

The surface state of the treated samples was captured using an Olympus DSX1000 digital microscope (Olympus Iberia, Barcelona, Spain) fitted with a DSX10-SXLOB lens and using a $1\times$ and $20\times$ magnification. Surface morphology was examined with a JSM-6460 Scanning Electron Microscope (SEM)(JEOL Ltd., Akishima, Japan).

3. Results and Discussion

3.1. Mass and Dimensional Changes

The mass and dimensional changes of all specimens subjected to the different post-processing techniques are summarized in Table 2. Differences in mass, height, width, and length are given as absolute values.

Table 2. Mass and dimensional changes as a function of the post-processing treatment.

Post-Process	Details	Δ Mass [g]	Δ Height [mm]	Δ Width [mm]	Δ Length [mm]
Support removal solvent	-	$+0.03 \pm 0.05$	-0.04 ± 0.05	-0.01 ± 0.01	-0.02 ± 0.03
Chloroform vapor smoothing	120 min	$+0.12 \pm 0.01$	-0.05 ± 0.01	-0.10 ± 0.04	-0.18 ± 0.02
	180 min	$+0.22 \pm 0.01$	$+0.01 \pm 0.05$	$+0.05 \pm 0.02$	-0.14 ± 0.02
	270 min	$+0.35 \pm 0.03$	$+0.10 \pm 0.02$	$+0.15 \pm 0.03$	$+0.16 \pm 0.01$
Thermal annealing	210 °C	$+0.00 \pm 0.01$	$+0.48 \pm 0.12$	-0.88 ± 0.19	-4.73 ± 0.84
	225 °C	-0.02 ± 0.01	$+0.52 \pm 0.18$	-0.93 ± 0.26	-5.11 ± 1.38
	240 °C	-0.01 ± 0.00	$+0.62 \pm 0.04$	-1.07 ± 0.06	-5.73 ± 0.49
Ball burnishing	-	$+0.00 \pm 0.03$	-0.11 ± 0.02	$+0.08 \pm 0.03$	$+0.30 \pm 0.09$
Abrasive shot blasting	White corundum	$+0.01 \pm 0.02$	-0.01 ± 0.06	$+0.02 \pm 0.03$	$+0.08 \pm 0.07$
	Glass beads	-0.01 ± 0.01	-0.05 ± 0.02	$+0.02 \pm 0.02$	$+0.03 \pm 0.07$
Shot peening	-	-0.02 ± 0.01	-0.02 ± 0.01	$+0.01 \pm 0.02$	$+0.05 \pm 0.06$

Overall, solvent support removal, abrasive shot blasting, and shot peening have not induced substantial changes in the mass or the main dimensions of the treated parts. This means that there is no detectable solvent absorption or Ultem dissolution during the support removal process. In addition, abrasive mechanical post-processes, performed under the previously described treatment conditions, do not abrade the material enough to induce detrimental changes in their shape.

Regarding vapor smoothing, it is the only treatment that has induced a significant weight increase in the samples. This change is more pronounced with increased treatment times, indicating a gradual absorption of chloroform vapors. Considering the initial mass of the samples was around 6 grams, the 0.35-gram increase reported after 270 min of treatment represents a change of almost 6%. A point to note concerning the dimensional analysis of this particular treatment is that, during the first 120 min, there is a slight reduction in all dimensions due to an initial smoothing of the outer surface as adjacent Ultem filaments fuse. As time progresses, despite retaining their overall shape, samples expand or swell in all directions. With even more prolonged exposure, samples would probably start to completely melt and lose their shape, which would be highly undesirable.

In terms of dimensional accuracy, specimens subjected to thermal annealing suffered the most remarkable transformation: they all expanded in the building direction (an average of 0.5 mm in height) and contracted in the remaining directions (1 and 5 mm in width and length, respectively). This correlates with the theory proposed by Zhang et al. [30] concerning the relaxation of thermal stresses created in the building direction, which seems to be valid at temperatures higher than the material's T_g as long as exposure is maintained within the herein presented ranges. It is also noteworthy to mention that higher temperatures induce more significant dimensional changes.

Finally, ball burnished samples experienced a decrease in height (coinciding with the ball burnishing direction) and a moderate expansion in width and length. As demonstrated in previous publications [43], part of the applied burnishing force is used to allocate the material in the existing inner voids, resulting in surface densification. Therefore, the increase in width and length should not be attributed to an overall deformation of the part but to creating an overhanging edge due to the expansion of the pressed material on the upper layer.

3.2. Surface Roughness Evaluation

As discussed in the introduction, the surface roughness of an additively manufactured part tends to play a crucial role in determining its overall performance. A smoother surface will usually imply an enhanced mechanical performance (superficial defects tend to act as crack nucleation sites) and will also be better received by the end consumer as parts resemble their conventionally manufactured counterparts.

In this sense, the analysis of the surface roughness parameters R_a and R_z presented in Figure 1 shows that all finishing techniques herein presented have lowered the surface roughness of FFF Ultem parts to a certain degree. However, an exception should be made in the chemical treatment to remove Ultem's support material, as changes in surface roughness are almost negligible. This result was expected as the purpose of this treatment is to affect Ultem's integrity as little as possible.

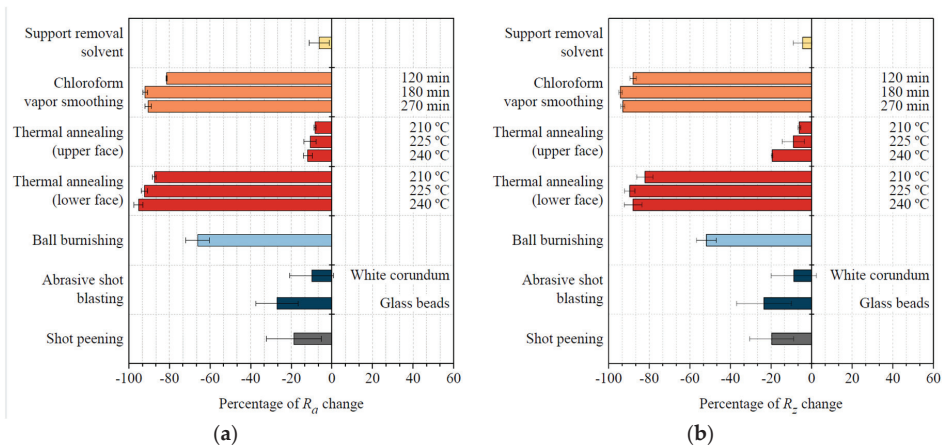


Figure 1. (a) Changes in average surface roughness; (b) Changes in average peak-to-valley height of the roughness profile.

Results obtained from the other chemical treatment, namely vapor smoothing with chloroform, are drastically different. Improvements on Ultem's surface roughness are as remarkable as 90–95% ($R_a = 1.4 \mu\text{m}$, $R_z = 3.57 \mu\text{m}$) after 180 min of treatment. Interestingly, there is no further improvement after this point (surface roughness after 270 min is similar to the one obtained after 180 min), while chloroform continues to be absorbed, as discussed in the mass and dimensional analysis section. For this reason, 180 min should be considered the maximum treatment time to achieve an excellent surface finish. The magnitude of the roughness improvements reported by Chohan et al. [17] (99.62%) is comparable to the results of the present study. It should be noted, though, that the initial surface roughness of their studied hip replica was two-times lower than the one of the Ultem parts used in this study and that their total contact time with the vaporized solvent was considerably lower (in the order of a 1 min) than in the present case. The roughness improvements reported by Rajan et al. [22] are more moderate (around 80%) when they used tetrahydrofuran (THF) vapors during a total time of 5 min to smooth FFF PLA parts. They also observed that the initial build orientation (and thus the initial surface roughness) plays a crucial role in the outcome of the vapor smoothing process. Considering that all consulted treatment times are lower than the ones needed to obtain similar results with Ultem, it is safe to affirm that Ultem's chemical resistance to chloroform is higher than the chemical resistance of ABS to acetone and of PLA to THF.

Concerning thermal annealing, no significant differences in surface roughness have been identified, regardless of the temperature of the treatment. Nevertheless, dimensional changes are higher at higher temperatures, implying that there is no benefit in increasing the temperature of the treatment from 210 °C to 240 °C. The obtained 15% improvement in

the surface roughness of the upper part ($R_a = 12.60 \mu\text{m}$, $R_z = 62.28 \mu\text{m}$) is probably due to the partial fusion of adjacent filaments. Interestingly, the lower part of the samples, which was in direct contact with the thermal chamber's tray, presented a glass-like finish, with improvements in R_a higher than 90% ($1.05 \mu\text{m}$) and higher than 80% in R_z ($8.69 \mu\text{m}$). This suggests that a physical contact that favors heat transfer by conduction is noticeably more effective in improving the surface finish of the parts than heat transfer by convection, as it happens on the air-exposed faces of the part.

Surface roughness obtained after mechanical post-processing of the parts differs considerably. When samples are ball burnished, R_a and R_z diminish by about 70% ($5.06 \mu\text{m}$) and 50% ($34.19 \mu\text{m}$), respectively, due to the plasticization of the outer layer because of the forced pressing of the peaks by the burnishing ball. This technique uses a stainless-steel tool that can be adapted to a numeric control machine, making it an easily automatable process, but presents some challenges when the totality of the part needs to be treated, or when the part has difficult-to-access zones. With abrasive shot peening or abrasive shot blasting using glass beads, the surface roughness has improved by 20% to 25% ($R_a = 10.83 \mu\text{m}$, $R_z = 3.57 \mu\text{m}$). The use of white corundum as blasting media has resulted in a more moderate improvement of around 10% ($R_a = 13.40 \mu\text{m}$, $R_z = 62.54 \mu\text{m}$). A noticeable fact is that the standard deviation of the roughness measurements after these finishing processes were applied to Ultem parts is considerably higher than with the other treatments, which indicates more limited repeatability as they depend on the experience of the operator performing the treatment, the contact time, and the wear of the beads, amongst others. In comparison with the 50% improvement in surface roughness reported by Valerga Puerta et al. [45] when they corundum blasted FFF PLA parts using analogous treatment time conditions as the ones reported in the present study, Ultem appears to have an increased initial toughness that could explain such more moderate improvements.

3.3. Surface Analysis

Even though obtaining a combination of lower R_a and R_z values is typically enough to affirm an improvement in the surface finish of a part, microscope imaging provides a deeper insight into the reasons behind surface changes and their nature. In this sense, Figures 3–5 present a series of optical microscope images and SEM micrographs aimed at the direct comparison between the macroscopic and microscopic state of the treated samples. Images of an untreated or pristine part have also been added in Figure 2.

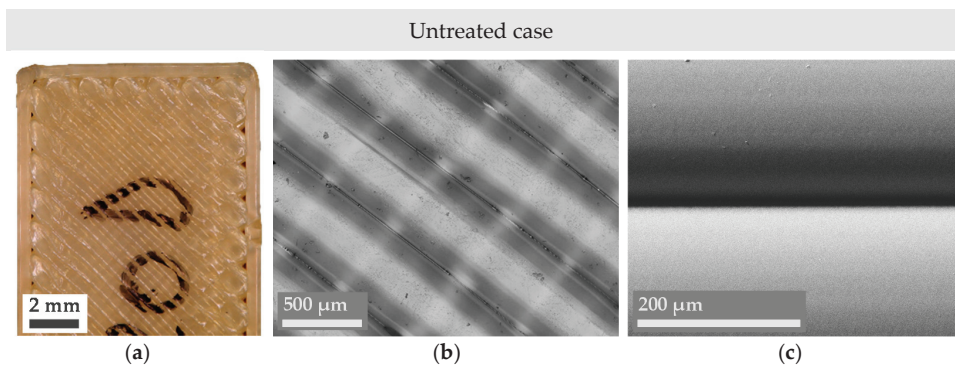


Figure 2. Digital microscope (a,b) and SEM micrographs (c) of untreated Ultem parts.

Figure 3a reveals that, compared to the pristine case, Ultem has lost some of its characteristic shine after being submerged in a mixture of 1,4-dioxane and toluene for 4 h. This tonality change could be explained by the presence of an Ultem residue that has been partially dissolved and non-uniformly redeposited along the interfilament space

(some zones are more coalesced, but some are not), as the more magnified central and right images (Figure 3b,c) show.

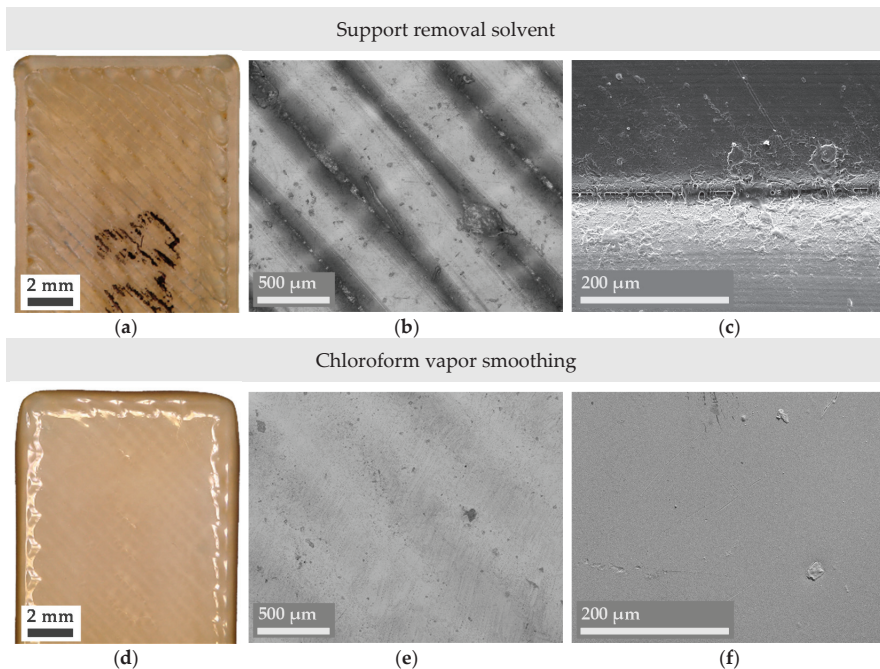


Figure 3. Digital microscope (a,b,d,e) and SEM micrographs (c,f) of the chemically treated Ultem parts.

As the roughness analysis has revealed, a drastically different surface is obtained when Ultem is vapor-smoothed in the presence of chloroform (Figure 3d–f). Microscopy results display a smooth surface where the additively manufactured nature of the part is almost inappreciable as Ultem filaments from the outer surface have completely melted and resolidified, forming a uniform layer. This result confers perspective and validates the effectiveness of the other analyzed chemical treatment: In comparison with vapor smoothing, Ultem’s surface is much less affected despite being in direct contact with a chemical mixture capable of dissolving a support material with a similar chemical structure to Ultem’s.

Regarding the visual inspection of the thermally annealed samples in Figure 4, the overall shape of the specimen is lightly modified as the corners appear more rounded, and the upper edge of the part has lost its perpendicularity with the other edges. Nonetheless, magnified images (Figure 4b,c,e,f) demonstrate that the air gap between adjacent filaments has diminished in the upper face and has almost completely disappeared in the lower face. Taking this into consideration, further experiments should be conducted at a slightly lower temperature (lower than 210 °C, but higher than the material’s T_g) to try to reduce dimensional changes while still achieving better filament adhesion. Ideally, the presence of a solid or liquid media that enters in direct contact with the totality of the part during the thermal treatment would help achieve an even smoother surface, as detected in the inspection of the lower side of the thermally annealed part.

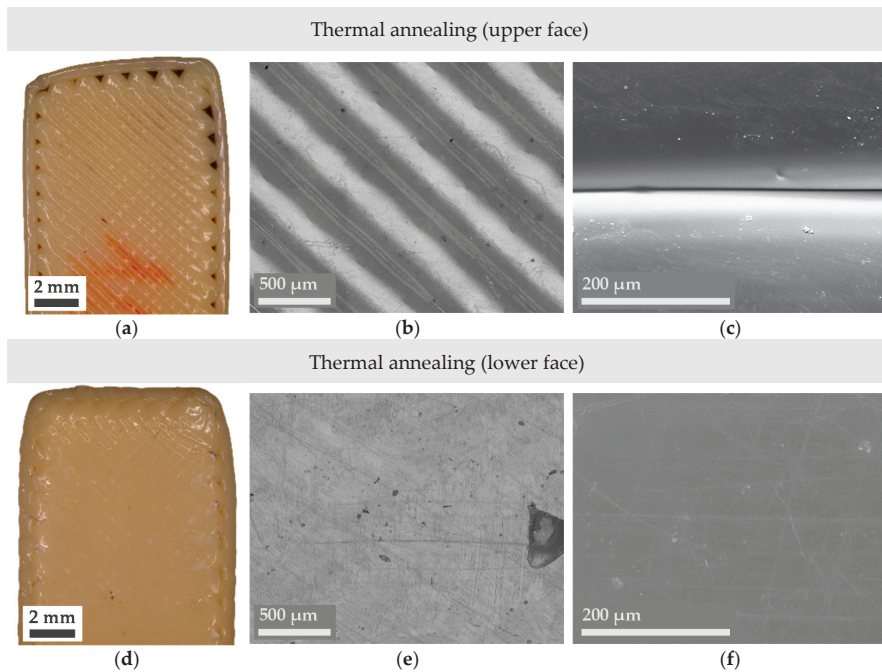


Figure 4. Digital microscope (a,b,d,e) and SEM micrographs (c,f) of the thermally treated Ultem parts.

Figure 5a–c demonstrates how the characteristic rounded shape of FFF manufactured parts is modified due to the ball burnishing process, as predicted from the roughness analysis. Ultem filaments appear flattered, and the overall state of the filament’s surface, not damaged. On the contrary, the surface of the mechanically treated parts using abrasive treatments shown in Figure 5d–l appears to be radically modified. While the average surface roughness or overall dimensions of the treated parts do not reveal such intense changes, the surface of a single filament has been deeply affected.

Samples that have been shot blasted with white corundum (Figure 5d–f) have suffered the most remarkable changes. The impact of small, non-rounded beads made of a material as hard as corundum has eroded the surface and completely changed its morphology. The Ultem part’s external filaments show cracks and numerous irregularities; Ultem has lost its shine, and the part appears more mattified. Nevertheless, the presence of filaments looks more blurred, meaning that the overall aspect of the part is more uniform. This can be regarded as a positive outcome, as a specific surface morphology can be desirable to promote adhesion of further coatings that want to be applied to the part.

In the case of abrasive shot blasting with glass beads (Figure 5g–i), the surface is not as eroded as with white corundum due to the softer nature of the used abrasive and its rounded shape, but the surface still shows noticeable alterations in the form of small protrusions generated by the beads’ impact. It should be remembered that initially spherical glass beads tend to break down into smaller and more protruded parts during the shot blasting process. Something to mention is that the right corner of the treated part shown in the macroscopic image Figure 5g has been more damaged than the rest of the surface, revealing one of the main drawbacks of these abrasive techniques: the need to automate or very precisely control the exact time, incidence angle, and distance of the abrasive gun. While in the case of chemical or thermal treatments a slight time deviation in the duration of the treatment is perfectly acceptable, in the case of abrasive shot blasting a few seconds’ deviation can be detrimental to the final result.

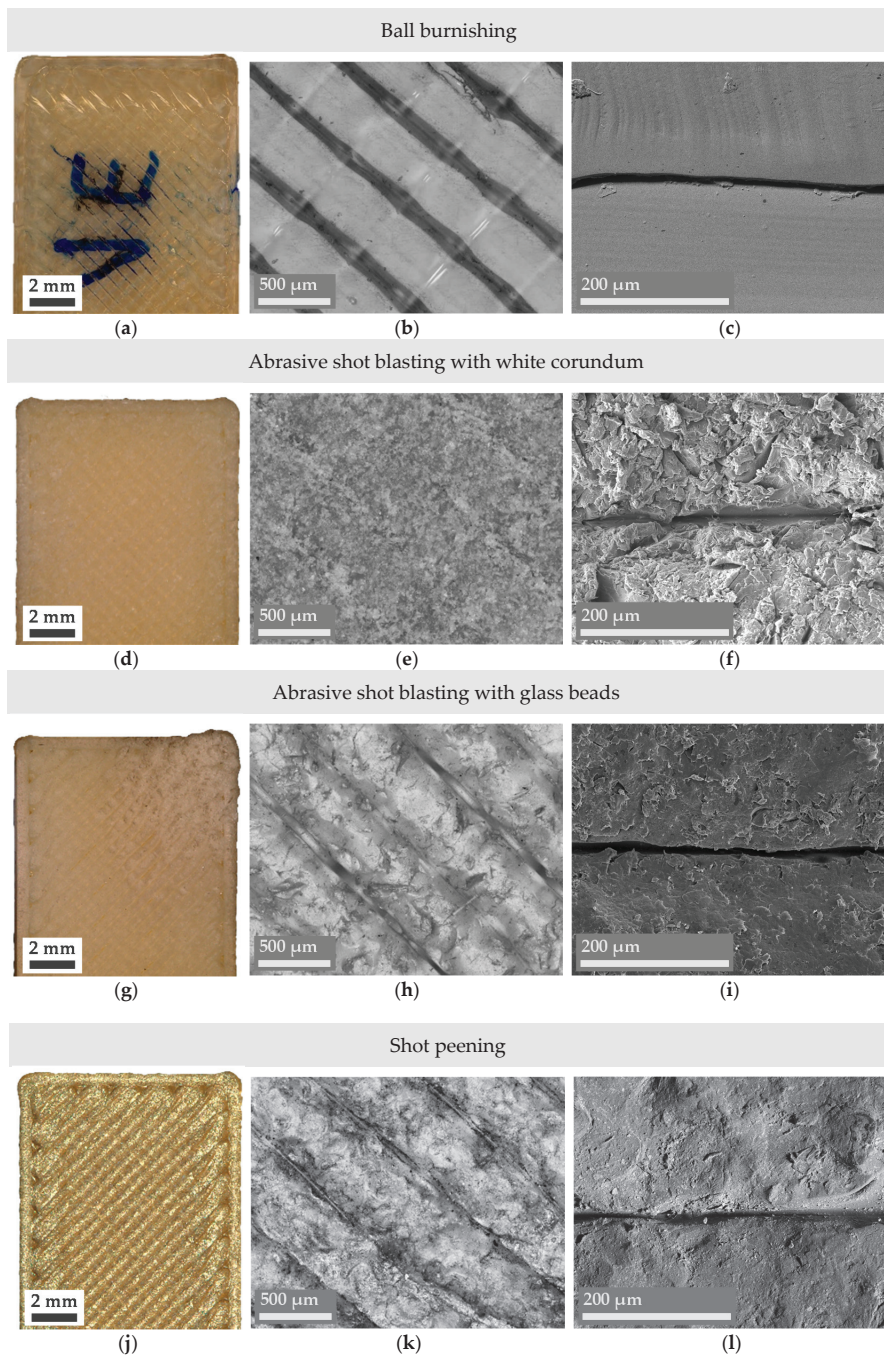


Figure 5. Digital microscope (a,b,d,e,g,h,j,k) and SEM micrographs (c,f,i,l) of the mechanically treated Ultem parts.

Finally, microscopy images from the shot peened samples (Figure 5j–l) show a shinier surface due to the presence of metallic residue from the stainless-steel beads. Interestingly, despite the longer duration of this treatment (10 min versus 10 to 20 s in the case of abrasive

shot blasting), it has resulted in a more uniform surface due to its more controlled nature (shot peening was performed in an automated chamber and with a higher distance between the gun and the samples). In addition, the impact of spherical metallic beads has induced pressing of the part's external filaments, which denotes the application of compressive stresses that could be beneficial for the fatigue life of the parts. Considering the simplicity of this process and the insignificant affectation of the parts' dimensions, shot peening's effect on the mechanical properties of FFF Ultem parts is a key point that should be addressed in future works.

4. Conclusions

In this work, six different post-processing techniques for fused filament fabricated Ultem parts have been proposed, and their effect on dimensional accuracy, mass, and surface roughness of the treated parts, compared. Microscope imaging has provided insight into the reasons behind the observed changes in surface roughness. From the obtained results, the following conclusions can be extracted:

- Overall, chemical and thermal treatments, as well as ball burnishing, have been postulated as valid candidates to significantly enhance the finish of FFF Ultem parts, despite requiring the use of solvents or inducing controlled dimensional changes.
- In particular, chemical vapor smoothing has resulted in the highest improvement in surface roughness, but the absorption of chemical vapors should be taken into consideration.
- Thermally annealed samples above Ultem's glass transition temperature retain their overall shape but have expanded in the building direction (indicating thermal stresses release) and contracted in width and length.
- Considering the observed differences between the upper and the lower side of the thermally treated samples, the addition of a physical media to conduct heat to the samples (instead of air convection) is expected to be beneficial to obtain a more uniform surface roughness. As dimensional changes increase with the treatment temperature, the use of a slightly lower temperature than the minimum 210 °C used in this study should also be considered. Ball burnishing has resulted in the best equilibrium between an improved surface roughness and minimal dimensional changes.
- The effects of abrasive shot blasting and abrasive shot peening are more moderate at a macroscopic scale but have modified the parts' surface morphology to the greatest extent.

Future works should focus on studying the affectation of the proposed finishing techniques on Ultem's mechanical performance and searching mathematical coefficients to predict dimensional and roughness changes.

Author Contributions: Conceptualization, G.G.-G. and M.A.P.; methodology, A.C.d.B.; validation, A.C.d.B.; formal analysis, G.G.-G.; investigation, A.C.d.B., G.G.-G. and M.A.P.; writing—original draft preparation, A.C.d.B.; writing—review and editing, G.G.-G. and M.A.P.; supervision, G.G.-G. and M.A.P.; funding acquisition, M.A.P. All authors have read and agreed to the published version of the manuscript.

Funding: This work has been supported by the Ministry of Science, Innovation and Universities through the project New Developments in Lightweight Composite Sandwich Panels with 3D Printed Cores (3DPC)-RTI2018-099754-A-I00; and by the RIS3CAT Llabor 3D Community co-financed by the Generalitat de Catalunya (ACCIÓ) through the project TRANS- PORT COMRDI16-1-0010 (2017–2020).

Institutional Review Board Statement: Not applicable.

Informed Consent Statement: Not applicable.

Conflicts of Interest: The authors declare no conflict of interest.

References

1. Sanaei, N.; Fatemi, A. Analysis of the effect of surface roughness on fatigue performance of powder bed fusion additive manufactured metals. *Theor. Appl. Fract. Mech.* **2020**, *108*, 102638. [[CrossRef](#)]
2. Jiang, Y.; Ding, J.; Yin, X.; Yan, J.; Yang, L.; Zhu, S.; Zeng, R.; Lu, C.; Yin, A.; Xian, X. The influence of U-Nb substrate roughness on the service performance of Ti/TiN multilayer coatings. *Surf. Coat. Technol.* **2021**, *405*, 126571. [[CrossRef](#)]
3. Kalami, H.; Urbanic, J. Exploration of surface roughness measurement solutions for additive manufactured components built by multi-axis tool paths. *Addit. Manuf.* **2021**, *38*, 101822. [[CrossRef](#)]
4. Boschetto, A.; Giordano, V.; Veniali, F. 3D roughness profile model in fused deposition modelling. *Rapid Prototyp. J.* **2013**, *19*, 240–252. [[CrossRef](#)]
5. Barari, A.; Kishawy, H.A.; Kaji, F.; Elbestawi, M.A. On the surface quality of additive manufactured parts. *Int. J. Adv. Manuf. Technol.* **2017**, *89*, 1969–1974. [[CrossRef](#)]
6. Gómez-Gras, G.; Pérez, M.A.; Fábregas-Moreno, J.; Reyes-Pozo, G. Experimental study on the accuracy and surface quality of printed versus machined holes in PEI Ultem 9085 FDM specimens. *Rapid Prototyp. J.* **2021**, *27*, 1–12. [[CrossRef](#)]
7. Taufik, M.; Jain, P.K. Characterization, modeling and simulation of fused deposition modeling fabricated part surfaces. *Surf. Topogr. Metrol. Prop.* **2017**, *5*, 045003. [[CrossRef](#)]
8. Haque, M.E.; Banerjee, D.; Mishra, S.B.; Nanda, B.K. A Numerical Approach to Measure the Surface Roughness of FDM Build Part. *Mater. Today Proc.* **2019**, *18*, 5523–5529. [[CrossRef](#)]
9. Giri, J.; Shahane, P.; Jachak, S.; Chadge, R.; Giri, P. Optimization of FDM process parameters for dual extruder 3d printer using Artificial Neural network. *Mater. Today Proc.* **2021**, *43*, 3242–3249. [[CrossRef](#)]
10. Wang, P.; Zou, B.; Ding, S. Modeling of surface roughness based on heat transfer considering diffusion among deposition filaments for FDM 3D printing heat-resistant resin. *Appl. Therm. Eng.* **2019**, *161*, 114064. [[CrossRef](#)]
11. Raj Mohan, R.; Venkatraman, R.; Raghuraman, S. Experimental analysis on density, micro-hardness, surface roughness and processing time of Acrylonitrile Butadiene Styrene (ABS) through Fused Deposition Modeling (FDM) using Box Behnken Design (BBD). *Mater. Today Commun.* **2021**, *27*, 102353. [[CrossRef](#)]
12. Chohan, J.S.; Singh, R. Pre and post processing techniques to improve surface characteristics of FDM parts: A state of art review and future applications. *Rapid Prototyp. J.* **2017**, *23*, 495–513. [[CrossRef](#)]
13. Boschetto, A.; Bottini, L. Accuracy prediction in fused deposition modeling. *Int. J. Adv. Manuf. Technol.* **2014**, *73*, 913–928. [[CrossRef](#)]
14. Pérez, M.; Medina-Sánchez, G.; García-Collado, A.; Gupta, M.; Carou, D. Surface Quality Enhancement of Fused Deposition Modeling (FDM) Printed Samples Based on the Selection of Critical Printing Parameters. *Materials* **2018**, *11*, 1382. [[CrossRef](#)]
15. Buj-Corral, I.; Domínguez-Fernández, A.; Durán-Llucià, R. Influence of Print Orientation on Surface Roughness in Fused Deposition Modeling (FDM) Processes. *Materials* **2019**, *12*, 3834. [[CrossRef](#)]
16. Kumbhar, N.N.; Mulay, A.V. Post Processing Methods used to Improve Surface Finish of Products which are Manufactured by Additive Manufacturing Technologies: A Review. *J. Inst. Eng. Ser. C* **2018**, *99*, 481–487. [[CrossRef](#)]
17. Chohan, J.S.; Singh, R.; Boparai, K.S.; Penna, R.; Fraternali, F. Dimensional accuracy analysis of coupled fused deposition modeling and vapour smoothing operations for biomedical applications. *Compos. Part B Eng.* **2017**, *117*, 138–149. [[CrossRef](#)]
18. Chohan, J.S.; Singh, R.; Boparai, K.S. Mathematical modelling of surface roughness for vapour processing of ABS parts fabricated with fused deposition modelling. *J. Manuf. Process.* **2016**, *24*, 161–169. [[CrossRef](#)]
19. Chohan, J.S.; Singh, R.; Boparai, K.S. Parametric optimization of fused deposition modeling and vapour smoothing processes for surface finishing of biomedical implant replicas. *Measurement* **2016**, *94*, 602–613. [[CrossRef](#)]
20. Mu, M.; Ou, C.-Y.; Wang, J.; Liu, Y. Surface modification of prototypes in fused filament fabrication using chemical vapour smoothing. *Addit. Manuf.* **2020**, *31*, 100972. [[CrossRef](#)]
21. Jin, Y.; Wan, Y.; Zhang, B.; Liu, Z. Modeling of the chemical finishing process for polylactic acid parts in fused deposition modeling and investigation of its tensile properties. *J. Mater. Process. Technol.* **2017**, *240*, 233–239. [[CrossRef](#)]
22. Rajan, A.J.; Sugavaneswaran, M.; Prashanthi, B.; Deshmukh, S.; Jose, S. Influence of Vapour Smoothing Process Parameters on Fused Deposition Modelling Parts Surface Roughness at Different Build Orientation. *Mater. Today Proc.* **2020**, *22*, 2772–2778. [[CrossRef](#)]
23. Nguyen, T.K.; Lee, B.-K. Post-processing of FDM parts to improve surface and thermal properties. *Rapid Prototyp. J.* **2018**, *24*, 1091–1100. [[CrossRef](#)]
24. Maciag, T.; Wiczorek, J.; Kalsa, W. Surface analysis of ABS 3d prints subjected to copper plating. *Arch. Metall. Mater.* **2019**, *64*, 639–646. [[CrossRef](#)]
25. Chen, L.; Zhang, X.; Gan, S. Effects of laser polishing on surface quality and mechanical properties of PLA parts built by fused deposition modeling. *J. Appl. Polym. Sci.* **2020**, *137*, 48288. [[CrossRef](#)]
26. Moradi, M.; Moghadam, M.K.; Shamsborhan, M.; Bodaghi, M.; Falavandi, H. Post-Processing of FDM 3D-Printed Polylactic Acid Parts by Laser Beam Cutting. *Polymers* **2020**, *12*, 550. [[CrossRef](#)]
27. Wach, R.A.; Wolszczak, P.; Adamus-Włodarczyk, A. Enhancement of Mechanical Properties of FDM-PLA Parts via Thermal Annealing. *Macromol. Mater. Eng.* **2018**, *303*, 1800169. [[CrossRef](#)]
28. Bhandari, S.; Lopez-Anido, R.A.; Gardner, D.J. Enhancing the interlayer tensile strength of 3D printed short carbon fiber reinforced PETG and PLA composites via annealing. *Addit. Manuf.* **2019**, *30*, 100922. [[CrossRef](#)]

29. Hart, K.R.; Dunn, R.M.; Sietins, J.M.; Mock, C.M.H.; Mackay, M.E.; Wetzel, E.D. Increased fracture toughness of additively manufactured amorphous thermoplastics via thermal annealing. *Polymers* **2018**, *144*, 192–204. [CrossRef]
30. Zhang, Y.; Moon, S. The Effect of Annealing on Additive Manufactured ULTEM™ 9085 Mechanical Properties. *Materials* **2021**, *14*, 2907. [CrossRef]
31. Shiou, F.-J.; Chen, C.-H. Freeform surface finish of plastic injection mold by using ball-burnishing process. *J. Mater. Process. Technol.* **2003**, *140*, 248–254. [CrossRef]
32. De Lacalle, L.N.L.; Rodriguez, A.; Lamikiz, A.; Celaya, A.; Alberdi, R.; De Lacalle, L.N.L.; Mentxaka, A.L. Five-Axis Machining and Burnishing of Complex Parts for the Improvement of Surface Roughness. *Mater. Manuf. Process.* **2011**, *26*, 997–1003. [CrossRef]
33. Boschetto, A.; Bottini, L. Surface improvement of fused deposition modeling parts by barrel finishing. *Rapid Prototyp. J.* **2015**, *21*, 686–696. [CrossRef]
34. Boschetto, A.; Bottini, L.; Veniali, F. Finishing of Fused Deposition Modeling parts by CNC machining. *Robot. Comput. Manuf.* **2016**, *41*, 92–101. [CrossRef]
35. Mali, H.S.; Prajwal, B.; Gupta, D.; Kishan, J. Abrasive flow finishing of FDM printed parts using a sustainable media. *Rapid Prototyp. J.* **2018**, *24*, 593–606. [CrossRef]
36. Nsengimana, J.; Van Der Walt, J.; Pei, E.; Miah, M. Effect of post-processing on the dimensional accuracy of small plastic additive manufactured parts. *Rapid Prototyp. J.* **2019**, *25*, 1–12. [CrossRef]
37. Ceruti, A.; Marzocca, P.; Liverani, A.; Bil, C. Maintenance in aeronautics in an Industry 4.0 context: The role of Augmented Reality and Additive Manufacturing. *J. Comput. Des. Eng.* **2019**, *6*, 516–526. [CrossRef]
38. Das, A.; Chatham, C.A.; Fallon, J.J.; Zawaski, C.E.; Gilmer, E.L.; Williams, C.B.; Bortner, M.J. Current understanding and challenges in high temperature additive manufacturing of engineering thermoplastic polymers. *Addit. Manuf.* **2020**, *34*, 101218. [CrossRef]
39. Forés-Garriga, A.; Pérez, M.A.; Gómez-Gras, G.; Pozo, G.R. Role of infill parameters on the mechanical performance and weight reduction of PEI Ultem processed by FFF. *Mater. Des.* **2020**, *193*, 108810. [CrossRef]
40. Stratasys. ULTEM 9085 Production-Grade Thermoplastic for Fortus 3D Printers. Available online: www.stratasys.com/materials/search/ultem9085 (accessed on 15 May 2021).
41. Cakar, F.; Moroglu, M.R.; Cankurtaran, H.; Karaman, F. Conducting poly(ether imide)–graphite composite for some solvent vapors sensing application. *Sens. Actuators B Chem.* **2010**, *145*, 126–132. [CrossRef]
42. de Bruijn, A.C.; Gómez-Gras, G.; Pérez, M.A. Mechanical study on the impact of an effective solvent support-removal methodology for FDM Ultem 9085 parts. *Polym. Test.* **2020**, *85*, 106433. [CrossRef]
43. de Bruijn, A.C.; Gómez-Gras, G.; Pérez, M.A. On the effect upon the surface finish and mechanical performance of ball burnishing process on fused filament fabricated parts. *Addit. Manuf.* **2021**, *46*, 102133. [CrossRef]
44. ISO 4288:1996-Geometrical Product Specifications (GPS)—Surface Texture: Profile method—Rules and Procedures for the Assessment of Surface Texture. Available online: www.iso.org/standard/2096.html (accessed on 3 June 2021).
45. Puerta, A.P.V.; Lopez-Castro, J.; López, A.O.; Vidal, S.R.F. On improving the surface finish of 3D printing polylactic acid parts by corundum blasting. *Rapid Prototyp. J.* **2021**, *27*, 1398–1407. [CrossRef]

Article

Optimization and Sensitivity Analysis of the Cutting Conditions in Rough, Semi-Finish and Finish Honing

Irene Buj-Corral ^{1,*}, Lourdes Rodero-de-Lamo ² and Lluís Marco-Almagro ²

¹ Department of Mechanical Engineering, Barcelona School of Industrial Engineering (ETSEIB), Universitat Politècnica de Catalunya (UPC), 08028 Barcelona, Spain

² Department of Statistics and Operations Research, Barcelona School of Industrial Engineering (ETSEIB), Universitat Politècnica de Catalunya (UPC), 08028 Barcelona, Spain; lourdes.rodero@upc.edu (L.R.-d.-L.); lluis.marco@upc.edu (L.M.-A.)

* Correspondence: irene.buj@upc.edu; Tel.: +34-934054015

Abstract: Honing processes are currently employed to obtain a cross-hatched pattern on the internal surfaces of cylinders that favors oil flow in combustion engines or hydraulic cylinders. The main aim of the present paper is to optimize the machining conditions in honing processes with respect to surface roughness, material removal rate and tool wear by means of the desirability function. Five process variables are considered: grain size, density, pressure, linear speed and tangential speed. Later, a sensitivity analysis is performed to determine the effect of the variation of the importance given to each response on the results of the optimization process. In the rough and semi-finish honing steps, variations of less than 5% of the importance value do not cause substantial changes in the optimization process. On the contrary, in the finish honing step, small changes in the importance values lead to modifications in the optimization process, mainly regarding pressure. Thus, the finish honing phase is more sensitive to changes in the optimization process than the rough and the semi-finish honing phases. The present paper will help users of honing machines to select proper values for the process variables.

Keywords: sensitivity analysis; honing; roughness; tool wear; material removal rate; optimization; desirability function; mixture design

Citation: Buj-Corral, I.; Rodero-de-Lamo, L.; Marco-Almagro, L. Optimization and Sensitivity Analysis of the Cutting Conditions in Rough, Semi-Finish and Finish Honing. *Materials* **2022**, *15*, 75. <https://doi.org/10.3390/ma15010075>

Academic Editors: Gilles Dessein and J. Antonio Travieso-Rodriguez

Received: 25 November 2021

Accepted: 19 December 2021

Published: 23 December 2021

Publisher's Note: MDPI stays neutral with regard to jurisdictional claims in published maps and institutional affiliations.



Copyright: © 2021 by the authors. Licensee MDPI, Basel, Switzerland. This article is an open access article distributed under the terms and conditions of the Creative Commons Attribution (CC BY) license (<https://creativecommons.org/licenses/by/4.0/>).

1. Introduction

Honing is an abrasive machining process in which a honing head provided with abrasive stones combines alternate linear movement with rotation in order to machine the internal surfaces of cylinders. The main goal of honing is to obtain a cross-hatched pattern with channels that favor oil flow in combustion engines or hydraulic cylinders. Several authors have indicated the key role of the surface topography of the cylinders' liners on the friction coefficient in the piston/cylinder assembly as well as on the amount of oil consumption. Thus, selecting proper honing parameters can reduce the emission of toxic compounds during the operation of combustion engines [1–3].

Some researchers have studied the honing process by means of statistical models. For example, Troglia [4] considered the grain size of the abrasive, lubricating oil and workpiece material as variables, and studied different roughness parameters, such as average roughness Ra and parameters of the Abbott–Firestone curve (Rk, Rpk, Rvk, Mr1, Mr2). Kanthababu et al. [5] varied rotation speed, linear speed, pressure, honing time and plateau-honing time. Responses were roughness parameters of the Abbott–Firestone curve. Roughness was mainly influenced by pressure and honing or plateau-honing time. Wos and Michalsky [6] found that main roughness parameters improving aircraft piston engine performances (output power, torque, fuel consumption and total efficiency) are Rvq and the linear triangle area for valleys A2, although they provide a higher oil consumption and greater emissions. More recently, Vrac et al. [7] obtained exponential models for roughness

and material removal rate as a function of process parameters, such as pressure or speed. In another study with diamond stones of grain size 151 and 181, they found that pressure was the most influential factor on roughness, followed by cutting speed and feed [8]. Vrabel et al. [9] analysed the influence of cutting speed, machining allowance and stone pressure on surface roughness, specifically on roughness parameters, the height of peaks (CR), the depth of the profile (CF) and the relative height of the holes (CL). On the other hand, Buj-Corral et al. searched for statistical models for both roughness and material removal rate in rough honing as a function of the main process parameters. They found that, in the range studied, abrasive grain size and pressure were the main parameters influencing both roughness and material removal rate [10]. Material removal rate values between 0.015 and 0.020 mm/s (0.090 and 0.120 cm/min) were found by Szabo [11] using cubic boron nitride (cBN) stones. In rough honing, Bai et al. [12] observed that the material removal rate increases with circumferential speed, reciprocate speed and cross-hatch angle, but decreases when the two speeds take too high values.

The semi-finish process was also studied, in which, as a general trend, roughness and material removal rate increase with grain size and density [13]. The finish honing process has been less well studied in the literature. For instance, Arantes et al. [14] compared the surface finish obtained in both conventional honing and flexible honing processes, including amplitude parameters, Rk family parameters, volume and feature parameters. In finish honing, Bai et al. [12] found that surface finish in finish processes improves when circumferential speed increases. Cabanettes et al. [15] studied the relationship between tool wear and different roughness parameters. They reported that only areal reduced summit height, arithmetic mean summit curvature and core roughness are correlated with tool wear.

Multi-objective optimization by means of the desirability function was developed by Derringer and Suich [16]. It has been applied in the past to machining processes, such as turning [17,18] or milling [19,20]. As for abrasive machining processes, Mukherjee et al. employed the desirability function and a metaheuristic technique for optimal process design [21]. Regarding honing processes, Lawrence and Rammamoorthy used robust process design and gray-relational analysis to define recommended values for process parameters in order to obtain required values for roughness Rz, roughness parameters from the Abbott–Firestone curve and honing angle, for three honing stages: rough, semi-finish and plateau-honing [22]. Nguyen et al. [23] carried out multi-response optimization of finishing honing with respect to surface finish and production rate. They noticed that both surface roughness and machining time depended mainly on grit size, followed by tangential speed and linear speed.

Sensitivity analysis is usually carried out in optimization problems, in order to assess the effect of the modification of either the objective function or the variables on the optimized values [24]. Different methods have been used in the past for performing sensitivity analysis after optimization. For example, Arsezer defined a methodology that consists of varying the parameters of the desirability function and analyzing their effect on desirability [25]. Malenovic et al. used a similar methodology for performing sensitivity analysis on the results of multi-objective optimization in a microemulsion LC system, and found the most sensitive parameters among importance, weight and ranges of the different responses [26]. In turning processes, Souza Rocha et al. [27] optimized tool life, surface roughness Ra and the ratio material removal rate/cutting force as a function of cutting speed, feed rate and depth of cut. They found that the weights used in the multi-objective optimization process influence the prediction variance. Mudhukrishnan et al. [28] optimized drilling parameters, such as spindle speed, feed and drill material, with respect to thrust force and torque, and performed a sensitivity analysis to assess the impact of control variables on the responses.

On the other hand, mixture design is a methodology that allows different kinds of mixtures to be tested; for example, in the formulation of cement or concrete pastes [29] or in the food industry [30]. This method is usually employed to determine the best

composition of a certain product. In the manufacturing area, for example, Misra et al. [31] employed mixture design to find the optimal electrolyte composition in electrochemical honing of gears.

In the present paper, regression models were obtained for average roughness R_a , material removal rate and tool wear for the three steps of the honing process, namely, rough, semi-finish and finish honing. Afterwards, multi-objective optimization was carried out by means of the desirability function. Importance values were defined for each response in the three honing steps, according to users' requirements. However, the selection of certain importance values for the responses could affect the results of the optimization process. Thus, in order to test the influence of the importance values on the optimal values of the variables in this work a sensitivity analysis was carried out. Mixture design was used to define different importance values to be tested. In order to assess the variability, the coefficient of variation CV was calculated for each response, considering different percentages of variation of the importance values.

This paper has two essential contributions. First, the recommendations for selecting the most appropriate parameters in each honing operation (rough, semi-finish and finish). Second, the final guidelines on how to define the importance of each parameter for the multi-objective optimization in each of the phases of the honing process.

2. Materials and Methods

2.1. Honing Experiments

Steel St-52 cylinders of 80 mm interior diameter and 390 mm length were machined in a Honingtec industrial machine (Honingtec S.A., Els Hostalets de Balenyà, Spain). This material is usually employed to manufacture hydraulic cylinders. Figure 1 shows the industrial machine used.

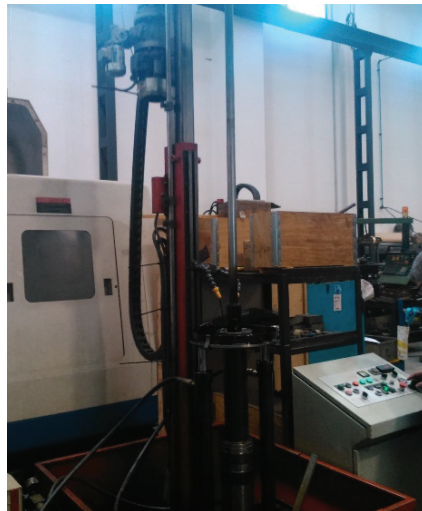


Figure 1. Industrial honing machine used in the experiment.

A central composite design was used to define the experiments in each one of the honing steps (rough, semi-finish and finish), which is explained in Section 2.5. Honing time was 30 min in all experiments. Two replicates were performed for each experiment.

Cubic boron nitride (cBN) honing stones were used with metallic bonds. Figure 2 depicts the honing head employed.



Figure 2. Honing head used in the experiment.

For each of the three experimental designs, three responses were measured: roughness (R_a), material removal rate (Q_m) and tool wear (Q_p).

2.2. Roughness Measurement

Arithmetical mean roughness R_a was measured with a Hommel-Etamic W5 contact roughness meter (Hommel-Etamic GmbH, Villingen-Schwenning, Germany), according to standard ISO 4287 [32] (Figure 3).

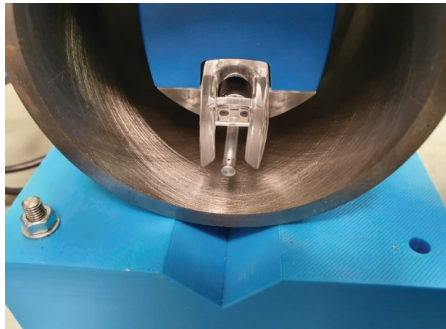


Figure 3. Contact roughness meter.

Nine measurements were taken along a diametral circumference in the internal surface of cylinders at a distance of 195 mm from the end of the cylinders. The average value of the nine measurements was calculated. The cut-off length was 0.8 mm and the measuring length was 4 mm.

2.3. Material Removal Rate Measurement

The material removal rate Q_m was measured by means of the weight difference of the workpieces, before and after the honing test. Workpieces were weighed with a Kern FCB 3K0.1 scale (Kern & Sohn GmbH, Balingen, Germany).

Q_m is defined as the volume of material removed in cm^3 per min and per unit area of abrasive wheel in cm^2 . Q_m in cm^3/min is calculated as follows (Equation (1)):

$$Q_m = \frac{V}{S \cdot t} \quad (1)$$

where V is removed volume in cm^3 , S is abrasive surface in cm^2 and t is honing time in min.

The removed volume V in cm^3 is calculated from the weight W of the workpiece before and after honing (Equation (2)).

$$V = \frac{W_i - W_f}{\rho} \quad (2)$$

where W_i is initial weight of the cylinder in g, W_f is the final weight of the cylinder in g, and ρ is the density of the cylinder in g/cm^3 .

2.4. Tool Wear Measurement

Tool wear Q_p in cm^3/min is calculated as follows (Equation (3)):

$$Q_p = \frac{V_p}{t} \quad (3)$$

where V_p is the volume of stone removed during honing (cm^3), obtained with the initial and final weight of the stone and with the density of the stone, and t is the honing time in min.

2.5. Design of Experiments (DOE)

For each honing step, a central composite design was conducted in order to be able to obtain second order models for the responses. Minitab statistical software version 19, (Minitab LLC, State College, PA, USA) was used. The cube experimental runs were defined as a fractional factorial design 2^{5-1} with 16 runs. The axial runs were defined with 10 face-centered points plus three central points. Table 1 shows the variables and levels employed for rough, semi-finish and finish operations.

Table 1. Low and high levels for the different variables employed in the rough, semi-finish and finish experiments.

	Rough	Semi-Finish	Finish
Grain size, G_s (ISO 6106 [33])	91–181	46–76	15–30
Density of abrasive, D_e (ISO 6104 [34])	30–60	15–45	10–20
Pressure, P_r (N/cm^2)	400–700	400–700	400–700
Tangential speed, V_t (m/min)	30–50	30–50	30–50
Linear speed, V_l (m/min)	20–40	20–40	20–40

As can be seen in Table 1, the same levels were used for pressure, tangential speed and linear speed for the three honing steps. The values for the different parameters were selected according to the manufacturers' recommendation and to the literature. For instance, Vrac et al. [7] recommended grain size 181 and 151 in normal honing. These values lie within the range that was selected in the present work for rough honing. Grain size and abrasive density usually decrease as the honing process advances in order to achieve finer and finer surfaces.

2.6. Multiobjective Optimization

In the present paper, the desirability function method was used to carry out multiobjective optimization [14].

The process searches for a combination of the factors that gives the best possible compromise for all the factors. This is achieved following these steps:

1. The individual desirability function for each response (d_i) is obtained.
2. The composite desirability function (D) is computed combining all the individual desirability functions, d_i , and considering the importance of each individual response.
3. The values of the factors that maximize the composite desirability function (D) are finally found.

The individual desirability functions map each one of the responses onto a value ranging from 0 to 1 (0 meaning that the level of the response is not what was wanted; 1 meaning that the level of the response is most preferred, the target). The formula depends on whether one wants to minimize the response, maximize the response or set the response to a target. In our study, we want to minimize roughness, R_a , and tool wear, Q_p , and maximize the material removal rate, Q_m .

Figure 4 shows the shape of the function when minimizing (left) or maximizing (right) the response. In our study, we use the target and upper and lower bounds as the maximum and minimum response values obtained, depending on the situation. A weight of 1 was used in all cases, corresponding to the use of a linear function.

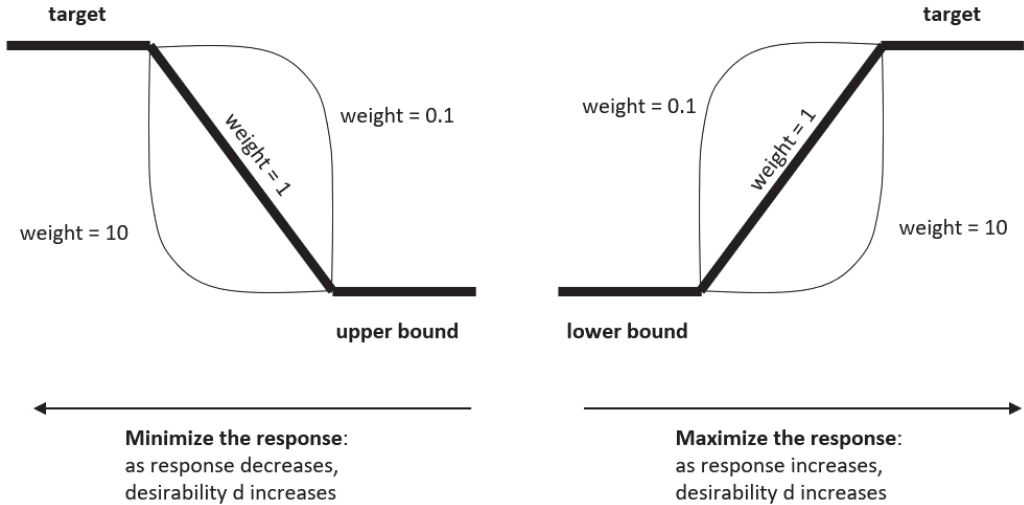


Figure 4. Desirability functions when minimizing (left) and maximizing (right) the response.

The composite desirability function D is computed using the formula shown in Equation (4).

$$D = \left(\prod d_i^{Imp_i} \right)^{\frac{1}{\sum Imp_i}} \tag{4}$$

Imp_i is the importance given to response i . $\sum Imp_i$ is the sum of all importance values, $\sum Imp_i$. One can set the importance for each response so that the sum is one, thus simplifying the formula and giving the idea that the importance for each response is a percentage of importance.

The importance values for each of the three responses in this study are shown in Table 2. They were selected from previous honing experiments. The following criteria were employed: in rough operations it is important to remove as much material as possible, while in finish operations surface finish is crucial. Thus, the importance values increase for roughness in subsequent honing operations, while they decrease for material removal rate and tool wear. In other words, in rough honing high importance values of Q_m and Q_p , as well as low values for R_a , are recommended. On the contrary, in finish honing high importance values are required for R_a and low values for Q_m and Q_p .

Table 2. Importance values used for each response and honing phase in the optimization.

Response	Rough	Semi-Finish	Finish
Average roughness, R_a (μm)	0.1	0.4	0.8
Material removal rate, Q_m (cm/min)	0.6	0.4	0.1
Tool wear, Q_p (cm ³ /min)	0.3	0.2	0.1

One of the main objectives of this study is assessing to what extent the results are dependent on the importance given to each of the responses. To achieve this objective, the importance of each response was later varied, in order to perform a sensitivity analysis of the optimization process (Section 2.7).

2.7. Sensitivity Analysis

The purpose of the sensitivity analysis is to determine the effect of a certain change in the importance values of the responses on the optimal values of the variables that are obtained from the multi-objective optimization. In order to achieve this, the values of the importance for the different responses were varied from the initially defined values in Table 2 with the help of a mixture design. Values of importance were varied from a slight degree (1%) to a considerable degree (15%) (the higher the variation in the initial importance values, the higher the expected impact on the optimization results).

Mixture designs are special experiments in which the product being studied is composed of different ingredients. These ingredients cannot be modified independently: if the percentage of one ingredient in the formula increases, the percentages of others must decrease, as the total always sums to 1 [29]. These experiments are commonly used in pharma or food investigations. We have used a mixture design to change in an organized and balanced way the importance of each response in our optimization problem.

For instance, Figure 5 shows the experiments performed for the finish step. The central point corresponds to the initial importance values shown in Table 2 ($R_a = 0.8$, $Q_m = 0.1$, $Q_p = 0.1$). The other points are slight variations of these importance values, always summing to 1.

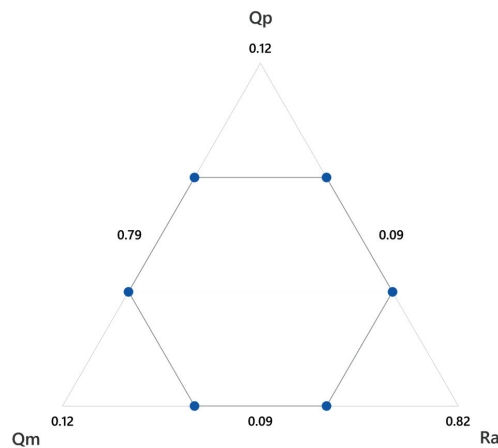


Figure 5. Optimization runs performed for the sensibility analysis in the finish step, with a 1% variation of the importance.

For each one of the runs coming from the mixture design we have a combination of values of the variables G_s , D_e , P_r , V_t and V_l that globally optimize the three responses. In order to see the extent to which these values vary depending on the run, the coefficient of variation CV was calculated for each variable, G_s , D_e , P_r , V_t and V_l , and for each percentage of variation of importance (1%, 3%, 5%, 10%, 15%).

3. Results and Discussion

3.1. Regression Models

For each response and honing stage, a second order model was adjusted. The residuals were checked, and a goodness of fit test was performed for each model. For each response, a graphic was obtained (Figures 3–5, respectively), in which the coefficients of each regressor are presented in the following way:

- Each horizontal line in the graph corresponds to one of the estimated effects (either the main effect or an interaction) and only the significant effects are represented with a ball.

- The size of the ball is proportional to the absolute value of the coefficient in the fitted model, so the biggest balls represent the effects with highest values.
- The color of the ball corresponds to the sign of the coefficient: red corresponds to positive and blue to negative.

In the following subsections the results for surface roughness, material removal rate and tool wear are presented.

3.1.1. Roughness, Ra

Equations (5)–(7) provide the regression models for Ra in the rough, semi-finish and finish operation respectively.

$$Ra, \text{ rough} = 2.64 - 0.00570 Gs + 0.0017 De + 0.00630 Pr + 0.0459 Vt - 0.394 VI - 0.000848 De^2 - 0.000007 Pr^2 + 0.00653 VI^2 + 0.000546 Gs \cdot De + 0.000145 Gs \cdot Vt - 0.000283 Gs \cdot VI - 0.000085 Pr \cdot Vt + 0.000249 Pr \cdot VI \quad (5)$$

$$Ra, \text{ semi-finish} = -2.869 + 0.0712 Gs - 0.0500 De + 0.000231 Pr - 0.0053 Vt + 0.1704 VI - 0.000683 Gs^2 + 0.000866 De^2 - 0.00444 VI^2 + 0.000019 Gs \cdot Pr + 0.000301 Gs \cdot Vt - 0.000036 De \cdot Pr + 0.000387 De \cdot Vt + 0.000047 Pr \cdot VI - 0.000896 Vt \cdot VI \quad (6)$$

$$Ra, \text{ finish} = 1.165 - 0.07211 Gs - 0.01334 De - 0.000773 Pr - 0.01099 Vt + - 0.00007 VI + 0.001133 Gs^2 + 0.000627 Gs \cdot De + 0.000036 Gs \cdot Pr + 0.000150 Gs \cdot Vt + 0.000013 Pr \cdot Vt \quad (7)$$

Figure 6 depicts the significant terms for the roughness parameter, Ra, in the rough, semi-finish and finish operations.

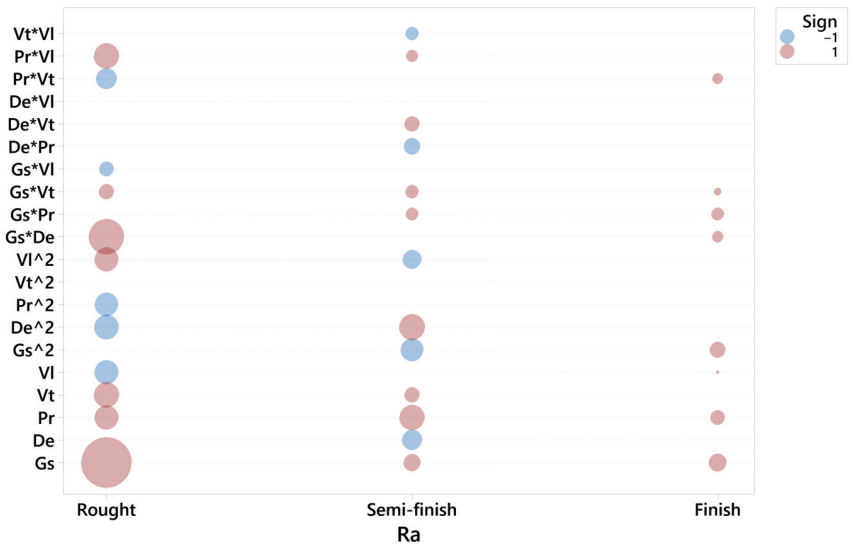


Figure 6. Significant terms for Ra in the rough, semi-finish and finish operations.

In the rough honing operation, the main factor influencing roughness is grain size, Gs, followed by Vt, Pr and VI. The higher the grain size, tangential speed and pressure, the higher roughness is. Conversely, the lower the linear speed, the higher roughness is. The interaction between grain size and density is significant, as has been observed in previous works [10]. The higher the grain size, the higher density should be in order to assure the correct cutting operation. Other significant interactions are Pr·VI, Pr·Pr and De·De. Lawrence and Ramamoorthy [22] found that rotational speed was the most influential factor on the Rz parameter, followed by oscillatory speed, honing time and pressure. These results are in accordance with the present work, considering that they did not vary grain

size nor abrasive density. Gunay and Korkmaz [35] also reported a higher influence of grit size compared to linear speed in honing processes.

In the semi-finish operation, the most significant term becomes De-De, followed by Pr, while the term Gs-Gs is also important. This suggests that, although roughness depends directly on pressure, it is also influenced by grain size and density. The fact that pressure influences roughness is in accordance with the results of Kanthababu et al. [5].

In the finish operation, grain size and pressure seem to be the only factors that have an influence on roughness, while density appears in the Gs-De interaction. Gs-Gs, Gs-Pr and Pr-Vt are also influential. Conversely, Bai et al. [13] found that surface roughness depends on tangential speed. In plateau honing processes, Gunay and Korkmaz [35] observed that roughness depended mainly on grain size, linear speed and number of strokes. A grain size of 150, a linear speed of 7 m/min and four strokes are recommended in order to minimize R_a .

In summary, in rough honing processes it is important to select low grain size and low density to ensure low roughness. In addition to grain size and density, pressure also becomes important in the semi-finish operation. The lower the pressure, the lower roughness is. In the finish operation, the main factor to be considered is grain size, followed by pressure. Thus, in finish honing processes, the density of the abrasive is not so important as in rough and semi-finish processes.

As an example, Figure 7 shows a roughness profile for Experiment 2 on (a) rough honing, (b) semi-finish honing and (c) finish honing.

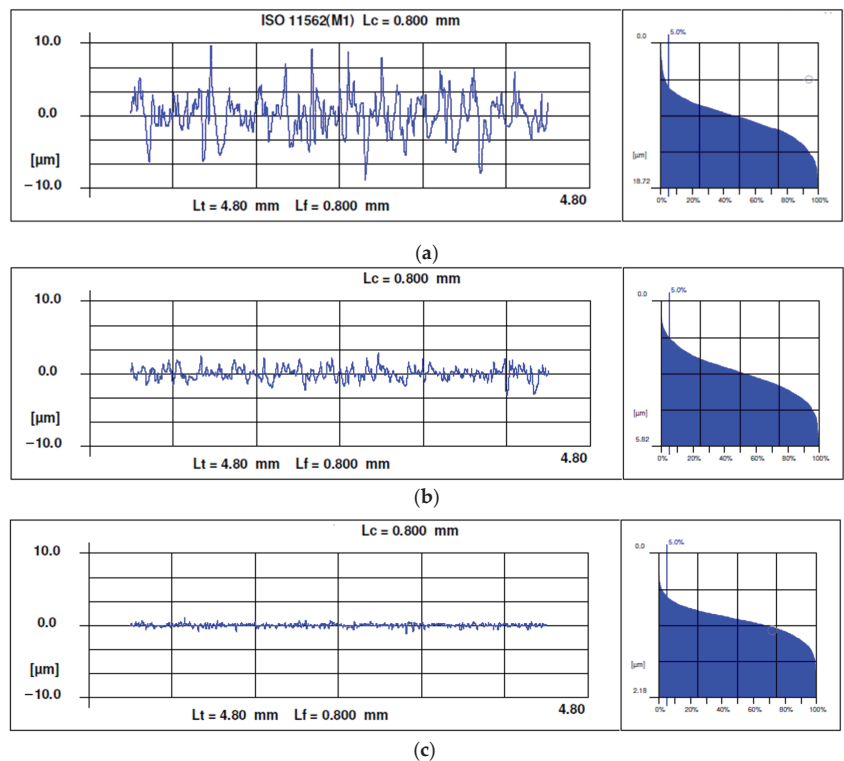


Figure 7. Examples of roughness profiles and Abbott–Firestone curves: (a) rough honing with grain size 181, (b) semi-finish honing with grain size 76 and (c) finish honing with grain size 30.

All the profiles present sharp peaks and rounded valleys, with an irregular shape that is characteristic of abrasive machining processes. As expected, the higher the grain size,

the higher roughness is. The Abbot–Firestone curves have the s-shape that is characteristic of the abrasive machining processes.

3.1.2. Material Removal Rate

Equations (8)–(10) correspond to the regression models for the material removal rate, Q_m , in the rough, semi-finish and finish operations, respectively:

$$Q_m, \text{ rough} = -0.419 - 0.000830 G_s + 0.00801 D_e + 0.001799 P_r - 0.00387 V_t - 0.00962 V_l - 0.000154 D_e^2 - 0.000002 P_r^2 + 0.000017 G_s \cdot D_e + 0.000027 G_s \cdot V_t + 0.000104 D_e \cdot V_l + 0.000006 P_r \cdot V_t + 0.000016 P_r \cdot V_l \quad (8)$$

$$Q_m, \text{ semi-finish} = -0.3379 + 0.01439 G_s - 0.00465 D_e + 0.000007 P_r - 0.002380 V_t + 0.000350 V_l - 0.000119 G_s^2 + 0.000063 D_e^2 + 0.000033 D_e \cdot V_t + 0.000004 P_r \cdot V_t \quad (9)$$

$$Q_m, \text{ finish} = 0.1621 - 0.001941 G_s - 0.001733 D_e - 0.000108 P_r - 0.001910 V_t - 0.00958 V_l + 0.000182 V_l^2 + 0.000088 G_s \cdot D_e + 0.000002 G_s \cdot P_r + 0.000002 P_r \cdot V_t + 0.000003 P_r \cdot V_l + 0.000051 V_t \cdot V_l \quad (10)$$

Figure 8 corresponds to the models of material removal rate, Q_m , in rough, semi-finish and finish processes, respectively.

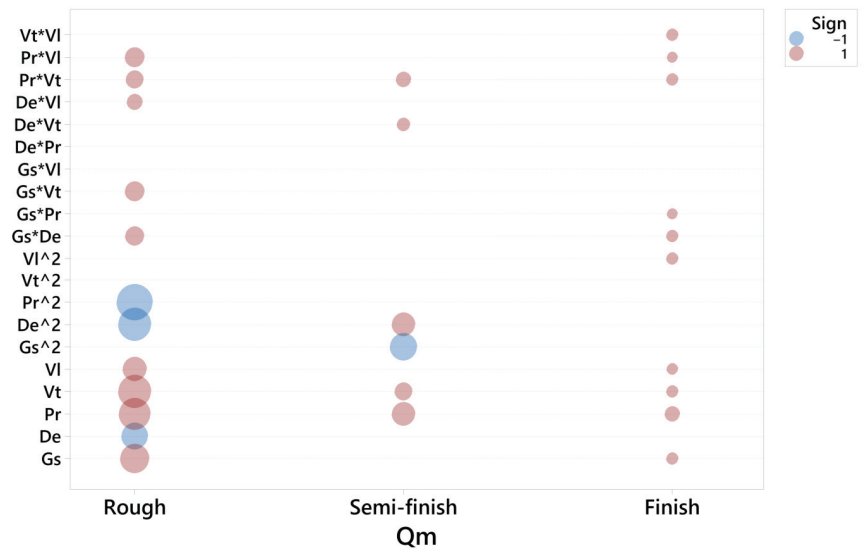


Figure 8. Significant terms for Q_m in the rough, semi-finish and finish operations.

In the rough honing operation, the most significant term influencing the material removal rate is $P_r \cdot P_r$, followed by V_t , P_r , $D_e \cdot D_e$ and G_s . Thus, pressure seems to be crucial to ensure a sufficient material removal rate in this operation, as has been previously observed [11], although the other parameters are also important in this case. In honing processes with diamond stones of grain size 181 and 151, respectively, Vrac et al. [7] found that cutting speed greatly influenced material removal rate, while pressure was less relevant.

As for the semi-finish operation, the main terms are $G_s \cdot G_s$, P_r and $D_e \cdot D_e$. This suggests that, as the quantity of material to be removed decreases in subsequent honing operations, the importance of pressure is reduced because the cutting operation becomes easier to perform.

In the finish operation, different factors show a similar impact: Pr, Gs, Vt and VI. VI·VI is also significant, and density appears in the Gs·De interaction.

In summary, all factors influence the material removal rate in rough honing. In semi-finish honing, mainly pressure, grain size and density should be considered, while in finish honing, all factors except density are important.

3.1.3. Tool Wear

Equations (11)–(13) show the regression models for tool wear, Qp, in the rough, semi-finish and finish operations respectively.

$$Q_{p, \text{rough}} = -0.001659 + 0.000001 G_s + 0.000037 De + 0.000003 Pr + 0.000025 Vt + 0.000005 VI - 0.000000 De^2 - 0.000000 De \cdot Pr - 0.000000 De \cdot Vt \tag{11}$$

$$Q_{p, \text{semi-finish}} = -0.000317 + 0.000021 G_s - 0.000015 De + 0.000002 Pr - 0.000019 Vt - 0.000034 VI - 0.000000 G_s^2 + 0.000000 G_s \cdot De - 0.000000 G_s \cdot Pr + 0.000000 G_s \cdot VI - 0.000000 De \cdot Pr + 0.000000 De \cdot Vt + 0.000001 Vt \cdot VI \tag{12}$$

$$Q_{p, \text{finish}} = 0.000906 - 0.000095 G_s + 0.000019 De - 0.000001 Pr - 0.000000 Vt + 0.000002 G_s^2 - 0.000001 G_s \cdot De + 0.000000 G_s \cdot Pr + 0.000000 G_s \cdot Vt - 0.000000 De \cdot Vt \tag{13}$$

Figure 9 depicts the main terms influencing tool wear, Qp, in the rough, semi-finish and finish operations.

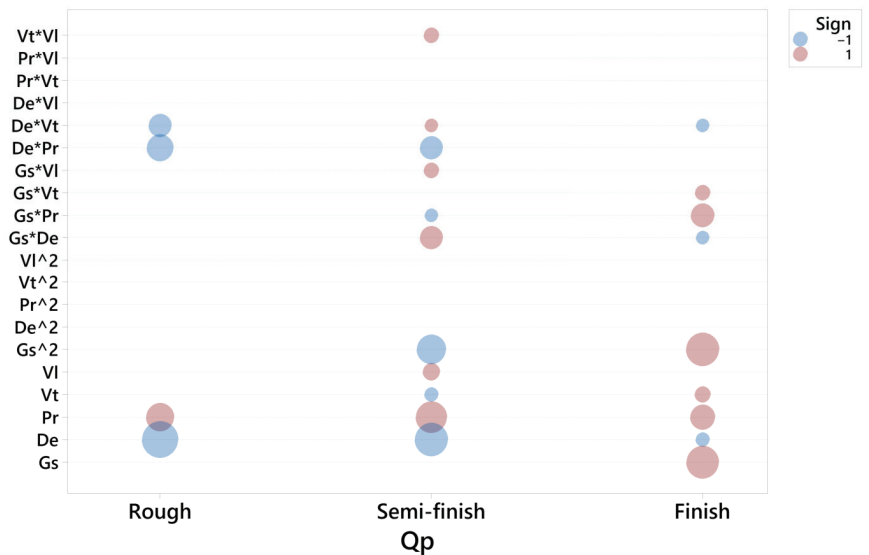


Figure 9. Significant terms for Qp in the rough, semi-finish and finish operations.

The main factor affecting tool wear in rough honing is the density of the abrasive, De, with a negative impact on tool wear. This suggests that a lower density favors the removal of grains from the bond, which restores the stones’ ability to cut but at the cost of increasing tool wear. Other important factors are pressure and the interaction between density and pressure.

In the semi-finish honing operation, density and pressure are still the most important factors. However, a new Gs·Gs starts to influence tool wear with a negative impact: higher grain size leads to lower tool wear.

In the finish operation, grain size is the most important factor influencing tool wear, with the terms Gs and Gs·Gs, followed by pressure and by the interaction between grain size and pressure.

In summary, the density of the abrasive is a crucial factor in rough honing. However, in semi-finish and finish honing, the grain of the abrasive becomes more important. In all the honing steps, pressure is a factor to be considered.

When using cBN tools, tool wear is characterized by low values. For this reason, tool wear has only a small influence on the performance of the present tests, in which honing time was relatively short.

3.2. Multi-Objective Optimization

The main results of the optimization step are presented in Sections 3.2.1, 3.2.2 and 3.3.3 for the rough, semi-finish and finish phases, respectively.

3.2.1. Rough Honing

Figure 10 presents the results of the multi-objective optimization for the rough honing operation.

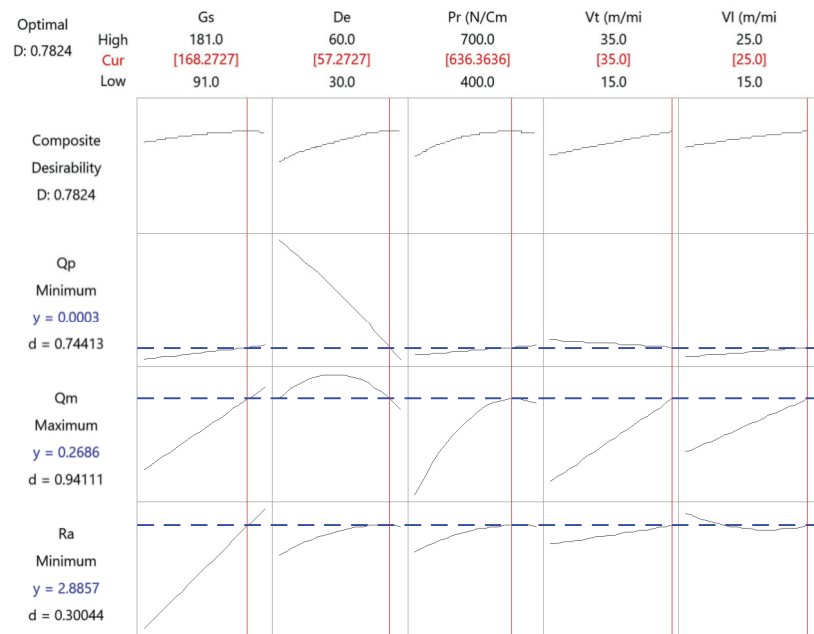


Figure 10. Multi-objective optimization of the rough honing operation.

The combination that minimizes tool wear and roughness while maximizing the material removal rate is presented in Table 3.

Table 3. Results of the multi-objective optimization in the rough honing operation.

Parameter	Gs	De	Pr	Vt	Vl
Value	168	57	636	35	25

This corresponds to medium grain size and high values for the rest of the factors. In rough honing, a high grain size would be recommended in order to provide a high material

removal rate, but a low grain size would provide a better surface finish [36]. Thus, medium grain size optimizes both responses.

3.2.2. Semi-Finish Honing

Figure 11 corresponds to the results of the multi-objective optimization for the semi-finish honing operation.

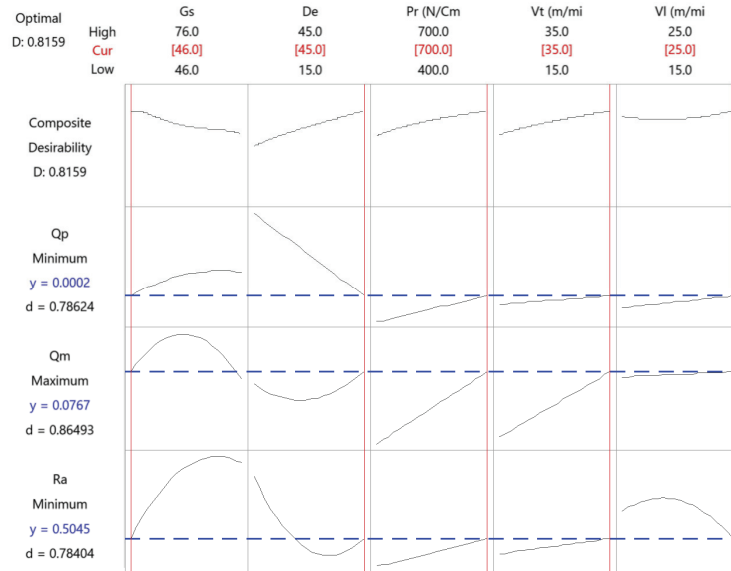


Figure 11. Multi-objective optimization of the semi-finish honing operation.

The combination that minimizes roughness and tool wear and maximizes the material removal rate is shown in Table 4.

Table 4. Results of the multi-objective optimization in the semi-finish honing operation.

Parameter	Gs	De	Pr	Vt	Vl
Value	46	45	700	35	25

This combination includes a low grain size, while the rest of the variables are kept at their high values.

3.2.3. Finish Honing

Figure 12 shows the results for the finish phase.

Table 5 presents the results of the multi-objective optimization in the finish honing operation.

Table 5. Results of the multi-objective optimization in the finish honing operation.

Parameter	Gs	De	Pr	Vt	Vl
Value	17	20	488	35	25

Recommended values for the variables are: low grain size (close to the lower limit of 15), high density, low pressure (close to the lower limit of 400), high tangential speed and high linear speed.

In all the honing phases, high linear and tangential speed values are to be selected.

3.3. Sensitivity Analysis

The results of the sensitivity analysis for the rough, semi-finish and finish phase are presented in Sections 3.3.1–3.3.3, respectively.

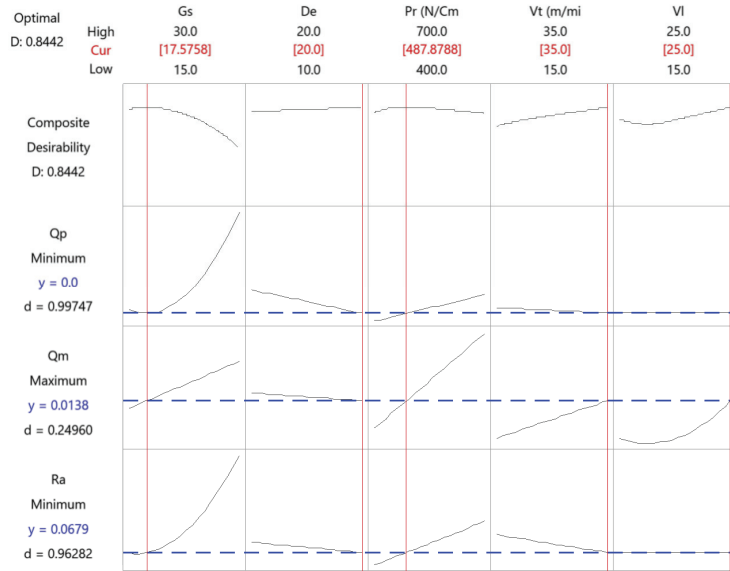


Figure 12. Multi-objective optimization of the finish honing operation.

3.3.1. Rough Honing

Figure 13 depicts the variation coefficient, CV, vs. the percentage of variation of the importance values in rough honing (% of importance range), from the initial numbers of 0.1 for roughness Ra, 0.6 for material removal rate, Qm, and 0.3 for tool wear (see Table 2).

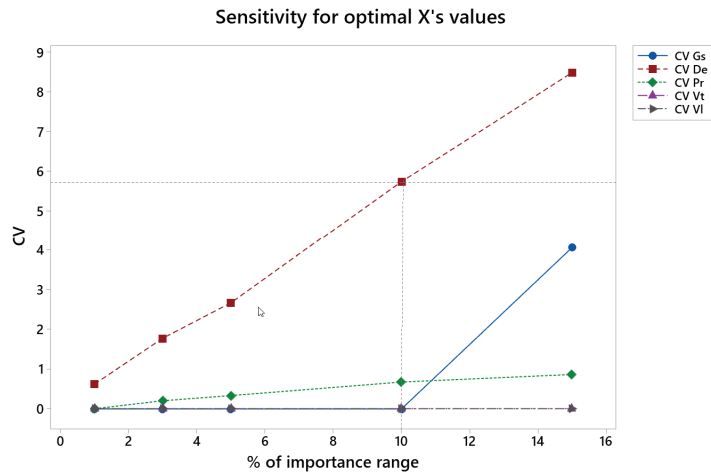


Figure 13. CV of the different factors vs. percentage of importance range in the rough honing operation.

In the rough honing operation, the coefficient of variation, CV, is lower than 3 for all the factors up to 5% of importance variation and lower than 6 for all the factors up to 10% variation of the importance. CV values are especially low for grain size, pressure, tangential speed and linear speed. CV increases noticeably for De.

3.3.2. Semi-Finish Honing

Figure 14 shows the coefficient of variation, CV, vs. percentage of variation of the importance values in semi-finish honing (% of importance range), from the initial numbers of 0.4 for roughness Ra, 0.4 for material removal rate, Qm, and 0.2 for tool wear (see Table 2).

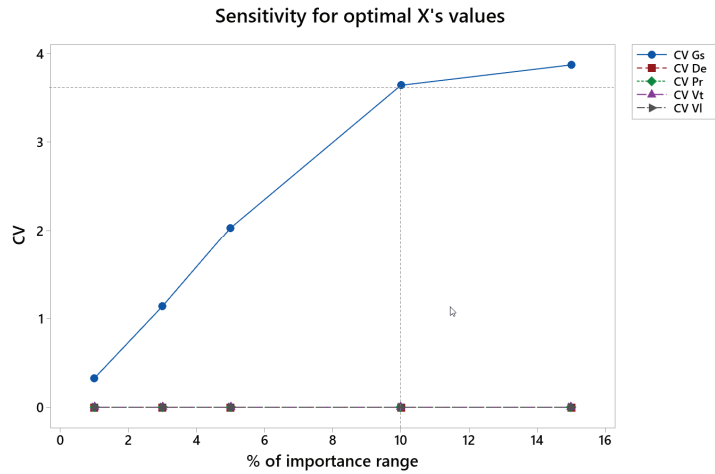


Figure 14. CV of the different factors vs. percentage of importance range in the semi-finish honing operation.

In the semi-finish phase the CV is lower than 3 for all the variables up to 5% of variation in the importance values, and it is lower than 4 up to 10% of variation in the importance values. CV increases greatly for Gs.

3.3.3. Finish Honing

In Figure 15 the CV for all variables vs. the variation of importance values in finish honing (% of importance range) is presented, from the initial numbers of 0.8 for roughness Ra, 0.1 for material removal rate, Qm, and 0.1 for tool wear (see Table 2).

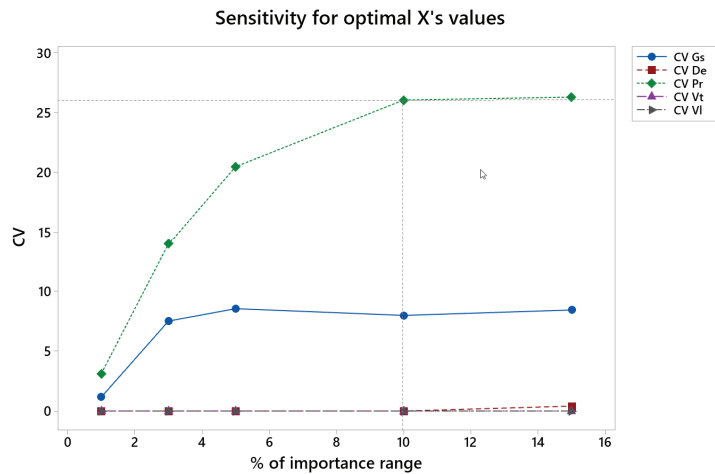


Figure 15. CV of the different factors vs. percentage of importance range in the finish honing operation.

In the finish phase the CV is lower than 10 for all the variables up to 5% of variation in the importance values, except for pressure, for which CV increases noticeably up to a variation of 10% in the importance value.

4. Conclusions

In the present paper, regression models are presented for roughness, material removal rate and tool wear in the rough, semi-finish and finish operations. A sensitivity study is presented for the multi-objective optimization process. The main conclusions of the work are as follows:

- Grain size is the most influential factor on roughness, while pressure influences the material removal rate in all the honing steps.
- In order to minimize roughness and tool wear, and to maximize the material removal rate, medium or high values for the different variables are recommended in the rough phase. In the semi-finish phase, low grain size is recommended, while the rest of the variables should be held at high values. In the finish phase, low grain size and pressure are recommended, with high values for the rest of the variables.
- The sensitivity analysis showed that, when performing a multi-objective optimization in the rough and in the semi-finish phases, variations of the importance values for each response that are lower than 5% do not significantly increase the variation coefficient of the different variables. This means one can reasonably decide on the importance for each response in the rough and semi-finish phases, being confident that mild changes in these importance values will not have a large effect. Conversely, in the finish phase, small changes in the importance values increase the variation coefficient of pressure. Thus, it is recommended to select accurately the importance values of the different responses in the finish phase.

Author Contributions: Conceptualization, I.B.-C.; methodology, I.B.-C., L.R.-d.-L. and L.M.-A.; software, I.B.-C. and L.R.-d.-L.; validation, L.R.-d.-L.; formal analysis, L.R.-d.-L. and L.M.-A.; investigation, I.B.-C., L.R.-d.-L. and L.M.-A.; resources, I.B.-C.; data curation, I.B.-C.; writing—original draft preparation, I.B.-C. and L.M.-A.; writing—review and editing, I.B.-C.; visualization, I.B.-C., L.R.-d.-L. and L.M.-A.; supervision, I.B.-C.; project administration, I.B.-C.; funding acquisition, I.B.-C. All authors have read and agreed to the published version of the manuscript.

Funding: This research was funded by the Spanish Ministry of Economy and Competitiveness, project number DPI2011-26300.

Institutional Review Board Statement: Not applicable.

Informed Consent Statement: Not applicable.

Data Availability Statement: The data presented in this study are available in Appendix A.

Acknowledgments: The authors would like to thank Alejandro Domínguez-Fernández and Ramón Casado-López for their help with the experimental tests, as well as the company Honingtec S.A. for lending the honing machine.

Conflicts of Interest: The authors declare no conflict of interest.

Appendix A

Table A1. Experimentation results in the rough phase.

Run	Gs	De	Pr (N/cm ²)	Vt (m/min)	Vl (m/min)	Ra (μm)	Qm (cm ³ /min)	Qp (cm ³ /min)
1	91	30	400	15	25	0.91	0.0822	0.000249
2	91	30	400	15	25	0.78	0.0602	0.000167
3	91	30	400	35	15	1.90	0.1151	0.000167
4	91	30	400	35	15	1.51	0.1260	0.000488

Table A1. Cont.

Run	Gs	De	Pr (N/cm ²)	Vt (m/min)	VI (m/min)	Ra (μm)	Qm (cm/min)	Qp (cm ³ /min)
5	91	30	700	15	15	1.48	0.1314	0.000381
6	91	30	700	15	15	1.37	0.1041	0.000716
7	91	30	700	35	25	1.67	0.2374	0.001010
8	91	30	700	35	25	1.59	0.2305	0.000652
9	91	45	550	25	20	1.22	0.1540	0.000367
10	91	45	550	25	20	1.20	0.1589	0.000346
11	91	60	400	15	15	0.61	0.0219	0.000225
12	91	60	400	15	15	0.62	0.0273	0.000149
13	91	60	400	35	25	0.59	0.0602	0.000029
14	91	60	400	35	25	0.52	0.0547	0.000087
15	91	60	700	15	25	0.70	0.0929	0.000214
16	91	60	700	15	25	0.81	0.0929	0.000062
17	91	60	700	35	15	0.82	0.0715	0.000116
18	91	60	700	35	15	0.78	0.0767	0.000029
19	126	30	550	25	20	1.76	0.1375	0.000356
20	126	30	550	25	20	1.88	0.1811	0.000990
21	126	45	400	25	20	1.54	0.1255	0.000361
22	126	45	400	25	20	1.33	0.1036	0.000195
23	126	45	550	15	20	1.61	0.1478	0.000722
24	126	45	550	15	20	1.80	0.1476	0.000086
25	126	45	550	25	15	2.42	0.1642	0.000264
26	126	45	550	25	15	2.00	0.1534	0.000562
27	126	45	550	25	20	1.85	0.2402	0.000300
28	126	45	550	25	20	1.76	0.1910	0.000452
29	126	45	550	25	20	1.81	0.1965	0.000511
30	126	45	550	25	20	1.93	0.2075	0.000274
31	126	45	550	25	20	1.99	0.2184	0.000447
32	126	45	550	25	20	1.90	0.2238	0.000473
33	126	45	550	25	20	1.83	0.1865	0.000561
34	126	45	550	25	20	1.91	0.1809	0.000461
35	126	45	550	25	20	1.72	0.2303	0.000318
36	126	45	550	25	20	1.72	0.1753	0.000342
37	126	45	550	25	25	1.79	0.2293	0.000581
38	126	45	550	25	25	1.76	0.2238	0.000137
39	126	45	550	35	20	2.21	0.1978	0.000333
40	126	45	550	35	20	1.73	0.2032	0.000652
41	126	45	700	25	20	1.70	0.1531	0.000423
42	126	45	700	25	20	2.08	0.2019	0.000513
43	126	60	550	25	20	1.55	0.1425	0.000532
44	126	60	550	25	20	1.36	0.1527	0.000497
45	181	30	400	15	15	2.11	0.0872	0.000219
46	181	30	400	15	15	1.84	0.0818	0.000232
47	181	30	400	35	25	2.10	0.1855	0.000562
48	181	30	400	35	25	1.77	0.1527	0.000599
49	181	30	700	15	25	2.19	0.1528	0.000807
50	181	30	700	15	25	2.55	0.1582	0.000689
51	181	30	700	35	15	2.14	0.1965	0.000808
52	181	30	700	35	15	2.86	0.2841	0.000915
53	181	45	550	25	20	2.57	0.2349	0.000315
54	181	45	550	25	20	2.80	0.2512	0.000416
55	181	60	400	15	25	1.96	0.0873	0.000189
56	181	60	400	15	25	1.78	0.0872	0.000231
57	181	60	400	35	15	3.90	0.1255	0.000068
58	181	60	400	35	15	3.47	0.1146	0.000126
59	181	60	700	15	15	3.23	0.0875	0.000184
60	181	60	700	15	15	2.79	0.0765	0.000184
61	181	60	700	35	25	3.16	0.2571	0.000384
62	181	60	700	35	25	3.21	0.2514	0.000076

Table A2. Experimentation results in the semi-finish phase.

Run	Gs	De	Pr (N/cm ²)	Vt (m/min)	VI (m/min)	Ra (μm)	Qm (cm/min)	Qp (cm ³ /min)
1	46	15	400	15	25	0.47	0.0183	3.82×10^{-4}
2	46	15	400	15	25	0.49	0.0258	2.68×10^{-4}
3	46	15	400	35	15	0.51	0.0183	2.54×10^{-4}
4	46	15	400	35	15	0.47	0.0183	1.40×10^{-4}
5	46	15	700	15	15	0.81	0.0403	8.98×10^{-4}
6	46	15	700	15	15	0.79	0.0477	7.48×10^{-4}
7	46	15	700	35	25	0.84	0.0587	7.42×10^{-4}
8	46	15	700	35	25	0.82	0.0622	7.28×10^{-4}
9	46	30	550	25	20	0.49	0.0331	2.57×10^{-4}
10	46	30	550	25	20	0.46	0.0405	1.85×10^{-4}
11	46	45	400	15	15	0.27	0.0110	0.00
12	46	45	400	15	15	0.30	0.0073	6.07×10^{-5}
13	46	45	400	35	25	0.39	0.0293	8.62×10^{-18}
14	46	45	400	35	25	0.38	0.0220	4.85×10^{-5}
15	46	45	700	15	25	0.36	0.0221	1.46×10^{-4}
16	46	45	700	15	25	0.58	0.0481	1.74×10^{-4}
17	46	45	700	35	15	0.57	0.0733	1.04×10^{-4}
18	46	45	700	35	15	0.58	0.0733	9.71×10^{-5}
19	64	15	550	25	20	0.86	0.0402	5.63×10^{-4}
20	64	15	550	25	20	1.02	0.0699	4.52×10^{-4}
21	64	30	400	25	20	0.37	0.0147	2.65×10^{-4}
22	64	30	400	25	20	0.31	0.0220	1.68×10^{-4}
23	64	30	550	15	20	0.71	0.0475	4.30×10^{-4}
24	64	30	550	15	20	0.65	0.0440	3.04×10^{-4}
25	64	30	550	25	15	0.57	0.0330	3.09×10^{-4}
26	64	30	550	25	15	0.54	0.0293	4.01×10^{-4}
27	64	30	550	25	20	0.96	0.0661	2.95×10^{-4}
28	64	30	550	25	20	0.77	0.0366	3.09×10^{-4}
29	64	30	550	25	20	0.91	0.0403	3.82×10^{-4}
30	64	30	550	25	20	0.74	0.0549	2.61×10^{-4}
31	64	30	550	25	20	0.66	0.0476	3.09×10^{-4}
32	64	30	550	25	20	0.72	0.0439	3.30×10^{-4}
33	64	30	550	25	20	0.56	0.0366	3.51×10^{-4}
34	64	30	550	25	20	0.66	0.0547	3.63×10^{-4}
35	64	30	550	25	20	0.76	0.0583	3.82×10^{-4}
36	64	30	550	25	20	0.60	0.0404	2.69×10^{-4}
37	64	30	550	25	25	0.59	0.0440	3.95×10^{-4}
38	64	30	550	25	25	0.64	0.0512	4.04×10^{-4}
39	64	30	550	35	20	0.65	0.0588	3.57×10^{-4}
40	64	30	550	35	20	0.70	0.0550	2.80×10^{-4}
41	64	30	700	25	20	1.09	0.0661	5.39×10^{-4}
42	64	30	700	25	20	1.02	0.0584	5.86×10^{-4}
43	64	45	550	25	20	0.89	0.0658	1.71×10^{-4}
44	64	45	550	25	20	0.79	0.0806	2.03×10^{-4}
45	76	15	400	15	15	0.57	0.0146	1.27×10^{-4}
46	76	15	400	15	15	0.62	0.0146	2.75×10^{-4}
47	76	15	400	35	25	0.47	0.0111	2.52×10^{-4}
48	76	15	400	35	25	0.47	0.0257	2.29×10^{-4}
49	76	15	700	15	25	1.06	0.0440	6.70×10^{-4}
50	76	15	700	15	25	1.07	0.0475	5.65×10^{-4}
51	76	15	700	35	15	1.27	0.0698	4.42×10^{-4}
52	76	15	700	35	15	1.37	0.0734	4.19×10^{-4}
53	76	30	550	25	20	0.47	0.0146	2.16×10^{-4}
54	76	30	550	25	20	0.70	0.0109	2.72×10^{-4}
55	76	45	400	15	25	0.27	0.0037	1.91×10^{-4}
56	76	45	400	15	25	0.27	0.0183	2.83×10^{-4}

Table A2. Cont.

Run	Gs	De	Pr (N/cm ²)	Vt (m/min)	VI (m/min)	Ra (μm)	Qm (cm/min)	Qp (cm ³ /min)
57	76	45	400	35	15	0.75	0.0293	0.00
58	76	45	400	35	15	0.69	0.0219	1.21×10^{-4}
59	76	45	700	15	15	0.38	0.0110	2.31×10^{-4}
60	76	45	700	15	15	0.50	0.0147	1.09×10^{-4}
61	76	45	700	35	25	0.65	0.0440	3.56×10^{-4}
62	76	45	700	35	25	1.07	0.0881	4.36×10^{-4}

Table A3. Experimentation results in the finish phase.

Run	Gs	De	Pr (N/cm ²)	Vt (m/min)	VI (m/min)	Ra (μm)	Qm (cm/min)	Qp (cm ³ /min)
1	15	10	400	15	25	0.24	0.0037	1.76×10^{-5}
2	15	10	400	15	25	0.09	0.0037	1.04×10^{-5}
3	15	10	400	35	15	0.06	0.0037	2.27×10^{-5}
4	15	10	400	35	15	0.09	0.0037	0.00
5	15	10	700	15	15	0.14	0.0110	3.09×10^{-5}
6	15	10	700	15	15	0.16	0.0110	5.88×10^{-5}
7	15	10	700	35	25	0.19	0.0313	9.41×10^{-5}
8	15	10	700	35	25	0.12	0.0313	7.71×10^{-5}
9	15	15	550	25	20	0.12	0.0037	4.15×10^{-5}
10	15	15	550	25	20	0.09	0.0055	8.30×10^{-5}
11	15	20	400	15	15	0.11	0.0037	0.00
12	15	20	400	15	15	0.09	0.0037	1.15×10^{-5}
13	15	20	400	35	25	0.06	0.0074	0.00
14	15	20	400	35	25	0.05	0.0073	3.46×10^{-5}
15	15	20	700	15	25	0.15	0.0092	6.95×10^{-5}
16	15	20	700	15	25	0.09	0.0073	3.37×10^{-5}
17	15	20	700	35	15	0.09	0.0093	2.31×10^{-5}
18	15	20	700	35	15	0.14	0.0166	9.88×10^{-6}
19	20	10	550	25	20	0.11	0.0037	1.13×10^{-5}
20	20	10	550	25	20	0.09	0.0037	1.13×10^{-5}
21	20	15	400	25	20	0.11	0.0037	2.76×10^{-5}
22	20	15	400	25	20	0.10	0.0037	6.22×10^{-5}
23	20	15	550	15	20	0.11	0.0074	3.61×10^{-5}
24	20	15	550	15	20	0.12	0.0092	4.66×10^{-5}
25	20	15	550	25	15	0.15	0.0092	4.15×10^{-5}
26	20	15	550	25	15	0.12	0.0092	4.15×10^{-5}
27	20	15	550	25	20	0.12	0.0037	5.92×10^{-5}
28	20	15	550	25	20	0.15	0.0037	7.10×10^{-5}
29	20	15	550	25	20	0.12	0.0037	0.00
30	20	15	550	25	20	0.11	0.0055	6.00×10^{-5}
31	20	15	550	25	20	0.12	0.0055	8.08×10^{-5}
32	20	15	550	25	20	0.14	0.0074	1.10×10^{-4}
33	20	15	550	25	20	0.11	0.0055	1.08×10^{-4}
34	20	15	550	25	20	0.12	0.0055	3.63×10^{-5}
35	20	15	550	25	20	0.12	0.0091	2.66×10^{-5}
36	20	15	550	25	20	0.12	0.0091	5.32×10^{-5}
37	20	15	550	25	25	0.11	0.0129	2.30×10^{-5}
38	20	15	550	25	25	0.12	0.0148	5.54×10^{-5}
39	20	15	550	35	20	0.10	0.0092	7.92×10^{-5}
40	20	15	550	35	20	0.11	0.0092	1.11×10^{-4}
41	20	15	700	25	20	0.17	0.0127	2.27×10^{-5}
42	20	15	700	25	20	0.16	0.0111	0.00

Table A3. Cont.

Run	Gs	De	Pr (N/cm ²)	Vt (m/min)	Vl (m/min)	Ra (μm)	Qm (cm/min)	Qp (cm ³ /min)
43	20	20	550	25	20	0.11	0.0055	5.77×10^{-5}
44	20	20	550	25	20	0.08	0.0055	5.77×10^{-5}
45	30	10	400	15	15	0.18	0.0018	6.03×10^{-5}
46	30	10	400	15	15	0.16	0.0037	1.61×10^{-4}
47	30	10	400	35	25	0.16	0.0037	2.84×10^{-4}
48	30	10	400	35	25	0.15	0.0037	2.64×10^{-4}
49	30	10	700	15	25	0.33	0.0165	4.11×10^{-4}
50	30	10	700	15	25	0.31	0.0182	4.32×10^{-4}
51	30	10	700	35	15	0.34	0.0350	6.60×10^{-4}
52	30	10	700	35	15	0.50	0.0056	6.60×10^{-4}
53	30	15	550	25	20	0.33	0.0203	4.00×10^{-4}
54	30	15	550	25	20	0.32	0.0184	4.45×10^{-4}
55	30	20	400	15	25	0.26	0.0091	1.61×10^{-4}
56	30	20	400	15	25	0.25	0.0093	0.00
57	30	20	400	35	15	0.19	0.0074	1.28×10^{-4}
58	30	20	400	35	15	0.21	0.0073	1.28×10^{-4}
59	30	20	700	15	15	0.38	0.0184	3.21×10^{-4}
60	30	20	700	15	15	0.41	0.0165	4.55×10^{-4}
61	30	20	700	35	25	0.42	0.0424	3.33×10^{-4}
62	30	20	700	35	25	0.43	0.0497	6.13×10^{-4}

References

- Lawrence, K.D.; Ramamoorthy, B. Structure function-based fractal characterisation of cylinder bore surfaces using stylus profile data. *Int. J. Precis. Technol.* **2014**, *4*, 19. [[CrossRef](#)]
- Grabon, W.; Pawlus, P.; Wos, S.; Koszela, W.; Wieczorowski, M. Effects of honed cylinder liner surface texture on tribological properties of piston ring-liner assembly in short time tests. *Tribol. Int.* **2017**, *113*, 137–148. [[CrossRef](#)]
- Kim, E.S.; Kim, S.M.; Lee, Y.Z. The effect of plateau honing on the friction and wear of cylinder liners. *Wear* **2018**, *400*, 207–212. [[CrossRef](#)]
- Troglio, A.J. Performance evaluation of multi-stone honing tool by experimental design methods. In Proceedings of the International Honing Conference, Itasca, IL, USA, 8–9 April 2003; Volume MR03-232, pp. 1–24.
- Kanthababu, M.; Shunmugam, M.S.; Singaperumal, M. Identification of significant parameters and appropriate levels in honing of cylinder liners. *Int. J. Mach. Mach. Mater.* **2009**, *5*, 80. [[CrossRef](#)]
- Woś, P.; Michalski, J. Effect of Initial Cylinder Liner Honing Surface Roughness on Aircraft Piston Engine Performances. *Tribol. Lett.* **2011**, *41*, 555–567. [[CrossRef](#)]
- Vrac, D.S.; Sidjanin, L.P.; Kovac, P.P.; Balos, S.S. The influence of honing process parameters on surface quality, productivity, cutting angle and coefficients of friction. *Ind. Lubr. Tribol.* **2013**, *64*. [[CrossRef](#)]
- Vrac, D.S.; Sidjanin, L.P.; Balos, S.S. Mechanical finishing honing: Cutting regimes and surface texture. *Ind. Lubr. Tribol.* **2013**, *63*, 427–432. [[CrossRef](#)]
- Vrabel', M.; Maňková, I.; Durakbasa, N.M. Effect of Honing Parameters on Generated Surface Quality of Cylinder Liner within Automotive Engine Production. *Solid State Phenom.* **2017**, *261*, 189–194. [[CrossRef](#)]
- Buj-Corral, I.; Vivancos-Calvet, J.; Coba-Salcedo, M. Modelling of surface finish and material removal rate in rough honing. *Precis. Eng.* **2014**, *38*, 100–108. [[CrossRef](#)]
- Szabo, O. Examination of Material Removal Process in Honing: Ebscohost. *Acta Tech. Corviniensis-Bull. Eng.* **2014**, *7*, 35–38.
- Bai, Y.J.; Zhang, L.H.; Ren, C.G. Experimental investigation on honing of small holes. *Key Eng. Mater.* **2007**, *329*, 303–308. [[CrossRef](#)]
- Buj-Corral, I.; Álvarez-Flórez, J.; Domínguez-Fernández, A. Effect of grain size and density of abrasive on surface roughness, material removal rate and acoustic emission signal in rough honing processes. *Metals* **2019**, *9*, 860. [[CrossRef](#)]
- Arantes, L.J.; Fernandes, K.A.; Schramm, C.R.; Leal, J.E.S.; Piratelli-Filho, A.; Franco, S.D.; Arencibia, R.V. The roughness characterization in cylinders obtained by conventional and flexible honing processes. *Int. J. Adv. Manuf. Technol.* **2017**, *93*, 635–649. [[CrossRef](#)]
- Cabanettes, F.; Dimkovski, Z.; Rosén, B.-G. Roughness variations in cylinder liners induced by honing tools' wear. *Precis. Eng.* **2015**, *41*, 40–46. [[CrossRef](#)]
- Derringer, G.; Suich, R. Simultaneous Optimization of Several Response Variables. *J. Qual. Technol.* **2018**, *12*, 214–219. [[CrossRef](#)]

17. Chabbi, A.; Yallese, M.A.; Meddour, I.; Nouioua, M.; Mabrouki, T.; Girardin, F. Predictive modeling and multi-response optimization of technological parameters in turning of Polyoxymethylene polymer (POM C) using RSM and desirability function. *Measurement* **2017**, *95*, 99–115. [[CrossRef](#)]
18. Aggarwal, A.; Singh, H.; Kumar, P.; Singh, M. Optimization of multiple quality characteristics for CNC turning under cryogenic cutting environment using desirability function. *J. Mater. Process. Technol.* **2008**, *205*, 42–50. [[CrossRef](#)]
19. Selaimia, A.-A.; Yallese, M.A.; Bensouilah, H.; Meddour, I.K.; Khattabi, R.; Mabrouki, T. Modeling and optimization in dry face milling of X2CrNi18-9 austenitic stainless steel using RMS and desirability approach. *Measurement* **2017**, *107*, 53–67. [[CrossRef](#)]
20. Mia, M. Multi-response optimization of end milling parameters under through-tool cryogenic cooling condition. *Measurement* **2017**, *111*, 134–145. [[CrossRef](#)]
21. Mukherjee, I.; Ray, P.K. Optimal process design of two-stage multiple responses grinding processes using desirability functions and metaheuristic technique. *Appl. Soft Comput.* **2008**, *8*, 402–421. [[CrossRef](#)]
22. Lawrence, K.D.; Ramamoorthy, B. Multi-surface topography targeted plateau honing for the processing of cylinder liner surfaces of automotive engines. *Appl. Surf. Sci.* **2016**, *365*, 19–30. [[CrossRef](#)]
23. Nguyen, T.T.; Vu, T.C.; Duong, Q.D. Multi-responses optimization of finishing honing process for surface quality and production rate. *J. Brazilian Soc. Mech. Sci. Eng.* **2020**, *42*, 604. [[CrossRef](#)]
24. Castillo, E.; Mínguez, R.; Castillo, C. Sensitivity analysis in optimization and reliability problems. *Reliab. Eng. Syst. Saf.* **2008**, *93*, 1788–1800. [[CrossRef](#)]
25. Aksezer, C.S. On the sensitivity of desirability functions for multiresponse optimization. *J. Ind. Manag. Optim.* **2008**, *4*, 685–696. [[CrossRef](#)]
26. Malenović, A.; Dotsikas, Y.; Mašković, M.; Jančić-Stojanović, B.; Ivanović, D.; Medenica, M. Desirability-based optimization and its sensitivity analysis for the perindopril and its impurities analysis in a microemulsion LC system. *Microchem. J.* **2011**, *99*, 454–460. [[CrossRef](#)]
27. Rocha, L.C.S.; de Paiva, A.P.; Rotela Junior, P.; Balestrassi, P.P.; da Silva Campos, P.H. Robust multiple criteria decision making applied to optimization of AISI H13 hardened steel turning with PCBN wiper tool. *Int. J. Adv. Manuf. Technol.* **2017**, *89*, 2251–2268. [[CrossRef](#)]
28. Mudhukrishnan, M.; Hariharan, P.; Palanikumar, K.; Latha, B. Optimization and sensitivity analysis of drilling parameters for sustainable machining of carbon fiber-reinforced polypropylene composites. *J. Thermoplast. Compos. Mater.* **2019**, *32*, 1485–1508. [[CrossRef](#)]
29. Shi, C.; Wu, Z.; Lv, K.; Wu, L. A review on mixture design methods for self-compacting concrete. *Constr. Build. Mater.* **2015**, *84*, 387–398. [[CrossRef](#)]
30. Buruk Sahin, Y.; Aktar Demirtaş, E.; Burnak, N. Mixture design: A review of recent applications in the food industry. *Pamukkale Univ. J. Eng. Sci.* **2016**, *22*, 297–304. [[CrossRef](#)]
31. Misra, J.P.; Jain, P.K.; Dwivedi, D.K.; Mehta, N.K. Mixture D-optimal design of electrolyte composition in ECH of bevel gears. *Adv. Mater. Res.* **2013**, *685*, 347–351. [[CrossRef](#)]
32. ISO 21920-2:2021 Geometrical product specifications (GPS)—Surface texture: Profile—Part 2: Terms, Definitions and Surface Texture Parameters, ISO: Geneva, Switzerland, 2021.
33. ISO 6106:2013. Abrasive Products—Checking the Grain Size of Superabrasives, ISO: Geneva, Switzerland, 2013.
34. ISO 6104:2005. Superabrasive Products—Rotating Grinding Tools with Diamond or Cubic Boron Nitride—General Survey, Designation and Multilingual Nomenclature, ISO: Geneva, Switzerland, 2005.
35. Günay, M.; Korkmaz, M.E. Optimization of honing parameters for renewal of cylinder liners. *Gazi Univ. J. Sci.* **2017**, *30*, 111–119.
36. Buj-Corral, I.; Álvarez-Flórez, J.; Domínguez-Fernández, A. Acoustic emission analysis for the detection of appropriate cutting operations in honing processes. *Mech. Syst. Signal Process.* **2018**, *99*, 873–885. [[CrossRef](#)]

Article

Influence of Axial Depth of Cut and Tool Position on Surface Quality and Chatter Appearance in Locally Supported Thin Floor Milling

Mikel Casuso ^{1,*}, Antonio Rubio-Mateos ¹, Fernando Veiga ¹ and Aitzol Lamikiz ²

¹ TECNALIA, Basque Research and Technology Alliance (BRTA), Parque Científico y Tecnológico de Gipuzkoa, E20009 Donostia-San Sebastián, Spain; antonio.rubio@tecnalia.com (A.R.-M.); fernando.veiga@tecnalia.com (F.V.)

² Department of Mechanical Engineering, University of the Basque Country (UPV/EHU), E48013 Bilbao, Spain; aitzol.lamikiz@ehu.eus

* Correspondence: mikel.casuso@tecnalia.com; Tel.: +34-902-760-000

Abstract: Thin floor machining is a challenging and demanding issue, due to vibrations that create poor surface quality. Several technologies have been developed to overcome this problem. Ad hoc fixtures for a given part geometry lead to meeting quality tolerances, but since they lack flexibility, they are expensive and not suitable for low manufacturing batches. On the contrary, flexible fixtures consisting of vacuum cups adaptable to a diversity of part geometries may not totally avoid vibrations, which greatly limits its use. The present study analyses the feasibility of thin floor milling in terms of vibration and roughness, in the cases where milling is conducted without back support, a usual situation when flexible fixtures are employed, so as to define the conditions for a stable milling in them and thus avoid the use of ad hoc fixtures. For that purpose, the change of modal parameters due to material removal and its influence on chatter appearance have been studied, by means of stability lobe diagrams and Fourier Transform analysis. Additionally, the relationship between surface roughness and chatter frequency, tooth passing frequency, and spindle frequency have been studied. Ploughing effect has also been observed during milling, and the factors that lead to the appearance of this undesirable effect have been analyzed, in order to avoid it. It has been proven that finish milling of thin floors without support in the axial direction of the mill can meet aeronautic tolerances and requirements, providing that proper cutting conditions and machining zones are selected.

Keywords: finish milling; chatter; part quality; AA2024 floor milling

Citation: Casuso, M.; Rubio-Mateos, A.; Veiga, F.; Lamikiz, A. Influence of Axial Depth of Cut and Tool Position on Surface Quality and Chatter Appearance in Locally Supported Thin Floor Milling. *Materials* **2022**, *15*, 731. <https://doi.org/10.3390/ma15030731>

Academic Editors: Gilles Dessein and J. Antonio Travieso-Rodriguez

Received: 14 December 2021

Accepted: 17 January 2022

Published: 19 January 2022

Publisher's Note: MDPI stays neutral with regard to jurisdictional claims in published maps and institutional affiliations.



Copyright: © 2022 by the authors. Licensee MDPI, Basel, Switzerland. This article is an open access article distributed under the terms and conditions of the Creative Commons Attribution (CC BY) license (<https://creativecommons.org/licenses/by/4.0/>).

1. Introduction

Achieving good surface quality in final parts is a widespread concern among manufacturers of all kinds. The milling of thin parts is an especially critical issue [1], since the stiffness of these parts is low, which eases the appearance of vibration, as chatter and forced vibration, which negatively affect final surface quality and tool life [2]. This problem can lead to the rejection of these parts or to the necessity of reprocessing, which entails high costs in terms of material, time, and energy.

However, as Kolluru and Axinte [3] and Irene Del Sol et al. [4] have pointed out, chatter avoidance in thin parts has traditionally focused on thin wall milling, whereas thin floor milling has been relegated, even though its importance is high in fields such as aeronautic and aerospace industries, where pockets are milled in parts as aircraft structures in order to lighten them and must comply with stringent surface requirements. Precisely, mechanical milling appears as an alternative to chemical milling for thin floors, which is hazardous and pollutant [5,6].

Chatter is a self-excited vibration that appears due to the dynamic excitation produced as a consequence of the chip thickness variation caused by the periodic irregular surface

generated by the precedent tool tooth pass [7]. Mainly, three types of solutions have been proposed to cope with vibrations in mechanical milling of thin floors: fixture design aiming to increase the stiffness of the part, damping systems aiming to dissipate vibration energy, and the prediction of stable machining conditions [8]. Both fixture and damping systems can be ad hoc for a given geometry or flexible and adjustable for different ones. On the one hand, if they are ad hoc, they are able to avoid vibrations as they completely support thin floors, but they also require investments that are neither feasible nor profitable when manufacturing low batches, as it is usual in aeronautic and aerospace sectors [9]. On the other hand, flexible fixtures usually consist of actuators that support the part by means of vacuum cups. In such a layout, due to the distance between actuators, some zones of the part may be without back support. Chatter vibration can appear easily in this situation of extremely low stiffness. Due to this fact, this kind of fixture is usually discarded for high precision milling, as it is usual in aeronautic and aerospace sectors, and they are employed only for other operations, such as drilling, trimming, or for milling processes that do not require demanding tolerances [10]. As a consequence, the potential of flexible fixtures has not been fully harnessed yet. A deeper analysis consisting of predicting and selecting proper cutting conditions and areas leading to a stable and precise machining can be a solution [2]. It would make feasible thin floor milling even in the situation of such a low stiffness that happens in flexible fixtures.

In this line, F.J. Campa et al. [11] suggest the mathematical analysis of the cutting process for thin floors, by means of stability lobes diagram (SLD) determination, which allows the selection of the pair of values of spindle speed and axial depth of cut leading to the most stable and productive machining. In the case of parts with low stiffness, as thin floors are, the dynamic parameters of the part continuously vary during milling, since both mass and stiffness decrease. So, in addition to the depth of cut and spindle speed, Bravo et al. [12] suggest taking into account the geometric state of the part during milling, thus leading to three-dimensional SLD. This approach is followed in the present study, due to the low stiffness and the relatively high material removal rate that thin floors undergo.

The experimental setup has been planned to test different cutting conditions in a context of extremely low stiffness, which is a thin floor simply screwed in its corners and without back support. It emulates a thin floor supported by four clamping vacuum cups, as it happens in flexible fixtures. The objective is to analyze the milling of thin floors aiming to optimize the surface quality achieved and to avoid chatter vibration. For that purpose, thin plates have been pocket milled. Vibration and surface roughness results have been measured, discussed, and compared to the available bibliography. Finally, some guidelines are proposed to make such thin floor milling feasible.

2. Materials and Methods

2.1. Tested Parts

Aiming to emulate a real industrial case, a series of pocketing tests were carried out in metal thin plates. Each thin plate is a square metal sample of $85 \times 85 \text{ mm}^2$ and 2 mm thick, very similar to the samples used by Del Sol et al. [13] and Rubio-Mateos et al. [14]. The material is aluminum alloy UNS 2024-T3, widely employed in the aeronautic industry.

Prior to any machining operation, each thin floor was drilled near its corners to make holes of 7 mm in order to screw it to an intermediate rigid block that maintains the stability of the process. Each thin floor was elevated, so the screws were its only support and clamping during the entire machining process, which causes a reduction of stiffness in the axial direction of the mill. The centers of the screws form a square of $69 \times 69 \text{ mm}^2$. This layout is an extrapolation of the milling of a thin floor locally supported by four vacuum cups. The general setup is shown in Figure 1.

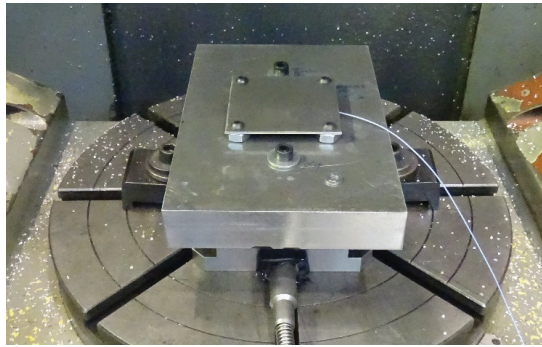


Figure 1. General setup of a sample to be machined, with the accelerometer below.

2.2. Methodology

The methodology employed in the present study of the pocket machining of thin plate samples comprises various steps.

First, the frequency response function (FRF) of the tool was measured prior to the machining, as well as the FRFs of the thin plates in four consecutive stages of the machining, in order to calculate the three-dimensional stability lobe diagrams (3D-SLD) of the system. Besides, the vibration of the sample during machining was continuously monitored, and it is used to calculate its Fast Fourier Transform (FFT). To this point, the methodology is similar to the one followed by Kolluru and Axinte [15] to analyze the impact dynamics in the machining of low rigidity workpieces, by means of the determination of dominant modes.

In addition, a roughness analysis was conducted at the end of the present study, in order to correlate it to the vibrations of the samples during machining. The general overview of the tasks is shown in Table 1.

Table 1. Conducted tasks.

Before Machining	During Machining	After Machining
Samples FRF measurement	Samples FRF measurement	SLD calculation
Tool FRF measurement	Vibration monitoring	Vibration FFT calculation
		Roughness measurement
		Roughness FFT calculation

2.3. Machining Operation

The machining operation that was performed in each thin floor consisted in a dry milling of a pocket of $50 \times 50 \text{ mm}^2$ by an outward helicoidal strategy, which is one of the most suitable machining strategies regarding final roughness, accuracy, and process time, as Del Sol et al. [16] have proved. This strategy follows the guidelines of Herranz et al. [7] taking advantage of the rigidity of the uncut part, which is higher near the screws.

The strategy comprised 33 straight cutting passes, consecutively numbered in Figure 2, plus an initial brief drilling in the center in order to start the milling.

The pocket machining was performed in a 5-axis NC center Ibarria ZV 25U600 EXTREME, with a two flutes bull-nose end-mill Kendu 4400, which has a 10 mm diameter, 30° helix angle and 2.5 mm edge radius (r).

Regarding the cutting conditions, conservative ones were selected, as they lead to lower part distortion and lower surface roughness in an aluminum alloy [17,18]. Even though the machining time is higher, this factor is out of the scope of the present study. So, the spindle spins at 4000 rpm and the feed rate was 800 mm/min (0.1 mm/tooth). The radial immersion of the mill was 5 mm.

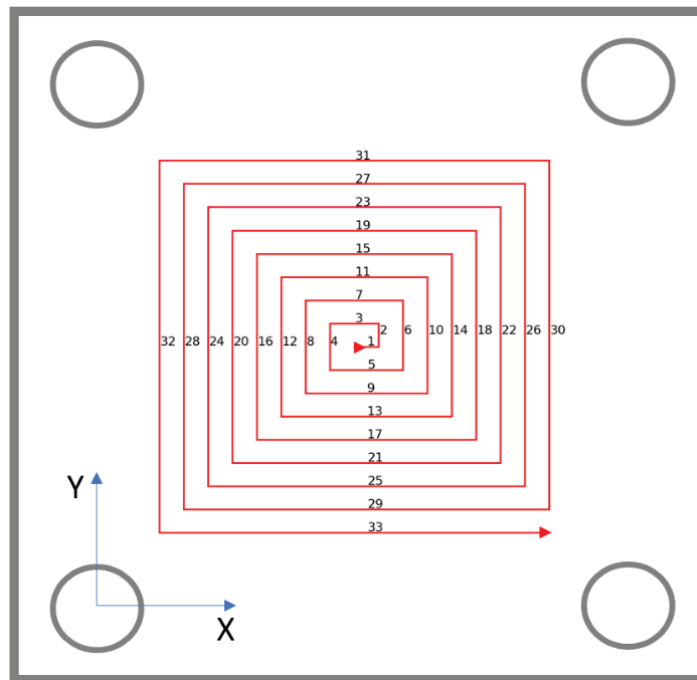


Figure 2. Followed outward helicoidal machining strategy.

A different axial depth of cut was employed for pocketing each thin floor (1, 0.8, 0.4 and 0.2 mm), in order to compare the influence of different material removal rates both in vibrations and in achieved final roughness. Due to the depths of cut employed, the thin plates can be named as shown in Table 2. Their remaining features, both in material and in machining operation, are identical.

Table 2. Thin plates according to the depth of cut.

Thin Plate Name	Axial Depth of Cut Employed
TP10	1 mm
TP08	0.8 mm
TP04	0.4 mm
TP02	0.2 mm

2.4. Vibration Monitoring, FRF Obtention and SLD Calculation

SLDs of the thin plate samples are calculated from their FRFs, which quantify the response of the sample–tool–spindle–machine system to an excitation. Nevertheless, the calculation of the SLDs of parts with low thickness as employed thin plates entails two phenomena. The first one is that the stiffness of the part is lower than the stiffness of the cutting tool, so chatter vibration is mostly affected by the dynamic properties and critical modes of the part [19]. The second phenomenon is the ratio of material removal, which is high compared to the global volume of the part and that leads to a continuous change in its modal parameters and FRF during machining [20]. In order to consider this feature, there are two possibilities. The first one is the use of Finite Element Analysis (FEA) that aims to simulate the FRFs of the samples. This option was used and validated by Dang et al. [21], who consider the second possibility impractical, that is, the Experimental

Modal Analysis (EMA), which aims to measure the FRFs of the samples conducting several impact hammer tests during machining and measuring the response of the system with an attached accelerometer [22]. Nevertheless, FEA also entails the requirement of high computational resources and time expended, so EMA is a suitable option, especially for short machining with a simple setup as the one presented in this study. This option was also followed by Qu et al. [23].

Consequently, aiming to obtain the SLDs of the system, several FRF tests were conducted at different stages of the machining. In each test, an impact hammer hit the sample at its top center, while an accelerometer placed at the bottom center registers the corresponding data. The first test was performed prior to any machining operation, the second one was performed after cutting pass 5, the third one after cutting pass 17, and the last one with the pocket completed, so four FRF tests were performed in each sample. As a consequence of performing each test in different stages of the machining, the calculated SLDs take into account not only the axial depth of cut and the spindle speed, but also the position reached by the tool along the cutting path.

The accelerometer is a uniaxial PCB model 352C22 with a measuring range from 1 to 10 kHz and a sensitivity of $1.0 \text{ mV}/(\text{m}/\text{s}^2)$, located at the bottom center of the thin floor. This accelerometer was also used to continuously monitor vibrations during machining.

The FRF was obtained only in the thick direction or Z direction of the sample, which is considered to be overwhelmingly less rigid than the others, so it is regarded that the workpiece only moves along this direction, an assumption also followed by Seguy et al. [24] and Arnaud et al. [25].

In the case of the tool, the FRF was obtained in its three spatial directions, gluing the accelerometer to the tool. As the FRF of the tool does not vary during machining, a single impact test before machining suffices for obtaining it.

Aiming to determine the machining conditions leading to chatter vibration, stability lobes were calculated. Since modal parameters of the samples vary during material removal, several stability lobes were obtained corresponding to different machining stages, precisely, the machining stages where FRF tests were undertaken, enabling the calculation of SLDs that also take into account the position reached by the tool along the cutting path. This kind of 3D-SLD was also obtained by Campa et al. [11], analyzing thin floor milling.

Thus, these SLDs show the maximum chatter-free axial depth of cut regarding each spindle speed for a given stage of the machining. They have been obtained by applying the three-dimensional mono-frequency model [26,27], and combining the FRF of the samples with the FRF of the tool.

The forces used in this calculation have been obtained employing the mechanistic approach [28,29], which relates the force components (tangential [F_t], radial [F_r] and axial [F_a]) acting in each differential element j of the edge of the mill during machining to the feed per tooth (f_z), and length (dS), angular position (Φ) and axial depth of cut (dz) of the element j .

$$\begin{bmatrix} dF_t(\Phi, z) \\ dF_r(\Phi, z) \\ dF_a(\Phi, z) \end{bmatrix}_j = \begin{bmatrix} K_{te} \\ K_{re} \\ K_{ae} \end{bmatrix} \cdot dS(z) + \begin{bmatrix} K_{tc} \\ K_{rc} \\ K_{ac} \end{bmatrix} \cdot f_z \cdot \sin \Phi(\Phi_j, z) \cdot dz \quad (1)$$

This relation is based on the friction (K_{te} , K_{re} , K_{ae}) and shearing (K_{tc} , K_{rc} , K_{ac}) cutting coefficients, which have been obtained prior to the pocketing operation. Precisely, they were obtained solving the equations using force values measured in a previous grooving test, taking a constant value for the spindle speed of 4000 rpm, which is the speed employed in the pocketing tests.

Bull-nose end mills have a lead angle that varies from 0° to 90° . For the case of the mill employed in the present study, these values would correspond to 0 and 2.5 mm of the axial depth of cut, respectively. Altintas [26] suggested that an average value of 45° could be taken. Since in the present study the axial depth of cut varies only from 0.2 mm to 1 mm,

a lower constant lead edge angle could be considered. Following Rubio-Mateos et al. [30], a constant lead edge angle of 20° is taken.

2.5. Roughness Measurement

The final roughness of the samples after machining was measured in a Mitutoyo Surftest SV-2000 equipment (Figure 3). The roughness profile and the average roughness value (R_a) were measured along 4 mm in the middle of cutting passes 5, 9, 13, 17, 21, 25, 29 and 33. In Figure 4 the accurate lines where roughness was measured can be seen.

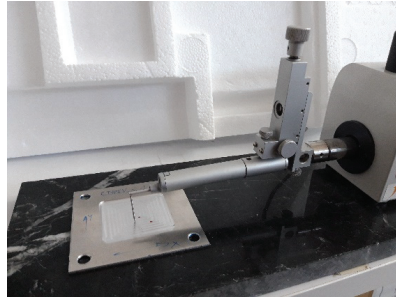


Figure 3. Measurement of final roughness in a sample.

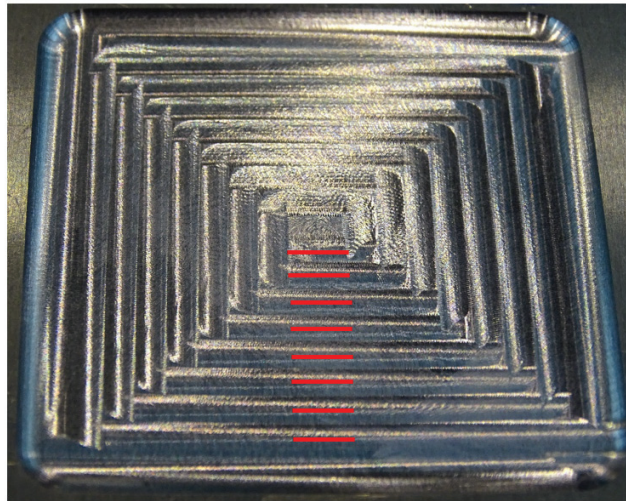


Figure 4. Roughness measurement lines.

2.6. Roughness Model

A surface roughness model is proposed to explain its causes and origins, based on the model suggested by Rubio-Mateos et al. [14].

In the experimental setup employed, the roughness in the samples can have three origins. Firstly, the theoretical average roughness (R_t) generated by the tool geometry and the feed per tooth. Secondly, the roughness generated as a consequence of the forced vibration and the axial displacement of the sample (R_f). The axial displacement can happen due to the deflection of the sample or to the relative displacement between sample and fixture. And thirdly, the roughness caused by chatter vibration (R_c). So, the global average roughness (R_a) can be defined as:

$$R_a = R_t + R_f + R_c \quad (2)$$

The floor theoretical average roughness is defined as:

$$R_h = \frac{f_z^2}{32r} \quad (3)$$

If chatter-free conditions are guaranteed, roughness caused by chatter is zero, so the difference between measured average roughness and theoretical average roughness will be caused by the axial displacement of the sample. Also, this axial displacement can be considered constant for a given setup and cutting conditions, so the chatter roughness will be the roughness surplus generated at chatter conditions. Cross effects, as well as the axial displacement and the vibration of the tool, are neglected.

3. Results and Discussion

3.1. SLD Analysis

The SLDs of the samples were calculated before, during, and after the pocketing tests at different axial depths of cut (Figure 5). SLDs show the frontier line under which axial depth of cut and spindle speed values lead to a chatter-free milling. As expected, the maximum chatter-free depth of cut is lower when machining has finalized, because the rigidity of the part is lower. Also, bigger material removals lead to lower maximum depths, as the decrease of the lobes is more pronounced for the cases of machining taking place at $a_p = 1$ mm and $a_p = 0.8$ mm. This phenomenon is more obvious if only the critical depth of cut is analyzed, namely, the lower maximum axial depth of cut that guarantees chatter-free milling irrespectively of spindle speed (Figure 6).

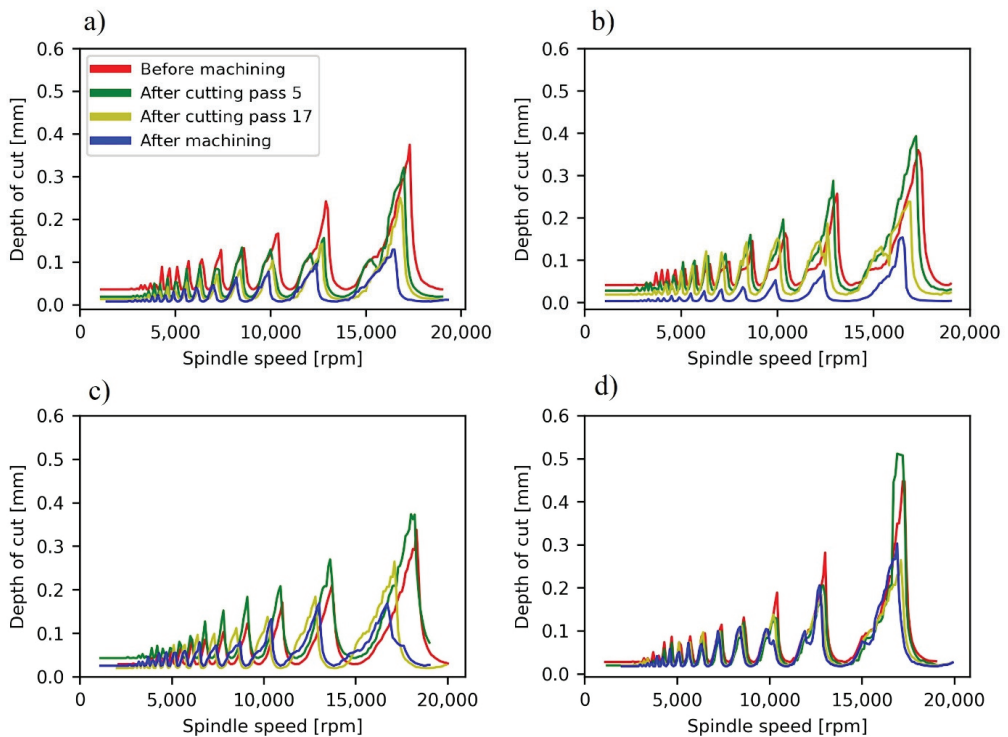


Figure 5. Stability lobe diagrams before, during and after pocket milling. (a) TP10. (b) TP08. (c) TP04. (d) TP02.

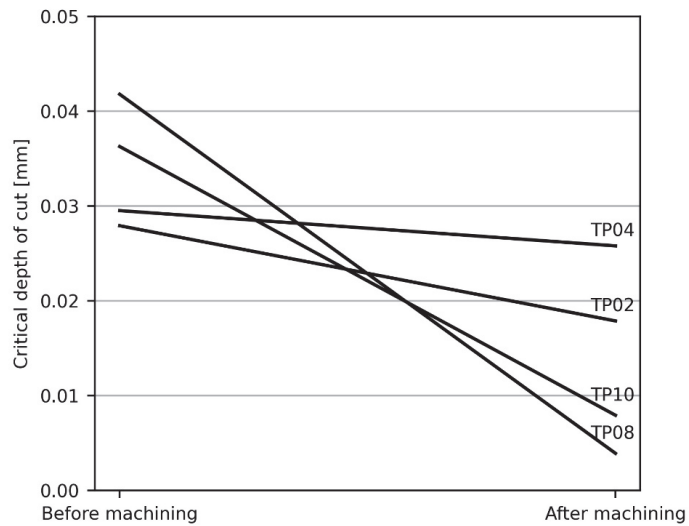


Figure 6. Critical axial depth of cut for the machining of each sample for different material removals.

An important initial conclusion that can be derived from these SLDs is the difficulty to globally avoid chatter when a milling operation is performed in this kind of sample as they were set up. Even the machining conditions that according to the SLD initially avoid chatter ($a_p = 0.3$ mm; 17,500 rpm) disappear because of material removal, which means that chatter would only be avoided at the beginning of the machining. In addition, the productivity would be low. Aiming to overcome these problems, a deeper analysis has been performed, studying separately each cutting pass of the machining path.

3.2. Vibration FFT Analysis

The Fast Fourier Transform (FFT) of the vibration signal is a useful and representative indicator of the dynamic behavior of the system, which can be employed for determining the appearance of chatter vibration. In the current study, an FFT of the vibration of the samples, measured by the accelerometer placed below them during machining, has been obtained per cutting pass, namely, 33 FFT per sample. They are shown in three-dimensional plots in Figure 7. In these plots, the cutting passes where chatter takes place can be observed, as well as the frequency at which chatter occurs. Also, the vibration content of low frequencies is remarkable.

Three main conclusions can be obtained from these plots. Firstly, it is noticeable that there are two zones where chatter can be initialized. The first zone is around cutting passes 3–5, and the second zone is around cutting pass 21. For TP10, chatter only appears in the first zone. For TP08 and TP04, chatter appears in both zones, but disappears at the middle. For TP02, chatter appears almost continuously between these two zones.

The existence of these two zones is due to the complex interrelation of different facts. On the one hand, at the beginning of the machining in the center of the sample, despite starting far from fixtures, the rigidity of the sample is still high, and chatter does not occur. On the other hand, the presence of modal nodes, where rigidity is higher, and antinodes, where it is lower, in addition to the progressive variation of modal parameters, leads to the alternative appearance and disappearance of chatter along the tool path [31].

Secondly, it is noticeable that chatter appearance is higher for lower material removals; namely, it affects more cutting zones. As Campa et al. [32] have stated, this phenomenon happens in the milling of thin floors with bull-nose end mills, and it is related to the fact that low depths of cut also involve low lead edge angles, that ease chatter appearance.

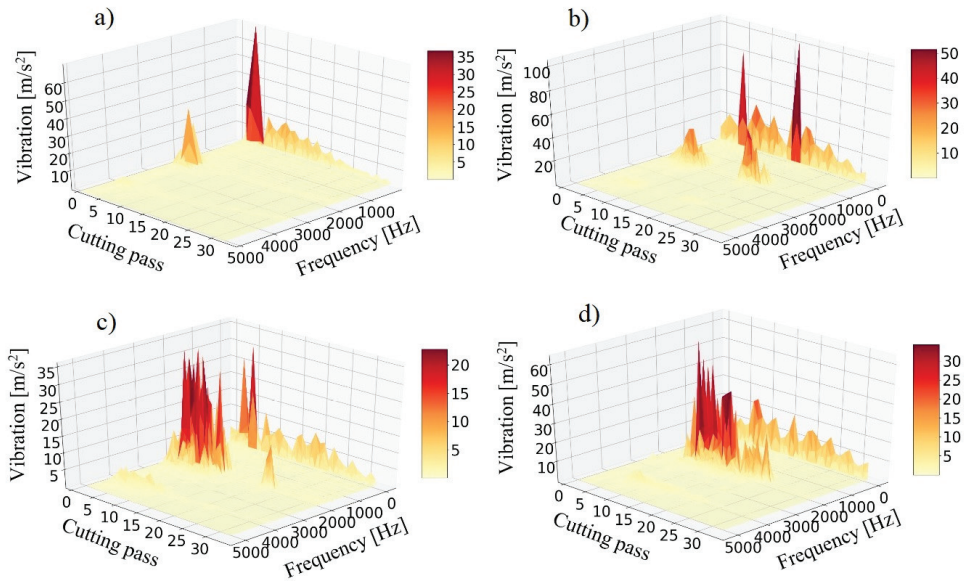


Figure 7. FFT of vibration signal of samples during machining. (a) TP10. (b) TP08. (c) TP04. (d) TP02.

And thirdly, it has been confirmed that chatter appears for all cases, as stated in the SLD analysis, but it disappears as long as the tool is reaching the fixtures. From cutting pass 25 the milling is stable for any depth of cut. That is to say that milling should be avoided in the central area between fixtures, but that milling is feasible and stable outside this area. In this case, the central area is approximately a central square of $30 \times 30 \text{ mm}^2$.

The accurate chatter frequency can be more clearly seen in Figure 8, where only the highest vibration frequencies are shown. This chatter frequency is close to the first natural frequency of the samples, that according to the conducted FRF tests it is around 1730 Hz before machining. A second chatter frequency, close to the second natural frequency of 4000 Hz, is also excited. Both chatter frequencies are excited simultaneously, which discards the possibility of each zone being created by the vibration of different modes, as happened in thin wall studies [25,33].

Besides, in Figure 8 the harmonics of chatter frequency can be seen. These harmonics can be expressed by the following binomial:

$$f_{\text{chatter}} + n \cdot f_{\text{tooth}} \quad (n \in N) \quad (4)$$

It is remarkable that the first and second harmonics are higher than the chatter frequency. There are also low frequencies with high amplitude. These are the tooth passing frequency (133.33 Hz) and its harmonics, or they are related to the shape of the signal. In any case, they are higher for passes with chatter appearance, which indicates that chatter also affects the shape of the vibration signal.

Chatter frequencies decrease due to material removal, as natural frequency does, although this decrease is very slight and it is only appreciable for the highest material removals. The detailed image in Figure 8 illustrates this effect, as it shows the variation of the chatter frequency of TP02 during machining.

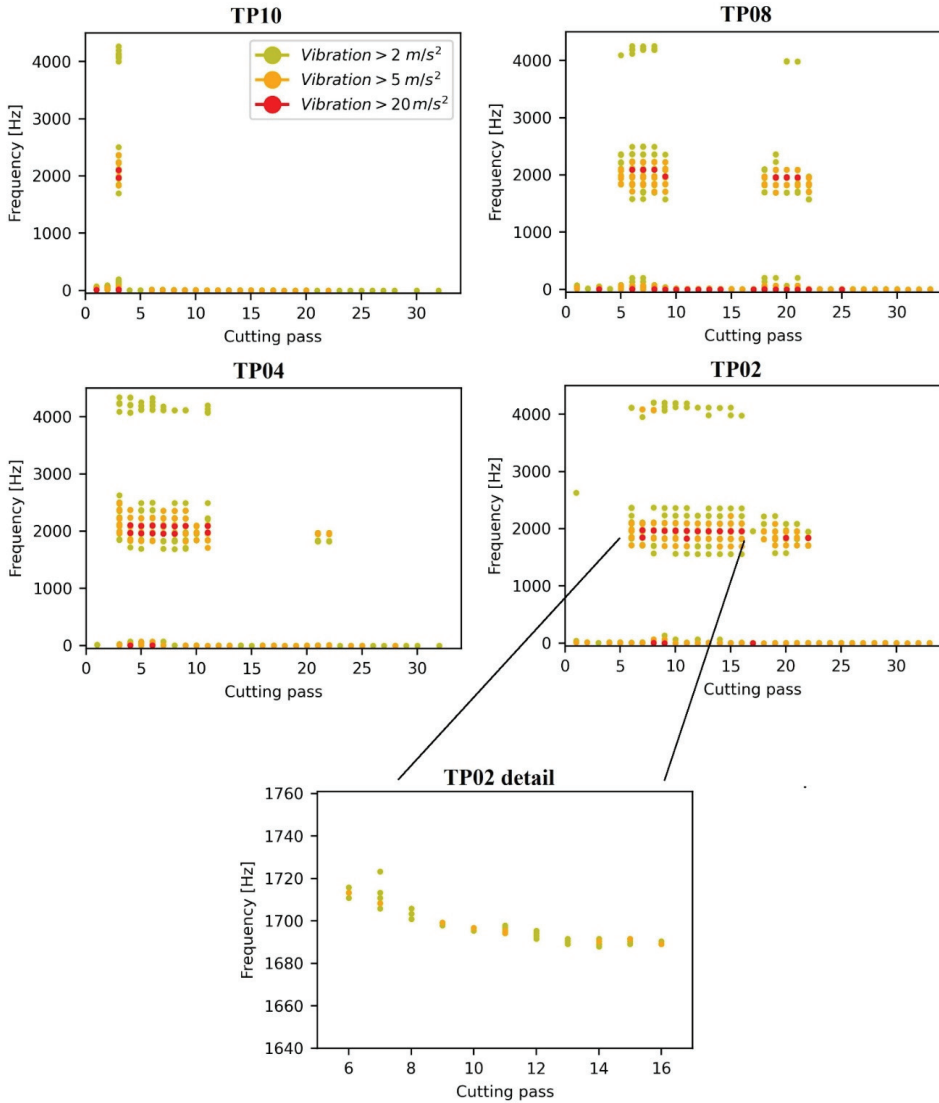


Figure 8. Frequencies with maximum vibration content per cutting pass, and TP02 detailed image.

3.3. Roughness Analysis

The final thin floors after milling are shown in Figure 9. In the four cases the first cutting pass does not exhibit chatter, but in the figure, due to the radial immersion of the successive passes, cutting pass 1 cannot be seen. In addition to chatter, there are ploughing marks at some changes of cutting direction.

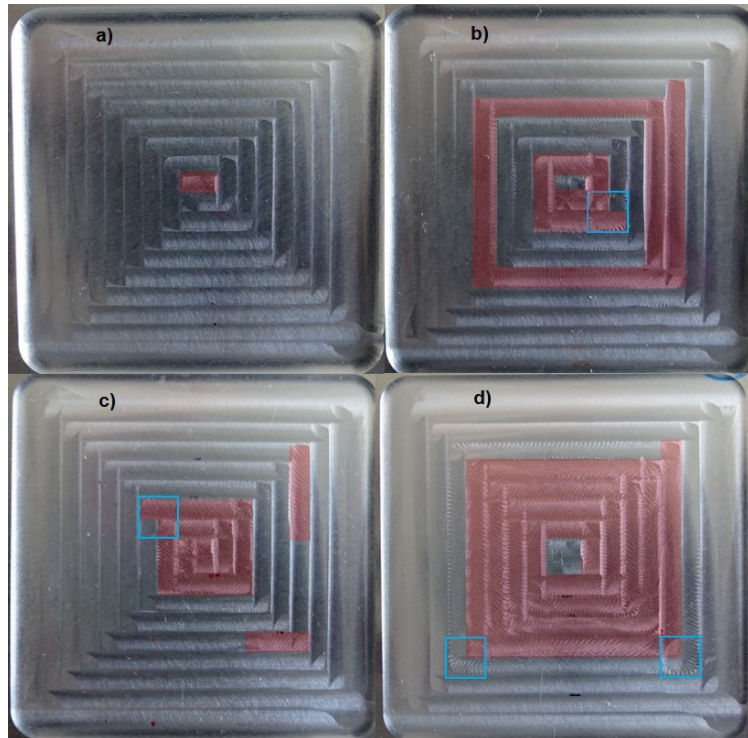


Figure 9. Samples after milling. Chatter marks in red, ploughing marks in blue square. (a) TP10. (b) TP08. (c) TP04. (d) TP02.

The average roughness (R_a) analysis (Figure 10) shows two types of passes clearly delimited. In the passes where chatter happens, the average roughness is higher than $0.9 \mu\text{m}$, whereas in passes without chatter this value is lower than $0.6 \mu\text{m}$. It must be noted that these values correspond to the middle of each cutting pass, where roughness has been measured.

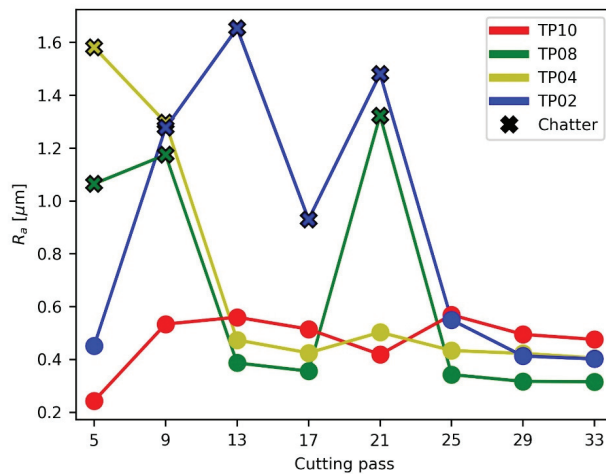


Figure 10. Average roughness per cutting pass.

Additionally, the roughness does not perceptibly change during machining. At most, it decreases very softly. This fact shows that, in absence of chatter, the roughness is affected by the a_p employed, but it is not affected by the change of modal parameters, and it is only very slightly affected by the tool position and the proximity to fixtures. So, it can be concluded that the change of modal parameters affects chatter appearance, as stated in the previous SLD analysis, but once stability is reached surface roughness is constant and depends primarily on the machining parameters. Del Sol et al. [13] consider the idea that this happens due to the influence that machining parameters have on the cutting forces. In any case, given the current experimental setup, this achieved final surface quality is under $0.6 \mu\text{m } R_a$ and thus it meets the industrial tolerances that are typically imposed on thin floors [13,24,34].

These results have also been compared to the available bibliography. Del Sol et al. [16] analyzed very similar kind of samples milled with the same mill, a feed rate of 0.08 mm/tooth and an axial depth of cut of 0.4 mm , although directly threaded to a plating sheet. Consequently, chatter does not appear in them. They exhibit an average roughness value of $0.25 \mu\text{m}$ measured in the direction of the milling. This value is lower than the average roughness value measured in the present case TP04 with a feed rate of 0.1 mm/tooth , which is around $0.4 \mu\text{m}$. In a following experiment of Del Sol et al. [13], also with the same samples directly threaded to a plating sheet, average roughness varies between $0.2 \mu\text{m}$ and $0.4 \mu\text{m}$. However, in this case roughness was not measured only in the direction of the milling, but also in the normal direction.

Rubio-Mateos et al. [14] studied the same type of samples milled with the same mill, clamped to a rubber-based vacuum fixture. Due to this fact, they do not exhibit chatter, and their average roughness value is between 0.4 and $0.6 \mu\text{m}$ for the same cutting conditions.

In another case, Campa et al. [32] milled various blocks of aluminum without back support from 30 mm thickness to 1 mm , employing a bull-nose end mill of 16 mm diameter, a feed of 0.05 mm/tooth , and depths of cut higher than 5 mm , as well as a parallel strategy (instead of helicoidal). The final average roughness was between 0.3 mm and 1.4 mm in absence of chatter. These results are consistent with the ones obtained in the present study, although the milling conditions were significantly different. Campa et al. [11] also conducted another similar experiment, where chatter marks were evident in some sections of the final part, as well as ploughing marks, a phenomenon in which the tool engages and penetrates on the part and that is related to the lack of stiffness. Arnaud et al. [25] consider ploughing as a type of process damping, in which the clearance face of the mill contacts the sample and thus leads to a more stable machining, a fact that can be confirmed in the present cases TP08 and TP04, where ploughing happens just before chatter disappearance.

In the present study, in addition to the lack of stiffness and to damping, it can be noticed in Figure 9 that ploughing is also related to the change of cutting direction. Milling strategies without sudden changes in the cutting direction, as circular ones, should be considered as they may avoid ploughing.

The FFT analysis of the roughness profile of several cutting passes (Figures 11 and 12) leads to two conclusions. On the one hand, the roughness caused by passes without chatter is mainly dominated by the tooth passing frequency (133.33 Hz , namely, 10 impacts/mm), the tool spin frequency (66.67 Hz , namely, 5 impacts/mm) and their harmonics. This phenomenon indicates that some tool runout is present during milling. These results also show that in the absence of chatter, surface roughness depends on the machining conditions. On the other hand, the roughness caused by passes with chatter appearance is higher and more chaotic. It does not appear at chatter frequencies (128 impacts/mm), but at low frequencies, even lower than the tooth passing frequency. It may be related to the previously described influence on the shape of the vibration signal caused by chatter.

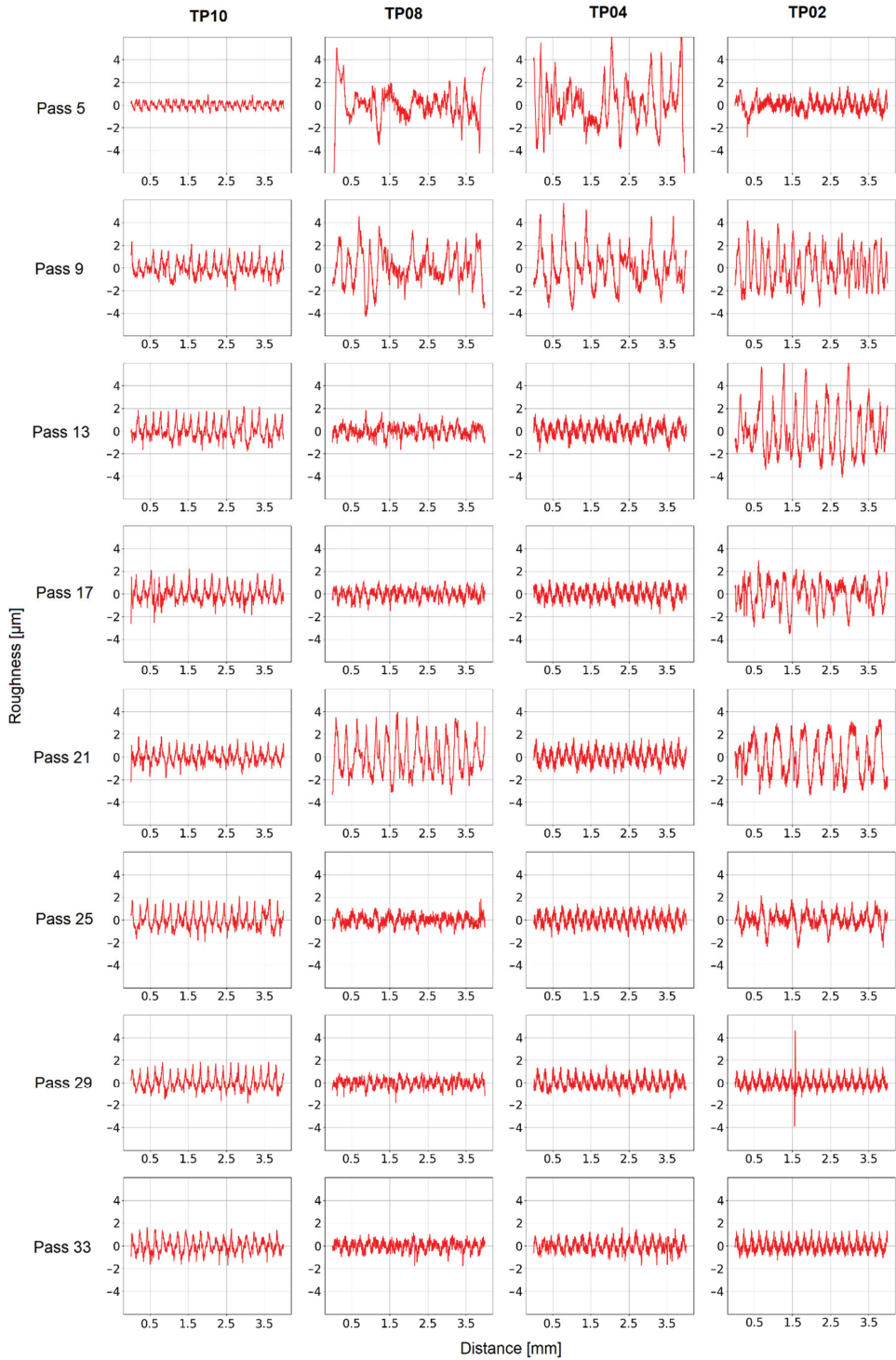


Figure 11. Roughness profile.

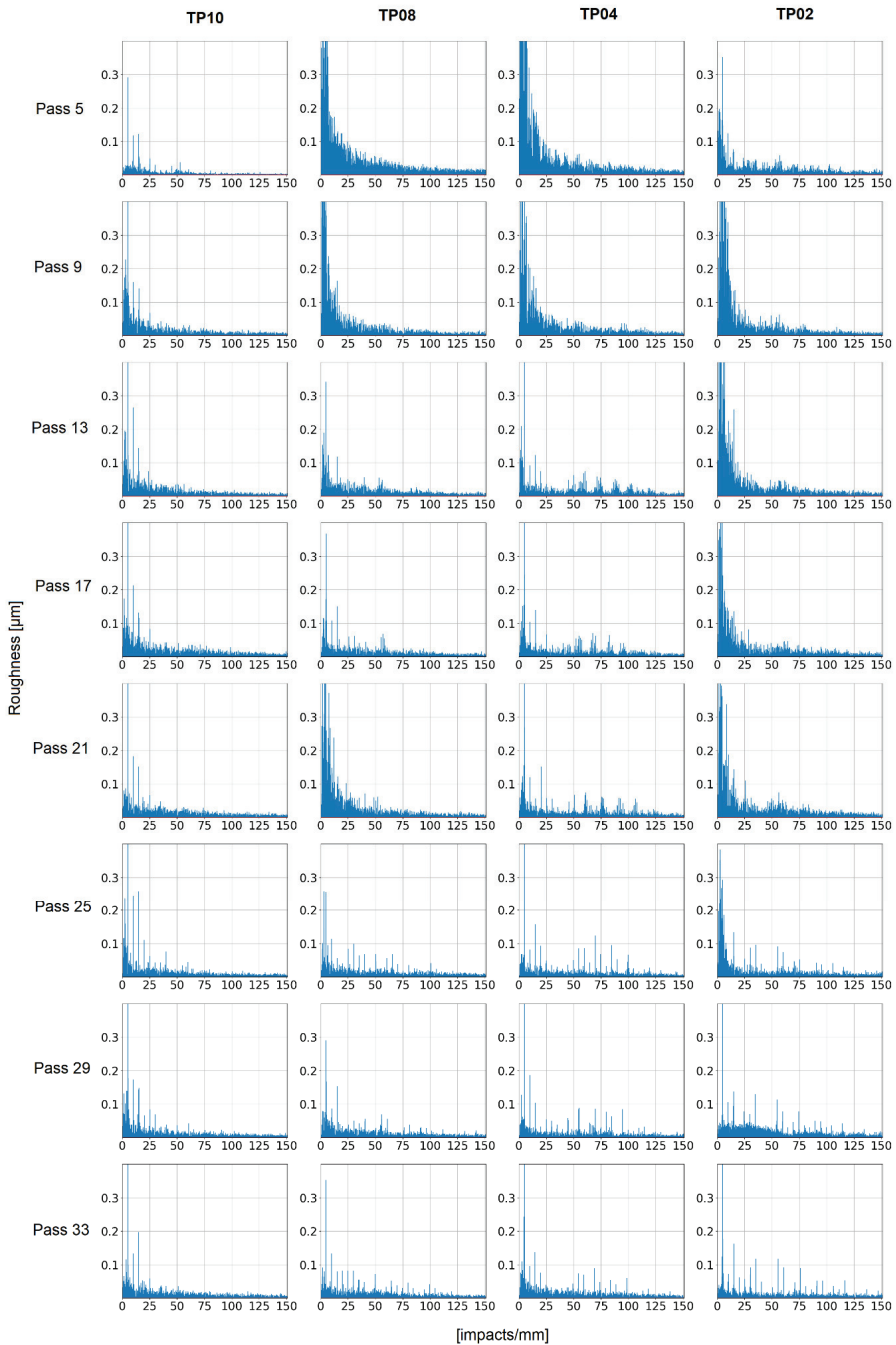


Figure 12. Roughness profile FFT.

Surface roughness is the result of the combination of various factors acting simultaneously, as chatter and deflection, being difficult to discern between them, as López de Lacalle et al. [35] have pointed out. With the purpose of determining the origins of surface roughness, the roughness model proposed has been applied and its results are shown in

Figure 13. In the case of chatter appearance, it causes up to 70% of roughness. In absence of chatter, the floor theoretical component of roughness (R_f) is the smallest one and it varies from 36% in the lowest roughness case (TP08) to 25% in the highest one (TP10). In these cases, the displacement of fixtures and relative movement of thin plates (R_f) cause at least 65% of R_a .

Figure 14 shows the mean and standard deviation values of R_a for each thin plate, as well as their components. Low axial depths of cut lead to a high and variable roughness, whereas higher ones achieve smaller R_a values. As previously stated while analyzing SLDs, this phenomenon happens because high axial depths of cut also entail high lead edge angles in bull-nose end mills, which make chatter appearance more difficult. Regarding R_h , it is inherent to the employed mill and machining conditions, so it is constant in all thin plates, because the applied feed per tooth and mill are the same. The remaining roughness is mainly caused by forced vibrations and the axial displacement of the tool (R_f); namely, it is attributable to the setup employed and the milled samples.

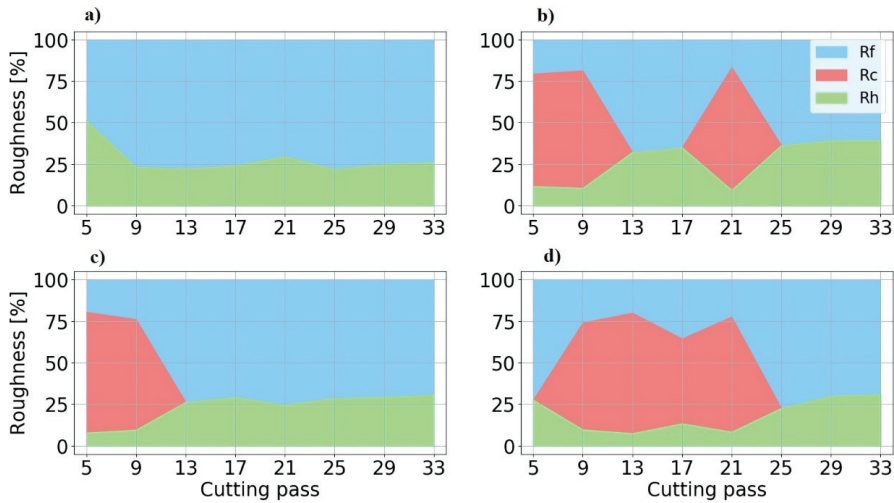


Figure 13. Average roughness components per cutting pass. (a) TP10. (b) TP08. (c) TP04. (d) TP02.

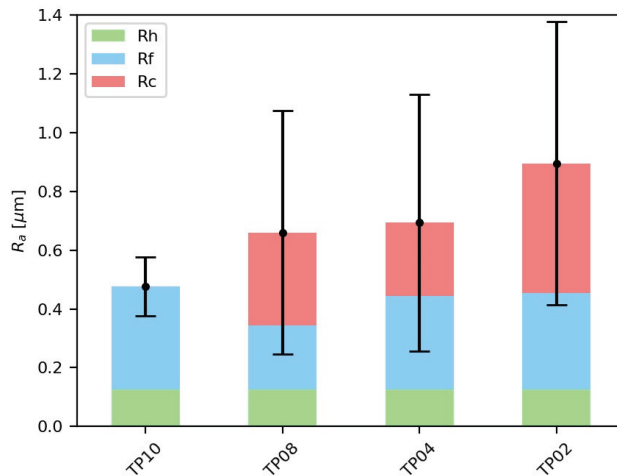


Figure 14. Components of the mean R_a for each thin plate.

4. Conclusions

Chatter vibration and surface roughness resulting from the pocket milling of aluminum alloy thin plates without back support are studied. This situation of low rigidity is common between vacuum cups in flexible fixtures that support thin floors. Aiming to determine the conditions under which a milling in a situation of such a low stiffness could be stable and feasible, vibrations during machining and final surface roughness are measured and analyzed. SLDs are calculated, as well as the FFT of the vibration and the FFT of the surface roughness.

Main results and practical recommendations can be summarized as follows:

- Given the current experimental setup, chatter appearance in thin floors is dominated by the excitation of the first mode of vibration and, at the center of the sample, it is virtually unavoidable, irrespective of the axial depth of cut and spindle speed employed. This fact can be analytically deduced from stability lobes calculation, and it is empirically confirmed in the milling experiments. However, chatter can be avoided by selecting a proper machining zone. Actually, chatter is not a continuous phenomenon, but it appears and disappears along the cutting path due to the interaction of several factors. When an outward helicoidal milling strategy is performed, these factors are as follows: the removal of material, which reduces the rigidity of the samples, the approximation of the tool to the fixtures, which increases it, and the reaching of the tool to modal nodes and antinodes. As a consequence, in the current experimental setup chatter does not appear from cutting pass 25. It means that the proximity of the tool to the fixtures should be considered and incorporated to further chatter prediction models. Also, it means that flexible fixtures could be used for milling thin floors, providing that milling is not conducted in the central area between vacuum cups.
- Chatter is the main cause of poor surface quality for the studied cases, as it causes roughness of at least $0.9\ \mu\text{m}$ in the current setup. In absence of chatter, irrespective of the depth of cut employed, roughness is always below $0.6\ \mu\text{m}$, so it would comply with industry quality requirements. As roughness caused by the displacement of fixtures and relative movement of thin plates is more than 60% of the global roughness, there is still potential for roughness reduction regarding clamping conditions. In those cases, roughness is dominated by the tooth passing frequency, so machining conditions can be employed to handle it.
- Given the current experimental setup, higher axial depths of cut (even 50% of the thickness of the sample) lead to a more stable machining than lower ones. It happens because higher depths of cut also entail higher lead edge angles, which avoid chatter. In addition to a more stable machining, higher depths of cut also lead to a more productive machining and to a surface roughness that complies with industry quality requirements.
- Process damping stabilizes the milling. However, it also entails ploughing effects, which are very harmful to surface quality. It is shown that the ploughing effect is a case of process damping also related to the change of cutting direction. Consequently, milling strategies without sudden changes in cutting direction should be considered as they may avoid ploughing.
- The methodology followed in the present study can be extended and applied to other aeronautic alloys, considering that they could have different surface quality requirements.

Author Contributions: Conceptualization, M.C., A.R.-M. and F.V.; Data curation, M.C. and A.R.-M.; Formal analysis, M.C., A.R.-M. and A.L.; Investigation, M.C., A.R.-M. and A.L.; Methodology, M.C. and A.L.; Project administration, A.R.-M. and A.L.; Supervision, A.L.; Validation, F.V. and A.R.-M.; Writing—original draft, M.C. and F.V.; Writing—review and editing, M.C., F.V., A.R.-M. and A.L. All authors have read and agreed to the published version of the manuscript.

Funding: This research has received funding from the ELKARTEK program of the Basque Government within the project OPTICED, grant number KK-2021/00003.

Institutional Review Board Statement: Not applicable.

Informed Consent Statement: Not applicable.

Data Availability Statement: Data available on request from the corresponding author.

Conflicts of Interest: The authors declare no conflict of interest.

References

- Casuso, M.; Polvorosa, R.; Veiga, F.; Suárez, A.; Lamikiz, A. Residual stress and distortion modeling on aeronautical aluminum alloy parts for machining sequence optimization. *Int. J. Adv. Manuf. Technol.* **2020**, *110*, 1219–1232. [[CrossRef](#)]
- Fei, J.; Xu, F.; Lin, B.; Huang, T. State of the art in milling process of the flexible workpiece. *Int. J. Adv. Manuf. Technol.* **2020**, *109*, 1695–1725. [[CrossRef](#)]
- Kolluru, K.; Axinte, D. Novel ancillary device for minimising machining vibrations in thin wall assemblies. *Int. J. Mach. Tools Manuf.* **2014**, *85*, 79–86. [[CrossRef](#)]
- Del Sol, I.; Rivero, A.; López de Lacalle, L.N.; Gamez, A.J. Thin-wall machining of light alloys: A review of models and industrial approaches. *Materials* **2019**, *12*, 2012. [[CrossRef](#)] [[PubMed](#)]
- Bao, Y.; Dong, Z.G.; Kang, R.K.; Li, Z.; Yuan, Y.C. Milling force and machining deformation in mirror milling of aircraft skin. *Adv. Mater. Res.* **2016**, *1136*, 149–155. [[CrossRef](#)]
- Bao, Y.; Kang, R.; Dong, Z.G.; Zhu, X.; Wang, C.; Guo, D. Model for surface topography prediction in mirror-milling of aircraft skin parts. *Int. J. Adv. Manuf. Technol.* **2018**, *95*, 2259–2268. [[CrossRef](#)]
- Herranz, S.; Campa, F.J.; López De Lacalle, L.N.; Rivero, A.; Lamikiz, A.; Ukar, E.; Sánchez, J.A.; Bravo, U. The milling of airframe components with low rigidity: A general approach to avoid static and dynamic problems. *Proc. Inst. Mech. Eng. Part B J. Eng. Manuf.* **2005**, *219*, 789–801. [[CrossRef](#)]
- Zhang, Z.; Li, H.; Liu, X.; Zhang, W.; Meng, G. Chatter mitigation for the milling of thin-walled workpiece. *Int. J. Mech. Sci.* **2018**, *138–139*, 262–271. [[CrossRef](#)]
- Zhou, Y.; Li, Y.; Wang, W. A feature-based fixture design methodology for the manufacturing of aircraft structural parts. *Robot. Comput. Integr. Manuf.* **2011**, *27*, 986–993. [[CrossRef](#)]
- Rubio, A.; Calleja, L.; Orive, J.; Mújica, A.; Rivero, A. Flexible Machining System for an Efficient Skin Machining. SAE Technical Paper. 2016, pp. 1–12. Available online: <https://www.sae.org/publications/technical-papers/content/2016-01-2129/> (accessed on 13 December 2021).
- Campa, F.J.; López De Lacalle, L.N.; Celaya, A. Chatter avoidance in the milling of thin floors with bull-nose end mills: Model and stability diagrams. *Int. J. Mach. Tools Manuf.* **2011**, *51*, 43–53. [[CrossRef](#)]
- Bravo, U.; Altuzarra, O.; López De Lacalle, L.N.; Sánchez, J.A.; Campa, F.J. Stability limits of milling considering the flexibility of the workpiece and the machine. *Int. J. Mach. Tools Manuf.* **2005**, *45*, 1669–1680. [[CrossRef](#)]
- Del Sol, I.; Rivero, A.; Gamez, A.J. Effects of machining parameters on the quality in machining of aluminium alloys thin plates. *Metals* **2019**, *9*, 927. [[CrossRef](#)]
- Rubio-Mateos, A.; Casuso, M.; Rivero, A.; Ukar, E.; Lamikiz, A. Vibrations characterization in milling of low stiffness parts with a rubber-based vacuum fixture. *Chin. J. Aeronaut.* **2020**, *34*, 54–66. [[CrossRef](#)]
- Kolluru, K.; Axinte, D. Coupled interaction of dynamic responses of tool and workpiece in thin wall milling. *J. Mater. Process. Technol.* **2013**, *213*, 1565–1574. [[CrossRef](#)]
- Del Sol, I.; Rivero, A.; Salguero, J.; Fernández-Vidal, S.R.; Marcos, M. Tool-path effect on the geometric deviations in the machining of UNS A92024 aeronautic skins. *Procedia Manuf.* **2017**, *13*, 639–646. [[CrossRef](#)]
- Kuczmaszewski, J.; Łogin, W.; Pieško, P.; Zawada-Michałowska, M. Influence of machining strategies and technological history of semi-finished product on the deformation of thin-wall elements after milling. *Adv. Sci. Technol. Res. J.* **2017**, *11*, 289–296.
- Kuczmaszewski, J.; Pieško, P.; Zawada-Michałowska, M. Surface roughness of thin-walled components made of aluminium alloy en aw-2024 following different milling strategies. *Adv. Sci. Technol. Res. J.* **2016**, *10*, 150–158. [[CrossRef](#)]
- Wu, G.; Li, G.; Pan, W.; Raja, I.; Wang, X.; Ding, S. A state-of-art review on chatter and geometric errors in thin-wall machining processes. *J. Manuf. Processes* **2021**, *68*, 454–480. [[CrossRef](#)]
- Yue, C.; Gao, H.; Liu, X.; Liang, S.Y.; Wang, L. A review of chatter vibration research in milling. *Chin. J. Aeronaut.* **2019**, *32*, 215–242. [[CrossRef](#)]
- Dang, X.B.; Mi, W.; Yang, Y.; Zhang, W.H. Efficient prediction of varying dynamic characteristics in thin-wall milling using freedom and mode reduction methods. *Int. J. Mech. Sci.* **2019**, *150*, 202–216. [[CrossRef](#)]
- Song, Q.; Liu, Z.; Wan, Y.; Ju, G.; Shi, J. Application of Sherman–Morrison–Woodbury formulas in instantaneous dynamic of peripheral milling for thin-walled component. *Int. J. Mech. Sci.* **2015**, *96–97*, 79–90. [[CrossRef](#)]
- Qu, S.; Zhao, J.; Wang, T. Three-dimensional stability prediction and chatter analysis in milling of thin-walled plate. *Int. J. Adv. Manuf. Technol.* **2016**, *86*, 2291–2300. [[CrossRef](#)]
- Seguy, S.; Campa, F.J.; López de Lacalle, L.N.; Arnaud, L.; Dessen, G.; Aramendi, G. Toolpath dependent stability lobes for the milling of thin-walled parts. *Int. J. Mach. Mach. Mater.* **2008**, *4*, 377–392. [[CrossRef](#)]

25. Arnaud, L.; Gonzalo, O.; Seguy, S.; Jauregi, H.; Peigné, G. Simulation of low rigidity part machining applied to thin-walled structures. *Int. J. Adv. Manuf. Technol.* **2011**, *54*, 479–488. [[CrossRef](#)]
26. Altintas, Y. Analytical prediction of three-dimensional chatter stability in milling. *JSME Int. J. Ser. C Mech. Syst. Mach. Elem. Manuf.* **2001**, *44*, 717–723. [[CrossRef](#)]
27. Campa, F.J.; López de Lacalle, L.N.; Lamikiz, A.; Sánchez, J.A. Selection of cutting conditions for a stable milling of flexible parts with bull-nose end mills. *J. Mater. Process. Technol.* **2007**, *191*, 279–282. [[CrossRef](#)]
28. Lee, P.; Altintas, Y. Prediction of ball-end milling forces from orthogonal cutting data. *Int. J. Mach. Tools Manuf.* **1996**, *36*, 1059–1072. [[CrossRef](#)]
29. Gradišek, J.; Kalveram, M.; Weinert, K. Mechanistic identification of specific force coefficients for a general end mill. *Int. J. Mach. Tools Manuf.* **2004**, *44*, 401–414. [[CrossRef](#)]
30. Rubio-Mateos, A.; Rivero, A.; Ukar, E.; Lamikiz, A. Influence of elastomer layers in the quality of aluminum parts on finishing operations. *Metals* **2020**, *10*, 289. [[CrossRef](#)]
31. Thevenot, V.; Arnaud, L.; Dessein, G.; Cazenave-Larroche, G. Influence of material removal on the dynamic behavior of thin-walled structures in peripheral milling. *Mach. Sci. Technol.* **2006**, *10*, 275–287. [[CrossRef](#)]
32. Campa, F.J.; López De Lacalle, L.N.; Urbicain, G.; Lamikiz, A.; Seguy, S.; Arnaud, L. Critical thickness and dynamic stiffness for chatter avoidance in thin floors milling. *Adv. Mat. Res.* **2011**, *188*, 116–121. [[CrossRef](#)]
33. Seguy, S.; Dessein, G.; Arnaud, L. Surface roughness variation of thin wall milling, related to modal interactions. *Int. J. Mach. Tools Manuf.* **2008**, *48*, 261–274. [[CrossRef](#)]
34. Meshreki, M.; Kovacs, J.; Attia, H.; Tounsi, N. Dynamics modeling and analysis of thin-walled aerospace structures for fixture design in multi-axis milling. *J. Manuf. Sci. Eng.* **2008**, *130*, 31011–31012. [[CrossRef](#)]
35. López De Lacalle, L.N.; Lamikiz, A.; Sánchez, J.A.; Fernández De Bustos, I. Recording of real cutting forces along the milling of complex parts. *Mechatronics* **2006**, *16*, 21–32. [[CrossRef](#)]

Article

Investigation of Surface Integrity Induced by Various Finishing Processes of AISI 52100 Bearing Rings

Nabil Jouini ^{1,2,*}, Philippe Revel ³ and Guillaume Thoquenne ⁴

- ¹ Mechanical Engineering Department, College of Engineering, Prince Sattam Bin Abdulaziz University, Alkharj 16273, Saudi Arabia
 - ² Laboratoire de Mécanique, Matériaux et Procédés (LR99ES05), École Nationale Supérieure d'Ingénieurs de Tunis, Université de Tunis, Tunis 1008, Tunisia
 - ³ Laboratoire Roberval de Mécanique FRE UTC-CNRS 2012, Université de Technologie de Compiègne, 60203 Compiègne, France; philippe.revel@utc.fr
 - ⁴ Centre Technique des Industries Mécaniques (CETIM), 52 Avenue Félix Louat, 60300 Senlis, France; Guillaume.Thoquenne@cetim.fr
- * Correspondence: n.jouini@psau.edu.sa

Abstract: Surface integrity induced by finishing processes significantly affects the functional performance of machined components. In this work, three kinds of finishing processes, i.e., precision hard turning, conventional grinding, and sequential grinding and honing, were used for the finish machining of AISI 52100 bearing steel rings. The surface integrity induced by these finishing processes was studied via SEM investigations and residual stress measurements. To investigate rolling contact fatigue performance, contact fatigue tests were performed on a twin-disc testing machine. As the main results, the SEM observations show that precision hard turning and grinding introduce microstructural alterations. Indeed, in precision hard turning, a fine white layer (<1 µm) is observed on the top surface, followed by a thermally affected zone in the subsurface, and in grinding only, a white layer with 5 µm thickness is observed. However, no microstructural changes are found after sequential grinding and honing processes. White layers induced by precision hard turning and grinding possess compressive residual stresses. Grinding and sequential grinding and honing processes generate similar residual stress distributions, which are maximum and compressive at the machined surface and tensile at the subsurface depth of 15 µm. Precision hard turning generates a “hook”-shaped residual stress profile with maximum compressive value at the subsurface depth and thus contributes as a prenominal factor to the obtainment of the longest fatigue life with respect to other finishing processes. Due to the high quality of surface roughness ($R_a = 0.05 \mu\text{m}$), honing post grinding improves the fatigue life of bearing rings by 2.6 times in comparison with grinding. Subsurface compressive residual stresses, as well as low surface roughness, are key parameters for extending bearing fatigue life.

Keywords: finishing processes; surface integrity; bearing steel; residual stresses; rolling contact fatigue

Citation: Jouini, N.; Revel, P.; Thoquenne, G. Investigation of Surface Integrity Induced by Various Finishing Processes of AISI 52100 Bearing Rings. *Materials* **2022**, *15*, 3710. <https://doi.org/10.3390/ma15103710>

Academic Editors: J. Antonio Travieso-Rodriguez and Gilles Dessein

Received: 6 April 2022
Accepted: 20 May 2022
Published: 22 May 2022

Publisher's Note: MDPI stays neutral with regard to jurisdictional claims in published maps and institutional affiliations.



Copyright: © 2022 by the authors. Licensee MDPI, Basel, Switzerland. This article is an open access article distributed under the terms and conditions of the Creative Commons Attribution (CC BY) license (<https://creativecommons.org/licenses/by/4.0/>).

1. Introduction

In the field of bearing manufacturing, the finishing process chain of the bearing ring consists of grinding and raceway honing. Honing is applied post grinding to achieve the necessary surface characteristics. Hard turning is emerging as a competitive finishing process, offering potential benefits over the grinding process such as cost-effectiveness, manufacture of complex shapes, dry machining, and high flexibility [1,2]. The surface integrity induced by finishing processes significantly affects the functional performance (e.g., friction, corrosion, and fatigue) of machined components [3,4]. In order to improve the fatigue life of bearing rings, innovative hard machining processes have been developed. Hashimoto et al. [5] provide guidelines for the selection of fine finishing processes in order to obtain the desired performance of functions such as fatigue life. Maiß et al. [6] used a

new hybrid process of hard turn-rolling to manufacture a bearing inner ring. As a result, the bearing fatigue life could be increased by a factor of 2.5. Revel et al. [7] proposed precision hard turning for the finishing of bearing steel components to improve the rolling fatigue life of bearing steel components. Arsalani et al. [8] used sequential hard turning, grinding, and ball-burnishing operations. They showed an improvement in the endurance limit with burnished pre-turned and burnished pre-ground samples compared to turned samples.

Rolling contact fatigue (RCF) has been commonly known as a key factor limiting bearing life [9]. Subsurface-originated spalling is recognized as one of the dominant mechanisms of failure in rolling element bearings [10]. Subsurface cracks are more likely to be initiated in the region of maximum shear stress under rolling contact below the surface and propagate toward the surface to form a surface spall [10,11].

Surface integrity is of particular importance when machining high-performance metals used for high-performance components in industries such as aerospace, biomedical, and automotive [3,12]. Surface integrity is characterized in terms of surface topography, as well as mechanical and metallurgical states of surface and subsurface layers.

Both hard turning and grinding processes introduce microstructural alterations in the surface layer known as white and dark layers [13–15]. These layers are visible under optical microscopy after being polished and etched or featureless under scanning electron microscopy (SEM). The white layer microstructure consists of nanocrystalline grains with grain size smaller than 100 nm [16,17] and is harder than the bulk material. The dark layer, which is located beneath the white layer, is generally softer than the bulk material. Two mechanisms, i.e., thermal and mechanical effects, are considered to be the major causes of white layer formation. Hosseini and Klement [18] investigated the characteristics and the formation of white and dark layers induced by hard turning. They showed that two different types of white layers exist: those that are either predominantly thermally or mechanically induced. Zhang et al. [19] showed that the white layer was formed by rapid austenite transformation and quenching process, and the dark layer was formed by the tempering process. Mao et al. [15] investigated the formation mechanisms and properties of the affected layer formed in grinding. They found that white layers may be generated when the grinding temperature is below the nominal phase transformation temperature. There are controversial opinions in the literature regarding how the white layer may impact the fatigue life of bearing steels. Guo et al. [20] showed that the machining-induced white layer can reduce the fatigue life of AISI 52100 steel by as much as 8 times. Opposite conclusions were achieved by Smith et al. [21], who carried out fatigue tests on AISI 52100 hardened bearing steel and concluded that there was no conclusive evidence suggesting that hard turning with a continuous white layer had a negative impact on axial fatigue performance.

Residual stresses can be either beneficial or detrimental for the components subjected to rolling contact fatigue life, depending upon their nature (compressive or tensile) and distribution at the subsurface depth. Shen et al. [22] used a three-ball-on-rod RCF test to experimentally assess the effects of retained austenite and residual stresses on the RCF of carburized AISI 8620 steel. Their results showed that the presence of compressive residual stresses is beneficial and increases RCF life. Matsumoto et al. [23] compared the fatigue life of ground and hard-turned bearing assembly. They found that the depth of compressive residual stresses is the major difference between hard-turned and ground surfaces. Indeed, hard turning produces compressive residual stresses in a deep subsurface, which improves the fatigue life of rolling bearings. Wang et al. [24] investigated the grinding mechanism of a bearing ring raceway and performed integrated modeling to control stress grinding. They showed that grinding can produce compressive residual stresses in the surface layer of the bearing ring raceway. Pape et al. [25] investigated the effect of residual stresses induced through production processes. They showed that the bearing fatigue life is improved due to the induced residual stresses on the bearing's inner ring by sequential hard turning and deep rolling processes.

Rolling contact fatigue has been commonly known as a key factor limiting bearing life. Thus, it is necessary to improve the fatigue life of bearings by controlling the surface

integrity of bearing raceways. In this respect, this paper investigates the surface integrity of AISI 52100 bearing rings finished by three kinds of finishing processes, i.e., precision hard turning, conventional grinding, and sequential grinding and honing, as well as the functional performance of the finished bearing rings. As shown in Figure 1, the surface integrity induced by these finishing processes was investigated via scanning electron microscopy investigations and in-depth residual stress measurements. Furthermore, contact fatigue tests were carried out on a twin-disc testing machine under two loading levels.

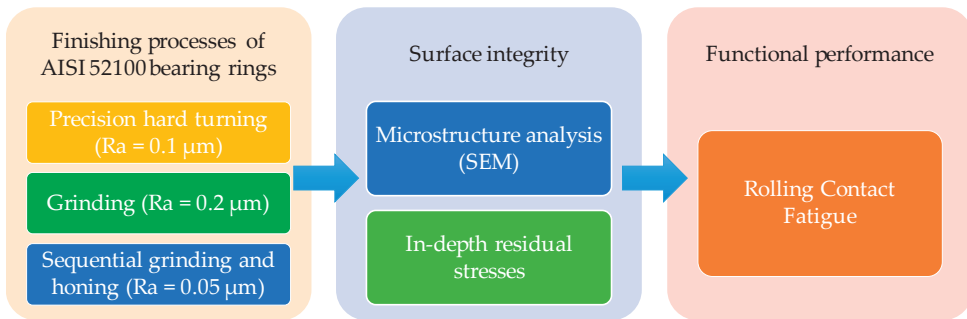


Figure 1. Workflow of the present study.

2. Materials and Methods

In this experimental work, the workpiece material was an AISI 52100 bearing steel (EN 100Cr6) ring. This steel material is widely used for the manufacture of bearing rings. The rings were heat-treated in order to obtain the desired hardness of 61 ± 1 HRC. AISI 52100 bearing steel material has a phase composition consisting of martensitic structure (95.3%), carbides (4.6%), and neglected retained austenite (<1%). The material properties of this steel are given in Table 1.

Table 1. Material properties of AISI 52100.

Parameter	Value
Chemical composition (wt%)	1.040% C; 0.32% Si; 0.34% Mn; 0.04% Ni; 1.52% Cr; 0.007% Mo.
Young's modulus E (GPa)	210
Poisson ratio	0.3
Hardness (HRC)	61 ± 1

Surface integrity induced by three kinds of finishing processes was studied via SEM investigations and residual stress measurements. Hard turning tests were conducted on a high-precision machine, a prototype lathe positioned in an air-conditioned room, and developed for machining polish-mirror surfaces and hard steel [7,26]. The cubic boron nitride (cBN) inserts and the machining process parameters used for the hard turning experiments have been precisely detailed elsewhere [7]. As the preconized surface roughness target from the bearing manufacturer, the bearing rings were finished by the Mcrorectif company, Saint-Étienne, France to a preferable target roughness average Ra of approximately $0.2 \mu\text{m}$ for grinding and $0.05 \mu\text{m}$ for sequential grinding and honing. The process parameters and roughness are controlled parameters. The roughness average (Ra) defined by ISO 4287 was measured using a scanning white-light interferometer Zygo™ NewView 200 (Zygo Corporation, Middlefield, CT, USA). As can be seen, by applying honing after grinding, the surface roughness becomes smooth. The surface roughness of the precision hard-turned specimen was investigated in previous studies [27,28]. Indeed, a very low surface roughness value $Ra = 0.1 \mu\text{m}$ is obtained in precision hard turning. Sequential grinding and

honing processes allow us to achieve very low surface roughness $R_a \approx 0.05$ with respect to precision hard turning.

The specimens were prepared following standard metallographic techniques, as shown in Figure 2. Preliminary specimens were cut using an abrasive cutter and the Struers Discotom 5 machine (Struers, Ballerup, Denmark). The sectioned specimens were then hot mounted in Struers PolyFast conductive resin. Mounted specimens were then ground using 180-grit paper, followed by 320-, 600-, 800-, and 1200-grit papers in a Struers TegraPol-31 system and polished with diamonds. The polished surfaces were cleaned using an ultrasonic bath and then etched with 2% Nital solution for approximately 10 s. Microstructural investigations were carried out using the environmental scanning electron microscope XL30 ESEM-FEG (Philips Electron Optics, Eindhoven, The Netherlands) equipped with an energy-dispersive X-ray (EDX) analyzer.

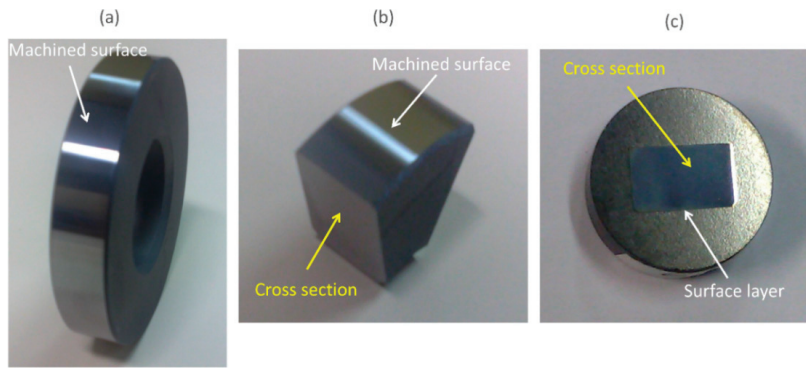


Figure 2. (a) Bearing ring finished by precision hard turning; (b) sectioned specimen; (c) mounted, polished, and etched specimen.

The bearing rings were investigated regarding in-depth residual stresses. These residual stresses were measured by the X-ray diffraction method using a PRECIX robotic system (Figure 3a). The measurements were performed using $\text{Cr-K}\alpha$ radiation diffracted at $2\theta = 156^\circ$ in the atomic plan $\{2\ 1\ 1\}$ of the steel. Thus, these conditions give access to the strain localized at a depth of approximately $6\ \mu\text{m}$ according to EN-15305 [29]. As shown in Figure 3b, the residual stresses were measured along the circumferential direction (σ_c) and tangential direction (σ_t). Both machined surface and in-depth residual stresses were measured. In the case of in-depth residual stresses, successive layers of material were removed by using chemical etching and electropolishing to avoid the reintroduction of residual stress. To evaluate residual stresses during the RCF test, the measurements were carried out on the bearing raceway, as shown in Figure 3c, thanks to a lead mask, which adapts the spot size of the X-ray beam with the raceway width.

The rolling contact fatigue tests were performed on a twin-disc testing machine (Figure 4) available at CETIM Senlis, France. The contact is made between two discs, one being cylindrical and the other one being crowned with a crown radius of 17.5 mm, as shown in Figure 5. The two contacting discs have the same external radius of 35 mm and width of 14 mm. Tests were carried out under pure rolling conditions (slide-to-roll ratio = 0%), entrainment speed of 11 m/s, and lubricated with MobilGear 629oil injection. The applied normal load is 1100 daN, which is equivalent to the Hertzian contact pressure of 4.5 GPa. For each finished ring, two tests were performed under the same conditions. The twin-disc testing machine is equipped with sensors at the proximity of each disc to detect spalling occurrence. Thus, the test is stopped until spalling forms or when reaching 10 million cycles.

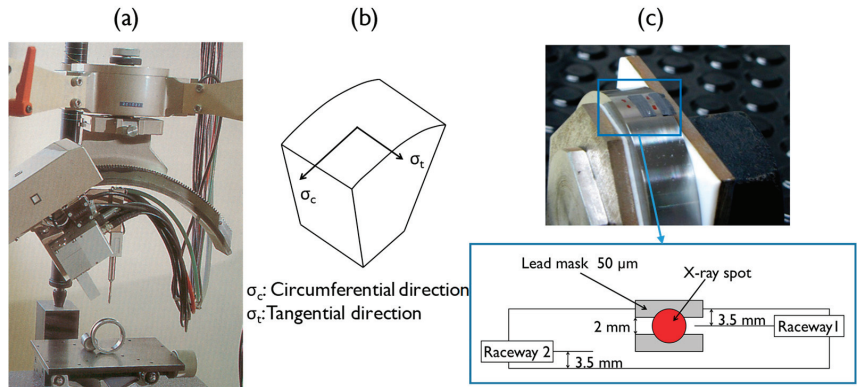


Figure 3. (a) Setup for the residual stress measurements; (b) residual stress measurement directions; (c) limiting device of X-ray beam with the raceway width.

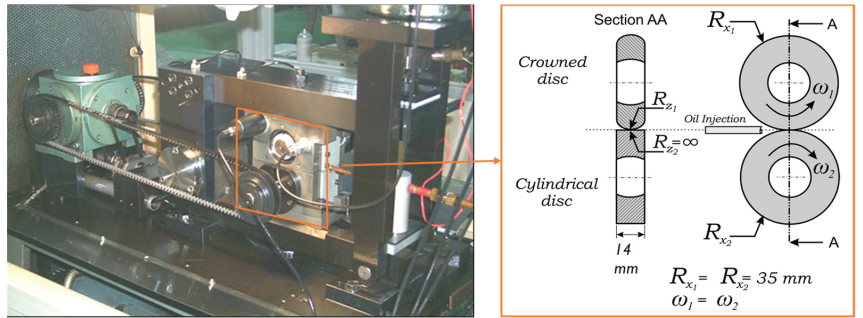


Figure 4. Twin-disc test machine and schematic representation of the geometry of ring specimens.

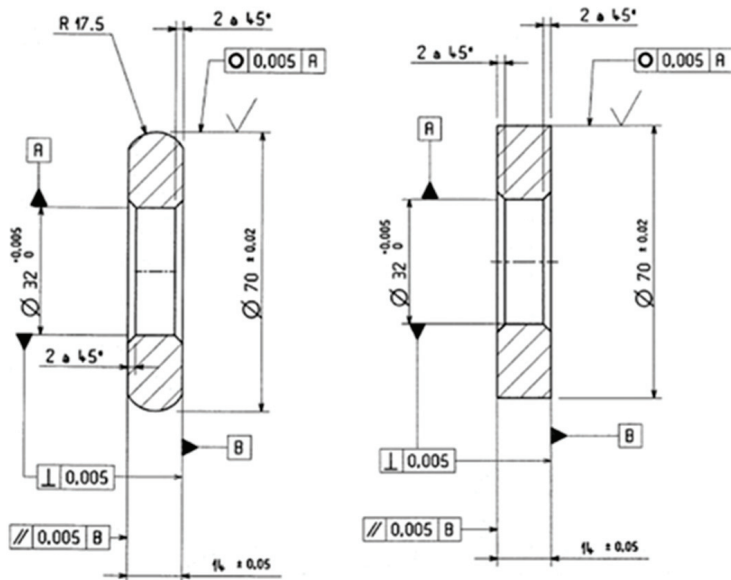


Figure 5. Drawing of ring specimens.

3. Results and Discussion

3.1. Microstructure Analysis

In order to highlight the metallurgical transformations, micrographic analyses were carried out on the cross-sectional samples of the three finishing processes under investigation. SEM observations show that precision hard turning and grinding introduce microstructural changes in the subsurface (Figure 6). Indeed, as shown in Figure 6a, after precision hard turning, a very thin white layer (<1 μm thickness) appears on the top surface, followed by a transition zone in the subsurface and then the bulk material. This very thin white layer can be attributed to the use of a new cutting tool for each machining test. Indeed, tool wear noticeably affects the white and dark layer thicknesses; a worn tool would generate a deep white layer [30,31]. This very thin white layer can also be beneficial for rolling contact fatigue performance. Schwach and Guo [32] showed that the white layer induced by hard turning is very detrimental to RCF life. Indeed, a component free of a white layer can have a life six times that of a white layer component. The transition zone was examined using energy-dispersive spectroscopy (EDS) to investigate the chemical composition and to determine the distribution of elements. The precipitated carbides are distributed spherical $(\text{Fe,Cr})_3\text{C}$ carbides covering the transition zone. These carbides are observed in the white layer and the transition zone, but their number and size are not the same in different regions. Indeed, the carbides spread in the transition zone are more numerous. After grinding, as shown in Figure 6b, only a white layer with 5 μm thickness is observed above the bulk material, which is greater than that found after precision hard turning. Guo and Sahni [33] found that the thickness of the white layer induced by grinding is greater than those obtained by hard turning. In their micrographic analyzes, Barbacki et al. [34] showed that the white layer thickness varies from 0 to 2 μm , and the dark layer thickness varies from 0 to 5 μm in 17 samples machined by grinding. The absence of the dark layer under the white layer supports that the white layer formation is mainly due to mechanical work. Hosseini et al. [35] reported that the predominantly mechanically formed white layer is accompanied by compressive residual stresses. After sequential grinding and honing processes, as shown in Figure 6c, no microstructural changes are observed. Indeed, the honing process removes the white layer induced by the grinding process.

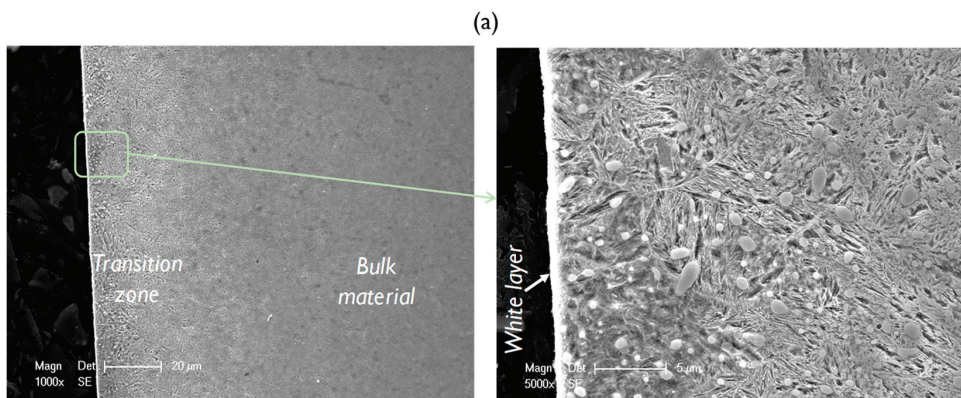


Figure 6. Cont.

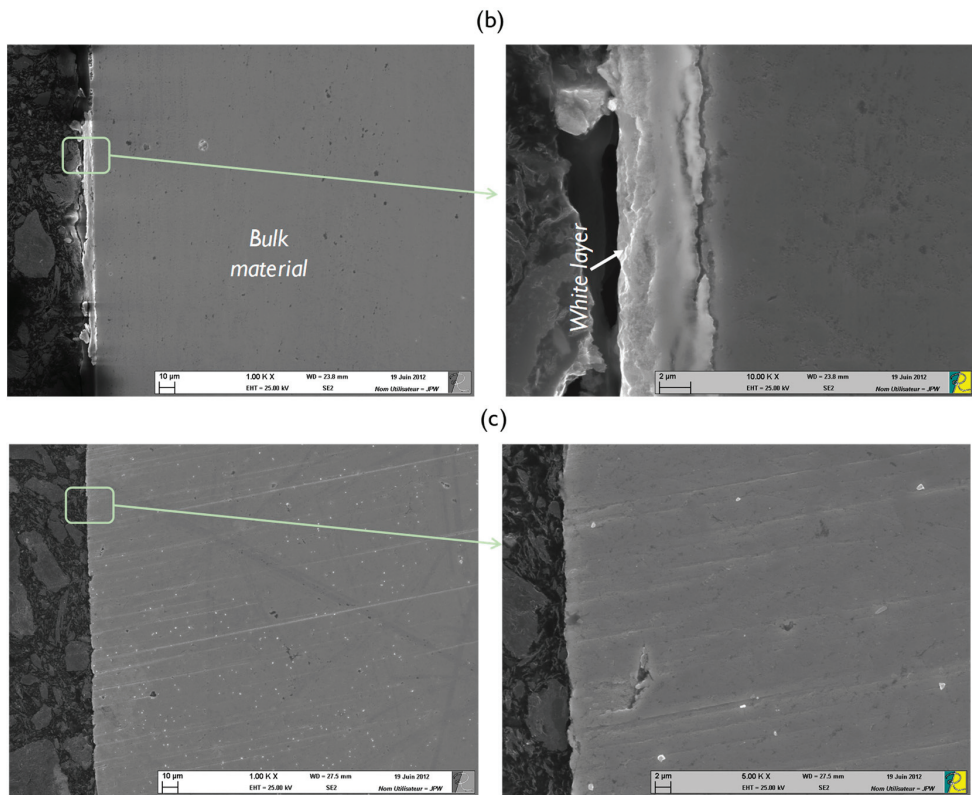


Figure 6. Micrographs of AISI 52100 steel after (a) precision hard turning, (b) grinding, and (c) sequential grinding and honing.

3.2. Residual Stresses

Figures 7 and 8 illustrate the in-depth residual stresses in the circumferential and tangential directions induced by each finishing process. In the circumferential direction, residual stresses induced by grinding and by sequential grinding and honing have similar trends; they start out compressive at the machined surface (-186 and -290 MPa, respectively) and become tensile at the subsurface depth. Then, they are stabilized at around 50 MPa. The affected depth of residual stress is around approximately 15 μm . Mao et al. [15] showed that phase transformation in the white layer formed by grinding plays an essential role in the build-up of tensile residual stresses. This implies that the predominant factor is deformation, which leads to compressive stresses. As shown in the investigations of Pape et al. [36], residual stresses for ground and honed bearings are compressively closely adjacent to the surface (-500 MPa) and eliminated at a depth of about 20 μm . However, residual stresses induced by precision hard turning show significant differences from those induced by grinding and by sequential grinding and honing. Indeed, they exhibit a “hook”-shaped profile along the depth with maximum compressive value (-680 MPa) at the subsurface depth of 25 μm . Additionally, the affected depth of residual stress is greater for precision hard turning (around 50 μm). These results are in agreement with those reported by Smith et al. [21], who revealed similar differences in the stress states generated by hard turning and grinding processes. They found that the overall residual stress state is significantly more compressive on the hard-turned surface than on the ground surface. Matsumoto et al. [23] reported that the depth of compressive residual stresses is the major difference between hard-turned and ground surfaces. Considering the difference between the plastic deformation that takes place on the ground surface and that on the hard-turned

surface, it is reasonable to expect that the compressive residual stress generated by hard turning is deeper, which may improve the fatigue life of rolling bearings. Otherwise, the results show that the white layers induced in both hard turning and grinding processes possess compression residual stresses. Hosseini et al. [35] showed that compressive residual stresses and decreased retained austenite content were found in the plastically created white layer. Residual stresses in the tangential direction (Figure 8) display similar trends to those described in the circumferential direction. Both grinding and sequential grinding and honing induce compressive and maximum residual stresses (respectively, -186 and -290 MPa) at the machined surface and become tensile at the subsurface depth. Residual stresses induced by precision hard turning start out compressive (-437 MPa) at the machined surface and exhibit a maximum compressive value of -800 MPa at the subsurface depth of $30\ \mu\text{m}$ before stabilizing at the level. The residual stresses in the tangential direction are more compressive than those in the circumferential direction.

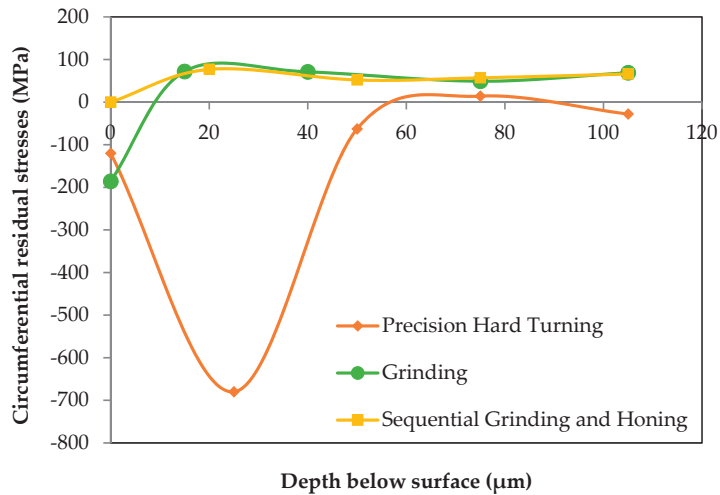


Figure 7. Residual stresses in circumferential direction.

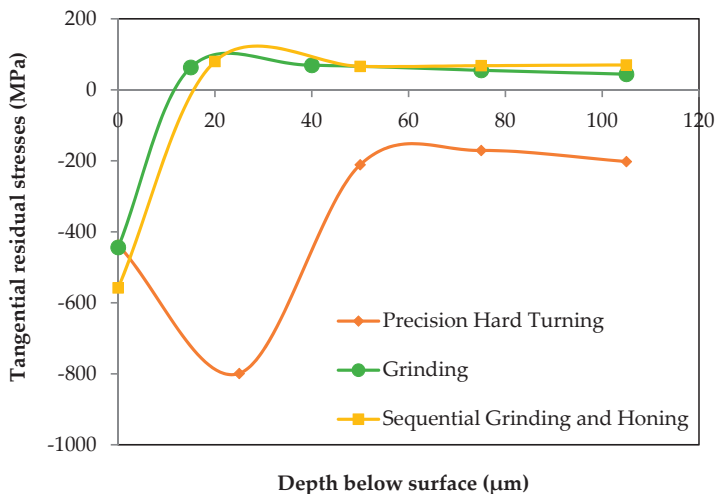


Figure 8. Residual stresses in tangential direction.

3.3. Rolling Contact Fatigue (RCF) Performance

Surface integrity induced by finishing processes significantly affects the functional performance of machined components. To investigate rolling contact fatigue performance, contact fatigue tests were performed on a twin-disc testing machine. Figure 9 presents RCF life per million cycles as a function of the three finishing processes under investigation. For each finished ring, two tests were carried out on each specimen, i.e., each test on one raceway, under the same conditions. The rings finished by precision hard turning have the longest life (5.2 million cycles), while rings finished by grinding ($R_a = 0.2 \mu\text{m}$) have the shortest (1.2 million cycles). The rings finished by sequential grinding and honing ($R_a = 0.05 \mu\text{m}$) reach 3.2 million cycles. This shows that using the honing process after grinding improves the fatigue life of bearing rings by 2.6 times. Grinding and sequential grinding and honing have similar residual stress distributions, maximum and compressive at the machined surface and tensile at the subsurface depth. The enhancement of the lifetime is due to the high quality of surface roughness obtained by the grinding process. Precision hard turning offers better fatigue life due to the low surface roughness, as well as the residual stress state, which is compressive and maximum at the subsurface depth. The residual stress distributions are of considerable importance; several investigations have reported that compressive residual stresses induced by the manufacturing process can extend the fatigue life of bearings up to 2.5 times [20,23,37]. Low surface roughness and subsurface residual stresses are the key parameters for extending bearing fatigue life.

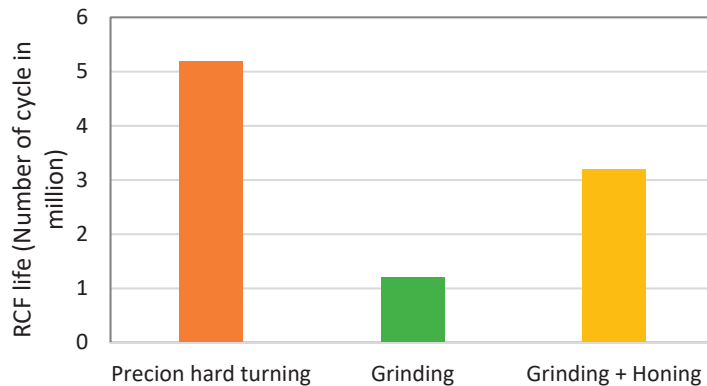


Figure 9. RCF life vs. finishing processes.

Furthermore, it is well known that residual stresses can be developed during the RCF test due to cyclic plasticity [38]. Thus, changes in in-depth residual stresses during the RCF test of ring specimens finished by grinding were investigated due to their shortest fatigue life. The experimental simulation of rolling contact fatigue has two phases: a running-in phase called break-in and a bearing life phase. The running-in phase is estimated at 30,000 cycles under these test conditions [28]. After the running-in phase, the contact geometry is stabilized for the entire lifetime. Table 2 illustrates the Hertzian pressure for 600 and 1100 daN normal loads used in the experimental simulation and the RCF life of the ring finished by grinding. This table shows decreasing Hertzian pressure from 3.8 to 3.6 GPa for 600 daN and from 4.5 to 3.8 GPa for 110 daN. In addition, increasing the normal load decreases RCF life.

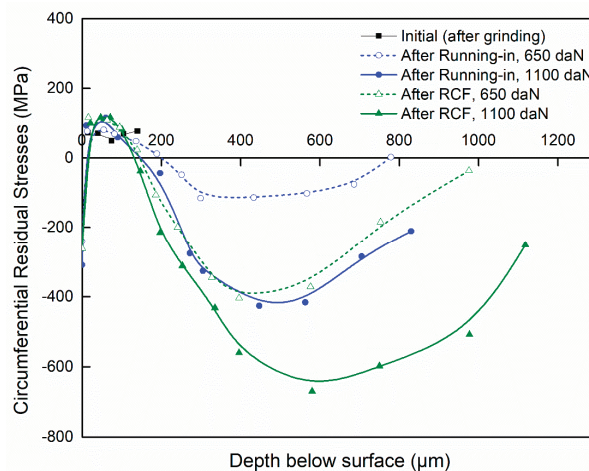
Table 2. Hertzian pressure variations after running-in and RCF life of rings finished by grinding.

	Normal Load (daN)	
	600	1100
Initial Hertzian pressure (GPa)	3.8	4.5
Hertzian pressure after running-in (GPa)	3.6	3.8
RCF life (number of cycles)	2.6×10^6	1.3×10^6

Figures 10 and 11 show the in-depth residual stresses with varying loads (650 and 1100 daN) after grinding (initial), after the running-in phase, and at the end of the RCF test. Before the RCF test, the ring specimen (initial) exhibits compressive residual stresses at the machined surface, originating from the machining operation, and tensile residual stresses at the subsurface depth. During the RCF test, the residual stresses changed from a moderate level of tensile residual stresses to compressive residual stress at the subsurface depth. Pape et al. [36] found a similar evolution, and the residual stresses remained constant after 10^6 to 10^8 revolutions.

Figure 10 shows that during the RCF test, the evolution of circumferential residual stresses in the first 140 μm subsurface depth is not noticeable. At a larger subsurface depth, the residual stresses changed from a moderate level of tensile residual stresses (around 50 MPa for initial) to peak compressive values. Indeed, after running-in with 650 and 1100 daN applied load, the maximum residual stresses are -116 MPa at 299 μm depth and -426 MPa at 427 μm depth, respectively. At the end of the RCF test, the maximum residual stresses are -116 MPa at 299 μm depth and -404 MPa at 396 μm depth. As shown in the investigations of Voskamp [39], the compressive residual stress peaks at a depth ranging from 0.1 to 0.5 mm as the cycles increase. This depth coincides with the maximum shear stress [11,39].

Figure 11 shows that at the shallow depth, ranging from 10 to 140 μm , the tangential residual stresses are tensile and become compressive at the subsurface depth with peak compressive values. Indeed, after running-in with 650 daN and 1100 daN normal load, the maximum residual stresses are -188 MPa at 433 μm depth and -527 MPa at 447 μm depth, respectively. After the end of the RCF test, the maximum residual stresses are -380 MPa at 396 μm depth and -700 MPa at 750 μm depth. As can be seen also that in both directions the peak compressive residual stress increases with increasing the normal load.

**Figure 10.** Circumferential residual stresses after different phases.

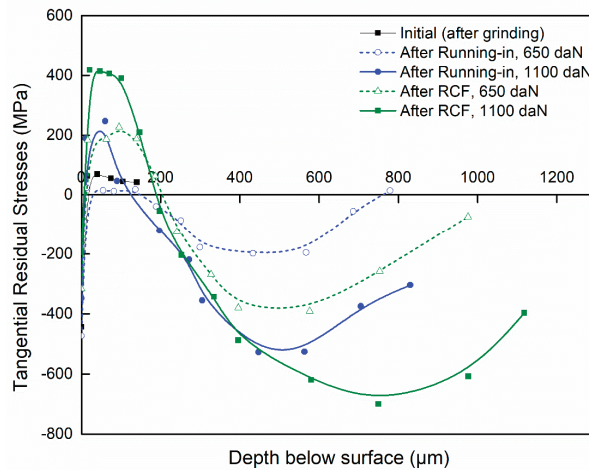


Figure 11. Tangential residual stresses after different phases.

4. Conclusions

In this paper, the surface integrity of bearing rings induced by three finishing processes was investigated, and the following conclusions may be drawn:

- White layers induced by precision hard turning ($<1 \mu\text{m}$) and grinding ($5 \mu\text{m}$) possess compressive residual stresses.
- Subsurface compressive residual stress is the major difference between finishing processes. Grinding and sequential grinding and honing exhibit maximum and compressive residual stresses at the machined surface (-186 and -290 MPa, respectively) and tensile at the subsurface depth of $15 \mu\text{m}$. Precision hard turning exhibits compressive residual stresses at the machined surface and maximum compressive value (-680 MPa) at the subsurface depth of $25 \mu\text{m}$.
- Sequential grinding and honing improve the fatigue life of bearing rings by 2.6 times in comparison with grinding due to the improvement in surface roughness.
- Precision hard turning produces the longest fatigue life (5.2 million cycles) due to subsurface compressive residual stresses.
- The changes in subsurface residual stresses after the running-in process and after the spalling of bearing rings finished by grinding, which has the shortest fatigue life (1.2 million cycles), reveal that subsurface residual stresses are changed from a moderate level of tensile stresses to compressive ones, and such a change can positively affect the fatigue life.
- Subsurface compressive residual stresses originating from the finishing process, as well as low surface roughness, are the key parameters for extending bearing fatigue life.
- The future challenge will be the development of novel technology to enhance the fatigue performance of bearing rings. Thus, the effect of adding a honing operation after precision hard turning will be experimentally studied.

Author Contributions: Conceptualization, N.J. and P.R.; methodology, N.J.; software, N.J. and G.T.; validation, N.J.; formal analysis, N.J.; investigation, N.J.; resources, N.J., P.R. and G.T.; data curation, N.J. and G.T.; writing—original draft preparation, N.J.; writing—review and editing, N.J. and P.R.; visualization, N.J.; supervision, N.J. and P.R.; project administration, N.J. and P.R.; funding acquisition, P.R. and G.T. All authors have read and agreed to the published version of the manuscript.

Funding: This work was supported by the Deanship of Scientific Research, Prince Sattam Bin Abdulaziz University, Saudi Arabia under research project (2020/01/14260).

Institutional Review Board Statement: Not applicable.

Informed Consent Statement: Not applicable.

Data Availability Statement: Data are available on reasonable request.

Acknowledgments: The authors would like to acknowledge the financial and technical support received from Université de Technologie de Compiègne (CETIM) and Prince Sattam Bin Abdulaziz University.

Conflicts of Interest: The authors declare no conflict of interest.

References

1. Klocke, F.; Brinksmeier, E.; Weinert, K. Capability profile of hard cutting and grinding processes. *CIRP Ann.* **2005**, *54*, 22–45. [[CrossRef](#)]
2. Suresh, R.; Basavarajappa, S.; Gaitonde, V.N.; Samuel, G.L.; Davim, J.P. State-of-the-art research in machinability of hardened steels. *Proc. Inst. Mech. Eng. Part B J. Eng. Manuf.* **2013**, *227*, 191–209. [[CrossRef](#)]
3. Liao, Z.; la Monaca, A.; Murray, J.; Speidel, A.; Ushmaev, D.; Clare, A.; Axinte, D.; M'Saoubi, R. Surface integrity in metal machining—Part I: Fundamentals of surface characteristics and formation mechanisms. *Int. J. Mach. Tools Manuf.* **2020**, *162*, 103687. [[CrossRef](#)]
4. Xu, Q.; Liu, Y.; Lu, H.; Liu, J.; Cai, G. Surface integrity and corrosion resistance of 42CrMo4 high-strength steel strengthened by hard turning. *Materials* **2021**, *14*, 6995. [[CrossRef](#)] [[PubMed](#)]
5. Hashimoto, F.; Yamaguchi, H.; Krajncik, P.; Wegener, K.; Chaudhari, R.; Hoffmeister, H.-W.; Kuster, F. Abrasive fine-finishing technology. *CIRP Ann.* **2016**, *65*, 597–620. [[CrossRef](#)]
6. Maiß, O.; Denkena, B.; Grove, T. Hybrid machining of roller bearing inner rings by hard turning and deep rolling. *J. Mater. Process. Technol.* **2016**, *230*, 211–216. [[CrossRef](#)]
7. Revel, P.; Jouini, N.; Thoquenne, G.; Lefebvre, F. High precision hard turning of AISI 52100 bearing steel. *Precis. Eng.* **2016**, *43*, 24–33. [[CrossRef](#)]
8. Arsalani, M.; Razfar, M.R.; Abdullah, A.; Khajehzadeh, M. Fatigue behavior improvement of hardened parts using sequential hard turning, grinding, and ball burnishing operations. *Proc. Inst. Mech. Eng. Part L J. Mater. Des. Appl.* **2020**, *235*, 87–99. [[CrossRef](#)]
9. Kang, J.H.; Hosseinkhani, B.; Rivera-Díaz-del-Castillo, P.E.J. Rolling contact fatigue in bearings: Multiscale overview. *Mater. Sci. Technol.* **2012**, *28*, 44–49. [[CrossRef](#)]
10. Sadeghi, F.; Jalalahmadi, B.; Slack, T.S.; Rajee, N.; Arakere, N.K. A review of rolling contact fatigue. *J. Tribol.* **2009**, *131*, 041403. [[CrossRef](#)]
11. Bhadeshia, H.K.D.H. Steels for bearings. *Prog. Mater. Sci.* **2012**, *57*, 268–435. [[CrossRef](#)]
12. Ammarullah, M.I.; Afif, I.Y.; Maula, M.I.; Winarni, T.I.; Tauviqirrahman, M.; Akbar, I.; Basri, H.; van der Heide, E.; Jamari, J. Tresca stress simulation of metal-on-metal total hip arthroplasty during normal walking activity. *Materials* **2021**, *14*, 7554. [[CrossRef](#)] [[PubMed](#)]
13. Tönshoff, H.K.; Arendt, C.; Amor, R.B. Cutting of hardened steel. *CIRP Ann. Manuf. Technol.* **2000**, *49*, 547–566. [[CrossRef](#)]
14. Akcan, S.; Shah, W.S.; Moylan, S.P.; Chandrasekar, S.; Chhabra, P.N.; Yang, H.T.Y. Formation of white layers in steels by machining and their characteristics. *Met. Mater. Trans. A* **2002**, *33*, 1245–1254. [[CrossRef](#)]
15. Mao, C.; Zhou, Z.; Zhang, J.; Huang, X.; Gu, D. An experimental investigation of affected layers formed in grinding of AISI 52100 steel. *Int. J. Adv. Manuf. Technol.* **2011**, *54*, 515–523. [[CrossRef](#)]
16. Hossain, R.; Pahlevani, F.; Witteveen, E.; Banerjee, A.; Joe, B.; Prusty, B.G.; Dippenaar, R.; Sahajwalla, V. Hybrid structure of white layer in high carbon steel—Formation mechanism and its properties. *Sci. Rep.* **2017**, *7*, 13288. [[CrossRef](#)]
17. Hosseini, S.B.; Thuvander, M.; Klement, U.; Sundell, G.; Rytberg, K. Atomic-scale investigation of carbon atom migration in surface induced white layers in high-carbon medium chromium (AISI 52100) bearing steel. *Acta Mater.* **2017**, *130*, 155–163. [[CrossRef](#)]
18. Hosseini, S.B.; Klement, U. A descriptive phenomenological model for white layer formation in hard turning of AISI 52100 bearing steel. *CIRP J. Manuf. Sci. Technol.* **2021**, *32*, 299–310. [[CrossRef](#)]
19. Zhang, F.-Y.; Duan, C.-Z.; Wang, M.-J.; Sun, W. White and dark layer formation mechanism in hard cutting of AISI52100 steel. *J. Manuf. Process.* **2018**, *32*, 878–887. [[CrossRef](#)]
20. Guo, Y.B.; Warren, A.W.; Hashimoto, F. The basic relationships between residual stress, white layer, and fatigue life of hard turned and ground surfaces in rolling contact. *CIRP J. Manuf. Sci. Technol.* **2010**, *2*, 129–134. [[CrossRef](#)]
21. Smith, S.; Melkote, S.N.; Lara-Curzio, E.; Watkins, T.R.; Allard, L.; Riester, L. Effect of surface integrity of hard turned AISI 52100 steel on fatigue performance. *Mater. Sci. Eng. A* **2007**, *459*, 337–346. [[CrossRef](#)]
22. Shen, Y.; Moghadam, S.M.; Sadeghi, F.; Paulson, K.; Trice, R.W. Effect of retained austenite—Compressive residual stresses on rolling contact fatigue life of carburized AISI 8620 steel. *Int. J. Fatigue* **2015**, *75*, 135–144. [[CrossRef](#)]
23. Matsumoto, Y.; Hashimoto, F.; Lahoti, G. Surface integrity generated by precision hard turning. *CIRP Ann. Manuf. Technol.* **1999**, *48*, 59–62. [[CrossRef](#)]

24. Wang, D.; Sun, S.; Jiang, J.; Liu, X. From the grain/workpiece interaction to the coupled thermal-mechanical residual stresses: An integrated modeling for controlled stress grinding of bearing ring raceway. *Int. J. Adv. Manuf. Technol.* **2019**, *101*, 475–499. [[CrossRef](#)]
25. Pape, F.; Coors, T.; Poll, G. Studies on the influence of residual stresses on the fatigue life of rolling bearings in dependence on the production processes. *Front. Mech. Eng.* **2020**, *6*, 56. [[CrossRef](#)]
26. Revel, P.; Khanfir, H.; Fillit, R.-Y. Surface characterization of aluminum alloys after diamond turning. *J. Mater. Process. Technol.* **2006**, *178*, 154–161. [[CrossRef](#)]
27. Jouini, N.; Revel, P.; Bigerelle, M. Relevance of roughness parameters of surface finish in precision hard turning. *Scanning* **2014**, *36*, 86–94. [[CrossRef](#)]
28. Jouini, N.; Revel, P.; Thoquenne, G. Influence of surface integrity on fatigue life of bearing rings finished by precision hard turning and grinding. *J. Manuf. Process.* **2020**, *57*, 444–451. [[CrossRef](#)]
29. EN-15305; Non-destructive Testing—Test Method for Residual Stress analysis by X-ray Diffraction. British Standard: London, UK, 2009.
30. Attanasio, A.; Umbrello, D.; Cappellini, C.; Rotella, G.; M'Saoubi, R. Tool wear effects on white and dark layer formation in hard turning of AISI 52100 steel. *Wear* **2012**, *286–287*, 98–107. [[CrossRef](#)]
31. Čilliková, M.; Mičietová, A.; Čep, R.; Jacková, M.; Minárik, P.; Neslušan, M.; Kouřil, K. Analysis of surface state after turning of high tempered bearing steel. *Materials* **2022**, *15*, 1718. [[CrossRef](#)]
32. Schwach, D.W.; Guo, Y.B. A fundamental study on the impact of surface integrity by hard turning on rolling contact fatigue. *Int. J. Fatigue* **2006**, *28*, 1838–1844. [[CrossRef](#)]
33. Guo, Y.B.; Sahni, J. A comparative study of hard turned and cylindrically ground white layers. *Int. J. Mach. Tools Manuf.* **2004**, *44*, 135–145. [[CrossRef](#)]
34. Barbacki, A.; Kawalec, M.; Hamrol, A. Turning and grinding as a source of microstructural changes in the surface layer of hardened steel. *J. Mater. Process. Technol.* **2003**, *133*, 21–25. [[CrossRef](#)]
35. Hosseini, S.B.; Rytberg, K.; Kaminski, J.; Klement, U. Characterization of the surface integrity induced by hard turning of bainitic and martensitic AISI 52100 steel. *Procedia CIRP* **2012**, *1*, 494–499. [[CrossRef](#)]
36. Pape, F.; Neubauer, T.; Maiß, O.; Denkena, B.; Poll, G. Influence of residual stresses introduced by manufacturing processes on bearing endurance time. *Tribol. Lett.* **2017**, *65*, 70. [[CrossRef](#)]
37. Breidenstein, B.; Denkena, B.; Krödel, A.; Prasanthan, V.; Poll, G.; Pape, F.; Coors, T. Production-related surface and subsurface properties and fatigue life of hybrid roller bearing components. *Metals* **2020**, *10*, 1339. [[CrossRef](#)]
38. Voskamp, A.P.; Österlund, R.; Becker, P.C.; Vingsbo, O. Gradual changes in residual stress and microstructure during contact fatigue in ball bearings. *Met. Technol.* **1980**, *7*, 14–21. [[CrossRef](#)]
39. Voskamp, A.P. Microstructural Changes During Rolling Contact Fatigue. Ph.D. Thesis, Technical University of Delft, Delft, The Netherlands, 1996.

Article

Influence of Slide Burnishing Parameters on the Surface Layer Properties of Stainless Steel and Mean Positron Lifetime

Agnieszka Skoczylas ^{1,*}, Kazimierz Zaleski ¹, Jakub Matuszak ¹, Krzysztof Ciecieląg ¹, Radosław Zaleski ² and Marek Gorgol ²

- ¹ Department of Production Engineering, Mechanical Engineering Faculty, Lublin University of Technology, 36 Nadbystrzycka, 20-618 Lublin, Poland
- ² Department of Materials Physics, Institute of Physics, Faculty of Mathematics, Physics and Computer Science, Maria Curie-Skłodowska University, Maria Curie-Skłodowskiej Sq. 5, 20-031 Lublin, Poland
- * Correspondence: a.skoczylas@pollub.pl; Tel.: +81-538-4707

Abstract: This paper presents the results of an experimental study on the impact of slide burnishing on surface roughness parameters (S_a , S_z , S_p , S_v , S_{sk} and S_{ku}), topography, surface layer microhardness, residual stress, and mean positron lifetime (τ_{mean}). In the study, specimens of X6CrNiTi18 stainless steel were subjected to slide burnishing. The experimental variables were feed and slide burnishing force. The slide burnishing process led to changes in the surface structure and residual stress distribution and increased the surface layer microhardness. After slide burnishing, the analyzed roughness parameters decreased compared with their pre-treatment (grinding) values. The slide burnishing of X6CrNiTi18 steel specimens increased their degree of strengthening e from 8.77% to 42.74%, while the hardened layer thickness g_h increased after the treatment from about 10 μm to 100 μm . The maximum compressive residual stress was about 450 MPa, and the maximum depth of compressive residual stresses was $g_\sigma = 1.1$ mm. The positron mean lifetime τ_{mean} slightly yet systematically increased with the increase in burnishing force F , while an increase in feed led to changes of a different nature.

Citation: Skoczylas, A.; Zaleski, K.; Matuszak, J.; Ciecieląg, K.; Zaleski, R.; Gorgol, M. Influence of Slide Burnishing Parameters on the Surface Layer Properties of Stainless Steel and Mean Positron Lifetime. *Materials* **2022**, *15*, 8131. <https://doi.org/10.3390/ma15228131>

Academic Editors: J. Antonio Travieso-Rodríguez and Gilles Dessein

Received: 24 October 2022
Accepted: 11 November 2022
Published: 16 November 2022

Publisher's Note: MDPI stays neutral with regard to jurisdictional claims in published maps and institutional affiliations.



Copyright: © 2022 by the authors. Licensee MDPI, Basel, Switzerland. This article is an open access article distributed under the terms and conditions of the Creative Commons Attribution (CC BY) license (<https://creativecommons.org/licenses/by/4.0/>).

Keywords: slide burnishing; X6CrNiTi18 stainless steel; surface roughness 3D; topography; microhardness; residual stress; positron mean lifetime τ_{mean}

1. Introduction

The properties of the surface layer of machined elements have a significant influence on the service life of the components. In terms of service life, advantageous properties of the surface layer can be obtained by subjecting manufactured items to treatment methods such as burnishing [1], shot peening [2] and brushing [3]. Numerous studies have shown that the use of these treatment methods makes it possible to improve the functional properties of elements made of various materials. Following the use of shot peening, the fatigue life of AZ80 magnesium alloy was shown to increase by about 75% [4], while the burnishing of 41Cr4 steel resulted in an increase in its fatigue life by 22.7% [5]. The use of burnishing improved the fatigue life of X19NiCrMo4 steel shafts by 28.5% compared with non-burnished shafts [6]. The fatigue life of elements made of titanium alloys increased from 125 to 420% as a result of shot peening, depending on the process parameters such as impact energy and shot peening time [7]. Shot peening also affects the redistribution of the residual stress field in friction stir welding [8]. It was also found that burnishing led to an increased wear resistance of steel [9] and titanium alloy [10]. Comparative studies of surface wear after turning, grinding, ball burnishing, and vibroburnishing showed that the most wear-resistant surface was obtained after vibroburnishing [11]. Burnishing also reduces wear due to fretting [12].

The surface layer properties of elements subjected to burnishing and shot peening depend on many factors, including the structure of a burnishing tool [13], burnishing

strategy [14], process parameters [15], pre-machining prior to burnishing [16], regularity of shot peening tool hits on the treated surface [17], and properties of the machining fluid [18]. Burnishing processes are analyzed using experimental and numerical methods [19]. An important aspect of the treatment carried out is the amount of energy consumed [20].

Depending on the impact of a burnishing tool on the burnished object, a distinction is made between roller burnishing [21], ball burnishing [16], and slide burnishing [18], which is a process wherein the tool works in sliding contact with the treated surface. The slide burnishing process can be carried out using tools with a polycrystalline diamond and cemented carbide tip [22]. The surface of the slide burnishing tool adjacent to the burnished surface usually has the shape of a spherical ball with a radius ranging from 1 to 4 mm, and the force with which the tool is pressed against the workpiece is usually in the range of 20–250 N [23–25]. Given the relatively low value of the tool force on the burnished element, the slide burnishing method can be used to shape the surface layer of objects with low stiffness. The advantage of slide burnishing is that its use causes a significant reduction in the surface roughness. For example, after the slide burnishing of carbon steel samples with an initial surface roughness of $R_a = 1.39\text{--}12.90\ \mu\text{m}$, the surface roughness was reduced to $R_a = 0.31\text{--}0.53\ \mu\text{m}$ [26]. The authors of [27] stated that nano-crystalline structures in the 10–300 nm grain size range formed at the subsurface layer after slide burnishing normalized carbon steel. Grain sizes increase approximately linearly with the depth below the surface.

One of the types of elements subjected to burnishing and shot peening are made of stainless steels. These steels are used, among others, for the production of installation elements in the food, chemical, transport and paper industries, as well as parts of aircraft engines, automotive vehicles, and energy devices.

Increased fatigue life due to shot peening has also been observed for stainless steels. Research by Yang et al. showed that with an increase in the shot peening intensity of austenitic 304 stainless steel ranging from 0.1 mmA to 0.4 mmA, its compressive residual stresses and fatigue life increased [28]. A significant improvement in surface layer properties can be achieved by multiple shot peening. According to Chen et al., the use of three-time shot peening for SAF 2507 duplex stainless steel specimens with decreasing peening intensity allowed for an increase in the compressive residual stress, increase in the content of α' martensite and reduce surface roughness compared with single-shot peening [29]. Menezes et al. obtained an increased depth of surface layer hardening as well as higher wear and corrosion resistance of AISI 316L stainless steel by using shot peening prior to the sequential plasma treatment of this particular steel grade [30]. Furthermore, the wear tests of 316L stainless steel carried out by Gopi et al. showed that shot peening reduced the mass wear and friction coefficient of samples made from this steel grade [31]. A study by Walczak et al. showed that shot peening conducted with the use of ceramic shots on 17-4PH stainless steel additively produced by direct metal laser sintering resulted in grain refinement, reduced surface roughness, as well as increased wear and corrosion resistance [32]. A study by Spadaro et al. showed that shot peening caused a greater increase in the fatigue life of 235MA austenitic stainless steel compared with laser shock processing [33].

Burnishing is also used as the finishing method for stainless steel components. Bouzid Sai et al. examined the surface layer of duplex stainless steel after turning, grinding, and burnishing with a 9 mm diameter ball, which showed that the best results were obtained after burnishing [34]. Attabi et al. reported the results of a study investigating the effect of the number of passes in the ball burnishing process for 316L stainless steel on the steel's microhardness, nano-hardness, and wear resistance [35]. The wear resistance was also tested after the slide burnishing process. The authors of [36] proved that diamond burnishing CuAl8Fe3 aluminum bronze with six passes provided the highest wear resistance under the condition of boundary lubrication friction; the procedure also increased the wear resistance 5.1 times more than fine turning. Diamond burnishing with one pass resulted in the highest wear resistance under the dry friction condition and increased the wear

resistance 1.75 times more than fine turning. Valiorgue et al. conducted a comparative study on the effect of turning, belt grinding, and roller burnishing on the properties of 15-5PH martensitic stainless steel, which demonstrated that the greatest compressive residual stress and highest fatigue life were obtained after the rolling burnishing process [37]. Konefal et al. investigated the corrosion resistance of X6CrNiMoTi17-12-2 stainless steel samples that were subjected to the following types of treatment: drawing, polishing, and slide diamond burnishing. The burnishing parameters were maintained at a constant $F = 150$ N force and $f = 0.11$ mm/rev feed. It was found that the burnished samples showed the greatest corrosion resistance [38].

The surface layer properties of elements can be tested with various techniques that use both destructive and non-destructive methods. Previous studies have shown that positron annihilation lifetime spectroscopy can be used to study the surface layer. This research technique allows for the estimation of the concentration of various material defects on an atomic scale (dislocations, vacancies, etc.), with these defects being positron trapping centers. In contrast to microscopic techniques, an advantage of this non-destructive method is the possibility of obtaining data that is averaged over a relatively large volume of the material (for steels, it is a layer with a thickness of several dozen micrometers on an area of about a square millimeter). Horodek et al. used positron annihilation methods to investigate the depth of a subsurface zone in 304 austenitic stainless steel processed by various processes such as laser cutting, abrasive water jet, and milling techniques [39]. Positron annihilation spectroscopy was also used to test 316L austenitic stainless steel that was subjected to laser shock peening [40]. Zaleski et al. [41] studied the influence of vibratory shot peening of C45 steel, 7075 aluminum alloy, and Ti6Al2Mo2Cr titanium alloy on the positron annihilation parameters. The influence of the impulse shot peening on the surface layer properties of Inconel 718 nickel alloy was also investigated using positron annihilation spectroscopy [42].

The literature review indicates that there is currently a lack of the studies on the surface layer properties of X6CrNiTi18 steel after a slide burnishing process has been carried out with annihilation techniques and simulation FEM. Therefore, it seems advisable to determine the impact of the technological parameters of slide burnishing on the surface layer properties with the use of positron annihilation and FEM analyses. The aim of this experimental and numerical study was to evaluate the effect of slide burnishing on the surface layer properties of X6CrNiTi18 stainless steel as well as on the positron lifetime.

2. Materials and Methods

Experiments were conducted on specimens of austenitic corrosion-resistant steel X6CrNiTi18 (1.4541) (in accordance with EN 10088-1: 2014). This steel grade is used in the chemical industry (for manufacturing equipment of plants producing nitric acid and its salts, chemical fertilizers). X6CrNiTi18 steel is also used to make transmission pipelines, heat exchangers, reactors (petrochemical industry), tanks, autoclaves, pasteurizers, mixers, pump elements, and cisterns (food industry). This corrosion-resistant steel grade is characterized by very good weldability regardless of the welding method used. X6CrNiTi18 steel is produced in the form of tubes, sheets (cold- and hot-rolled), bars, profiles, wires, flat-die and die forgings, and tapes [43].

Table 1 shows the chemical composition and selected properties of the tested material. The tests were carried out on the samples, which were shaped as thin-walled rings with the following dimensions: external diameter: $d = 56$ mm, internal diameter: $d_o = 50$ mm, and width: $b = 10$ mm.

Table 1. Chemical composition and selected properties of X6CrNiTi18 stainless steel.

Element	Fe	Cr	Ni	Mn	Si	P	S
wt%	70.4	18.9	8.3	1.7	0.5	0.1	0.1
						220 MPa	
						720 MPa	
						215 HB	

The ring-shaped specimens were ground before the slide burnishing procedure. The machining process was carried out on a cylindrical grinder. The grinding process was conducted with a grinding wheel peripheral speed of $v_s = 30$ m/s and a grinding depth of $a_p = 0.01$ mm. An aloxite grinding wheel was used.

Slide burnishing was performed on a universal lathe (Figure 1). The test samples were mounted on a mandrel (2) that performed a rotary motion. A slide burnishing tool (3) with a spherical diamond tip (4) described by a radius R and burnishing force-exerting mechanism was pressed to the machined samples with a force F . The burnishing tool performed a feed motion f .

**Figure 1.** View of the test stand used in the experiment: 1: specimen; 2: mandrel with mounted samples; 3: slide burnishing tool; 4: diamond tip with radius R .

A tool with a spherical diamond tip with a radius of $R = 3$ mm was used for the slide burnishing process. Machine oil was used to reduce the friction during the slide burnishing. The oil used during slide burnishing was Mobil Vactra™ Oil No. 2 synthetic oil (Mobil, Bavaria, Germany) The applied burnishing parameters selected based on preliminary tests and a literature review are listed in Table 2.

Table 2. Technological parameters of slide burnishing (F : slide burnishing force; f : feed, v_n : burnishing speed; i : number of passes).

No.	F [N]	f [mm/rev]	v_n [m/min]	i
1.	90			
2.	160			
3.	230	0.06		
4.	300			
5.		0.03	35	1
6.		0.09		
7.	230	0.12		
8.		0.16		
9.		0.20		

In the next step, the selected properties of the surface layer of stainless steel after slide burnishing were examined, as shown in Figure 2.

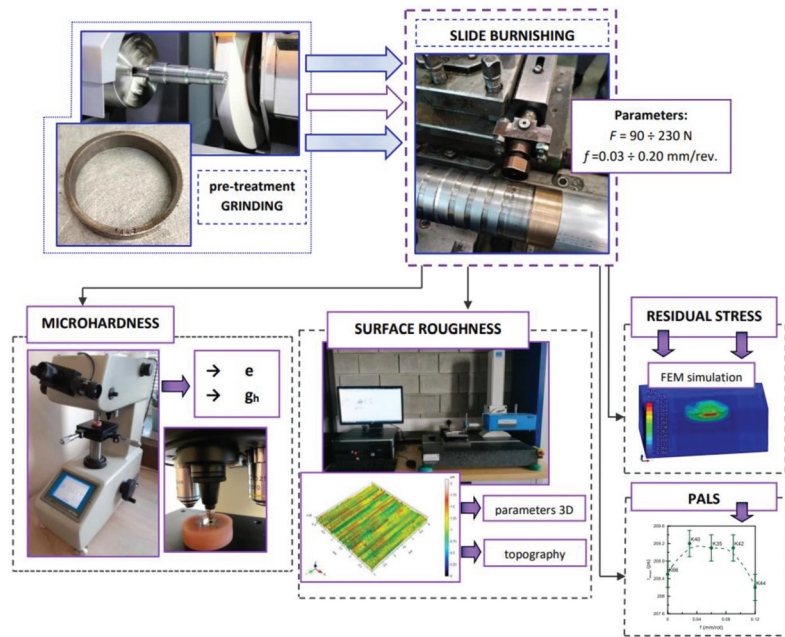


Figure 2. Methodology of the conducted research. The parameters of the experiment, stands research and achieved results.

The Hommel-Etamic T8000 RC120-400 device was used to measure the surface topography and surface roughness parameters in 3D. RC is a tactile roughness and contour measurement system. The scanned surface area was 3×3 mm. Measurements were carried out along the external surface of the samples (perpendicular to the traces after slide burnishing). The measurements were taken in compliance with the EN ISO 25178-2:2022 standard. The analyzed 3D parameters of the surface roughness were as follows:

- Sa*: arithmetical mean height of the surface;
- Sz*: maximum height of the surface;
- Sp*: maximum peak height of the surface;
- Sv*: maximum pit height of the surface;
- Ssk*: skewness;
- Sku*: kurtosis

The LM 700at microhardness tester (Leco, St. Joseph, MI, USA) was used to measure the surface layer microhardness before and after the slide burnishing process. The Vickers method was used for this purpose, which assumed an indenter weight of 50 g (HV 0.05). The specimens were subjected to standard treatment, and the angled microsections were examined. The results of the microhardness measurements were used to determine the degree of strengthening e and hardened layer thickness g_h . Equation (1) was used to calculate the degree of strengthening.

$$e = 100 \cdot \frac{HV_{\max} - HV_0}{HV_{\max}}, \% \quad (1)$$

where HV_{\max} is the maximum microhardness of the surface layer after slide burnishing and HV_0 is the microhardness after grinding.

The slide burnishing process was modelled using the explicit module of the Abaqus/CAE 2021 software. The simulations were carried out as part of dynamic calculations, considering the contact relations. The Johnson–Cook constitutive model was used with the

following parameters: $A = 280$ MPa, $B = 1215$ MPa, $n = 0.43$, $C = 0.031$, and $m = 1.15$. The model considered the effect of strain hardening, strain rate, and temperature on the stress–strain relationship. The numerical model was modified in relation to the real one, yet it was ensured that all process conditions faithfully reproduced the real slide burnishing process. In the simulation, a 7.5×5 mm sample modelled with C3D8R-type elements was used, with the mesh density maintained in the central area of the burnished object. The grid size at the analysis site was 0.05 mm. The total number of elements in the mesh was 147,840, which amounted to 156,465 nodes. The burnishing element was modelled as a non-deformable solid using two types of finite elements: R3D4 (140 elements) and R3D3 (1840 elements), with compaction in the area of contact with the workpiece. The successive passes of the burnishing element in the real burnishing process were represented as hemispheres with a rounding radius equal to 3 mm. The distance of the burnishing elements used in the simulation was consistent with the feed per revolution. In the FEM simulation, 11 burnishing elements were used, which allowed for the burnishing process to be carried out on a length equal to 10 feed values per revolution of the burnishing element, which for the adopted process conditions gave a burnished surface length ranging from 0.3 to 2 mm. The area of the compacted mesh was 2.5×2.5 mm and was located in the center of the workpiece. In addition, along the Y-axis, each of the burnishing elements used in the simulation was offset from the next to represent the conditions in which the burnishing element would partially cover the previous pass of the tool after each revolution of the workpiece. This methodology made it possible so that in the case of a speed of $v_n = 35$ m/min and simulation time of $t = 0.008572$ s, each of the burnishing elements covered a distance of 5 mm, thus burnishing the area with a dense mesh of the finite elements. The stresses S11 reflecting the residual stresses in the surface layer after the burnishing process and the PEEQ equivalent plastic strains were analyzed. Figure 3 shows the simulated burnishing process for the established 11 passes of the burnishing element, where the marked interval is equal to the feed (distance between successive burnishing element passes).

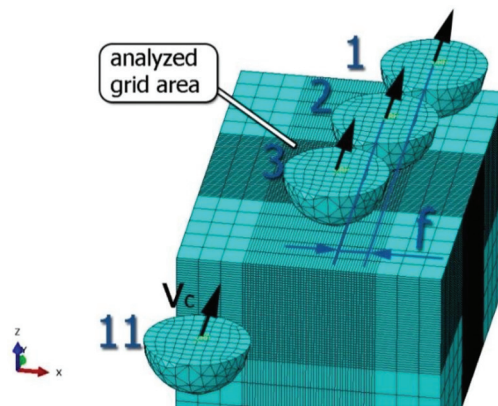


Figure 3. FEM simulation of the slide burnishing process.

The non-zero equivalent plastic strain at variable feeds had a depth ranging from 0.4 mm (for $f = 0.2$ mm/rev) to 0.6 mm (for $f = 0.03$ mm/rev). In turn, during the experiment with variable burnishing force, the non-zero equivalent plastic strain had a depth ranging from 0.25 mm (for $F = 90$ N) to 0.8 mm (for $F = 300$ N).

To evaluate the influence of the pressing force and feed rate on the effects of the process, FEM simulations were carried out for the parameters specified in Table 2. The S11 stress plots obtained from the simulations were determined as the average value of three cross-section lines perpendicular to the surface, as shown in Figure 4. The cross-

sections were examined in the area of the compacted mesh under the symmetry axis of the burnishing element (taking into account the fixed feed per revolution in each case).

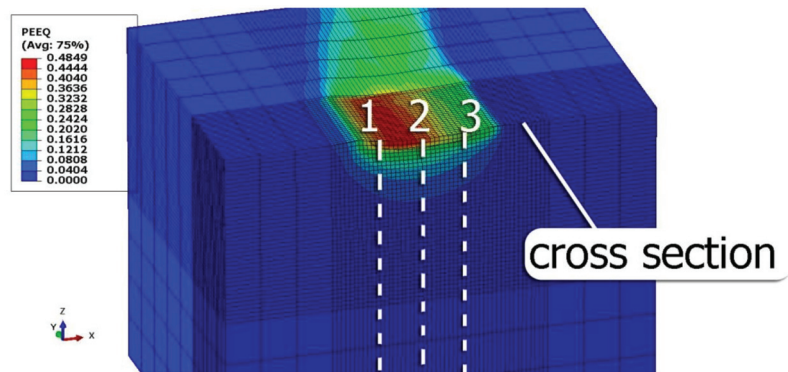


Figure 4. Method of creating paths for determining the residual stresses in the surface layer.

Positron annihilation lifetime spectra were measured with a digital lifetime spectrometer. Two scintillation detectors equipped with BaF₂ scintillators fixed in the immediate vicinity of the samples were used to detect gamma quanta with an energy of 1274 keV (which indicates the formation of a positron in the β^+ decay) and annihilation quanta with an energy of 511 keV. Voltage pulses from the detectors were recorded with the Agilent U1065A digitizer at a sampling rate of 4 GS/s and then examined with dedicated software [44] to determine the time difference between gamma and annihilation signals. ²²NaCl (0.3 MBq) in an 8 μm -thick Kapton envelope served as a source of positrons and was placed between two identical samples fixed in a dedicated holder. The sample–source–sample “sandwich” was shifted below the edge of the scintillators to avoid the coincidence of the collinear annihilation quanta of 511 keV–511 keV. The total count number in the positron lifetime spectra slightly exceeded 2.1×10^7 for each sample.

Results were analyzed using the PALSfit program [45], which allowed us to determine the lifetimes and relative intensities of the individual components as well as the positron mean lifetime. A good fit was obtained, assuming two dominant components of the lifetime spectrum. Typically for the low-background spectrum from a digital spectrometer, it was also necessary to assume a long-life component with a lifetime of approx. 1.5 ns and negligible intensity of $\sim 0.2\%$. The contribution of a source correction (annihilation in the Kapton envelope) with a lifetime of 382 ps was determined at 14.3% using the Positron Fraction program [46]. A single Gaussian with an FWHM of 201 ps was sufficient to describe the resolution function.

3. Results and Discussion

The following subsections present the results of the research on the analyzed properties of the surface layer and lifetime of positrons.

3.1. Topography and Surface Roughness

Micro-irregularities on the ground surface have a unidirectional pattern (Figure 5), which is characteristic of this machining method. There are numerous depressions on the surface, which are confirmed by the high value of the S_v parameter. The profile of the ground surface is characterized by sharp elevations and depressions that were formed on the surface as a result of the work by abrasive grains of the grinding wheel.

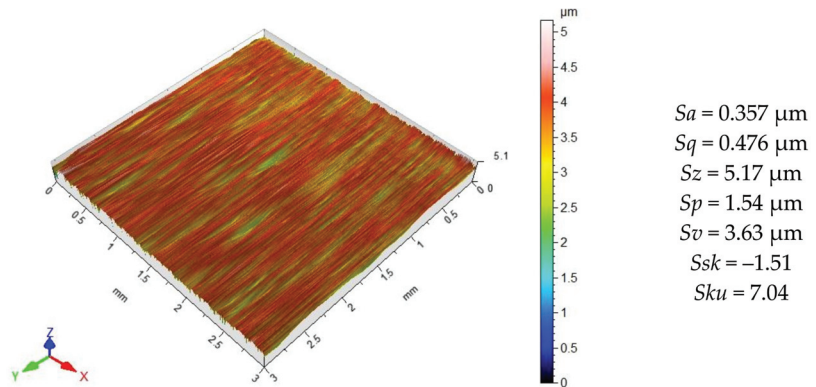


Figure 5. X6CrNiTi18 steel surface topography after grinding pre-treatment.

After the slide burnishing process conducted with a feed $f = 0.03\text{--}0.09$ mm/rev (Figure 6a,c), the shape of the micro-irregularities was more irregular compared with the surface after grinding (Figure 5). There were numerous visible deformations of micro-inequalities that were not reflected in the burnishing kinematics. This is most likely due to the friction and adhesive interaction between the surface of the workpiece and the diamond tip of the tool. The use of the burnishing feed value of $f = 0.12\text{--}0.20$ mm/rev led to a deterioration of the geometric structure of the surface. For $f = 0.12\text{--}0.20$ mm/rev (Figure 6d,e), a characteristic unidirectional pattern of surface micro-irregularities was visible, with noticeable elevations and depressions on the surface. The obtained values of the Sa parameter were greater than the Sa values after grinding. For the entire tested feed range, the obtained values of the Sz parameter were lower than those after the pre-treatment. The minimum values of Sa and Sz were obtained for $f = 0.06$ mm/rev.

Figures 7 and 8 present the influence of the feed value on the analyzed 3D surface roughness parameters. It can be seen that for the burnishing feeds in the lower range, the analyzed surface roughness parameters decreased to the minimum for $f = 0.06$ mm/rev.; a further increase in the burnishing feed led to an increase in the surface roughness. The increase in the burnishing feed increased the distance between successive passes of the tool (no deformation of surface micro-irregularities after the pre-treatment), which caused an increase in the Sa , Sz , Sp , and Sv parameters. The increase in the Sa parameter for $f = 0.03$ mm/rev. may be due to multiple deformations of the same surface micro-irregularities. For the feed ranging $f = 0.03\text{--}0.09$ mm/rev. (Figure 7b), no changes in the Sz parameter value can be observed. Similar changes in the roughness parameters as a function of the feed in the slide burnishing of AISI 316Ti steel were observed by Maximov et al. [47]. After the slide burnishing of X6CrNiTi18 steel, the surface roughness profile is changed. In the total surface profile after slide burnishing, the elevations (parameter Sp) had a greater share than the depression (parameter Sv). After grinding, the surface micro-irregularities were deformed, and their shape and dimensions were changed. The values of the skewness ratio Ssk and kurtosis Sku were changed as well. For $f = 0.12$ mm/rev. the obtained values were $Ssk = 0.058$ and $Sku = 2.66$, which means that there will be less friction between the mating surfaces, which agrees with the results reported in [48]. The same properties will be characteristic of the surface after grinding [49], but with a significantly worse surface quality (high values of the Sa and Sz parameters).

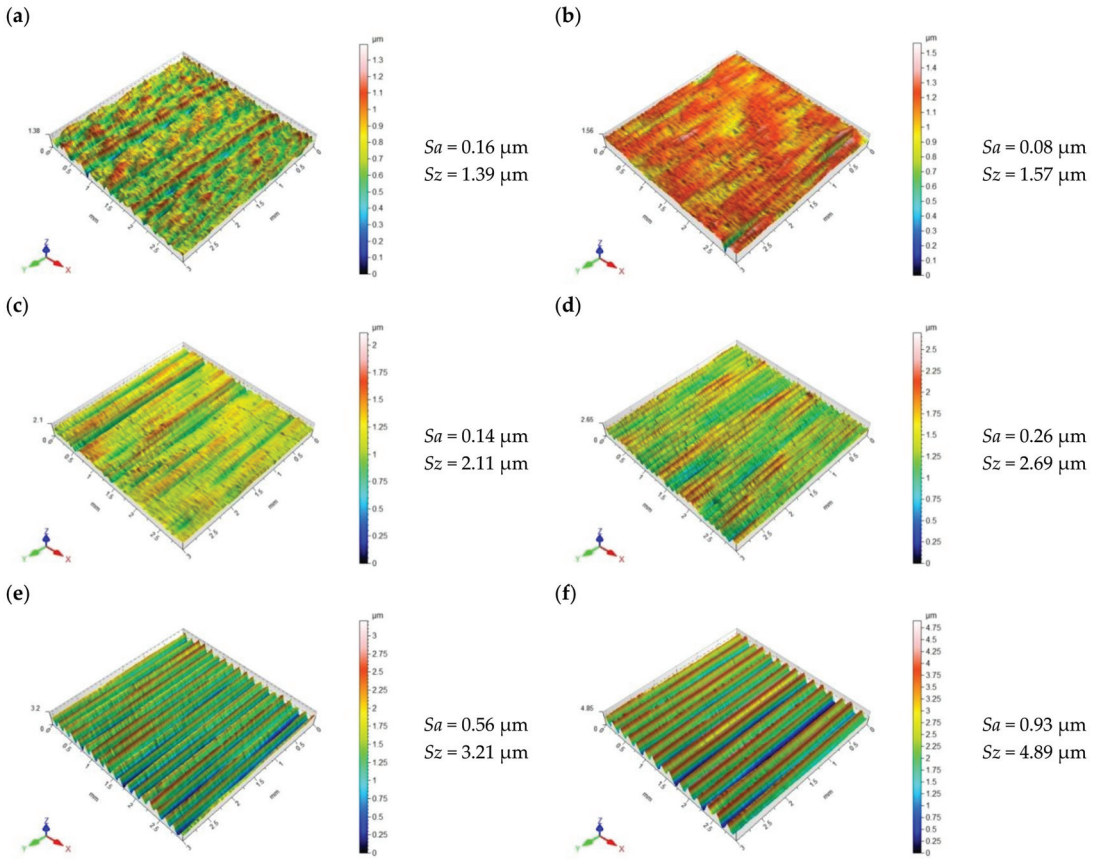


Figure 6. Topography of X6CrNiTi18 steel surface after slide burnishing: (a) $f = 0.03$ mm/rev., $F = 230$ N; (b) $f = 0.06$ mm/rev., $F = 230$ N; (c) $f = 0.09$ mm/rev., $F = 230$ N; (d) $f = 0.12$ mm/rev., $F = 230$ N; (e) $f = 0.16$ mm/rev., $F = 230$ N; (f) $f = 0.20$ mm/rev., $F = 230$ N.

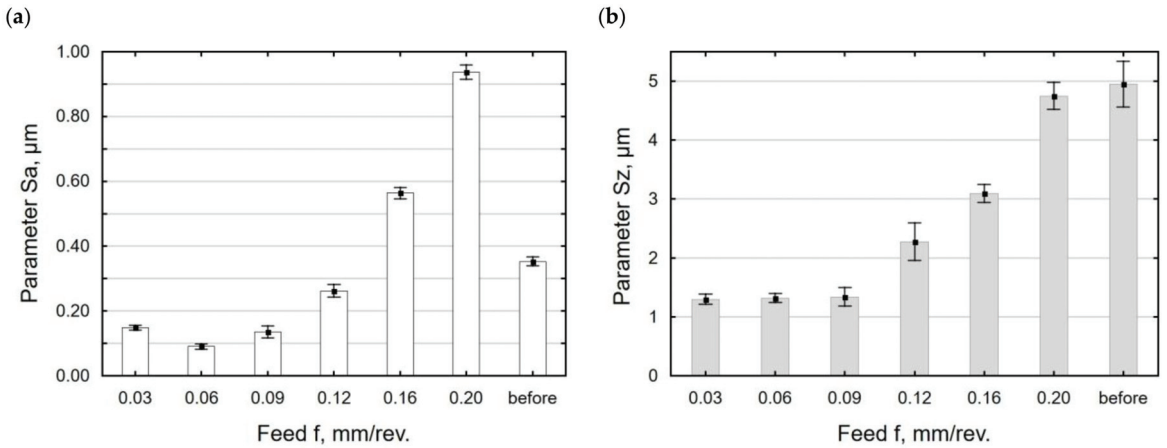


Figure 7. Feed versus surface roughness parameters Sa (a) and Sz (b) ($F = \text{const.} = 230$ N, $v_n = 35$ m/min, $i = 1$).

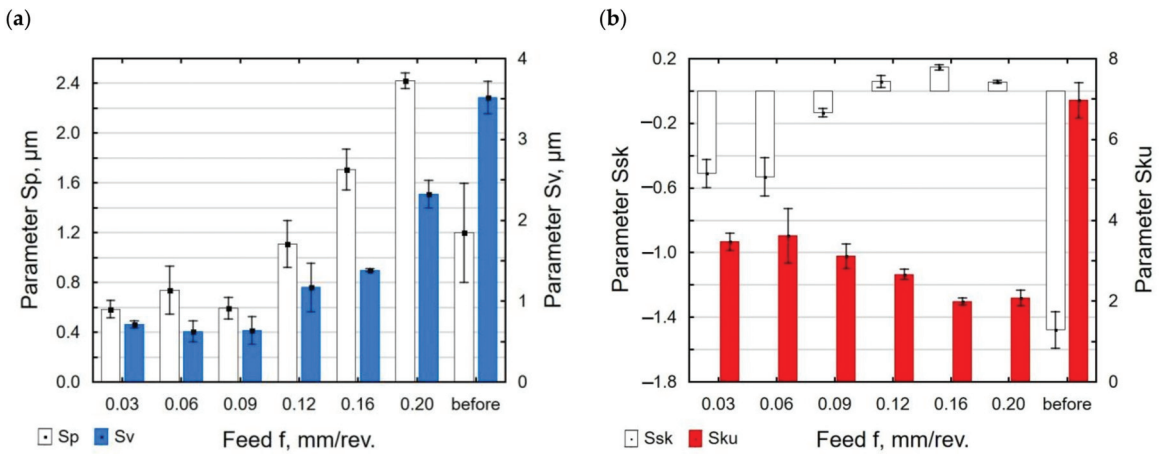


Figure 8. Feed versus surface roughness parameters: Sp and Sv (a); Ssk and Sku (b) ($F = \text{const.} = 230 \text{ N}$, $v_n = 35 \text{ m/min}$, $i = 1$).

Figure 9 shows the surface topography of X6CrNiTi18 steel after the slide burnishing process when conducted with a different force value. The use of a higher force value caused the deformation of the sample surface to be “fuller”; the surface micro-irregularities were smoothed after the pre-treatment, which translated into a four-fold reduction in the Sa parameter for $F = 230 \text{ N}$. The surface topography obtained after slide burnishing when conducted with $F = 90\text{--}230 \text{ N}$ was characterized by flattened micro-irregularities. The obtained values of the parameter Sz for the force $F = 90\text{--}230 \text{ N}$ had similar values. The use of the force $F > 230 \text{ N}$ caused a slight increase in the Sa and Sz parameters (Figure 10); the “flattening” of the surface and the presence of individual surface defects were also visible. The presence of these surface defects leads to a higher Sz value. It should be explained that the use of higher burnishing forces causes shear damage under the sample surface and surface flaking [50]. The obtained changes in the Sa and Sz parameters as a function of the force F are similar to the results described in [49,50]. The surface roughness parameters Sa and Sz ranged from 62% to 77% lower compared with the values obtained after grinding.

During slide burnishing, the diamond tip is in constant contact with the surface of the workpiece. This causes intensive deformation of the surface micro-irregularities. As a result, the values of the Sp and Sv parameters decreased from 36% to 82% compared with their values after grinding (Figure 11a). The kurtosis coefficient Sku and asymmetry Ssk also changed (Figure 11b). The obtained absolute values of the Ssk and Sku coefficients were smaller than those after grinding, but the values of $Ssk < 0$ and $Sku > 0$ mean that the material was concentrated around the profile peaks; therefore, this surface can be considered to be a good bearing surface [49].

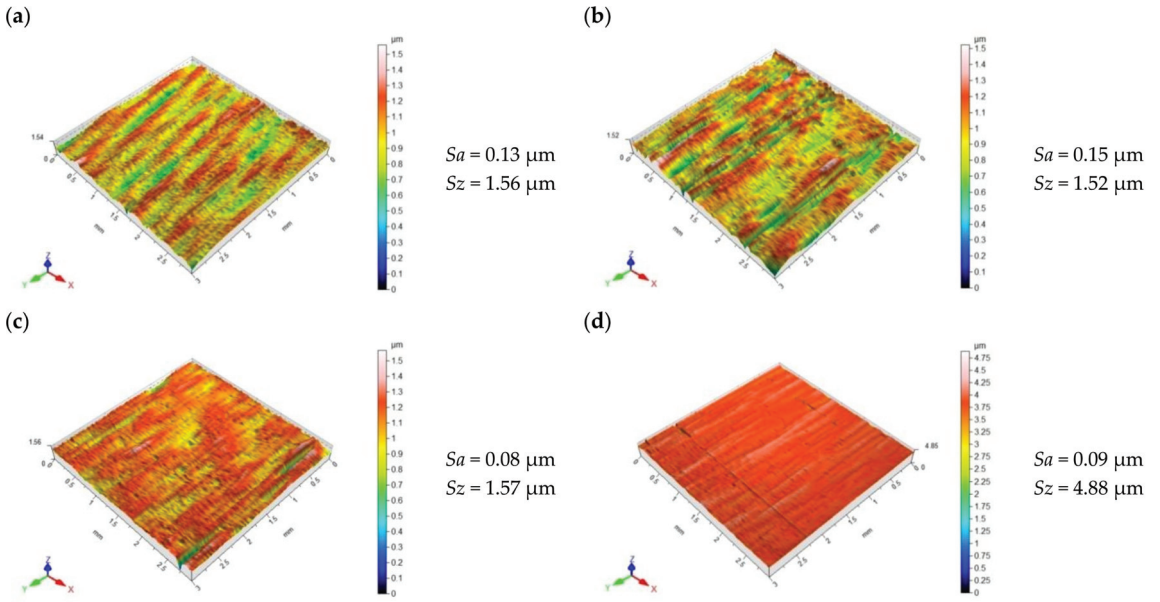


Figure 9. Topography of X6CrNiTi18 steel surface after slide burnishing (a) $F = 90\text{ N}$, $f = 0.06\text{ mm/rev.}$; (b) $F = 160\text{ N}$, $f = 0.06\text{ mm/rev.}$; (c) $F = 230\text{ N}$, $f = 0.06\text{ mm/rev.}$; (d) $F = 300\text{ N}$, $f = 0.06\text{ mm/rev.}$

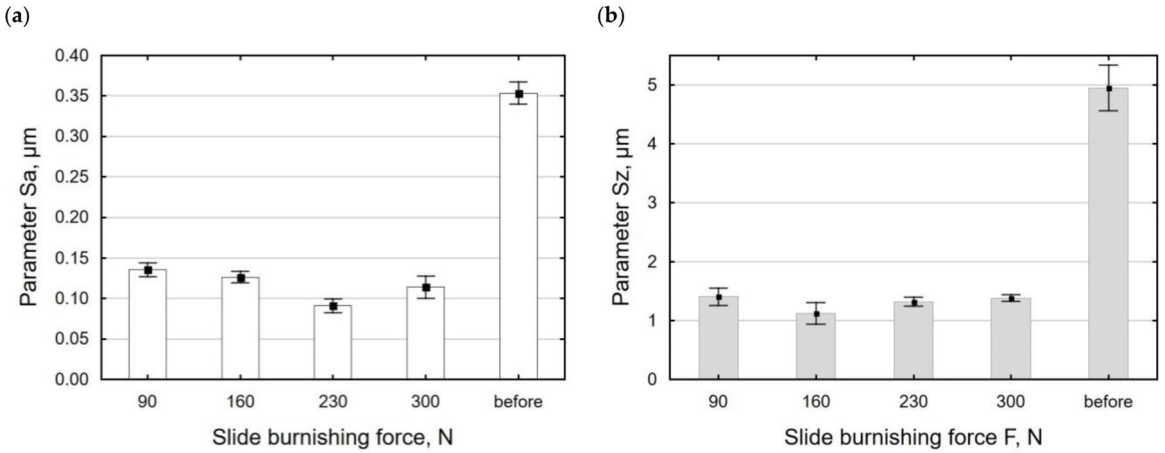


Figure 10. Burnishing force versus surface roughness parameters S_a (a) and S_z (b) ($f = \text{const} = 0.06\text{ mm/rev.}$, $v_n = 35\text{ m/min}$, $i = 1$).

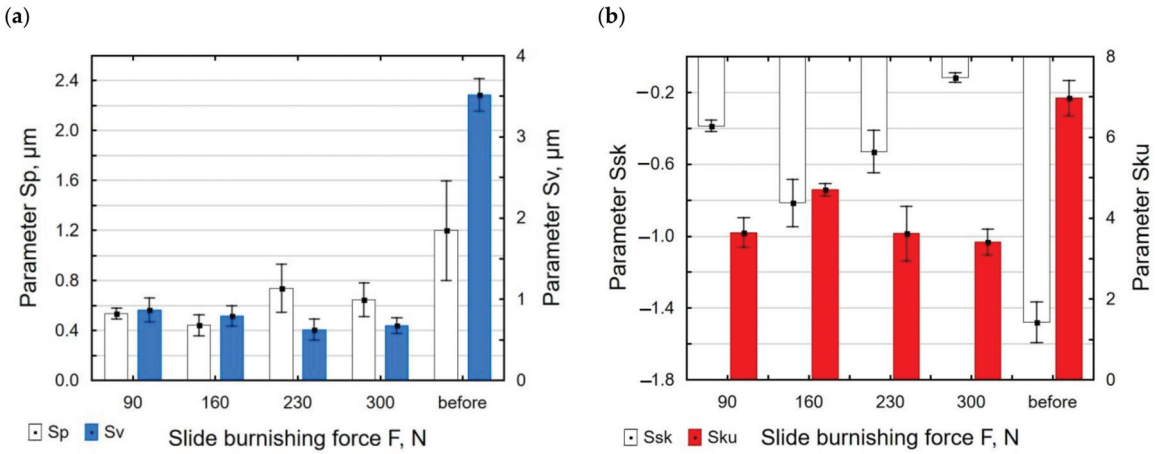


Figure 11. Burnishing force versus surface roughness parameters: Sp and Sv (a); Ssk and Sku (b) ($f = \text{const.} = 0.06 \text{ mm/rev.}$, $v_n = 35 \text{ m/min}$, $i = 1$).

3.2. Microhardness

As a result of slide burnishing and grinding, the material was strengthened (Figure 12). Following grinding conducted close to the surface at a depth of $1 \mu\text{m}$, the microhardness of the surface layer was approx. 15% higher than the microhardness of the core. From a depth of $5 \mu\text{m}$, the microhardness of the surface layer of the ground sample was similar to the microhardness of the core. The distribution of microhardness for the slide burnished sample shows that the highest microhardness occurred at a depth of $3 \mu\text{m}$ from the surface. The obtained microhardness distribution is characteristic of this treatment method.

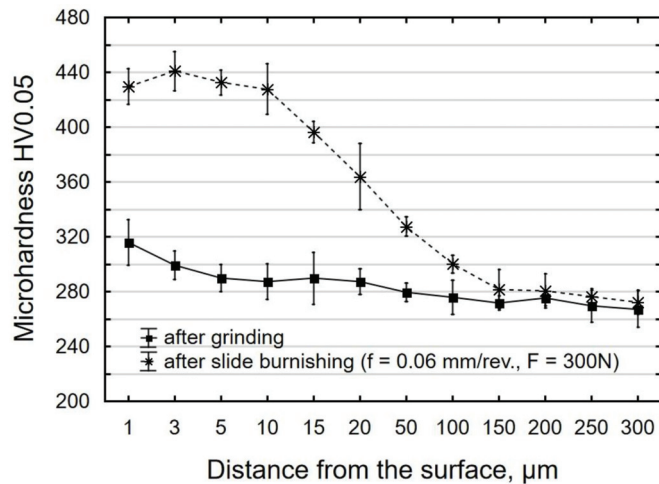


Figure 12. Distribution of microhardness on the surface layer of samples after grinding (pre-treatment) and slide burnishing.

Figure 13 shows the degree of strengthening e and hardened layer thickness g_h as a function of burnishing feed (Figure 13a) and slide burnishing force (Figure 13b). The hardening degree was determined for the depth $g_h = 3 \mu\text{m}$, for which the microhardness is the highest. The slide burnishing of X6CrNiTi18 steel specimens resulted in the degree of strengthening e ranging from 8.77% to 42.74%, which was higher than the degree of strengthening obtained for X19NiCrMo4 steel ($e = 32\%$) [6]. The hardened layer thickness

g_h after slide burnishing ranged from about 10 μm to 100 μm , while in [6], the reported changes in microhardness reached a depth of up to 18 μm .

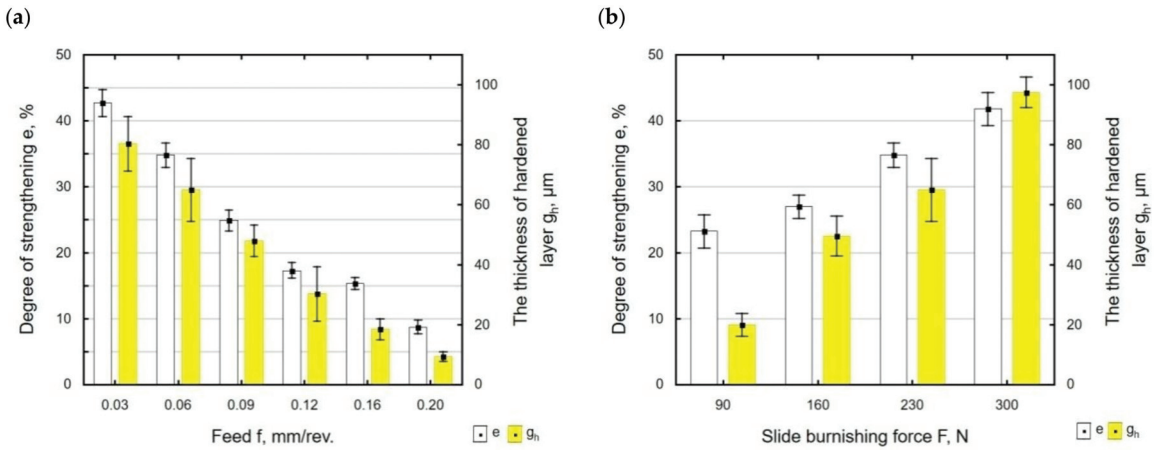


Figure 13. Degree of strengthening and hardened layer thickness after slide burnishing as a function of: (a) feed f ($F = 230$ N, $v_n = 35$ m/min, $i = 1$); (b) force F ($f = 0.06$ mm/rev., $v_n = 35$ m/min, $i = 1$).

When burnishing is conducted with a higher feed (Figure 13a), the traces of the diamond tip passes are at a greater distance from each other. This causes a decrease in the structural homogeneity and, consequently, a lower degree of strengthening e and decrease in the hardened layer thickness g_h .

The greatest differences between the values of the strengthening degree e occurred for the forces $F = 230$ N and $F = 300$ N. The application of a higher burnishing force caused an increase in the degree of strengthening e . This is most likely due to intense plastic deformation caused by friction, which leads to grain refinement of the microstructure. The use of a higher burnishing force causes the plastic deformation to take place deeper in the material, which results in increased microhardness of the surface layer extending further from the treated surface. The obtained results of the influence of F on g_h are similar to the results described in [26], where the slide burnishing process was conducted on carbon steel with a hardness of 250 HV.

3.3. Residual Stress

Figure 14 shows the results of the influence of the burnishing force on the distribution of stresses S11 occurring in the surface layer. As the burnishing force increased, the depth of compressive stresses increased. The maximum value of the compressive residual stress (about 400 MPa) was obtained for the burnishing forces $F = 230$ N and $F = 300$ N. The burnishing force significantly affected the depth of compressive residual stresses from $g_\sigma = 0.4$ mm (for the force $F = 90$ N) to $g_\sigma = 1.1$ mm (for the force $F = 300$ N). It should be assumed that the increase in the depth of residual stresses will allow the place of fatigue crack initiation to be shifted from the surface to the subsurface layers. This means that the phenomenon of nucleation and crack propagation will be delayed [51].

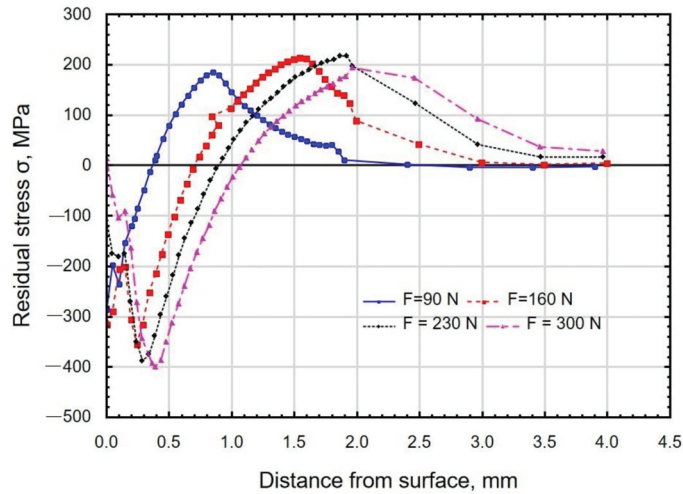


Figure 14. Distribution of residual stresses as a function of distance from the surface of X6CrNiTi18 steel samples after slide burnishing with a variable burnishing force ($f = 0.06$ mm/rev; $v_n = 35$ m/min; $i = 1$; $R = 3$ mm).

Figure 15 shows the effect of burnishing feed on the distribution of S11 stresses. The depth of the compressive residual stresses was about $g_{\sigma} = 0.9$ mm. No significant influence of the feed on the residual stress distribution was observed. The obtained depths of residual stresses are greater than those observed after the slide burnishing of C45 steel [52]. The compressive residual stress zone was much deeper than the plastically deformed zone. The results are similar to those presented in the paper [53].

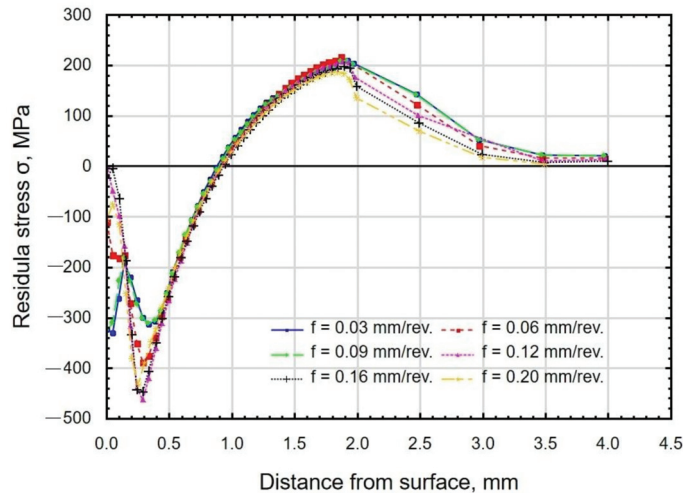
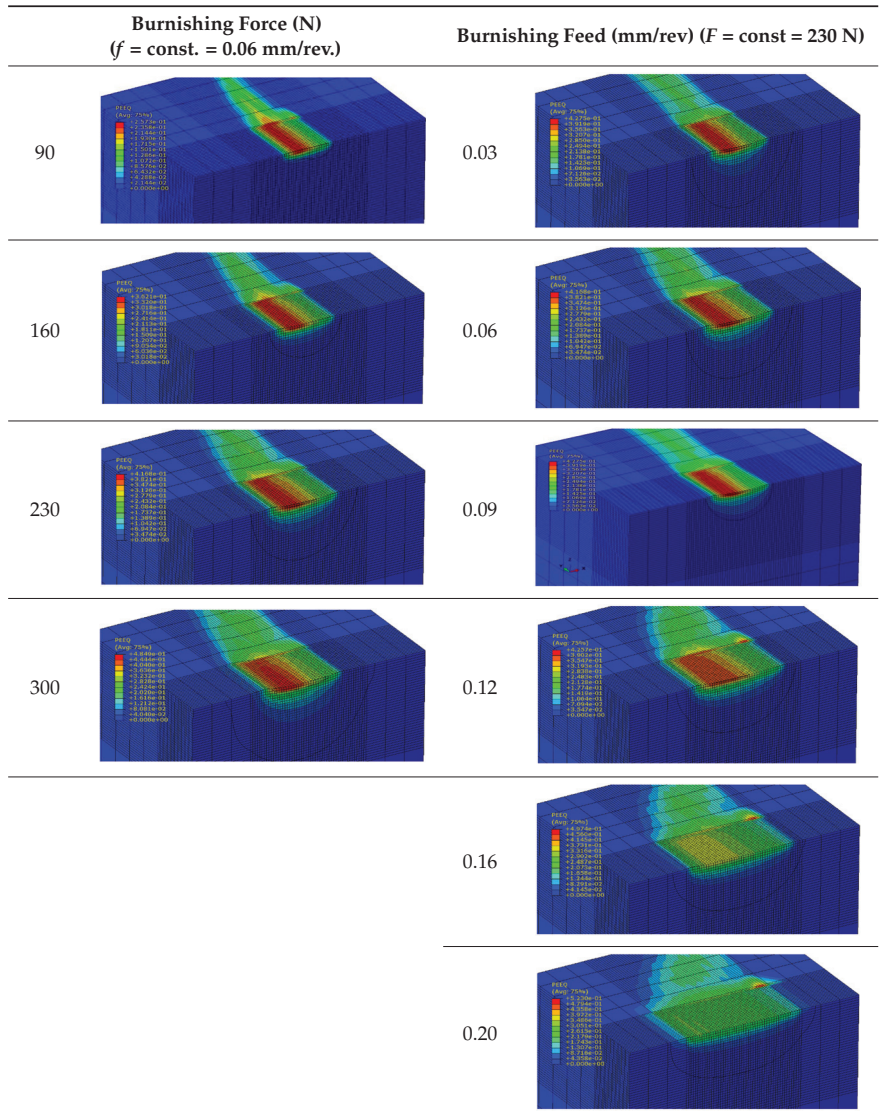


Figure 15. Distribution of residual stresses as a function of distance from the surface of X6CrNiTi18 steel samples after slide burnishing with a variable feed ($F = 230$ N; $v_n = 35$ m/min; $i = 1$; $R = 3$ mm).

Table 3 shows the visualization of the PEEQ equivalent plastic strains. For variable burnishing forces, the feed rate $f = 0.06$ mm/rev. was used; for variable feeds, the burnishing force was $F = 230$ N. A symmetrical cross-section was created to illustrate deformation on the surface as well as in the subsurface layers. The PEEQ color maps demonstrate that the plastic deformation wave resulting from the passages of successive burnishing

elements shifted the area of maximum plastic deformation concentration away from the axis of symmetry of the workpiece. This phenomenon was not observed for the feeds $f = 0.16$ mm/rev. and $f = 0.20$ mm/rev.

Table 3. Influence of burnishing force and feed on equivalent plastic strains.



3.4. Positron Annihilation Lifetime Spectroscopy

The obtained positron lifetimes and intensities of both components in individual samples slightly differed from each other. The short-lived component with an intensity of $80.5 \pm 0.3\%$ dominated in the spectra, and its lifetime of 168.7 ± 0.3 ps indicated its origin to mainly come from the positrons trapped at edge dislocations, where a lifetime of 162 was observed [54]. The lifetime of the second component was 360 ± 2 ps and corresponds to quite large vacancy clusters, i.e., approx. 15 vacancies [55]. However, it should be noted that this is an average value and that the vacancies can vary in size. Due to slight changes

in lifetimes and intensities, the differences between the samples are best reflected by a change in the mean lifetime (τ_{mean}), defined as:

$$\tau_{mean} = \frac{\tau_1 I_1 + \tau_2 I_2}{I_1 + I_2} \quad (2)$$

where τ_1 , τ_2 and I_1 , I_2 are the lifetimes and the intensities of the first and second components of the positron lifetime spectrum, respectively. An increase in τ_{mean} means an increase in the probability of positron trapping in vacancy clusters (most likely due to an increase in their concentration) and/or an increase in the average size of the clusters. It has been shown that this parameter is a good indicator of changes in the microhardness of the surface layer of samples [42].

The positron mean lifetime τ_{mean} increased slightly yet systematically with an increase in the burnishing force F (Figure 16). This dependence is consistent with the results of the microhardness measurements (Figures 12 and 13). On the other hand, the decreasing dependence of microhardness on burnishing feed f was not reproduced by the τ_{mean} . This suggests a different nature of the change in material defects when changing burnishing feeds than those induced by changing the burnishing force. The correlation of the dependence between τ_{mean} and burnishing feed with an analogous dependence for the Sa parameter suggests that the change in surface topography and roughness may also affect the positron implantation profile.

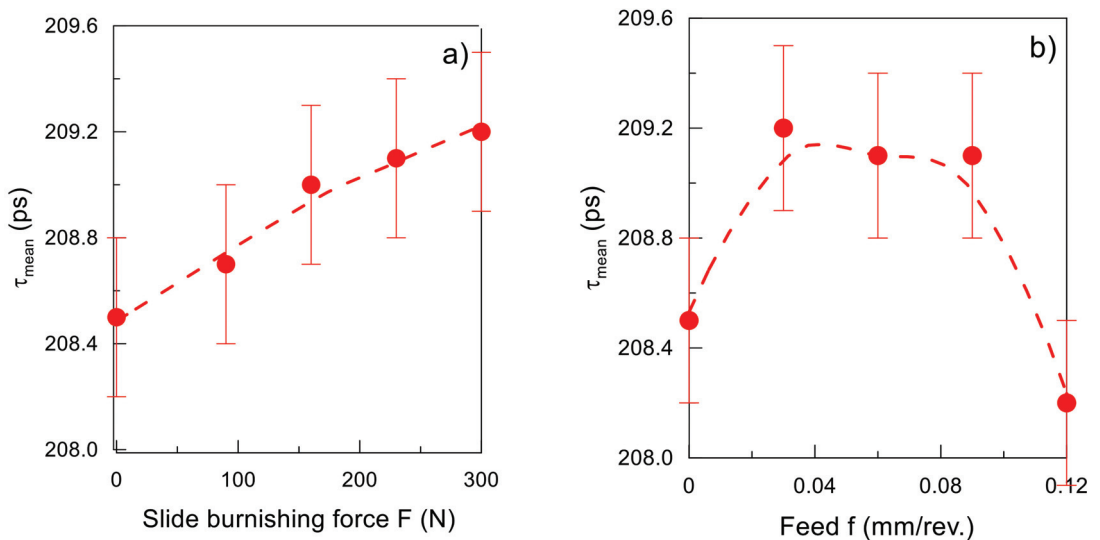


Figure 16. Mean positron lifetime τ_{mean} as a function of (a) burnishing force F ($f = 0.06$ mm/rev., $v_n = 35$ m/min, $i = 1$), (b) burnishing feed f ($F = 230$ N, $v_n = 35$ m/min, $i = 1$). The dashed lines are only an eye-guide.

4. Conclusions

Based on the results of slide burnishing of X6CrNiTi18 steel specimens conducted with variable technological parameters, the following conclusions can be drawn:

1. The use of the burnishing feed ranging $f = 0.03$ – 0.12 mm/rev. and slide burnishing force ranging $F = 90$ – 300 N led to a decrease in the analyzed surface roughness parameters (Sa , Sz , Sp , and Sv) in relation to their reference values (after grinding).
2. The surface shape after slide burnishing was plastically deformed. Changes in the shape and dimensions of the surface micro-irregularities were visible.
3. The obtained skewness value and kurtosis for the surface after slide burnishing mean that this surface can be considered a good bearing surface.

4. After slide burnishing, the surface layer was strengthened. The microhardness of the surface layer and depth of the hardened layer g_h increased. The maximum degree of strengthening e was obtained after slide burnishing conducted with $F = 230$ N and $f = 0.03$ mm/rev ($e = 42\%$), while the greatest increase in the hardened layer thickness of $g_h = 97.50$ μm was obtained for $F = 300$ N and $f = 0.06$ mm/rev.
5. The FEM simulations of the slide burnishing process demonstrated the favorable nature of the residual compressive stresses occurring in the subsurface zones. It was noticed that the slide burnishing force had a greater impact on the depth of the compressive residual stresses than the feed.
6. The plastic deformation wave moved the area of concentration of the maximum equivalent plastic strains from the axis of symmetry of the workpiece toward the end passes of the burnishing element.
7. The positron mean lifetime τ_{mean} increased slightly yet systematically with the increase in the burnishing force F ; with an increase in feed, those changes had a different nature.

Author Contributions: Conceptualization, A.S. and K.Z.; methodology, A.S., J.M., and R.Z.; software, J.M., K.C., R.Z., and M.G.; formal analysis, A.S., K.Z., and R.Z.; investigation, A.S., J.M., K.C., R.Z., and M.G.; data curation, A.S., J.M., and R.Z.; writing—original draft preparation, A.S., K.Z., J.M., K.C., R.Z., and M.G.; writing—review and editing, A.S., J.M., and R.Z.; visualization, A.S., J.M., and R.Z.; supervision, K.Z. and R.Z.; project administration, A.S. and K.C. All authors have read and agreed to the published version of the manuscript.

Funding: The project/research was financed in the framework of the project Lublin University of Technology-Regional Excellence Initiative, which is funded by the Polish Ministry of Science and Higher Education (Contract no. 030/RID/2018/19).

Informed Consent Statement: Not applicable.

Data Availability Statement: The data presented in this study are available on request from the corresponding author.

Conflicts of Interest: The authors declare no conflict of interest.

References

1. Silva-Alvarez, D.F.; Marquez-Herrera, A.; Saldana-Robles, A.; Zapata-Torres, M.; Mis-Fernandez, R.; Pena-Chapa, J.L.; Moreno-Palmerin, J.; Hernandez-Rodriguez, E. Improving the surface integrity of CoCrMo alloy by the ball burnishing technique. *J. Mater. Technol.* **2020**, *9*, 7592–7601. [[CrossRef](#)]
2. Das, T.; Erdogan, A.; Kursuncu, B.; Maleki, E.; Unal, O. Effect of severe vibratory peening on microstructural and tribological properties of hot rolled AISI 1020 mild steel. *Surf. Coat. Technol.* **2020**, *403*, 126383. [[CrossRef](#)]
3. Kulisz, M.; Zagórski, I.; Matuszak, J.; Klonica, M. Properties of the surface layer after trochoidal milling and brushing: Experimental and artificial neural network simulation. *Appl. Sci.* **2020**, *10*, 75. [[CrossRef](#)]
4. Zhang, P.; Lindemann, J.; Leyens, C. Shot peening on the high-strength wrought magnesium Alloy AZ80—Effect of peening media. *J. Mater. Process. Technol.* **2010**, *210*, 445–450. [[CrossRef](#)]
5. Maximov, J.T.; Duncheva, G.V.; Anchev, A.P.; Dunchev, V.P.; Ichkova, M.D. Improvement in fatigue strength of 41Cr4 steel through slide diamond burnishing. *J. Bras. Soc. Mech. Sci. Eng.* **2020**, *42*, 197. [[CrossRef](#)]
6. Zielecki, W.; Bucior, M.; Trzepicki, T.; Ochał, K. Effect of slide burnishing of shoulder fillets on the fatigue strength of X19NiCrMo4 steel shafts. *Int. J. Adv. Manuf. Technol.* **2020**, *106*, 2583–2593. [[CrossRef](#)]
7. Zaleski, K. The effect of shot peening on the fatigue life of parts made of titanium alloy Ti6Al4V. *Eksplot. Niezawodn.–Maint. Reliab.* **2009**, *4*, 65–71.
8. Nie, L.; Wu, Y.; Gong, H.; Chen, D.; Guo, X. Effect of shot peening on redistribution of residual stress field in friction stir welding of 2219 aluminum alloy. *Materials* **2020**, *13*, 3169. [[CrossRef](#)]
9. Dzierwa, A.; Gałda, L.; Tupaj, M.; Dudek, K. Investigation of wear resistance of selected materials after slide burnishing process. *Eksplot. Niezawodn.–Maint. Reliab.* **2020**, *22*, 432–439. [[CrossRef](#)]
10. Revankar, G.D.; Shetty, R.; Rao, S.S.; Gaitonde, V.N. Wear resistance enhancement of titanium alloy (Ti-6Al-4V) by ball burnishing process. *J. Mater. Res. Technol.* **2017**, *6*, 13–32. [[CrossRef](#)]
11. Nagit, G.; Slatineau, L.; Dodun, O.; Mihalache, A.M.; Ripanu, M.I.; Hrituc, A. Influence of some microchanges generated by different processing methods on selected tribological characteristics. *Micromachines* **2022**, *13*, 29. [[CrossRef](#)]
12. Swirad, S.; Pawlus, P. The effect of ball burnishing on dry fretting. *Materials* **2021**, *14*, 7073. [[CrossRef](#)]

13. Maheshwari, A.S.; Gawande, R.R. Influence of specially designed high—Stiffness ball burnishing tool on surface quality of titanium alloy. *Mater. Today Proc.* **2017**, *4*, 1405–1413. [[CrossRef](#)]
14. Swirad, S.; Wydrzynski, D.; Nieslony, P.; Krolczyk, G.M. Influence of hydrostatic burnishing strategy on the surface topography of martensitic steel. *Measurement* **2019**, *138*, 590–601. [[CrossRef](#)]
15. Ahmed, A.A.; Mhaede, M.; Basha, M.; Wollman, M.; Wagner, L. The effect of shot peening parameters and hydroxyapatite coating on surface properties and corrosion behavior of medical grade AISI 316L stainless steel. *Surf. Coat. Technol.* **2015**, *280*, 347–358. [[CrossRef](#)]
16. Skoczylas, A.; Zaleski, K. Selected properties of Surface layer of C45 steel parts subjected to laser cutting and ball burnishing. *Materials* **2020**, *13*, 3429. [[CrossRef](#)]
17. Matuszak, J.; Zaleski, K.; Skoczylas, A.; Ciecielag, K.; Kęcik, K. Influence of semi—Random and regular shot peening on selected surface layer properties of aluminum alloy. *Materials* **2021**, *14*, 7620. [[CrossRef](#)]
18. Zaleski, K.; Skoczylas, A. Effect of slide burnishing on the surface layer and fatigue life of titanium alloy parts. *Adv. Mater. Sci.* **2019**, *19*, 35–45. [[CrossRef](#)]
19. Kowalik, M.; Trzepieciński, T.; Kukielka, L.; Paszta, P.; Maciag, P.; Legutko, S. Experimental and numerical analysis of the depth of the strengthened layer on shafts resulting from roller burnishing with roller braking moment. *Materials* **2021**, *14*, 5844. [[CrossRef](#)]
20. Sidhu, A.S.; Singh, S.; Kumar, R.; Pimenov, D.Y.; Giasin, K. Prioritizing Energy-Intensive Machining Operations and Gauging the Influence of Electric Parameters: An Industrial Case Study. *Energies* **2021**, *14*, 4761. [[CrossRef](#)]
21. Rinaldi, S.; Rotella, G.; Umbrello, D. Experimental and numerical analysis of roller burnishing of Waspaloy. *Procedia Manuf.* **2019**, *34*, 65–72. [[CrossRef](#)]
22. Kluz, R.; Antosz, K.; Trzepieciński, T.; Bucior, M. Modelling the Influence of Slide Burnishing Parameters on the Surface Roughness of Shafts Made of 42CrMo4 Heat-Treatable Steel. *Materials* **2021**, *14*, 1175. [[CrossRef](#)] [[PubMed](#)]
23. Korzynski, M.; Zarski, T. Slide diamond burnishing influence stereometric structure of an AZ91 alloy. *Surf. Coat. Technol.* **2016**, *307*, 590–595. [[CrossRef](#)]
24. Nestler, A.; Schubert, A. Effect of machining parameters on surface properties in slide diamond burnishing of aluminum matrix composites. *Mater. Today Proc.* **2015**, *2*, 156–161. [[CrossRef](#)]
25. Toboła, D.; Brostow, W.; Czechowski, K.; Rusek, P. Improvement of wear resistance of some cold working tool steels. *Wear* **2017**, *382*, 29–39. [[CrossRef](#)]
26. Kato, H.; Hirokawa, W.; Todaka, Y.; Yasunaga, K. Improvement in Surface roughness and hardness for carbon steel by slide burnishing process. *Mater. Sci. Appl.* **2021**, *12*, 171–181. [[CrossRef](#)]
27. Kato, H.; Yamamoto, K.; Yasunaga, K. Nano-Crystallization of Steel Surface by Slide-Burnishing. *Key Eng. Mater.* **2020**, *841*, 48–53. [[CrossRef](#)]
28. Yang, S.; Zeng, W.; Yang, J. Characterization of shot peening properties and modelling on the fatigue performance of 304 austenitic stainless steel. *Int. J. Fatigue* **2020**, *137*, 105621. [[CrossRef](#)]
29. Chen, M.; Liu, H.; Wang, L.; Zhu, K.; Xu, Z.; Jiang, C.; Ji, V. Evaluation of the residual stress and microstructure character in SAF 2507 duplex stainless steel after multiple shot peening process. *Surf. Coat. Technol.* **2018**, *344*, 132–140. [[CrossRef](#)]
30. Menezes, M.R.; Godoy, C.; Buono, V.T.L.; Schwartzman, M.M.M.; Wilson, J.C.A.-B. Effect of shot peening and treatment temperature on wear and corrosion resistance of sequentially plasma treated AISI 316L steel. *Surf. Coat. Technol.* **2017**, *309*, 651–662. [[CrossRef](#)]
31. Gopi, R.; Saravanan, I.; Devaraju, A.; Loganathan, G.b. Investigation of shot peening process on stainless steel and its effects for tribological applications. *Mater. Today Proc.* **2020**, *22*, 580–584. [[CrossRef](#)]
32. Walczak, M.; Szala, M. Effect of shot peening on the surface properties, corrosion and wear performance of 17-4PH steel produced by DMLS additive manufacturing. *Arch. Civ. Mech. Eng.* **2021**, *21*, 157. [[CrossRef](#)]
33. Spadaro, L.; Herenu, S.; Strubbia, R.; Gomez-Rosas, G.; Bolmaro, R.; Rubio-Gonzalez, C. Effects of laser shock processing and shot peening on 253MA austenitic stainless steel and their consequences on fatigue properties. *Opt. Laser Technol.* **2020**, *122*, 105892. [[CrossRef](#)]
34. Bouzid Sai, W.; Lebrun, J.L. Influence of finishing by burnishing on surface characteristics. *J. Mater. Eng. Perform.* **2003**, *12*, 37–40.
35. Attabi, S.; Himour, A.; Laouar, L.; Motalebzadeh, A. Mechanical and wear behaviors of 316L stainless steel after ball burnishing treatment. *J. Mater. Res. Technol.* **2021**, *15*, 3255–3267. [[CrossRef](#)]
36. Duncheva, G.V.; Maximov, J.T.; Anchev, A.P.; Dunchev, V.P.; Argirov, Y.B. Improvement in Wear Resistance Performance of CuAl8Fe3 Single-Phase Aluminum Bronze via Slide Diamond Burnishing. *J. Mater. Eng. Perform.* **2022**, *13*, 2466–2478. [[CrossRef](#)]
37. Valiorgue, F.; Zmelty, V.; Dumas, M.; Chomienne, M.; Verdu, C.; Lefebvre, F.; Rech, J. Influence of residual stress profile and surface microstructure on fatigue life of a 15-5PH. *Procedia Eng.* **2018**, *213*, 623–629. [[CrossRef](#)]
38. Konefal, K.; Korzynski, M.; Byczkowska, Z.; Korzynska, K. Improved corrosion resistance of stainless steel X6CrNiMoTi17-12-2 by slide diamond burnishing. *J. Mater. Process. Technol.* **2013**, *213*, 1997–2004. [[CrossRef](#)]
39. Horodek, P.; Dryzek, J.; Wróbel, M. Positron annihilation study of defect induced by various cutting methods in stainless steel grade 304. *Tribol. Lett.* **2012**, *45*, 341–347. [[CrossRef](#)]
40. Skowron, K.; Dryzek, E.; Wróbel, M.; Cieniek, E. Laser peened austenitic stainless steel studied by positron annihilation spectroscopy. *Acta Phys. Pol. B* **2020**, *51*, 317–321. [[CrossRef](#)]

41. Zaleski, R.; Zaleski, K.; Gorgol, M.; Wiertel, M. Positron annihilation study of aluminum, titanium and iron alloys surface after shot peening. *Appl. Phys. A* **2015**, *120*, 551–559. [[CrossRef](#)]
42. Skoczylas, A.; Zaleski, K.; Zaleski, R.; Gorgol, M. Analysis of Surface properties of nickel alloy elements exposed to impulse shot peening with use of positron annihilation. *Materials* **2021**, *14*, 7328. [[CrossRef](#)] [[PubMed](#)]
43. Ashby, M.; Shercliff, H.; Cebon, D. *Material Engineering*; Galaktyka Publishing House: Łódź, Poland, 2011. (In Polish)
44. Becvár, F. Methodology of positron lifetime spectroscopy: Present status and perspectives. *Nucl. Instrum. Methods Phys. Res. Sect. B* **2007**, *261*, 871–874. [[CrossRef](#)]
45. Olsen, J.V.; Kirkegaard, P.; Pedersen, N.J.; Eldrup, M. PALSfit: A new program for the evaluation of positron lifetime spectra. *Phys. Stat. Solidi C* **2007**, *4*, 4004–4006. [[CrossRef](#)]
46. Djourelov, N.; Misheva, M. Source correction in positron annihilation lifetime spectroscopy. *J. Phys. Condens. Matter* **1996**, *8*, 2081. [[CrossRef](#)]
47. Maximov, J.T.; Duncheva, G.V.; Anchev, A.P.; Ganey, N.; Amudjev, I.M.; Dunchev, V.P. Effect of slide burnishing method on the surface integrity of AISI 316Ti chromium–nickel steel. *J. Bras. Soc. Mech. Sci. Eng.* **2018**, *40*, 194. [[CrossRef](#)]
48. Tayebi, N.; Polycarpou, A.A. Modeling the effect of skewness and kurtosis on the static coefficient of rough surfaces. *Tribol. Int.* **2004**, *37*, 491–505. [[CrossRef](#)]
49. Sedlacek, M.; Podgornik, B.; Vizitin, J. Influence of surface preparation on roughness parameters, friction and wear. *Wear* **2009**, *266*, 482–487. [[CrossRef](#)]
50. Sachin, B.; Rao, C.M.; Naik, G.M.; Puneet, N.P. Influence of slide burnishing process on the surface characteristics of precipitation hardenable steel. *SN Appl. Sci.* **2021**, *3*, 223. [[CrossRef](#)]
51. Maximov, J.T.; Anchev, A.V.; Dunchev, V.P.; Ganey, N.; Duncheva, G.V.; Selimov, K.F. Effect of slide burnishing basic parameters on fatigue performance of 2024-T3 high-strength aluminium alloy. *Fatigue Fract. Eng. Mater. Struct.* **2017**, *40*, 1893–1904. [[CrossRef](#)]
52. Skoczylas, A.; Zaleski, K. Study on the Surface Layer Properties and Fatigue Life of a Workpiece Machined by Centrifugal Shot Peening and Burnishing. *Materials* **2022**, *15*, 6677. [[CrossRef](#)]
53. Salahshoor, M.; Guo, Y.B. Surface integrity of magnesium-calcium implants processed by synergistic dry cutting-finish burnishing. *Procedia Eng.* **2011**, *19*, 288–293. [[CrossRef](#)]
54. Park, Y.-K.; Waber, J.T.; Meshii, M.; Snead, C.L.; Park, C.G. Dislocation studies on deformed single crystals of high-purity iron using positron annihilation: Determination of dislocation densities. *Phys. Rev. B* **1986**, *34*, 823. [[CrossRef](#)]
55. Ohkubo, H.; Tang, Z.; Nagai, Y.; Hasegawa, M.; Tawara, T.; Kiritani, M. Positron annihilation study of vacancy-type defects in high-speed deformed Ni, Cu and Fe. *Mater. Sci. Eng. A* **2003**, *350*, 95–101. [[CrossRef](#)]

Article

Influence of the Stainless-Steel Microstructure on Tribological Behavior and Surface Integrity after Ball Burnishing

Alejandra Torres ^{1,2}, Nuria Cuadrado ^{1,3}, Jordi Llumà ³, Montserrat Vilaseca ¹ and J. Antonio Travieso-Rodríguez ^{2,*}

- ¹ Eurecat, Centre Tecnològic de Catalunya, Unit of Metallic and Ceramic Materials, Plaça de la Ciència 2, 08243 Manresa, Spain
- ² Department of Mechanical Engineering, Universitat Politècnica de Catalunya, Av. Eduard Maristany 10-14, 08019 Barcelona, Spain
- ³ Department of Science and Material Engineering, Universitat Politècnica de Catalunya, Av. Eduard Maristany 10-14, 08019 Barcelona, Spain
- * Correspondence: antonio.travieso@upc.edu

Abstract: Burnishing is a plastic deformation process that reduces roughness while increasing hardness by introducing compressive residual stresses near the surface zone. These improvements will depend mainly on two fundamental variables: the applied load and the friction derived from the tool–surface interaction. Nevertheless, microstructural differences in the materials have not yet been considered within this interaction. This leads to a generalization of the process that can result in the failure of industrial components. Therefore, the aim of this work is to study the microstructural influence of the ball-burnishing process from a tribological perspective. Thus, martensitic and austenitic stainless steels were evaluated in terms of friction and surface integrity. The results show that parameterizing the process according to the tool–surface interaction is critical since improvements depend on friction as a function of the availability of plastic deformation of the crystallographic structures.

Keywords: ball burnishing; tribological interaction; stainless steel; friction coefficient; surface integrity

Citation: Torres, A.; Cuadrado, N.; Llumà, J.; Vilaseca, M.; Travieso-Rodríguez, J.A. Influence of the Stainless-Steel Microstructure on Tribological Behavior and Surface Integrity after Ball Burnishing. *Materials* **2022**, *15*, 8829. <https://doi.org/10.3390/ma15248829>

Academic Editor: Francesco Iacoviello

Received: 18 November 2022
Accepted: 8 December 2022
Published: 10 December 2022

Publisher's Note: MDPI stays neutral with regard to jurisdictional claims in published maps and institutional affiliations.



Copyright: © 2022 by the authors. Licensee MDPI, Basel, Switzerland. This article is an open access article distributed under the terms and conditions of the Creative Commons Attribution (CC BY) license (<https://creativecommons.org/licenses/by/4.0/>).

1. Introduction

Several industries make extensive use of steel components, among which are two different microstructure designations that are distinctive: austenitic AISI 316 and martensitic UNS S46500 stainless steels [1,2]. Since turning and milling are the conventional processes to machine these materials, the presence of irregularities and defects is inherent. This unevenness on metal surfaces causes considerable energy dissipation (friction), surface damage, and fracture during the service life of these components [3]. To minimize these issues, a reduction in roughness and an increase in mechanical properties are required [4,5]. Accordingly, numerous final machining operations have been proposed as applicable solutions, among them, the ball-burnishing process [6,7].

This procedure confers extra mechanical properties on the treated pieces, maintaining low costs and reducing execution times [7–10]. Properties such as strain hardening are amplified on a metal surface due to the plastic deformation prompted by the displacement of an indenter at a given pressure [7,10]. At the same time, wear, corrosion, and fatigue resistance are improved due to the newly induced residual compressive state [7,8]. Furthermore, the surface appearance is enhanced because of the decrease in roughness [6,10,11]. However, to achieve these advantages, process (overloading) and material limitations (loss of ductility) [12], which depend on the microstructure [13–15], must be overcome by using a satisfactory configuration [10–13,16–18]. Industrial components, such as lasting valve seals, pistons, bearing bores, and shafts for pumps, are burnished to reduce friction and noise levels and increase their service life [17,18]. Nevertheless, the burnishing of reinforced martensitic stainless steel (such as UNS S46500) components has not been studied so far,

enabling innovation in the improvement of this material's surfaces. UNS S46500 is a stainless steel characterized by the presence of Ni_3Ti nanometric precipitates in a martensitic matrix [2]. The few previous works quote the process's ability to introduce a deep, highly compressive layer into steel surfaces of this nature (martensitic), with a maximum value location (subsurface level) that is mainly influenced by the applied load and, to a lesser extent, by the speed, feed rate, and number of passes [13]. High loads result in shear stress toward the surface [12]. However, an undue load leads to excessive shear stress and therefore premature degradation of the surface finish [11,12,16–18]. Thus, experimental approaches and simplified predictable models have been conceptualized in order to set the parameters for the process in the search for good surface quality (smooth finish) and an optimum surface residual stress state. For instance, a prior study established a correlation between the roughness and the compressive layers. The interrelation between martensitic wear volume and residual stresses showed a strong inversely proportional linear dependence [19]. In most cases, an inverse relationship between the skewness parameter (S_{sk}) and wear volume is also recognized [19]. On the other hand, models have achieved a reliable roughness prediction, but only allow for qualitative adjustment (inaccurate results) in terms of residual stresses [20].

These hits and misses address the study of the burnishing-induced plastic deformation phenomenon as a tribological interaction in which it is essential to consider the first basic integral parameter that governs the process: friction. It is the tribo-contact between the burnishing ball and the machined material (roughness, microstructure, and mechanical properties) that determines the intensity of the strain-induced behavior at the material subsurface [12]. The high friction generated by an increase in the load leads to an induced stress state in the leading bulge similar to that induced by uniaxial compression loading. In contrast, the rear zone behind the indenter reacts as if a uniaxial tension is imposed. The higher the friction coefficient, the shallower the maximum shear stress at the sub-surface. Consequently, the plastic strain is concentrated in a thinner surface layer. Nevertheless, overextended friction values could lead to surface decline (fracture, tensile residual stresses) [12]. When friction decreases, the depth of the maximum shear strain increases (reducing the efficiency of cold-work nanostructuring) [12] and could eventually promote residual stress relaxation, reducing crack propagation inhibition [21]. Thus, the burnishing tribo-interaction defines the geometry (by the plastic deformation degree) and the maximum residual tensor location (by the shear-stress depth). In this regard, the tribological interaction between the ball and the rough surface during the ball-burnishing process is tackled numerically through simulations. Amini et al. [21] developed a model that takes into account the alterations of the friction coefficient between the ball and an extruded ferritic AISI 1038 steel surface. Depending on the defined preload, a low friction coefficient could not spawn significant advancements in the roughness and compression stress state. By contrast, a high friction coefficient could lead to an intensification in the pile-up and a decline in the stress state. This means that a factual friction coefficient must feed the models in order to reproduce and enhance the final surface integrity required for industrial components [19,21]. Moreover, Amini et al. proved that the direction of the highest induced residual stress concentration depends on the burnishing route, regardless of the initial stress state produced by machining [21]. The utmost burnishing effect is made in the perpendicular direction to the process, which means that the burnishing process can induce anisotropic properties in the target piece, in agreement with its final application [19,22]. Consequently, each parameter needs to be established according to the use of the piece, prioritizing the geometric (roughness) or metallurgic (hardness and compression stress state) characteristics [13,22,23]. Therefore, both the micro- and macro-responses to the process must be investigated through the microstructure's influence on friction behavior.

Consequently, this study reveals that surface improvements (finish and residual stress state) also depend on the tribological interaction degree between the ball and a defined microstructure. Thus, this tribological interaction is now conceptualized numerically by the friction coefficient. Accordingly, a reinforced martensitic stainless steel matrix and

an austenitic stainless steel textured surface are evaluated under the same milling and burnishing process conditions (in agreement with the machining conditions applied to the already characterized ferritic AISI 1038 steel [11,21,23–25]) in terms of friction and surface integrity using a scratch test procedure, 3D optical profilometry (surface finish), and X-ray diffraction (XRD) technique (residual stresses induced by cold working). The results show that under the same machining configurations, the induced surface integrity depends on the self-hardening coefficient due to the different tribo-contacts during the execution of the burnishing while providing reliable inputs for future integral modeling and process parameterization. Therefore, the interaction of the ball with an established macro-texture is not enough to generalize the process; it is necessary to consider the contact at the micrometric level to define the burnishing applicability.

2. Materials and Methods

2.1. Materials

Austenitic AISI 316 stainless steel (processed according to EN 10028-7-2016) and martensitic precipitation-hardened UNS S46500 stainless steel (aged according to ASTM A564/A564M) were selected for the present study.

2.1.1. Chemical Composition and Material Processing

Table 1 shows the chemical composition of the analyzed materials using spark emission spectrometry (SPECTROMAXx LMF08, SPECTRO, Kleve, Germany).

Table 1. Chemical composition of analyzed steels (in wt %).

Material	Fe	C	Mn	Ti	Cr	Ni	Mo
AISI 316	68.50 ± 0.03	0.02 ± 2 × 10 ⁻⁴	1.25 ± 4 × 10 ⁻³	0.01 ± 1 × 10 ⁻⁴	16.69 ± 0.01	9.92 ± 0.02	2.21 ± 0.005
UNS S46500	74.40 ± 0.02	0.01 ± 6 × 10 ⁻⁴	0.03 ± 3 × 10 ⁻⁴	1.70 ± 0.02	11.69 ± 0.03	10.89 ± 0.01	1.01 ± 6 × 10 ⁻³

2.1.2. Microstructural Characterization

After mechanical polishing to a mirror-surface finish (0.03 µm colloidal silica suspension), the AISI 316 and UNS S46500 samples were etched with aqua regia solution and Kalling I reagent, respectively. Microstructural characterization was performed using optical microscopy (Epiphot 200, Nikon, Tokyo, Japan) (Figure 1). The AISI 316 microstructure consisted of austenitic grains, some of which exhibited twinning, whereas the UNS S46500 stainless steel showed mainly a martensitic matrix.

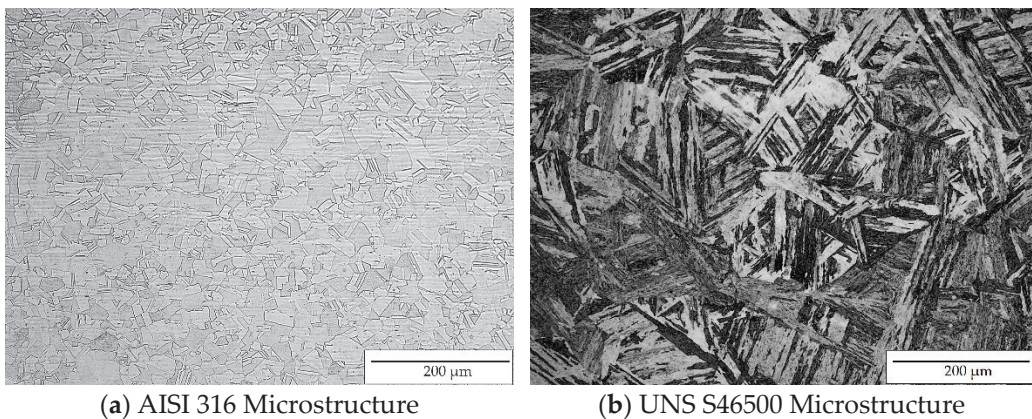


Figure 1. Stainless steel microstructural characterization.

2.1.3. Hardness

The hardness values of the austenitic AISI 316 and martensitic UNS S46500 stainless steels were 168 ± 6 HV and 521 ± 10 HV, respectively. The values were the mean of 10 measurements acquired using the Vickers microindentation test at a load of 1000 g (Micrometer HV1, Future Tech, FM-700, Tokyo, Japan). Ferritic AISI 1038 steel, used as a reference in this study, has a hardness value of $175 \text{ HV} \pm 10$ [21].

2.1.4. Surface Roughness

In the first step, the specimens were subjected to the milling conditions indicated in Table 2 using a CNC router milling machine (LAGUN 600, MAHER HOLDING, Legutiano, Spain). The macro-texture surface parameters after the milling and burnishing processes were acquired using an Alicona microscope (InfiniteFocusSL, Bruker, Karlsruhe, Germany) and further processed with image analysis software (Mountains 5.1.1.5944, Digital Surf, Besançon, France) according to the ISO-25178-2:2016 standard [26].

Table 2. Initial Milling Conditions.

Tool	Ball Mill UT Coating ϕ 10 [mm]—Two Teeth
Lateral pass width	0.30 [mm]
Depth of cut	0.20 [mm]
Feed rate	600 [mm/min]
Cutting speed	2000 [rpm]

In order to assess the surface changes due to the burnishing process, the 3D roughness parameters were computed for each of the studied materials. Accordingly, the arithmetical mean height (S_a), root mean square height (S_q), skewness (S_{sk}), kurtosis (S_{ku}), texture aspect ratio (S_{tr}), and ten-point height (S_{10z}) were processed.

2.2. Experimental Methods

2.2.1. Ball-Burnishing Process

Previous works on ferritic milled surfaces provided the path for the ball-burnishing configuration of the austenitic and martensitic microstructures [11]. Nevertheless, due to the low hardening coefficient and high hardness conferred by the martensitic matrix, UNS S46500 required a load increase in contrast to AISI 316. The ball-burnishing process was performed using a hard, metal ball with a 10 mm diameter adapted to the force transmission unit of the *Acustomill* tool (Spanish patent number 201730385) [27]. The process setup and its descriptive scheme are shown in Figure 2.

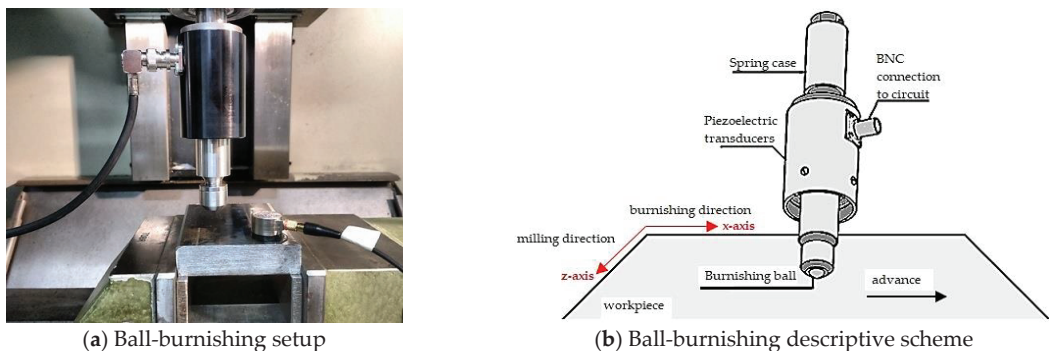


Figure 2. Ball-burnishing configuration.

The set assembled in the CNC router milling machine was displaced once in the perpendicular direction (x-axis) to the milling finish (z-axis) on a 10 mm × 10 mm patch for each material. The ball-burnishing operational parameters are summarized in Table 3.

Table 3. Ball-burnishing operational parameters.

Load	270 [N]/470 [N]
Feed rate	600 [mm/min]
Lateral pass width	0.30 [mm]
Vibration-assistance	No

2.2.2. Uniaxial Tensile Properties

The elastic properties were established using an ultrasonic method (Panametrics 5900 PR pulser, Olympus, Tokyo, Japan) and an oscilloscope (Hameg HM1508, RS, Corby, UK). The longitudinal plastic tensile properties were acquired using the conventional tensile test configuration (ISO 6892-1 standard) [28]. Three AISI 316 and five UNS S46500 tensile specimens fitted to the standard requirements (width = 6 mm and $L_c = 34$ mm) [28] were tested. The strain measurements (0.0067 s^{-1} until the failure) were obtained by a video-extensometer device. Table 4 shows the measured mechanical properties for both materials.

Table 4. Mechanical properties of the AISI 316 and UNS S46500 stainless steels.

Material	E [GPa]	ν	$\sigma_{0.2}$ [MPa]	UTS [MPa]	n
AISI 316	203.6 ± 0.4	$0.287 \pm 6 \times 10^{-4}$	327 ± 2	588 ± 1	$0.307 \pm 8 \times 10^{-4}$
UNS S46500	198.8 ± 0.4	$0.294 \pm 2 \times 10^{-4}$	1571 ± 8	1656 ± 5	0.029 ± 0.002

2.2.3. Friction Coefficient

The interaction of the tool and the textured surface was resolved according to the classical Hertzian theory of non-adhesive contact [29]. The pressure in the center of the contact region (p_0) was computed as a function of the normal force (F), the indenter radius (R), and the reduced elastic modulus (E^*), in agreement with Equation (1), and applied to the normal contact between a rigid sphere and an elastic half-space.

$$p_0^3 = 6F \cdot E^{*2} / \pi^3 \cdot R^2 \quad (1)$$

E^* was defined using Young's modulus (E_1, E_2) and the Poisson coefficient (ν_1, ν_2) of the interacting materials according to Expression (2):

$$1/E^* = [(1 - \nu_1^2)/E_1] + [(1 - \nu_2^2)/E_2] \quad (2)$$

The pressure values under the cited conditions in 2.2.1 were 2700 MPa for AISI 316 and 2700 MPa and 3100 MPa for UNS S46500. Friction test configurations were adopted for the sequence for the design of laboratory friction and wear proposed by the American Society of Materials (ASM) [30]. The coefficient of friction (COF) resulting from the interaction between the indenter ball and the milled surfaces of the studied steels was measured using a scratch test (Micro-Indentation Scratch Tester (MHT), CSM Instruments, Filderstadt, Germany). In order to achieve the same pressures at the laboratory scale, three linear scratches of 20 mm in length at 600 mm/min by a Tungsten carbide ball indenter of a 2.5 mm diameter were performed under dry conditions. The micro-indentation scratch tester (MHT) and the scratch test's descriptive scheme are shown in Figure 3.

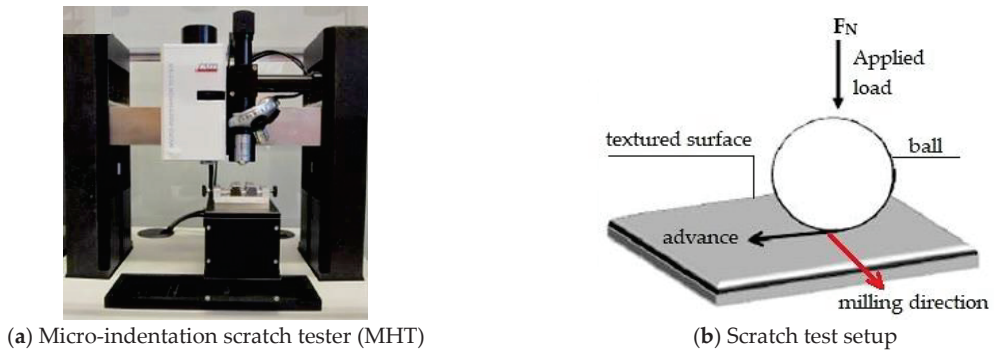


Figure 3. Scratch test configuration.

2.2.4. Surface Integrity Characterization

Residual Stresses

Residual stress components (σ_x , σ_z) up to a 4 μm depth were obtained using X-ray diffraction equipment (PANalytical—model X’Pert-PRO-MRD, UCDavis, Davis, CA, USA) according to the $\sin^2\Psi$ mode Ω -tilt method. The point detector (pixel size of 255 $\mu\text{m} \times 255 \mu\text{m}$) was assembled on a parallel plate collimator with a 0.27° angular opening and a planar graphite secondary monochromator. It is well known that machining and finishing operations can induce a phase transformation in austenitic steels. Then, the X-characterization of the milled and burnished austenitic and martensitic surfaces was performed in the reflection (211) of the bcc phase (martensite). The fcc phase corresponding to austenitic steels was not found up to a 4 μm depth. This indicates that martensitic transformation occurs during the milling process. Therefore, the final conditions on the austenitic surface are not influenced by a phase change.

3. Results

3.1. Friction

In order to evaluate the microstructural response to the tribo-contact during the burnishing process, the COF was computed for each of the studied stainless steels. Figure 4 summarizes the COFs generated by the interactions of austenitic and martensitic milled textured surfaces as a function of the contact pressure. The friction on the already characterized AISI 1038 ferritic steel textured surface [11] was established for comparison purposes.

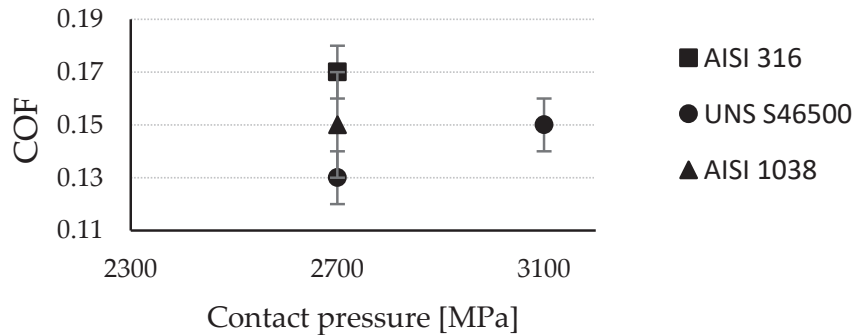


Figure 4. COF at different contact pressures.

Under the same ball-burnishing configuration, the steels’ microstructure responses were not coincident. The COF on austenitic steel (0.17) exceeded the COF on ferritic steel

(0.15) by 15%. The gap between the austenitic (0.17) and martensitic (0.13) stainless steels' COFs amounted to a 30 % difference. This means that the frictional shear stress and, therefore, the surface finish and compressive layer induced by the process will be substantially different. After load increment on the martensitic surface, the friction coefficient increased. Henceforth, it is convenient to take into account the tribological performance of the process (which includes the COF, initial roughness, and initial stress state of the target material [21]) in order to achieve a particular surface integrity depending on the machined microstructure.

3.2. Surface Integrity

3.2.1. Surface Roughness

Figure 5 displays the milled and burnished areas ($4 \text{ mm} \times 4 \text{ mm}$) of each target surface in order to provide the qualitative effect of the burnishing operation under the stated operational and tribological conditions.

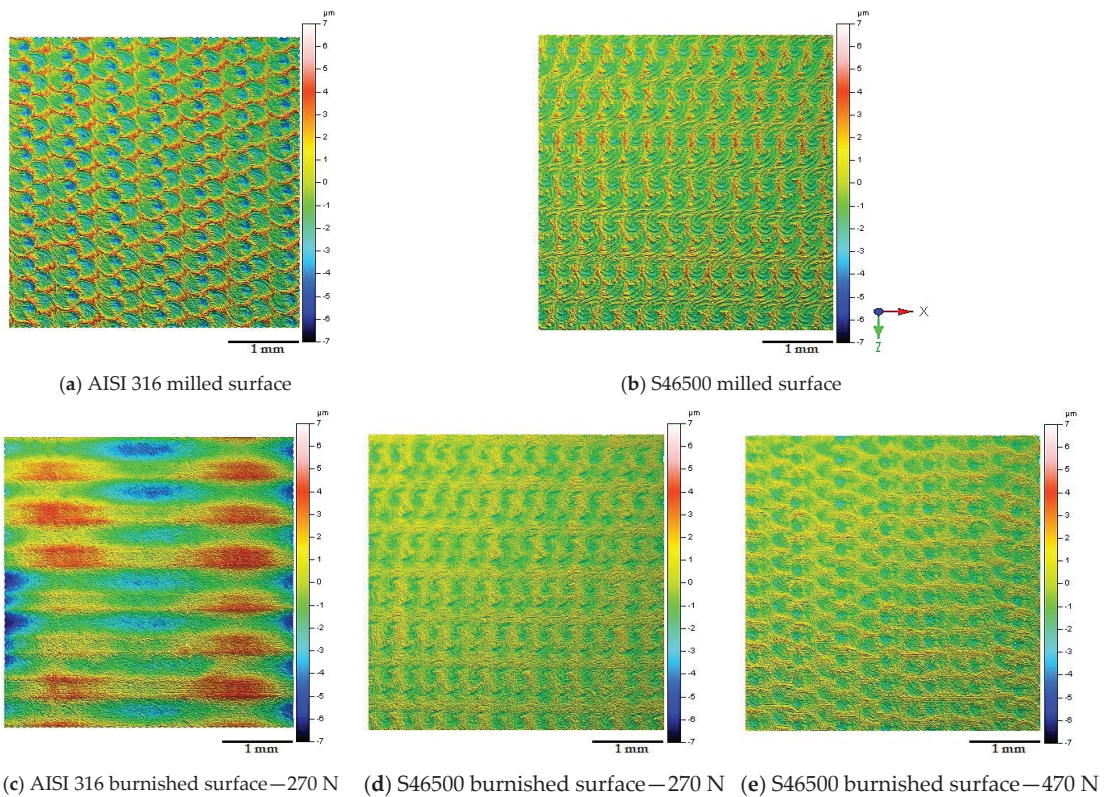


Figure 5. Textured surfaces after milling and burnishing processes at different contact pressures.

It can be observed that the macro-texture conferred by surface milling was more prominent on the austenitic stainless steel than on the martensitic stainless steel. However, under the same burnishing conditions, the texture of the austenitic milled surface disappeared and was replaced by an imprint of the burnishing tool (Figure 5c), showing the extent of the contact area, as well as the magnification of the interaction between the ball and the surface. Regarding the surface finish obtained on the martensitic steel, a softened texture can be seen in comparison with the AISI 316 surface under the same conditions (270 N). It can also be observed that the peaks intensified as the load increased (470 N). Figure 6

summarizes the macro-texture parameters obtained after milling and ball burnishing in order to provide a quantitative description of the analyzed surface modifications.

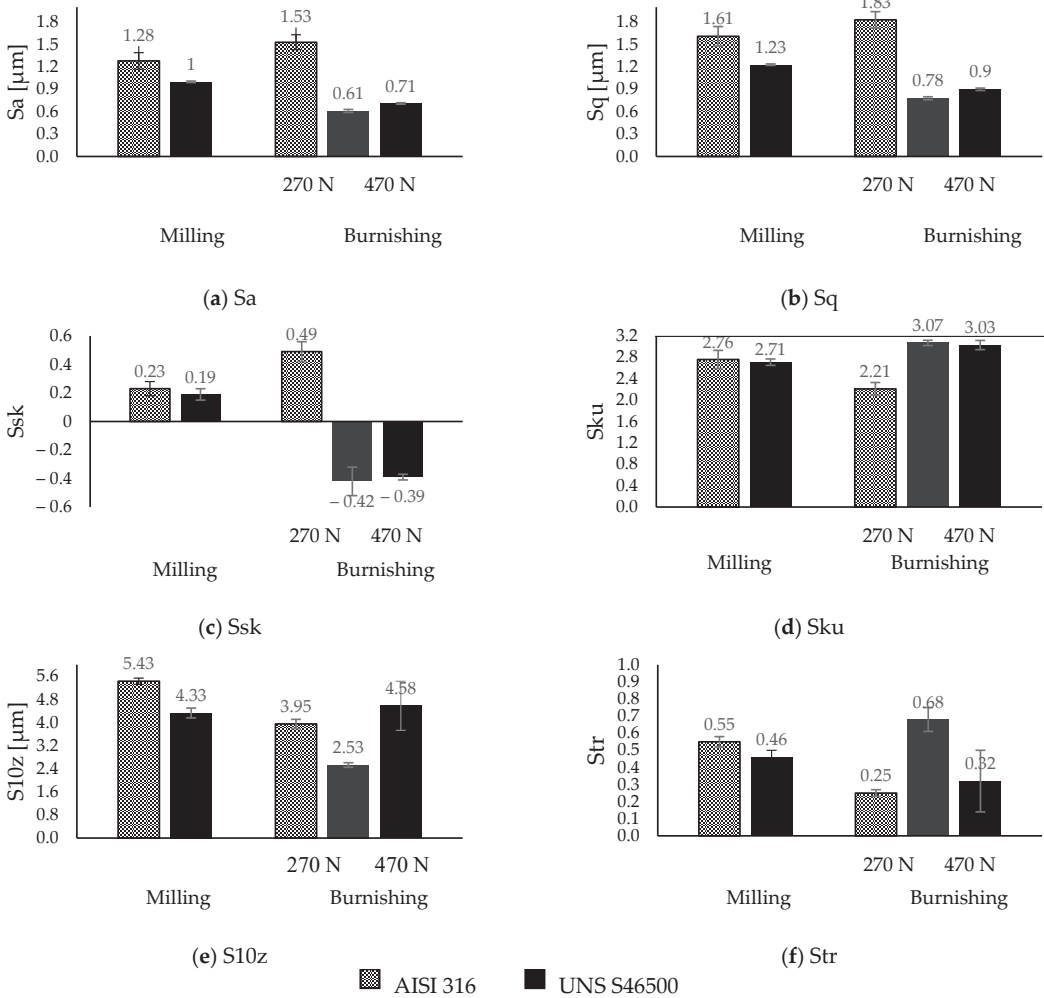


Figure 6. Textured surfaces after milling and burnishing processes at different contact pressures.

Based on the height parameters Sa and Sq, a normal distribution of heights ($Sa = 0.8 Sq$) was evidenced under milling conditions for both materials. This observation was corroborated by the skewness values ($Ssk \sim 0$) under the same milling conditions. This tendency varied after ball burnishing. Thus, under the same load conditions, the statistical asymmetry after burnishing on AISI 316 stainless steel showed a mass distribution skewed to below the mean plane ($Ssk > 0$), while the surface of UNS S46500 stainless steel is skewed to above the main plane ($Ssk < 0$) in equal proportion. The load increment on the second one slightly varied under this condition. With regard to kurtosis ($Sku \sim 3$), it was observed that the austenitic surface became a non-abrupt platykurtic condition, whereas the martensitic surface responded with a better fit to a Gaussian distribution despite the load increase.

The S10z parameter provides a practical criterion for the statistical behavior of the height. It reveals that the five-point peak height and five-point pit height were 20% more prominent on the austenitic surface. However, this was reduced by 36% on martensitic

stainless steel and only 20% on austenitic stainless steel after ball burnishing. This was not consistent with Figure 5c. Since the austenitic crystal lattice had a higher deformation capability (reflected in the COF value), a redistribution of the surface texture was evidenced. Thus, the new average roughness profile may have been displaced below the level of the initial valleys, leading to a loss of tolerance. On the other hand, increasing the pressure on the martensitic surface led to the generation of a pile-up and consequently an increase in the S10z parameter (~15%). This elucidates the marked differences in the surface roughness depending on the stainless-steel microstructure during the ball-burnishing process.

The directional properties quantified through the Str parameter were shown to be moderately isotropic (Str ~ 0.5) after milling for both surfaces. After ball burnishing, the austenitic surface became directionally anisotropic (Str < 0.3), whereas under the same conditions, the martensitic surface increased its isotropy. At a 470 N load, the martensitic surface became anisotropic.

3.2.2. X-ray Difraccction

Figure 7 summarizes the parallel (σ_x) and perpendicular (σ_z) tensor components of the burnishing path obtained after the milling and burnishing processes.

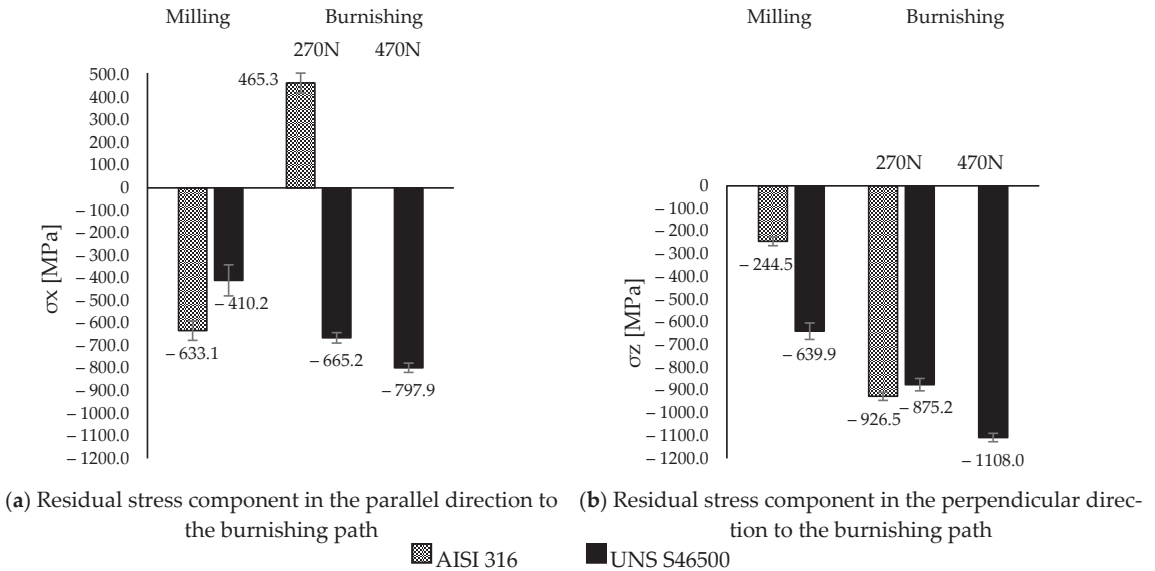


Figure 7. Residual tensor after milling and burnishing processes on stainless steel surfaces.

The residual tensor component introduced by milling on the austenitic surface was 61% higher in the parallel direction (σ_x) than in the perpendicular direction (σ_z) to the burnishing path. The opposite occurred on martensitic and ferritic surfaces [21], where the perpendicular component exceeded the parallel component by 45%. In this manner, although the feed of the milling cutter on the austenitic surface increased the tensor component in its perpendicular direction, on the martensitic surfaces, it increased the tensor parallel to the milling route. However, after burnishing, on the austenitic surface there was a substantial increase in the lower compressive state component (σ_z) (4 times greater), whereas in the other direction (x-axis), a tensile state was induced. This extended the hypothesis of an anisotropic state independent of the initial tensor on ferritic surfaces [21] to austenitic surfaces. When burnishing was performed on the martensitic surface, the initial anisotropy was reduced by 9% at a 270 N load, whereas with increasing load, the anisotropy increased by 30%. Therefore, the residual isotropy was qualitatively in agreement with the directional isotropy (Str) for both materials after the burnishing process (Section 3.2.1).

Regarding the skewness (Ssk), there was no evidence of a directly proportional relationship with the surface tensor, as mentioned in another study [19]. Depending on the microstructure, the surface integrity varied considerably under the same burnishing conditions.

4. Discussion

The results elucidate the microstructural impact of the tribological behavior between the burnishing ball and the steel surface. According to Kuznetsov et al. [12], friction constitutes a fundamental parameter to obtain significant improvements or unwanted effects on surface integrity. Therefore, the consequences of high friction involve the generation of uniaxial tensile stress in the rear zone behind the indenter [12], as well as the increase in the pile-up [21]. However, based on the tribo-contact effects on the selected microstructures, the definitions of high and low friction are ambiguous. The allowable tribo-interaction ranges within the process will be given by the limited plastic deformation of the microstructure. In fact, the stress state conditions after ball burnishing with a 270 N load on the austenitic steel show the presence of a tensile state in the burnishing path direction (x-axis), which is in agreement with the approach of Kuznetsov et al. [12]. A clearly detrimental austenitic surface (reflected in the increase in the macro-texture parameters; Figure 6) and a residual anisotropic state [21,22] beyond the compressive condition (Figure 7) were evidenced. As a consequence, a new finish distribution (skipping tolerances) with valleys and peaks defined by the ball track (Figure 5c) was displayed. This high plastic deformation capacity of the austenitic crystallographic lattice allowed for low surface integrity. Nevertheless, under the same conditions (270 N), the textured martensitic stainless-steel surface offered a contrasting microstructural response to the ball-burnishing process. The lower COF (Figure 4) as an effect of the martensitic matrix, determined the displacement of the peaks toward the milling valleys, conferring uniformity on the surface (Figure 5d), whereas the compressive surface state improved in both directions according to the initial trend established by the milling finish. A higher COF (0.17 after load increment) led to the compressive layer's relocation to the surface (as stated by Kuznetsov et al. [12]), a heightening anisotropy (Figure 7), and an onset of pile-up (Figure 5e, Figure 6e). As seen in Figure 7, the new pressure exerted on the martensitic surface was far from inducing a tensile state in the parallel direction on the burnishing path (which defines high friction [12]) so the hypothesis of high tribo-interactions on this material was limited to the pile-up initiation. Therefore, defining the burnished component's functionality is pertinent. The process configuration must be prioritized, either the contact interactions with other components (roughness) [3] or the exposure to the corrosion, wear, and fatigue conditions whose resistance improves through the generation or increment of the surface compressive residual state [6–8,10,11]. It should be noted that determining the compressive layer's thickness (sub-surface residual state) as a function of the tribo-interaction degree may modify the high-friction hypothesis of martensitic steels established in this study. Nevertheless, excessive tribo-interaction (overloading) within the process must be prevented in order to allow the treated microstructures to retain some degree of ductility, as cited by Kuznetsov et al. [12].

5. Conclusions

In the quest to enhance the surface finish and mechanical properties of stainless steels using a ball-burnishing process, the tribological performance of the process must be considered first. The interaction capability between the ball and the machined surface, quantified by the friction coefficient, defines the surface integrity improvements of the burnished components. Neither the friction value nor its effects are trivial during the ball-burnishing setup. Therefore, to obtain a balance between roughness reduction, design tolerance, and directional and residual anisotropy, or to prioritize one of them, a pertinent COF must be defined. Hence, the present work provides the starting point for a new methodology to parameterize the process based on its interaction (tribological characteristics) at the time when the friction coefficient is delivered as a factual variable in the current numerical methodologies. In addition, this study provides the friction effect on two previously tex-

tured microstructures (austenitic and martensitic surfaces) in order to contribute to the guidelines for future ball-burnishing crystalline plasticity numerical conceptualization while demonstrating the process's capability of enhancing the surface integrity of martensitic stainless steel UNS S46500. The microstructural deformation mechanisms at the local level due to the different tribo-contacts (dislocations, crystallographic orientations, recrystallization, hardness modification, self-hardening), as well as their effect on the thickness of the compressive layer, should be addressed in further research.

Author Contributions: Conceptualization, A.T., N.C., J.A.T.-R., J.L. and M.V.; methodology, A.T., N.C., J.A.T.-R. and J.L.; software, A.T., N.C., J.A.T.-R. and J.L.; validation, N.C., J.A.T.-R., J.L. and M.V.; formal analysis, A.T., N.C., J.A.T.-R., J.L. and M.V.; investigation, A.T., N.C.; J.A.T.-R. and J.L.; resources, N.C., J.A.T.-R., J.L. and M.V.; data curation, N.C.; writing—original draft preparation, A.T. and N.C.; writing—review and editing, A.T., N.C., J.A.T.-R., J.L. and M.V.; visualization, A.T. and N.C.; supervision, N.C., J.A.T.-R., J.L. and M.V.; project administration, M.V.; funding acquisition, J.A.T.-R., J.L. and M.V. All authors have read and agreed to the published version of the manuscript.

Funding: This research was funded by Eurecat's "Vicente López" PhD grant program and by the Ministry of Science and Innovation of Spain, through grant PDC2022-133596-I00, which is greatly appreciated.

Institutional Review Board Statement: Not applicable.

Informed Consent Statement: Not applicable.

Data Availability Statement: The raw/processed data required to reproduce these findings cannot be shared at this time as they also form part of an ongoing study.

Conflicts of Interest: The authors declare no conflict of interest.

Abbreviations

Ssk	Skewness
XRD	X-ray diffraction
Sa	Arithmetical mean height
Sq	Root mean square height
Sku	Kurtosis
Str	Texture aspect ratio
S10z	Ten-point height
Lc	Parallel length
E	Young's modulus
ν	Poisson coefficient
$\sigma_{0.2}$	Yield strength
UTS	Ultimate tensile strength
n	Self-hardening coefficient
p_0	Pressure in the center of the contact region
F	Normal force
R	Indenter radius
E*	Reduced elastic modulus
ASM	American Society of Materials
COF	Coefficient of friction

References

1. Kumar, N.; Kumar, M.; Sharma, N.; Shah, P.; Ranganath, M.S.; Mishra, R.S. *Mechanical Properties and Microstructural Analysis of AISI 316 During Different Types of Welding Processes: A Review Manufacturing*; IJAPIE: New Delhi, India, 2017.
2. Magnabosco, R.; Alonso-falleiros, N. Effect of Aging Heat Treatment H950 and H1000 on Mechanical and Pitting Corrosion Properties of UNS S46500 Stainless Steel. *Mater. Res.* **2018**, *22*, 1–9. [[CrossRef](#)]
3. El-Tayeb, N.S.M.; Low, K.O.; Brevern, P.V. Influence of roller burnishing contact width and burnishing orientation on surface quality and tribological behaviour of Aluminium 6061. *J. Mater. Process. Technol.* **2007**, *186*, 272–278. [[CrossRef](#)]
4. Callister, W.D.; Rethwisch, D.G. *Materials Science and Engineering*, 9th ed.; Wiley: Hoboken, NJ, USA, 2014.

5. Michael, A.; Shercliff, H.; Cebon, D. *Materials: Engineering, Science, Processing and Design*, 1st ed.; Butterworth-Heinemann: Cambridge, UK, 2007; ISBN 978-0-7506-8391-3.
6. Yang, S.; Li, W. *Surface Finishing Theory and New Technology*; Springer: Berlin/Heidelberg, Germany, 2018. [[CrossRef](#)]
7. Bouzid Saï, W.; Lebrun, J.L. Influence of finishing by burnishing on surface characteristics. *J. Mater. Eng. Perform.* **2003**, *12*, 37–40. [[CrossRef](#)]
8. Konefal, K.; Korzyński, M.; Byczkowska, Z.; Korzyńska, K. Improved corrosion resistance of stainless steel X6CrNiMoTi17-12-2 by slide diamond burnishing. *J. Mater. Process. Technol.* **2013**, *213*, 1997–2004. [[CrossRef](#)]
9. Kułakowska, A.; Patyk, R.; Bohdal, Ł.; Kałduński, P.; Chodór, J.; Koszalińska, P. Wybrane aspekty ekoinnowacyjnej obróbki nagniataniem, Środkowo-Pomorskie Towarzystwo Naukowe Ochrony Środowiska. *Rocz. Ochr. Sr.* **2016**, *Tom 18*, 478–492.
10. Balland, P.; Tabourot, L.; Degre, F.; Moreau, V. Mechanics of the burnishing process. *Precis. Eng.* **2013**, *37*, 129–134. [[CrossRef](#)]
11. Jerez-Mesa, R. *Study and Characterization of Surface Integrity Modification after Ultrasonic Vibration-Assisted Ball Burnishing*; Mechanics of materials [physics.class-ph]; Université Paul Sabatier, Toulouse III: Toulouse, France, 2018.
12. Kuznetsov, V.P.; Smolin, I.Y.; Dmitriev, A.I.; Tarasov, S.Y.; Gorgots, V.G. Toward control of subsurface strain accumulation in nanostructuring burnishing on thermostrengthened steel. *Surf. Coat. Technol.* **2016**, *285*, 171–178. [[CrossRef](#)]
13. Chomienne, V.; Valiorgue, F.; Rech, J.; Verdu, C. CIRP Journal of Manufacturing Science and Technology Influence of ball burnishing on residual stress profile of a 15-5PH stainless steel. *CIRP J. Manuf. Sci. Technol.* **2016**, *13*, 90–96. [[CrossRef](#)]
14. Jerez-Mesa, R.; Fargas, G.; Roa, J.J.; Llumà, J.; Travieso-Rodríguez, J.A. Superficial effects of ball burnishing on trip steel AISI 301LN sheets. *Metals* **2021**, *11*, 82. [[CrossRef](#)]
15. Zaborski, A.; Tubielewicz, K.; Major, B. Contribution of burnishing to the microstructure and texture in surface layers of carbon steel. *Arch. Metall* **2000**, *45*, 333–341.
16. Capilla-González, G.; Martínez-Ramírez, I.; Díaz-Infante, D.; Hernández-Rodríguez, E.; Alcántar-Camarena, V.; Saldaña-Robles, A. Effect of the ball burnishing on the surface quality and mechanical properties of a TRIP steel sheet. *Int. J. Adv. Manuf. Technol.* **2021**, *116*, 3953–3964. [[CrossRef](#)]
17. Mahajan, D.; Tajane, R. A Review on Ball Burnishing Process. *Int. J. Sci. Res. Publ.* **2013**, *3*, 1–8.
18. Malleswara Rao, J.N.; Chenna Kesava Reddy, A.; Rama Rao, P.V. The effect of roller burnishing on surface hardness and surface roughness on mild steel specimens. *Int. J. Appl. Eng. Research.* **2011**, *1*, 777–785.
19. Dzierwa, A.; Markopoulos, A.P. Influence of ball-burnishing process on surface topography parameters and tribological properties of hardened steel. *Machines* **2019**, *7*, 11. [[CrossRef](#)]
20. Zhang, T.; Bugtai, N.; Marinescu, I.D. Burnishing of aerospace alloy: A theoretical—experimental approach. *J. Manuf. Syst.* **2015**, *37*, 472–478.
21. Amini, C.; Jerez-Mesa, R.; Travieso-Rodríguez, J.A.; Llumà, J.; Estevez-Urra, A. Finite element analysis of ball burnishing on ball-end milled surfaces considering their original topology and residual stress. *Metals* **2020**, *10*, 638. [[CrossRef](#)]
22. Jerez-mesa, R.; Travieso-rodríguez, J.A.; Landon, Y.; Dessein, G.; Llumà-fuentes, J. Comprehensive analysis of surface integrity modi fication of ball-end milled Ti-6Al-4V surfaces through vibration-assisted ball burnishing. *J. Mater. Process. Technol.* **2019**, *267*, 230–240. [[CrossRef](#)]
23. Travieso-Rodríguez, J.A.; Jerez-Mesa, R.; Gómez-Gras, G.; Llumà-Fuentes, J.; Casadesús-Farràs, O.; Madueño-Guerrero, M. Hardening effect and fatigue behavior enhancement through ball burnishing on AISI 1038. *J. Mater Res. Technol.* **2019**, *8*, 5639–5646. [[CrossRef](#)]
24. Jerez-Mesa, R.; Landon, Y.; Travieso-Rodríguez, J.A.; Dessein, G.; Llumà, J.; Wagner, V. Topological surface integrity modification of AISI 1038 alloy after vibration-assisted ball burnishing. *Surf. Coat. Technol.* **2018**, *349*, 364–377. [[CrossRef](#)]
25. Mesa, R.J.; Gómez, G.; Travieso-Rodríguez, J.A.; Llumà, J.; Casadesús, O.; Madueño, M. *Estudio Experimental del Efecto de Bruñido Sobre la Vida a Fatiga de Probetas de Acero AISI 1038*; Mecánica: Elche, Spain, 2016.
26. *ISO 25178-2:2016*; Geometrical Product Specifications (GPS)—Surface Quality Texture: Areal—Part 21: Terms, Definitions and Surface Quality Parameters Indication of Surface Texture. ISO: Geneva, Switzerland, 2016.
27. Jerez-Mesa, R.; Gómez Gras, G.; Travieso-Rodríguez, J.A.; Llumà, J. *Ultrasonic Vibration-Assisted Ball Burnishing Tool*; Universitat Politècnica de Catalunya: Barcelona, Spain, 2018.
28. *ISO 6892-1:2009*; Metallic Materials—Tensile Testing—Part 1: Method of Test at Room Temperature, European Committee for Standardization. ISO: Geneva, Switzerland, 2009.
29. Popov, V.L. Tratamiento riguroso del contacto—El Contacto Hertziano. In *Principios y Aplicaciones de la Mecánica de Contacto en Tribología, Fricción y Adherencia*, 3rd ed.; Martín-Martínez, J.M., Moreno-Flores, S., Eds.; Publicaciones de la Universitat d’Alacant: Alicante, España, 2015; pp. 79–85.
30. Gresham, R.M. *ASM HANDBOOK Volume 18: Friction, Lubrication, and Wear Technology*; Tribology & Lubrication Technology; Totten, G.E., Ed.; Portland State University: Portland, OR, USA, 2018; Volume 74, p. 84.

Article

Analysis of Ultrasonic Vibration-Assisted Ball Burnishing Process on the Tribological Behavior of AISI 316L Cylindrical Specimens

Eric Velázquez-Corral ^{1,*}, Vincent Wagner ², Ramón Jerez-Mesa ¹, Jordi Lluma ³,
J. Antonio Travieso-Rodríguez ¹ and Gilles Dessein ²

¹ Department of Mechanical Engineering, Universitat Politècnica de Catalunya, 08019 Barcelona, Spain; ramon.jerez@upc.edu (R.J.-M.); antonio.travieso@upc.edu (J.A.T.-R.)

² Laboratoire Génie de Production, École Nationale d'Ingénieurs de Tarbes, 47 Avenue d'Azereix, 65000 Tarbes, France; vincent.wagner@enit.fr (V.W.); gilles.dessein@enit.fr (G.D.)

³ Department of Science and Materials Engineering, Universitat Politècnica de Catalunya, 08019 Barcelona, Spain; jordi.lluma@upc.edu

* Correspondence: eric.velazquez.corral@upc.edu

Abstract: In this study, we analyzed the effects of vibration assistance, combined with a ball burnishing process, in terms of topology, residual stresses, and tribological properties on 316L shafts. The burnishing variables consisted of the variation of the input force, the number of passes, and the activation of the vibration assistance, which is based on a 40 kHz frequency and 8 μm of vibration amplitude, derived in a screening design of three factors. The results show that the medium–high level of burnishing force, high level of the number of passes, and the activation of the vibration assistance are the best options in order to improve the average roughness, the microstructure, the increase in the compressive residual stresses, and the wear enhancement, besides all variables being significant in the *p*-value analysis through ANOVA. Statistically, the vibration-assisted ball burnishing improved the average roughness by 2.9%, enlarged the von Mises stress on the surface by 11.5% and enhanced the wear resistance of a 316L shaft and WC-Co ball contact up to 7.3%.

Citation: Velázquez-Corral, E.; Wagner, V.; Jerez-Mesa, R.; Lluma, J.; Travieso-Rodríguez, J.A.; Dessein, G.

Analysis of Ultrasonic Vibration-Assisted Ball Burnishing Process on the Tribological Behavior of AISI 316L Cylindrical Specimens.

Materials **2023**, *16*, 5595. <https://doi.org/10.3390/ma16165595>

Academic Editor: Pawel Pawlus

Received: 3 July 2023

Revised: 3 August 2023

Accepted: 10 August 2023

Published: 12 August 2023



Copyright: © 2023 by the authors. Licensee MDPI, Basel, Switzerland. This article is an open access article distributed under the terms and conditions of the Creative Commons Attribution (CC BY) license (<https://creativecommons.org/licenses/by/4.0/>).

Keywords: vibration-assisted ball burnishing; tribology; residual stresses

1. Introduction

Stainless steels are one of the most used materials for biomedical applications, such as prostheses or orthopedic implant manufacturing, through additive deposition [1,2] or traditional machining. However, for this purpose, most of the final workpieces need to enhance their mechanical properties, such as the wear resistance due to the friction present in the joints of a hip prosthesis [3] or lower corrosion by coating applications [4]. In particular, AISI 316L austenitic SS presents excellent corrosion resistance, high ductility, and good mechanical properties but poor resistance to wear, which often requires a surface upgrade. This enhancement is determined by surface integrity modification and improvement, so finishing operations have become a suitable solution for biomedical steel treatment.

Some surface deforming processes, such as burnishing or shot peening, have been widely used during the last few years to achieve the standard required by the biomedical community in terms of high wear resistance, durability improvement, and surface topology enhancement [5]. Mechanical surface treatments such as shot peening and burnishing are increasingly applied to biomedical parts to achieve the high requirements of surface finishing, surface hardness, wear resistance, and fatigue durability [6,7]. In particular, the use of the ball burnishing process in stainless steel parts for biomedical applications has grown significantly during the last few years [8–10]. This process consists of a cold deformation process, where the material is compressed using a rolling ball, obtaining a

more regular and smoother surface and generating a hardened surface while keeping constant the dimensions of the part treated [11]. The ball burnishing can be divided into the elastoplastic flow of the material and the residual sink-in effect on each burnishing passage. Some of the authors reported a higher resistance to the wear between two sliding surfaces, a friction reduction, and a topology improvement by a material's Gaussian redistribution [12–14]. Concerning the residual stresses, many authors declared the beneficial effects of increasing the compressive residuals in reducing crack propagation after applying a ball burnishing process [15–17]. In fact, there is a consensus that the increase in the burnishing force derives from a larger amount of residual compressive stresses at the surface, which benefits in slowing the crack propagation at the surface, enlarging its resistance to wear [18] or fatigue [19]. The ball burnishing process has also been described as an effective methodology to enhance wear resistance and reduce the coefficient of friction between two colliding surfaces [18]. More specifically, it was seen that the most important parameters to improve both properties were the burnishing force applied onto the surface and the number of passes performed, resulting in a hardness increase and a wear reduction. Attabi et al. [20,21] analyzed the wear enhancement and the surface integrity of 316L ball burnished specimens, finding a wear improvement of up to 65.2% compared to baseline material. It was also found that the increase in the number of passes had a big influence on surface hardness, which has a relation with friction reduction, while the improvement in resultant roughness also helped to reduce the coefficient of friction. However, it is also reported that despite all applied ball burnishing inputs helping to improve roughness, only the optimal ones reduced the friction compared to the baseline material.

One evolution of ball burnishing is vibration-assisted ball burnishing (VABB), which is based on the base physics of ball burnishing and the acoustoplasticity phenomenon studied by Blaha and Langenecker et al. [22]. The combination of both results in a larger material deformation due to the superimposition of the vibratory component on the deforming force applied onto the surface, deriving in a relaxation of the quasi-static stresses of the surface and, therefore, being easier to deform during the process. Teimouri et al. [23] studied the effects of the ultrasonic ball burnishing process on aluminum AA6061-T6 and concluded that the addition of the vibration assistance, using a 5 and 10 μm of frequency amplitude, improved the surface roughness by 15% and the superficial hardness by a 24%, respectively. In addition, it was found that the value of the compressive residual stresses increased deeper heights due to the ultrasonic impacts caused by the tool, and through this, the degree of mechanical working increased, and further refinement in microstructure was observed. This observation was also seen by Liu et al. [24], who described the greater influence of the microstructure, treated with VABB, as a consequence of the local severe deformation originated by the tool's vibration when assisted.

Despite a lot of information available about the influence that ball burnishing has in terms of wear enhancement and the improvement of compressive residual stresses, there is a void space for vibration-assisted ball burnishing. Most VABB investigations are focused on surface integrity and residual stress enhancement, but not so many on wear enhancement or friction reduction. Generally, VA demonstrated positive applications to enhance the surface integrity factors within manufacturing processes, but its contribution in terms of tribo-characteristics is still controversial and not sufficiently investigated. For this reason, the main objective of this work is to analyze the impact analysis of the vibration assistance within a ball-burnishing process in terms of wear resistance enhancement and friction reduction on 316L ball-burnished stainless-steel shafts while confirming surface enhancement by this phenomenon. The results will be processed through an Analysis of Variance (ANOVA). This statistical tool permits quantifying the mean effects of the factors used on the response variables and evaluating the significance of each factor, then giving valuable information to determine the VA contribution to the final properties.

2. Materials and Methods

2.1. Specimens' Preparation

The machining and finishing processes of the AISI 316L stainless steel used for this test (chemical composition shown in Table 1) are performed in a 3-axis CNC Machine Lathe "Pinacho SE 200 × 750" (Pinacho, Castejón del Puente, Spain).

Table 1. Nominal chemical composition of 316L SS.

Material		Chemical Composition by Element (wt. in %)								
AISI 316L	Fe Bal.	C 0.03	Si 1.00	Mn 2.00	P 0.05	S 0.02	Cr 17.50	Ni 11.50	N 0.10	Mo 2.00

The machining conditions prior to the burnishing were kept constant for all the specimens, being 60 m/min as cutting speed, 0.20 mm/rev as feed per turn, and a final diameter of 13 mm achieved in 3 passes. The insert used for this process was a rhombic 80° shape with a negative geometry CNMG120408-MM-YG213, made of carbide with a CVD TiCN+Al₂O₃+TiN coating, the clearance angle is set to 6°, and the rake angle to −6° once is assembled on the PCLNR 2020K 12 shank tool. The average quality roughness prior to burnishing was set to 1.5 ± 0.2 μm in order to obtain significant differences between all burnishing conditions applied to the specimens.

2.2. Ball Burnishing Equipment and Specimens

The vibration-assisted ball burnishing system used for this investigation is composed of the burnishing tool (the union of a base armor, a pre-load unit force based on a calibrated spring, one ultrasonic actuation unit built by a resonant ceramic piezoelectric excited to 40 kHz of frequency and an operational head formed by one 10 mm diameter 100Cr6 chromium steel ball at the top) and an external 40 kHz wave generator both plugged by a UFH connector, characterized by Fernández-Osete et al. [25]. The amplitude of vibration obtained at the top of the tool by the resonance of the system is about 8 μm.

The definitive force applied onto the surface is a combination of multiple forces: the forces due to the irregularities of the material when the feed movement is performed, the force related to the vibration of the sonotrode when the assistance is applied, and the preadjusted force of the spring lodged. The final result of the process is shown in Figure 1.

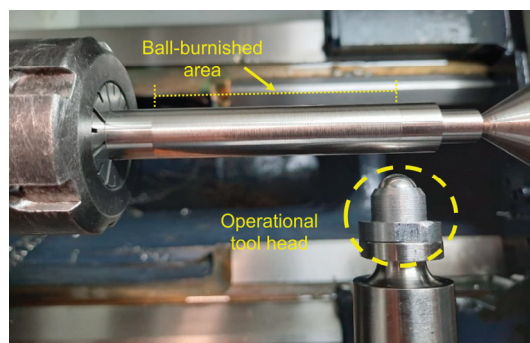


Figure 1. Burnishing tool head and specimen manufactured.

2.3. Experimental Campaign and Specification

Based on the research group's previous experience with the process on other materials such as AISI 1045 [12] or AISI301LN [26], a screening design of experiments was planned with the following factors and their corresponding levels:

- Burnishing force F_b : three numerical levels, from 80 N to 160 N with a central point in 120 N. Attabi et al. [21] found a surface degradation at slim plates with 240 N and a

10 mm ball, so by applying the radius corrections (in the function of ball mechanical and geometrical properties of the specimen) it is decided to apply a maximum force of 160 N to avoid surface degradation.

- Number of passes n_p : three numerical levels, from 1 to 5 passes with a central point in 3 passes.
- Frequency of the VA f : two different levels, being 0 or 40 kHz. Treated as a categorical variable.
- Burnishing speed: one level, being 2000 mm/min for all the specimens.
- Burnishing feed: one level, being 0.15 mm/rev for all the specimens.

The final experimental campaign resulted in a total of 12 specimens, and all combinations are shown in Table 2.

Table 2. Design of Experiments for the burnishing operation.

Nomenc.	F_b (N)	n_p	f (kHz)
80-1-40	80	1	40
80-3-0	80	3	0
80-5-0	80	5	0
80-5-40	80	5	40
120-1-0	120	1	0
120-3-0	120	3	0
120-3-40	120	3	40
120-5-40	120	5	40
160-1-0	160	1	0
160-1-40	160	1	40
160-3-40	160	3	40
160-5-0	160	5	0

The tribological procedure performed is based on Velázquez-Corral et al. previous work [12] and the ASTM G132-96 standard [27], see Figure 2. The conditions used are the following:

- Indenter characteristics: WC-Co 6 mm ball of diameter, with 600 GPa and 0.22 values for Young's modulus and Poisson's ratio, respectively.
- Specimen characteristics: AISI 316L SS 13 mm cylinder of diameter, with 200 GPa and 0.25 values for Young's modulus and Poisson's ratio, respectively.
- Physical inputs: Force applied of 20 N, making an imprint length of 20 mm, sliding at 10 cm/s during 5 min of testing.

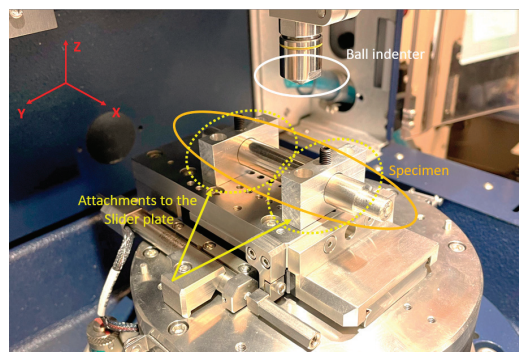


Figure 2. Tribology setup used for the testing.

During the execution of each test, the friction and input force is tracked and the cof (Coefficient of friction) is calculated in real-time at 100 Hz sampling frequency. The final acquisition is filtered using a low-pass filter, using a minimum-order filter with a stopband

attenuation of 60 dB and compensating the delay introduced by the filter itself, with a passband frequency of 20 Hz. After that, the total worn imprint is measured using the 3D non-contact profilometer Alicona with a 10 nm of resolution, obtaining a 3D surface and measuring the volume difference between this surface and the one prior to the tribology testing, which defines the wear of the test in volumetric units.

2.4. Topology Acquisition

In order to acquire the surface and perform roughness measurements, it was used a non-contact 3D profilometer ALICONA Infinite Focus G5 (Alicona Imaging GmbH, Raaba, Austria) with an adaptive focus. The amplitude parameters measured prior to the tribology test are:

- Sa: Represents the arithmetical deviation of the roughness profile of the sampling length.
- Sq: Represents the root mean square of the heights.

2.5. Microstructure Analysis

Finally, Scanning Electron Microscopy (SEM) analysis was performed in order to see the microstructure evolution of the material for different burnishing, using an EVO HD15 by ZEISS (Zeiss and Quorum technologies, Oberkochen, Germany) equipped with an energy-dispersive X-ray spectrometer (SEM-EDX). Typical working parameters were an accelerating voltage of 15 kV and a working distance of 10 mm.

2.6. Residual Stress

In order to evaluate the residual stresses onto the treated surfaces, it is used an X-ray diffraction method based on applying Bragg's law while quantifying the change in the inter-planar spacings. The experimental application was performed with a V- α anode, 600 s of exposition time, and 20 measures. The post-processing method was curve fitting vs. $\sin^2(\psi)$.

The application of the test was delivered in terms of the residual stress tensor. In which σ_i corresponds to the tangential direction and σ_{ii} corresponds to the axial direction of the specimen's generatrix (see Figure 3), τ_{12} and τ_{21} are the shear stresses.

$$\sigma = \begin{bmatrix} \sigma_i & \tau_{12} \\ \tau_{21} & \sigma_{ii} \end{bmatrix} \quad (1)$$

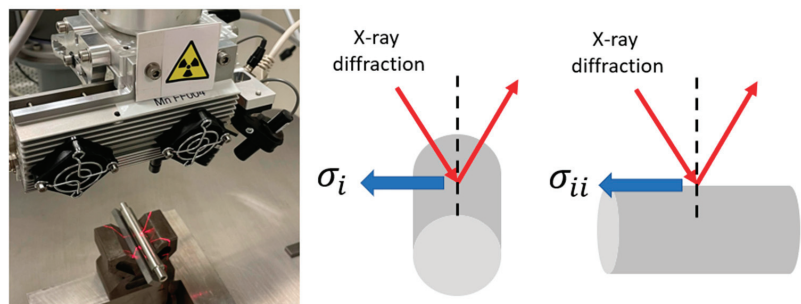


Figure 3. Residual stresses measurement unit and setup for cylindrical samples.

However, another indicator may be included to analyze the general residual stress state of the surface, the von Mises stress which is described in Equation (2).

$$\sigma_{vm} = \sqrt{\sigma_i^2 + \sigma_{ii}^2 - \sigma_i \sigma_{ii} + 3\tau_{12} \tau_{21}} \quad (2)$$

3. Results

3.1. Topography

The Sa and height parameters were measured according to the ISO 25178 Standard [28]. The results are presented in Figure 4.

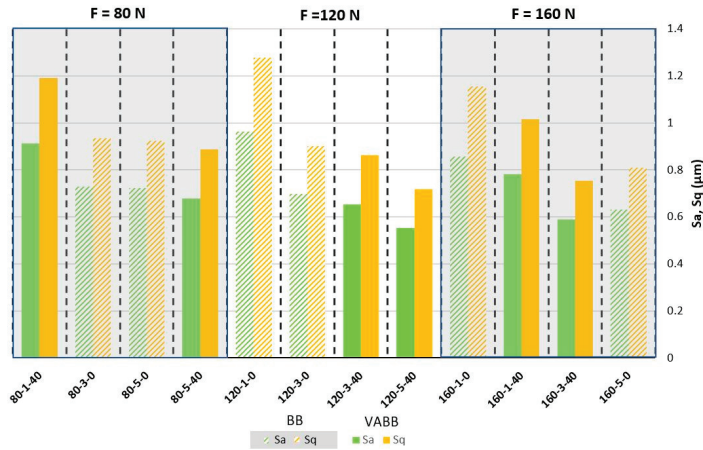


Figure 4. Three-dimensional Roughness results for 316L specimens.

Results show a reduction of the Sa and Sq when the number of passes is increased, and the vibration assistance is activated. It is clear that there is a decreasing tendency of the average and maximum roughness from lower levels of the number of passes plus the non-addition of vibration assistance to high levels of the number of passes and the vibration assistance activated [29]. It seems that the number of passes has the more significant importance in order to enhance the surface in terms of roughness, having a great association with the vibration assistance. When looking more carefully, it can also be appreciated that when those medium–high levels of the number of passes are applied, the input force seems to enhance the topology when this one is increased. For example, comparing the specimens 80-5-40 vs. 120-5-40 or 120-3-40 vs. 160-3-40, it is noticed a roughness improvement by only increasing the input force. The best combinations obtained are 120-5-40, 160-3-40, and 160-5-0 (obtaining 63%, 61%, and 58% of Sa enhancement, respectively, as it is shown in Table 3), in that order, which may indicate that the number of passes is the most significant parameter and, combined with the vibration assistance and a high force, boosts the final surface roughness improvement.

Table 3. Sa improvement for each specimen compared to the initial surface after machining.

Nomenc.	Sa (µm)	ΔSa (%)
80-1-40	0.912	39
80-3-0	0.729	51
80-5-0	0.723	52
80-5-40	0.678	55
120-1-0	0.963	36
120-3-0	0.699	53
120-3-40	0.654	56
120-5-40	0.554	63
160-1-0	0.856	43
160-1-40	0.781	48
160-3-40	0.590	61
160-5-0	0.631	58

As can be seen, roughness is reduced by increasing the degree of plastic deformation by means of the augmentation of the three burnishing inputs analyzed. In particular, the increase in the burnishing force seems to not exceed the material limit at high forces, meaning that there could still be scope for force increase to obtain optimized roughness. The roughness trend is descending if an equal number of passes and VA value pairs are compared, as is seen by analyzing 120-3-0 with 80-3-0 or 160-3-40 with 120-3-40, so it is confirmed the positive effect of increasing the burnishing force to enhance the resultant roughness. In similar studies, Attabi et al. [21] obtained average roughness improvement with 240 N of force with a 10 mm ball but also experienced texture deterioration (compared to this optimal value) if the ball diameter was reduced, thus increasing the equivalent contact pressure. The descending trend of roughness when the number of passes and the VA is applied is evident and agrees with the bibliography [30,31]. In terms of force and number of passes increase, improvement can be explained by the fact that the ball is rolling and smoothing out the bulged edges of the initial machining or the previous pass, so the probability of deforming the asperities is increased by augmenting the force and performing successive burnishing passes; thus, the surface is being smoothed at each pass. Concerning the VA, the kinematic energy added to the process enhances the work-hardening but to a lower degree than the burnishing force [32], explaining why VABB roughness values are better than BB when the same level of plastic deformation (burnishing force and several passes) is applied.

The mean effects and the interaction plots of the model, taking the Sa as the output, are presented in Figure 5. First of all, the p -value analysis determines that the number of passes, the burnishing force, and the vibration assistance, in that order, are the most important and significant parameters due to having a p -value lower than 5%. However, none of the interactions analyzed are significant enough to be considered, so they are rejected as a hypothesis. The 0.000 p -value registered for the number of passes means the huge impact that this variable has on the final value of the average roughness.

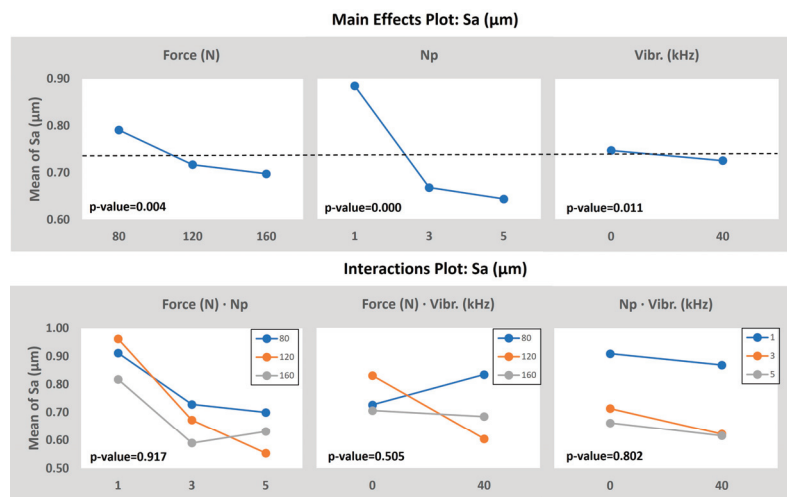


Figure 5. ANOVA results taking the Sa as the output value.

As it was alleged in the experimental results section, the increase in the force and the number of passes, plus the addition of the vibration assistance, improve the final topology of the specimen after the ball burnishing process within the parameter interval chosen in this study.

3.2. Microstructure Analysis

The microstructures shown in Figure 6 correspond to a cross-sectional part of samples 80-5-0 for ball burnishing (BB) and 80-5-40 for vibration-assisted ball burnishing (VABB). It also extracted a non-burnished sample section in order to make a comparison between the three resultant microstructures. The general images (see Figure 6, 1st column) show a perspective of austenite grains, which defines the general microstructure of these AISI 316L specimens.

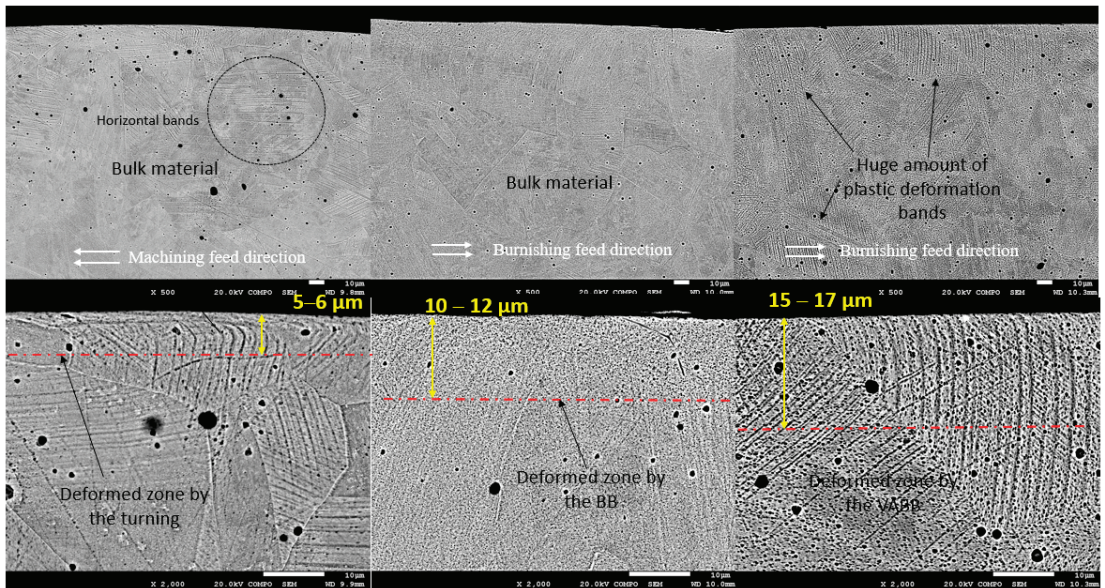


Figure 6. Cross-section microstructures by columns: 1st corresponds to machined surface, 2nd column corresponds to the 80-5-0 sample (BB), and 3rd column corresponds to the 80-5-40 sample (VABB).

Firstly, the M specimen reveals some plastic deformation boundaries at the coating due to the shearing induced during the turning. It is visible that the grain orientation of these remarked boundaries (see Figure 6 first column) is quite more horizontal compared to other specimens at 30 μm of depth, showing no excessive deformation compared to other processes. More in detail, when the coating is zoomed, it can be revealed that there is a change in the plastic deformation boundaries in the same direction as the turning feed, estimated on 5–6 μm of depth and then defining the affectation profundity. Regarding the BB specimen, it can be seen a major density of plastic deformation traces, or plane slides, in higher depths compared to the M specimen. According to the bibliography [33], these bands present in all 316L surfaces are caused by different degrees of plastic deformations on the austenite grains. These deformations are compatible with a twinning formation microstructure on a nanometric scale [33], which could induce nanograin refinement and, combined with a dislocation network similar to the present on these specimens, could derive hardness enhancement and the increase in the compressive residual stresses due to the exerted pressure on the surface. Looking in detail at the top coating, it is visible that the deformation caused by the ball is pushing the material toward the center of the specimen, thus homogenizing the surface compactness and achieving a depth of affectation around 10–12 μm . Finally, the VABB specimen shows a huge density of plastic deformation traces along the entire surface. This mechanism of deformation is enhanced by the application of the VA, which combines the acoustoplastic phenomena plus the superimposition of dynamic and static forces during the process, thus exerting more pressure and deforming

the material. In this case, the coating deformation due to the VABB process is estimated at 15 μm , but the higher presence of parallel bands at deeper depths points to a higher effect.

3.3. Residual Stress

The residual stress measurement was made to obtain both stress components, σ_i and σ_{ii} , and Equation (2) was applied in order to calculate von Mises's stress value. The results obtained are presented in Figure 7.

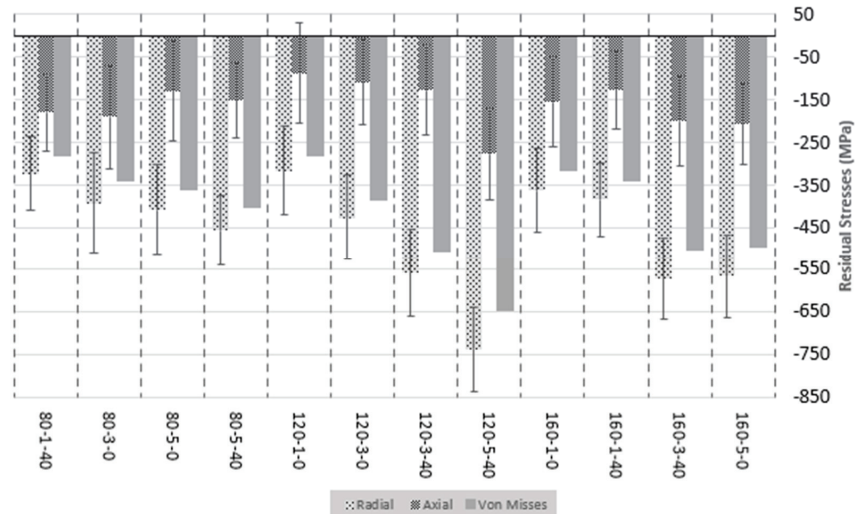


Figure 7. Residual stress results for all the combinations.

First of all, results show that compressive (negative) stress values are present in all specimens, which may prevent crack growth in fatigue regimes, confirming that positive property. In addition, no positive value of stress is reported, which is caused by the shearing suffered during the previous machining process. Therefore, the burnishing totally counteracts the effect of the machining in terms of stress, having a value near the 550 MPa of von Mises stress.

Secondly, it is also reported that the tangential direction of stress measuring, σ_i is higher than the axial direction of stress, σ_{ii} . This can be explained due to the fact that the burnishing input force applied in a normal direction onto the surface (X-axis in a lathe) is way higher than the dragging force applied due to the feed of the tool (Z-axis in a lathe) during the burnishing operation and, therefore, causing more deformation that relates directly to the stress.

The increase in the residual stresses is directly associated with the amount of strain induced during the plastic deformation. Several investigations pointed out that the pressure exerted on the surface was the most important parameter to induce compressive residual stresses [34,35] by means of augmenting the amount of strain and the depth of affectation. Indeed, this plastic deformation is previously described as a combined effect of static force, the number of passes exerted, and the superimposition of the dynamic component of the force (VA). The process consists of inducing this plastic deformation (after surpassing the initial elastic deformation) through the rolling ball pressure onto the surface, axial and tangential to the generatrix of the shaft. The material flow and redistribution caused by shearing provoke an increment in the stress-strain field in the surface and subsurfaces. Next, the work hardening produced is caused by the dislocation movement and rearrangement of the inner crystals, known as dislocation density evolution, and concludes at grain refinement by means of dynamic recrystallization. When the rolling ball is no longer pressurizing, the remains of the stress are relaxed and converge to residual stress. In

terms of the number of passes, some investigations declared that the parameter is not significant enough [17]. However, as was seen with roughness results previously presented, burnishing force values used seem to be quite low to heavily deform the AISI 316L texture. Residual stresses are directly dependent on the plastic deformation degree and work hardening and increase when a higher number of passes is applied [36]. Regarding the VA, Teimouri et al. [37] state that VA enhances the plastic flow stress by means of dislocation drag and thermal activation, concluding that increasing the vibration amplitude results in further strain and strain rate because of a greater value of deformation radius (augmented by the increase in the kinetic energy) and impact velocity. Furthermore, the author points out that the increased ultrasonic energy density at further vibration amplitude contributes to the reduction of activation energy and subsequent flow stress. The recrystallization is also enhanced by the softening effect during the plastic deformation, thus enhancing the strain induced [37]. This affirmation correlates with the results obtained in terms of microstructure, where the VABB specimen showed a higher amount and greater effect of deformation mechanisms than the BB specimen. Therefore, the increase in plastic deformation caused by the VA is greater and favorable for the mechanical properties and surface integrity factors [23]. In general, residual stresses are defined as a complex distribution of mechanical, thermal, and metallurgical effects simultaneously that often actuate synergistically.

When analyzing the tendency of the von Mises calculated values, it is quite clear that the effect enhances the induction of higher negative values when the combination of a high number of passes and the activation of vibration assistance is applied. The force, in this case, seems to be less significant than the other input parameters, but it has the desired effect as it increases. The best combinations are 120-5-40, 160-3-40, and 120-3-40, demonstrating that also the VABB enhances more than BB. The mean effects and the interaction plots of the model, taking the Residual stresses of both components measured and the von Mises stress as the output, are presented in Figure 8.

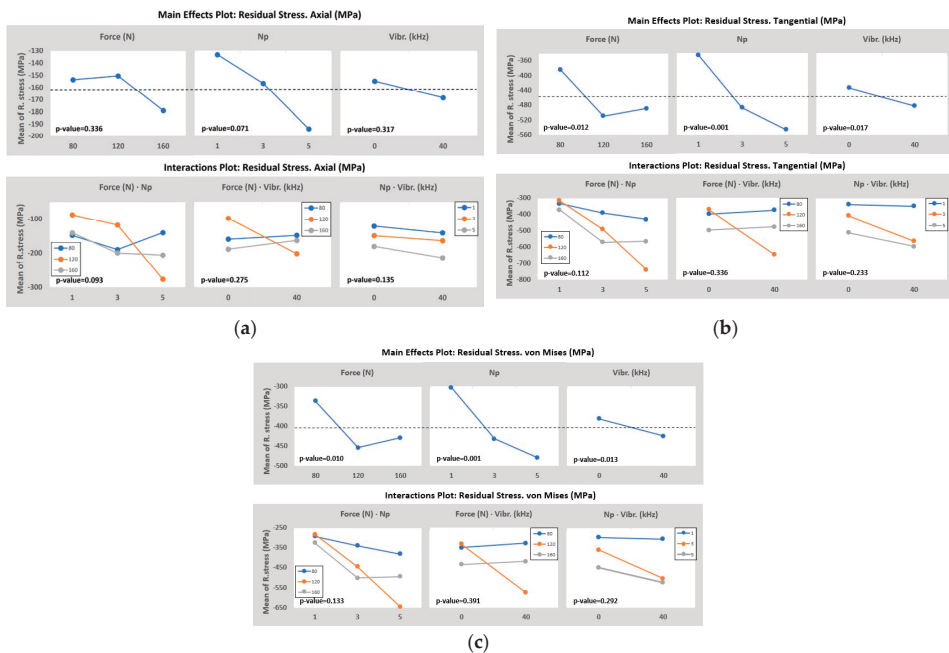


Figure 8. ANOVA results taking the: (a) Axial; (b) Tangential; (c) von Mises; residual stress as the output value.

The results of the tangential direction (see Figure 8b), corresponding to σ_i , determine that the number of passes, burnishing force, and the addition of the vibration assistance, in that order, are significant. When the number of passes increases, the value of the residual stress increases, and the same is applied to the vibration assistance. In the case of the force, it is appreciated that the best point is 120 N instead of 160 N. This happens due to the best combination reported is 120-5-40 and is especially higher than the rest, so the mean of the 120 N force group is higher than 160 N. However, looking at the evolution of both groups, if the design of experiments considered higher levels of force (160 N or more) with a high number of passes and vibration assistance, the expected result may be higher than the 120-5-40. The results of the Axial direction (see Figure 8a), corresponding to σ_{ii} , determine that the number of passes, the interaction of the burnishing force plus and the number of passes, and the interaction of the burnishing force plus and the number of passes, in that order, are the most important parameters but being not significant enough. All p -values reported are higher than 0.05. This concludes that no parameter used has a special effect on the second direction and other input parameters. This could be explained by the fact that burnishing deformation is mainly performed in the normal direction to the surface, while the forces in the perpendicular direction to the surface are lower and then provokes less deformation. This effect was also observed by Chomienne et al. [17], who observed that plastic deformation is not that intensive in both directions during a single revolution. In the circumferential direction, the work material is always deformed in the same direction, whereas in the axial direction, the work material is deformed in two different directions. Von Mises stress values (see Figure 8c) are almost completely influenced by the first component of the stress σ_i , so both plots' graph results are essentially the same, changing a bit the p -values rates but not the grade of significance.

In terms of residual stresses, it is reported an increase in the von Mises residual stress at the surface by increasing the burnishing force and the number of passes, also applying VABB instead of BB to enhance them, which is estimated in an 11.5% increase. These results are within the scope because increasing the burnishing force causes a larger plastic deformation and is boosted by the vibration amplitude of the assistance. The number of passes has been reported as another very influential parameter to enhance the residual stresses within a burnishing process [38]. In conclusion, the combination 120-5-40 is the best to maximize the compressive residual stresses, either tangential or axial to the specimen, thus the equivalent von Mises stress.

3.4. Frictional Performance

The tests performed under dry conditions in the tribometer concluded that all tests have a coefficient of friction evolution between 0.6 and 1.1 (see Figure 9). The cof evolution corresponds to the evolution along all the tests and the stationary period. All tests executed show a fast increase during the first seconds of the test, even arriving to surpass the $cof = 1.0$, and then start decreasing while the initial track is formed and the formation of the debris from the surface asperities of each specimen.

Therefore, as can be seen in Figure 9, the first 40–60 s of execution is part of the transitory state, and then the stationary state initiates. When analyzing the results, it can be seen that VABB specimens (continuous lines) are evolving homogeneously during the first stages and, especially after 4–5 s, show similar results. In fact, after 5 s of testing, all specimens enter the first stage of stabilization within the transient mode; they will start to decrease the friction force along the time but in the same trend until the 40–60 s of the steady-state period. Figure 10a shows that the maximum peak of friction corresponds to the BB specimen (dotted lines); when this first stabilization point is reached, BB remains systematically over the VABB, pointing to a friction reduction when using VA. This apparent improvement caused by friction reduction could be related to the higher degree of deformation of the AISI 316L microstructure for VABB specimens, where it was observed a major presence of deformation bands at major depths, which is caused by a bigger accumulation of deformation energy that could be a symptom of a dynamic recrystallization activation. Therefore,

grain refinement derives a hardening effect and higher residual stresses. As is seen in previous sections, VA increases the values of compressive residual stress, so it makes sense that friction reduction is enhanced due to the VA application. Following the previous explanation, it seems that VA may enhance friction reduction during the steady-state period, and this trend is kept during the posterior decrease in the *cof*. Figure 10b shows that the average stationary coefficient of friction is between 0.55 and 0.72 for all specimens, and again it is visible that VABB is systematically less frictional than BB specimens. These results agree with other bibliographic references where it is tested the reduction of the friction force when VA is applied [39,40]. The comparison between similar pairs, such as 120-3-40 and 120-3-0 or 80-5-40 and 80-5-0, shows that the average *cof* is reduced when the specimens are VABB, so it could be said that VABB enhances friction reduction but under a limited range and within the tribo-setup conditions tested. Again, no particular relation between roughness parameters and *cof* is found, so it seems that the main contributors to the friction reduction are residual stresses enhancement and microstructure evolution for VABB specimens. VA seems beneficial to reduce the friction force during the fretting test, which agrees with the bibliography [39,40].

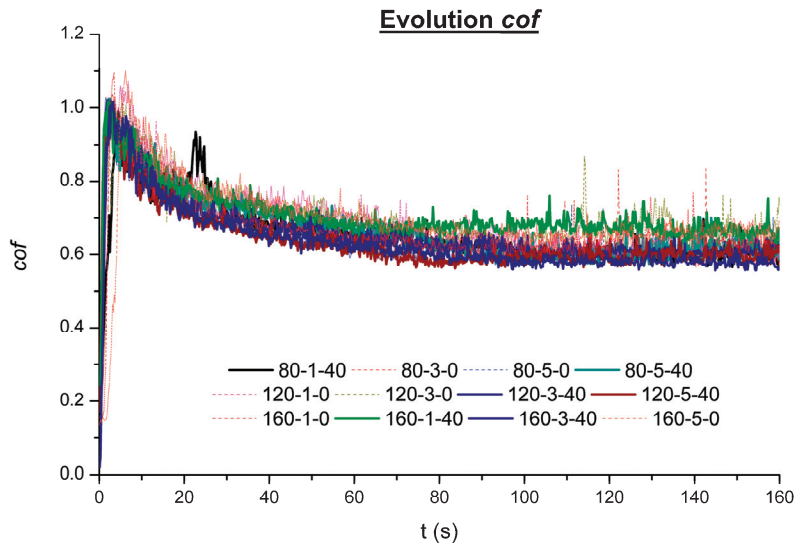


Figure 9. Evolution of the *cof*.

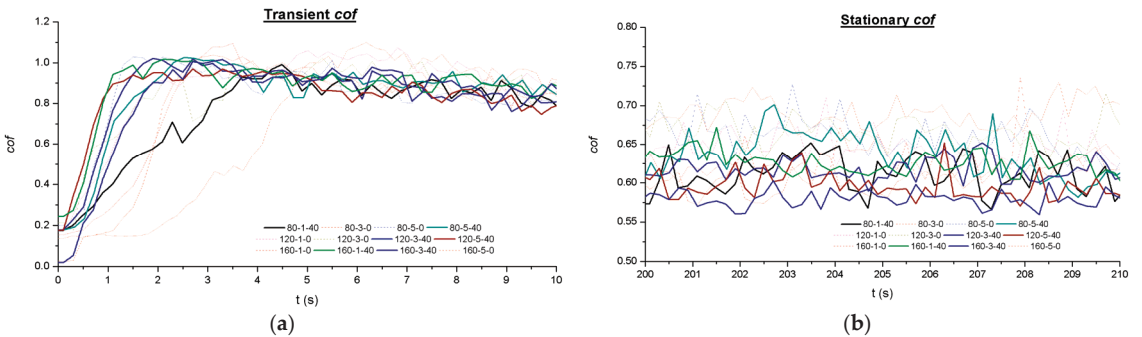


Figure 10. *cof* plot for the: (a) Transient; (b) Stationary.

3.5. Wear Resistance Analysis

The results obtained after the tribology and surface acquisition tests are presented in Figure 11.

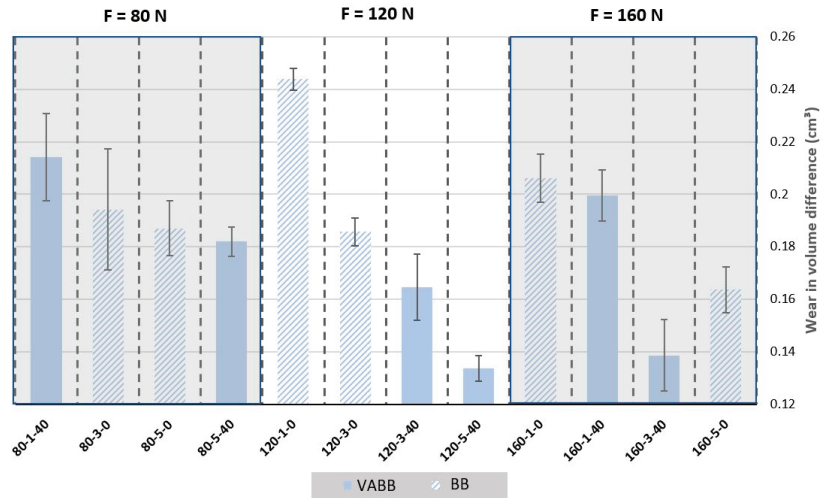


Figure 11. Wear results for 316L specimens.

The plot shows that, at first glance, the number of passes and the activation of the vibration assistance have a positive effect in terms of reducing the wear after the tribology tests. However, the burnishing force may improve the results but not for all combinations. For example, the worst specimen in terms of wear resistance is 120-1-0, but the best one is 120-5-40, making the most accentuated evolution of the different levels of forces applied. However, despite this first sample, if equal samples in terms of force are compared, such as 80-3-0 vs. 120-3-0 or 120-3-40 vs. 160-3-40, it is observed that increasing the burnishing force helps enhance the wear resistance. The same happens with the addition of vibration assistance, with 120-3-0 vs. 120-3-40 as a good example of it. The use of a low number of passes is clearly not improving as much as the other combinations. Despite experimenting with a lower standard deviation than other parameters, it is still difficult to determine if the number of passes and the addition of the vibration assistance enhances the wear resistance always and if they are significant, so for that, an ANOVA will be performed.

The mean effects and the interaction plots of the model, taking the final Wear as the output, are presented in Figure 12. First of all, the *p*-value analysis determines that the number of passes, the vibration assistance, and the vibration burnishing force, in that order, are the most important and significant parameters due to having a *p*-value lower than 5%. However, none of the interactions analyzed are significant enough to be considered. The 0.002 *p*-value registered for the number of passes means the huge impact that this variable has on the final value of the average roughness.

This investigation points to a wear enhancement by adding VA to a conventional ball burnishing process on 316L stainless steel shafts, which is estimated at a 7.3% of statistical improvement within the input range selected. It is found that a medium-high number of passes, the addition of the VA, and a high burnishing force is the best combination possible of the tested. The residual stress-wear relation found for this set of parameters hints that when residual stress is boosted, which is mainly caused by an increment of the plastic deformation at the surface due to the burnishing, the wear resistance is enhanced too. In fact, it was known that the increase in the burnishing force derives from a hardness increase, with a more homogeneous and compacted microstructure, which is the main consequence of a wear enhancement between two colliding surfaces [18]. Furthermore, the number of passes also increases the superficial hardness by plastically deforming several

times in the same spot, obtaining a more condensed grain microstructure. The VA is also described as a hardness increase factor in terms of depth of affectation and helping the incrementation of plastic deformation, thus boosting the effectiveness of the burnishing force-number of passes set. In addition, the reduction of the superficial roughness leads to a wear enhancement of 316L shafts [21], then makes sense that the VA really enhances the wear.

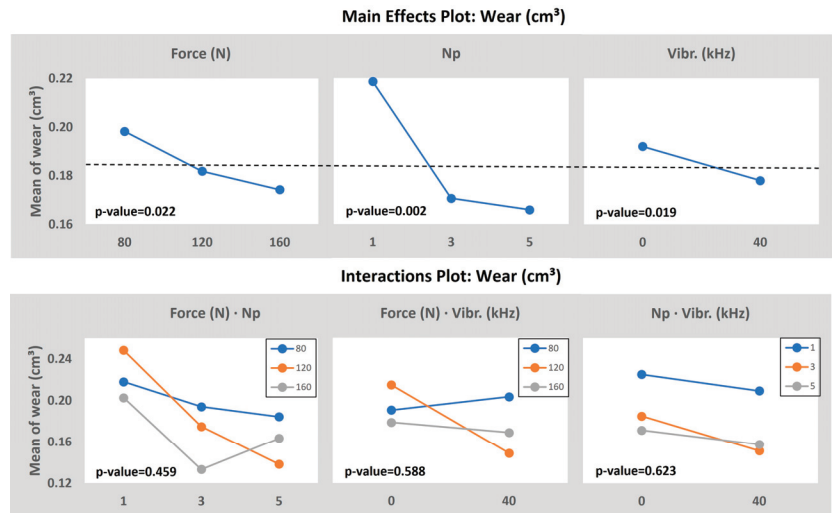


Figure 12. ANOVA results taking the Wear as the output value.

In terms of tribological properties enhancement, it can be interpreted that *cof* and wear are enhanced when VA is applied, mainly by a major impact of the compressive residual stress induction. Furthermore, the deformation features revealed in the microstructure pointed out major compactness, homogeneity, and depth of affectation by means of the VA. The possible formation of nano-structures in the form of twinings and dynamic recrystallization can contribute to wear resistance by accommodating deformation and preventing crack initiation and propagation. Plastic deformation helps distribute the applied load and reduces the concentration of stress at localized points, which can reduce wear and may explain the evolution of both properties when the burnishing inputs are augmented. The work-hardening induced strengthens the material subsurfaces by increasing dislocation density and promoting grain refinement, making the surface more resistant to wear.

4. Discussion

The roughness results determine that the number of passes is the most influential parameter and is followed by the burnishing force, which coincides with some bibliographic references with the same material [21]. It has also been proven that VABB offers better results than BB in terms of surface quality, as was also expected [41,42].

Micro-structural results present deformation due to the shearing of machining and BB/VABB processes. It is reported an increase in the depth of affectation when the VA is applied, and, especially, a major presence of deformation mechanisms expressed as plan sliding. These deformations are compatible with a twinning formation microstructure on a nanometric scale [33], which could induce nanograin refinement and, combined with a dislocation network similar to the present on these specimens. This assumption makes sense after noticing an improvement in the compressive residual stresses and roughness when applying VA. However, further confirmations should be made in the future by performing EBSD and TEM analysis at the surface to understand better the overall plastic deformation.

In terms of residual stresses, it is reported an increase in the von Mises residual stress at the surface by increasing the burnishing force and the number of passes, also applying VABB instead of BB to enhance them, which is estimated in an 11.5% increase. These results are within the scope because increasing the burnishing force causes a larger plastic deformation and is boosted by the vibration amplitude of the assistance [30]. The number of passes has been reported as another very influential parameter to enhance the residual stresses within a burnishing process [38].

The results in terms of *cof* show no heavy variation between specimens, which may indicate that the input range of values is not very influential. However, results displayed that may exist a friction reduction when VA is applied, as it is shown in Figure 10, during the stationary zone. This could be explained due to the fact that it is demonstrated that friction reduction is directly related to the initial roughness by decreasing as well as roughness [30]. Therefore, by modifying the burnishing force and number of passes to wider values, maybe a more incisive conclusion can be achieved in order to see if the VA really boosts the performance or if it is insignificant in terms of friction reduction. Furthermore, it was kept constant the counter-part material and the tribology testing force, so more tests should be performed in this field to arrive at a definitive conclusion about the VA within this VABB-tribology combination.

The main contribution of this investigation points to a wear enhancement by adding VA to a conventional ball burnishing process on 316L stainless steel shafts, which is estimated at a 7.3% of improvement within the input range selected. It is found that a medium–high number of passes, the addition of the VA, and a high burnishing force is the best-performing combination of all tested. The residual stress–wear relation found for this set of parameters hints that when residual stress is boosted, which is mainly caused by a hardness increase in the surface due to the burnishing, the wear is enhanced too. In fact, it was known that the increase in the burnishing force derives from a hardness increase, with a more homogeneous and compacted microstructure, which is the main consequence of a wear enhancement between two colliding surfaces [18]. Furthermore, the number of passes also increases the superficial hardness by plastically deforming several times in the same spot, obtaining a more condensed grain microstructure. The VA is also described as a hardness increase factor in terms of depth of affectation and helping the incrementation of plastic deformation, thus boosting the effectiveness of the burnishing force–number of passes set. In addition, the reduction of the superficial roughness leads to a wear enhancement [21] of 316L shafts, then makes sense that the VA really enhances the wear. Indeed, the VABB microstructure pictures revealed a higher density of plastic deformation plans or traces. This is caused by a more intense stress field due to the compression exerted by the ball during the process, and the depth of affectation is enhanced by the easiness of dislocation inductions during the assistance. This compressive field, observed as an increase in the compressive residual stress, actuates as a protector coating by means of a potential hardness increase on the surface, thus reducing the implicit wear and sliding force during the tribology testing.

5. Conclusions

With all the tests and analyses performed, it can be concluded that

- Ball burnishing improves the average roughness of 316L shaft surfaces, and the vibration assistance improves this property, statistically, by 9% in average terms. The best parameters found in this study correspond to 160 N of force, five passes, and the activation of the vibration assistance.
- The coefficient of friction seems to be similar for all specimens tested. However, it is noticed that the vibration assistance could reduce up to 2.2% despite not being statistically significant.
- The increase in the residual stresses in the tangential direction is directly dependent on the number of passes and the force applied, while the axial seems to be similar for

all specimens. The VA enhances the von Mises stress value by 11.5% compared to conventional ball burnishing.

- The wear decreased by 7.3% when using VABB instead of BB. It is also reported that the increase in the number of passes and the burnishing force helps to enhance its resistance. It is also found that there exists a relation between the von Mises residual stress and the wear of the tribology testing.

These results confirm the positive effect of vibration-assisted ball burnishing compared to conventional ball burnishing in terms of wear resistance and increase in residual stresses in 316L shafts. However, further questions can be made starting with the analysis of the microstructure evolution and depth affectation when using different burnishing parameters. This may help to understand the hardness profile in depth and add more complementary information to the residual stresses and the wear reported, which may be related. Another point of focus is to perform a wider range of burnishing parameters and see if there is a variation in the coefficient of friction once the microstructure is analyzed by performing EBSD and TEM tests.

Author Contributions: Conceptualization, E.V.-C., V.W., R.J.-M., J.A.T.-R., J.L. and G.D.; methodology, E.V.-C., V.W., R.J.-M. and J.L.; software, E.V.-C., V.W. and J.L.; validation, V.W., R.J.-M., J.A.T.-R., J.L. and G.D.; formal analysis, E.V.-C., V.W., J.L. and G.D.; investigation, E.V.-C., J.A.T.-R. and J.L.; resources, V.W., R.J.-M., J.A.T.-R., J.L. and G.D.; data curation, E.V.-C.; writing—original draft preparation, E.V.-C.; writing—review and editing, E.V.-C., V.W., R.J.-M., J.A.T.-R., J.L. and G.D.; visualization, E.V.-C.; supervision, V.W., R.J.-M., J.A.T.-R., J.L. and G.D.; project administration, G.D.; funding acquisition, R.J.-M., J.A.T.-R., J.L. and G.D. All authors have read and agreed to the published version of the manuscript.

Funding: This research was funded by the Ministry of Science and Innovation of Spain, through grant PDC2022-133596-I00, which is greatly appreciated.

Institutional Review Board Statement: Not applicable.

Informed Consent Statement: Not applicable.

Data Availability Statement: The raw/processed data required to reproduce these findings cannot be shared at this time, as the data also form part of an ongoing study.

Acknowledgments: We would like to really thank Karl Delbé and Metallicadour’s staff for the help with testing machines.

Conflicts of Interest: The authors declare no conflict of interest.

References

1. Lodhi, M.J.K.; Deen, K.M.; Greenlee-Wacker, M.C.; Haider, W. Additively manufactured 316L stainless steel with improved corrosion resistance and biological response for biomedical applications. *Addit. Manuf.* **2019**, *27*, 8–19. [[CrossRef](#)]
2. Teo, A.Q.A.; Yan, L.; Chaudhari, A.; O’Neill, G.K. Post-processing and surface characterization of additively manufactured stainless steel 316l lattice: Implications for biomedical use. *Materials* **2021**, *14*, 1376. [[CrossRef](#)] [[PubMed](#)]
3. Bartolomeu, F.; Buciumeanu, M.; Pinto, E.; Alves, N.; Carvalho, O.; Silva, F.S.; Miranda, G. 316L stainless steel mechanical and tribological behavior—A comparison between selective laser melting, hot pressing and conventional casting. *Addit. Manuf.* **2017**, *16*, 81–89. [[CrossRef](#)]
4. Vafa, E.; Bazargan-Lari, R.; Bahrololoom, M.E. Electrophoretic deposition of polyvinyl alcohol/natural chitosan/bioactive glass composite coatings on 316L stainless steel for biomedical application. *Prog. Org. Coat.* **2021**, *151*, 106059. [[CrossRef](#)]
5. Bekmurzayeva, A.; Duncanson, W.J.; Azevedo, H.S.; Kanayeva, D. Surface modification of stainless steel for biomedical applications: Revisiting a century-old material. *Mater. Sci. Eng. C* **2018**, *93*, 1073–1089. [[CrossRef](#)]
6. Tugay, I.O.; Hosseinzadeh, A.; Yapici, G.G. Hardness and wear resistance of roller burnished 316L stainless steel. *Mater. Today Proc.* **2021**, *47*, 2405–2409. [[CrossRef](#)]
7. Bikdeloo, R.; Farrahi, G.H.; Mehmanparast, A.; Mahdavi, S.M. Multiple laser shock peening effects on residual stress distribution and fatigue crack growth behaviour of 316L stainless steel. *Theor. Appl. Fract. Mech.* **2020**, *105*, 102429. [[CrossRef](#)]
8. Slavov, S.; Dimitrov, D.; Konsulova-Bakalova, M.; Vasileva, D. Impact of ball burnished regular reliefs on fatigue life of AISI 304 and 316L austenitic stainless steels. *Materials* **2021**, *14*, 2529. [[CrossRef](#)]
9. Yilmaz, H.; Sadeler, R. Impact wear behavior of ball burnished 316L stainless steel. *Surf. Coat. Technol.* **2019**, *363*, 369–378. [[CrossRef](#)]

10. Kovács, Z.F.; Viharos, Z.J.; Kodácsy, J. Surface flatness and roughness evolution after magnetic assisted ball burnishing of magnetizable and non-magnetizable materials. *Measurement* **2020**, *158*, 107750. [[CrossRef](#)]
11. Jerez-Mesa, R.; Landon, Y.; Travieso-Rodríguez, J.A.; Dessein, G.; Lluma-Fuentes, J.; Wagner, V. Topological surface integrity modification of AISI 1038 alloy after vibration-assisted ball burnishing. *Surf. Coat. Technol.* **2018**, *349*, 364–377. [[CrossRef](#)]
12. Velázquez-Corral, E.; Jerez-Mesa, R.; Llumà, J.; Wagner, V.; Dessein, G.; Travieso-Rodríguez, J. A Wear resistance enhancement of AISI 1045 steel by vibration assisted ball burnishing process. *Procedia CIRP* **2022**, *108*, 287–292. [[CrossRef](#)]
13. Dzierwa, A.; Markopoulos, A.P. Influence of ball-burnishing process on surface topography parameters and tribological properties of hardened steel. *Machines* **2019**, *7*, 11. [[CrossRef](#)]
14. Saldaña-Robles, A.; Plascencia-Mora, H.; Aguilera-Gómez, E.; Saldaña-Robles, A.; Marquez-Herrera, A.; Diosdado-De la Peña, J.A. Influence of ball-burnishing on roughness, hardness and corrosion resistance of AISI 1045 steel. *Surf. Coat. Technol.* **2018**, *339*, 191–198. [[CrossRef](#)]
15. Sova, A.; Courbon, C.; Valiorgue, F.; Rech, J.; Bertrand, P. Effect of turning and ball burnishing on the microstructure and residual stress distribution in stainless steel cold spray deposits. *J. Therm. Spray Technol.* **2017**, *26*, 1922–1934. [[CrossRef](#)]
16. Alshareef, A.J.; Marinescu, I.D.; Basudan, I.M.; Alqahtani, B.M.; Tharwan, M.Y. Ball-burnishing factors affecting residual stress of AISI 8620 steel. *Int. J. Adv. Manuf. Technol.* **2020**, *107*, 1387–1397. [[CrossRef](#)]
17. Chomienne, V.; Valiorgue, F.; Rech, J.; Verdu, C. Influence of ball burnishing on residual stress profile of a 15-5PH stainless steel. *CIRP J. Manuf. Sci. Technol.* **2016**, *13*, 90–96. [[CrossRef](#)]
18. Revankar, G.D.; Shetty, R.; Rao, S.S.; Gaitonde, V.N. Wear resistance enhancement of titanium alloy (Ti–6Al–4V) by ball burnishing process. *J. Mater. Res. Technol.* **2017**, *6*, 13–32. [[CrossRef](#)]
19. Avilés, R.; Albizuri, J.; Rodríguez, A.; De Lacalle, L. Influence of low-plasticity ball burnishing on the high-cycle fatigue strength of medium carbon AISI 1045 steel. *Int. J. Fatigue* **2013**, *55*, 230–244. [[CrossRef](#)]
20. Attabi, S.; Himour, A.; Laouar, L.; Motallebzadeh, A. Mechanical and wear behaviors of 316L stainless steel after ball burnishing treatment. *J. Mater. Res. Technol.* **2021**, *15*, 3255–3267. [[CrossRef](#)]
21. Attabi, S.; Himour, A.; Laouar, L.; Motallebzadeh, A. Effect of ball burnishing on surface roughness and wear of AISI 316L SS. *J. Bio-Tribo-Corros.* **2021**, *7*, 7. [[CrossRef](#)]
22. Blaha, F.; Langenecker, B. Elongation of zinc monocrystals under ultrasonic action. *Die Naturwiss.* **1955**, *42*, 556. [[CrossRef](#)]
23. Teimouri, R.; Amini, S.; Bami, A.B. Evaluation of optimized surface properties and residual stress in ultrasonic assisted ball burnishing of AA6061-T6. *Measurement* **2018**, *116*, 129–139. [[CrossRef](#)]
24. Liu, Y.; Wang, L.; Wang, D. Finite element modeling of ultrasonic surface rolling process. *J. Mater. Process. Technol.* **2011**, *211*, 2106–2113. [[CrossRef](#)]
25. Fernández-Osete, I.; Estevez-Urra, A.; Velázquez-Corral, E.; Valentín, D.; Llumà, J.; Jerez-Mesa, R.; Travieso-Rodríguez, J.A. Ultrasonic vibration-assisted ball burnishing tool for a lathe characterized by acoustic emission and vibratory measurements. *Materials* **2021**, *14*, 5746. [[CrossRef](#)] [[PubMed](#)]
26. Jerez-Mesa, R.; Fargas, G.; Roa, J.J.; Llumà, J.; Travieso-Rodríguez, J.A. Superficial effects of ball burnishing on trip steel AISI 301LN sheets. *Metals* **2021**, *11*, 82. [[CrossRef](#)]
27. *ASTM G132-96*; Standard Test Method for Pin Abrasion Testing. ASTM international: West Conshohocken, PA, USA, 2013.
28. *ISO 25178-2:2012*; Geometric Product Specification (GPS). Surface Texture: Areal. Part 2: Terms, Definitions and Surface Texture Parameters. International Organization for Standardization: Geneva, Switzerland, 2012.
29. Huuki, J.; Hornborg, M.; Juntunen, J. Influence of ultrasonic burnishing technique on surface quality and change in the dimensions of metal shafts. *J. Eng.* **2014**, *2014*, 124247. [[CrossRef](#)]
30. Liu, Z.; Dai, Q.; Deng, J.; Zhang, Y.; Ji, V. Analytical modeling and experimental verification of surface roughness in the ultrasonic-assisted ball burnishing of shaft targets. *Int. J. Adv. Manuf. Technol.* **2020**, *107*, 3593–3613. [[CrossRef](#)]
31. Salmi, M.; Huuki, J.; Ituarte, I.F. The ultrasonic burnishing of cobalt-chrome and stainless steel surface made by additive manufacturing. *Prog. Addit. Manuf.* **2017**, *2*, 31–41. [[CrossRef](#)]
32. Teimouri, R.; Liu, Z. An analytical prediction model for residual stress distribution and plastic deformation depth in ultrasonic-assisted single ball burnishing process. *Int. J. Adv. Manuf. Technol.* **2020**, *111*, 127–147. [[CrossRef](#)]
33. Agrawal, A.K.; Singh, A. Limitations on the hardness increase in 316L stainless steel under dynamic plastic deformation. *Mater. Sci. Eng. A* **2017**, *687*, 306–312. [[CrossRef](#)]
34. Mhaede, M. Influence of surface treatments on surface layer properties, fatigue and corrosion fatigue performance of AA7075 T73. *Mater. Des.* **2012**, *41*, 61–66. [[CrossRef](#)]
35. Zhang, T.; Bugtai, N.; Marinescu, I.D. Burnishing of aerospace alloy: A theoretical–experimental approach. *J. Manuf. Syst.* **2015**, *37*, 472–478. [[CrossRef](#)]
36. El-Khabeery, M.M.; El-Axir, M.H. Experimental techniques for studying the effects of milling roller-burnishing parameters on surface integrity. *Int. J. Mach. Tools Manuf.* **2001**, *41*, 1705–1719. [[CrossRef](#)]
37. Teimouri, R.; Skoczypiec, S. Theoretical study including physic-based material model to identify underlying effect of vibration amplitude on residual stress distribution of ultrasonic burnishing process. *J. Manuf. Process.* **2022**, *80*, 116–131. [[CrossRef](#)]
38. Shivalingappa, D. The influence of ball and roller burnishing process parameters on surface integrity of Al 2024 alloy. *Mater. Today Proc.* **2020**, *27*, 1337–1340. [[CrossRef](#)]

39. Chowdhury, M.A.; Helali, M. The effect of amplitude of vibration on the coefficient of friction for different materials. *Tribol. Int.* **2008**, *41*, 307–314. [[CrossRef](#)]
40. Gao, H.; Guo, Y.; Bao, G.; Reynaerts, D. Influence of vibrated area and normal force on friction reduction ratio between NBR/aluminum couple. *Tribol. Int.* **2015**, *82*, 95–100. [[CrossRef](#)]
41. Teramachi, A.; Yan, J. Improving the surface integrity of additive-manufactured metal parts by ultrasonic vibration-assisted burnishing. *J. Micro Nano-Manuf.* **2019**, *7*, 024501. [[CrossRef](#)]
42. Swirad, S.; Pawlus, P. The effect of ball burnishing on dry fretting. *Materials* **2021**, *14*, 7073. [[CrossRef](#)]

Disclaimer/Publisher’s Note: The statements, opinions and data contained in all publications are solely those of the individual author(s) and contributor(s) and not of MDPI and/or the editor(s). MDPI and/or the editor(s) disclaim responsibility for any injury to people or property resulting from any ideas, methods, instructions or products referred to in the content.

MDPI
St. Alban-Anlage 66
4052 Basel
Switzerland
www.mdpi.com

Materials Editorial Office
E-mail: materials@mdpi.com
www.mdpi.com/journal/materials



Disclaimer/Publisher's Note: The statements, opinions and data contained in all publications are solely those of the individual author(s) and contributor(s) and not of MDPI and/or the editor(s). MDPI and/or the editor(s) disclaim responsibility for any injury to people or property resulting from any ideas, methods, instructions or products referred to in the content.



Academic Open
Access Publishing

mdpi.com

ISBN 978-3-0365-9285-5